UNIVERSITÀ DEGLI STUDI DI MILANO

DIPARTIMENTO DI CHIMICA

PhD course in Chemical Sciences - XXVIII cycle

PATTERNING AND MODULATION OF OXIDE SURFACE PROPERTIES

PhD candidate:

Guido Soliveri

Tutor: Prof. Silvia Ardizzone
Co-tutor: Prof. Rita Annunziata
Coordinator: Prof. Emanuela Licandro

2015

Patterning and Modulation of Oxide Surface Properties

Guido Soliveri

November 2015

Abstract

Most of the topics dealt with in this thesis belong to surface science. The starting point was the fundamental understanding of phenomena at the oxide-gas interface and the effect of its modification. Such knowhow was then used to solve (or, at least, to attempt to solve) issues of critical impact in everyday life: the increasing lifetime of building materials employed in low-impact smart houses; the fouling prevention in electroanalytical sensors for neurotransmitter detection; the unspecialized laboratories accessibility to microlithography, critical to device miniaturization. These challenges might seem not related, but they actually share deep scientific and technological foundations. The physicochemical modification of oxide surfaces, the creation of organic/inorganic hybrids and the exploiting / the enhancing of semiconductor peculiar properties allowed us, starting from the foundation, the realization of proof-of-concept protocols and devices, ready for the pre-commercial development.

The Leitmotif of my research was the synthesis and the modification of titanium dioxide surfaces. TiO_2 has been the main character in physico, physicochemical and material science researches of the last 50 years. Biocompatibility and low cost make it engaging for many applications. Its (near-UV active) semiconductor features, well known and abundantly investigated by the scientific community, are acquiring central interest also in many markets with the development of self cleaning coatings, windows and asphalts, anti-fogging mirrors and self-sterilizing surgery rooms and instrumentations. New generation batteries and solar cells are going to be developed as commercial prototypes. One of the biggest challenges in the titania fundamental research is **the enhancement of activity in the solar spectrum**. First, the most recent aspects in titania doping and promotion were touched. While, in the last twenty years, great effort has been made in the mono-atomic doping of titania and in the understanding of the influence of the dopant position in the titania lattice and its electronic behavior, the most recent literature describes the co-promotion of the material by two (or more) atoms doping. The metal/non-metal codoping seems especially promising; the synergetic effect of the two atoms in the TiO_2 lattice was both theoretically and experimentally proved. In this contest, the N/Nb codoping was analyzed, investigating the effect of the atoms in the lattice from morphological (surface area, porosity and crystallographic structure) and electronic point of view (EXAFS, UV-Vis absorption and EPR analyses). N/Nb codoping was compared with N/Ta co-doped samples, synthesized by two different procedures. The photoactivity of the two sample families was tested by a model reaction (the degradation of ethanol, throughout acetaldehyde intermediate) both under UV and solar simulated irradiation.

Then, a different approach in the modification of surfaces was tested. **The assembly of organic/inorganic hybrids** was tested; thanks to the formation of organic mono- or multi-layers at the surface,they can tune the chemistry, the polarity and the adhesion properties of the interface. Siloxanes were used as active agents, thanks to their compatibility with oxide materials and, especially, for the ability to self-assemble at the surface to form a monolayer. Siloxanes are able to react with the -OH groups at the surface, chemisorbing and polymerizing at the interface in such a way to form a monolayer with

tunable functionalities. Many different silanes were tested and their dipole momenta were related to their wettability properties. Such siloxanes chemisorb strongly both from the gas phase and the liquid phase. Their reactivity, both on smooth and rough surfaces, was tested *vs* the temperature of functionalization in gas phase. Many characterization techniques were adopted to understand the behavior of such molecules from a molecular point of view: magnetic (solid state NMR), microscopic (SEM, TEM, AFM), optical and electrochemical (CV and EIS). The science of adhesion and wettability was also adopted for the development of superhydrophobic coatings. Titanium dioxide particles with engineered morphology were used as the best candidate to create superhydrophobic/superhydrophilic patch-wise surfaces, exploiting their photoactivity (photolithograpy).

The core of the thesis was the synthesis, modification and application of **transparent photoactive thin films**. A procedure for the synthesis of smooth, transparent and photoactive TiO_2 thin layers was developed, and used to produce highly applicative devices and protocols. Such synthetic strategy is highly tunable and reproducible; the obtained films are robust and active and, most of all, require simple instrumentation (sol-gel procedure), which is highly appealing for the market. The films were properly characterized both form the morphological/mechanical and photochemical point of view. Apart their transparency and their thickness, the films were highly crystalline (pure anatase phase). Such procedure was firstly designed as a proof-of-concept for self-cleaning windows, but, thanks to its versatility and the high activity of the films, it leads the path towards highly applicative procedures and devices. The smoothness and the photoactivity brought me to the field of photolithograpy, especially in the direction of microlithography. The high activity of the titania allowed the use of safe and low-energetic lamps. No collimation was required to obtain a resolution lower than 5 μm. First of all, I tested the lithography on siloxane monolayer films, as a proof-of-concept of resolution and efficiency. But siloxanes, as many other self-assembled monolayer molecules, can be the pillars for 3D fabrication. Such monolayers were used as polymerization initiators for polymer brushes. If the initiators of polymerization are patterned, patterned polymer brushes will be obtained. That was the first report of polymer-brushes lithography exploiting the photoactivity of TiO_2 . Remote photocatalytic lithography makes this procedure extremely versatile. Exploiting the remote photocatalysis, in principle, any material can be used as a support for patterned polymer brushes growth (provided that the initiator are able to graft the surface).

The developed protocol for the synthesis of TiO_2 thin films was also used to design and engineer **complex electrodes for cyclovoltammetric analyses of biological samples**. Electrochemistry seems to be the best candidate for the development of an analytical option with sensitivity comparable with present analytical procedures but reduced time-per-analysis and cost. Unfortunately, catecholamines chemisorb and polymerize on metal and oxide electrodes quickly, making the device useless. Covering the electrode by a homogeneous, nano-porous thin layer of titania makes the surface photoactive. That is the first example in literature of self-cleaning nano-engineered electrodes for cyclic voltammetry. After the detection, also in simulated human serum and liquor, a fast and simple irradiation of the device, under non-hazardous UV-A lamp, degrades all the fouling on the surface without altering its features. The sensor, after each UV treatment, recovers its pristine performances, with full recovery in terms of selectivity and sensitivity. Irradiation trials were also performed directly in the analytical mixture, as a proof of concept for on-site application.

Modern era requires **flexible and light materials** for the building industry. Polymers are acquiring more and more interest thanks to their increasing performances and their smart properties. The drawbacks of such materials are connected to the low resistance to the UV light, the softness and the difficulties in cleaning procedure. The use of organic/inorganic hybrid, or better the coverage of plastic materials with an oxidic thin layer, can solve many of these problems, lengthening the lifetime of such materials. If

the covering oxide is also photoactive, the material can be self-cleaned when exposed to solar light. That is a big chemical challenge, because of many synthetic problems. Two different approaches were tested to solve this relevant issue. On one side, the hydrophobicity of ionic liquid modified SPES (sulfonated polyether sulfone) was combined with designed morphological features to confer superhydrophobicity. On the other side, the polymeric surface was covered with a transparent titania layer active in the near UV-region, able to mineralize organic molecules chemisorbed at the surface.

Eventually, a different approach to modify oxidic (and not only) surfaces is the creation of a **homogeneous layer of Ag nanoparticles by an innovative microwave procedure**. That simple and accessible strategy allowed us to produce plasmonic surfaces (thanks to the dimension and the homogeneity of the Ag particles) with countless applications. The layer was shown to be a very active substrate for surface enhancement Raman spectroscopy (SERS). Thanks to the versatility of the synthetic method, all shapes and dimensions can be covered. That makes it a perfect candidate for the production of new generation of SERS sensors. The sensitivity towards molecules of environmental and biomedical interest was proved.

Contents

Chapter 1

Introduction

Modern chemistry is strongly involved in solving everyday problems. Environment, energy, medicine and smart materials are probably the most considerable topics. Almost all the scientific community, public organizations[1] and many companies are working in this direction, contributing to the wellness of present and next generations.

In this contest, *surface chemistry* has been one of the main characters. The understanding of the phenomena at the interface of materials, the case-effective relationship between microscopic features and macroscopic peculiarities, up to the design of complex, nano-engineered devices make surface chemistry principles at the ground of many different fields. Many examples can be found in bio-engineered materials for surgical application[2], solar cells[3] and batteries[4], nano-electronics, water and air purification devices[5], self cleaning surfaces[6, 7], and many other.

More than half of the materials used in such technologies are inorganic, principally oxides. This *Thesis* covers part of this area, starting from the fundamental understanding of the phenomena at the solid-gas interface and the effect of its modification. Such knowhow will be used to solve (or, at least, to attempt to solve) issues of critical impact in everyday life:

a) How to increase the lifetime of building materials employed in low-impact smart houses? b) How to prevent fouling in electroanalytical sensors for neurotransmitter detection? c) How to increase the accessibility to microlithography, critical to device miniaturization, to unspecialized laboratories?

These challenges might seem not related among them but they actually share deep scientific and technological foundations. The physico chemical modification of oxide surfaces, the creation of organic/inorganic hybrids and the exploiting and the enhancing of peculiar properties of semiconductors allowed me and my collaborators, starting from the foundation, the realization of proof-of-concept protocols and devices, ready for the pre-commercial development.

The *Leitmotif* of this doctoral thesis is the synthesis and the modification of titanium dioxide surfaces. TiO_2 , as well described in Appendix A, has been the major character in physico, physico chemical and material science researches of the last 50 years[5, 8], especially from the Fujishima and Honda's report in 1972[9], describing the photo-electrocemical activation of titania. TiO_2 has been long used as the white pigment (rutile phase) in coatings and as UV-absorber (also scatterer and refracter) in the suncream market. Biocompatibility and low cost make it engaging for many applications. Its (near-UV active) semiconductor features, well known and abundantly investigated by the scientific community, are acquiring central interest also in many markets with the development of self cleaning coatings, windows and asphalts, anti-fogging mirrors and self-sterilizing surgery rooms and instrumentations. New generation batteries and solar cells are going to be developed as commercial prototype. One of the biggest challenges

in the titania fundamentals research is the enhancement of activity in the solar spectrum[8]. The first section, titled *Titanium Dioxide Doping and Co-doping*, touches the most recent aspects in titania doping and promotion. While, in the last twenty years, great effort has been made in the mono-atomic doping of titania, and in the understanding of the influence of the dopant position in the titania lattice and their electronic behavior, the most recent literature describes the co-promotion of the material by two (or more) atmos doping. The metal/non-metal co-doping seems especially promising; the synergetic effect of the two atoms in the TiO_2 lattice was both theoretically[10] and experimentally proved[11, 12]. In this contest, Chapter 2 will analyze the N/Nb co-doping, investigating the effect of the atoms in the lattice from morphological and electronic point of view. Chapter 3 will compare N/Nb co-doping with N/Ta co-doped samples, synthesized by two different procedures. The photoactivity of the two sample families will be tested by a model reaction (the degradation of ethanol, throughout acetaldehyde intermediate) both under UV and solar simulated irradiation. Such valuable information, of great importance in the understanding of the behavior of this complex materials, were obtained thanks to the collaboration of many scientists and the support of ESRF (European Synchrotron Radiation Facility in Grenoble, France).

The second section, titled *Wettability Modulation of Oxide Surfaces*, will describe a different approach in the modification of surfaces, or rather, the creation of organic/inorganic hybrids, that, thanks to the formation of organic mono- or multi-layers at the surface, can tune the chemistry, the polarity and the adhesion properties of the interface[13, 14]. Siloxanes will be used as active agents, thanks to their compatibility with oxide materials and, especially for the ability to self-assemble at the surface in order to make a monolayer. This relevant feature was firstly discovered in Jacob Sagiv's group in 1983[15]; siloxanes are able to react with the -OH group at the surface, chemisorbing and polymerizing at the interface in such a way to form a monolayer with tunable functionalities [16] (as explained farther on, Figure 5.1). Many different silanes will be reported (Chapter 4) and their dipole momenta will be related to their wettability properties. Such siloxanes chemisorb strongly both from the gas and the liquid phase. Their reactivity, both on smooth and rough surfaces, will be tested *vs* the temperature of functionalization in gas phase (Chapter 5). In the following two chapters (Chapters 6 and 7), the science of adhesion and wettability will be adopted for the development of superhydrophobic coatings. An overview of the theoretical aspects behind that will be described in Appendix B. Titanium dioxide particles with engineered morphologies will be used as the best candidates to crate superhydrophobic/superhydrophilic patch-wise surfaces, exploiting its photoactivity (photolithograpy).

The core of the Thesis is the third section, *Titanium Dioxide Thin Film*, in which a procedure for a synthesis of smooth, transparent and photoactive TiO_2 thin layers will be developed (Chapter 8), and used to produce highly applicative devices and protocols. Such synthetic strategy is highly tunable and reproducible; the obtained films are robust and active and, most of all, require simple instrumentation (sol-gel procedure), which is highly appealing for the market. Such procedure was firstly designed as a proof of concept for self-cleaning windows, but, thanks to its versatility and the high activity of the films, it lids the path towards highly applicative procedures and devices. The smoothness and the photoactivity bring me to the field of photolithograpy(Chapter 9), especially in the direction of micro-lithography. The high activity of the titania allows the use of safe and low-energetic lamps. No collimation is required to obtain a resolution lower than 5 μm. Chapter 9 will report, in the first part, the lithography of siloxane monolayers, as a proof-of-concept of resolution and efficiency. But siloxanes, as many other self-assembled monolayer molecules, can be the pillars for 3D fabrication. Here, such monolayers will be used as polymerization initiators for polymer brushes. Polymer brushes are surface-tethered, highly-stretched polymer chains. They exhibit excellent robustness and well-organized chain conformation, which endow superior control over several surface properties such as morphology, grafting density and chemical

composition[17–19]. If the initiators of polymerization are patterned, patterned polymer brushes will be obtained. Here, the first example of polymer-brushes lithography exploiting the photoactivity of TiO_2 will be reported. Patterned polymer brushes [20, 21] are versatile building blocks for micro-fabrication and controlled assembly of small particles[22], sensors/biosensors and actuators[23–31], drug delivery systems[32], electronic devices[33], anti-biofouling coatings[34], and biocompatible scaffolds[35]. In general they are efficient means to confer smart, stimuli-responsive behavior to surfaces and interphases[36–38]. Remote photo-catalytic lithography makes this procedure extremely versatile[8]. Exploiting the remote photocalaysis (that will be described in Chapter 9 and Appendix A), in principle, any material can be used as a support for patterned polymer brushes growth (provided that the initiator are able to graft the surface). Polymer brushes allowed to tune, at will, the chemistry of the surface. That is not just an academic challenge; it can be crucial in many different fields with high technological impact. In this days, my colleagues and I are developing a cyclo voltammetric sensor that exploits those findings for implementation in micro-electronic devices.

Modern era requires flexible and light materials for the building industry[39, 40]. Polymer are acquiring more and more interest thanks to their increasing performances and their smarter properties. The drawbacks of such materials are connected to the low resistance to the UV light, the softness and the difficulties in cleaning procedure. The use of organic/inorganic hybrids, or better the coverage of plastic materials with an oxidic thin layer, can solve many of these problems, lengthening the life time of such materials. If the covering oxide is also photoactive, the material can be self-cleaned when exposed to solar light[39]. That is a big chemical challenge, because of many synthetic problems that will be listed in Chapter 10. In that chapter, two different approaches will be described in order to solve this relevant issue.

The developed protocol for the synthesis of TiO_2 thin films will be also used to design and engineer complex electrodes for cyclo voltammetric analysis of biological samples. Neurotrasmitters will be the target molecules. Their quantitative measurements under physiological conditions have critical importance in clinical diagnosis[41–43]. That is very true for catecholamine neurotransmitters, because of their key roles in behavior expression, during excessive oxidative stress events, for the early diagnosis of neurodegenerative diseases (such as Parkinson disease[44, 45]) and some kind of tumors (*e.g.* pheochromocytoma[46]). The principal analytical method used in clinical reality is based on an HPLC analysis connected to a conductivity detector; the sample must be pretreated by an acid solid phase extraction at high temperatures, to remove potential interferents. This technique allows the contemporaneous detection of the analytes, but requires a complicated pretreatment, long time of analysis and high costs. For these reasons many efforts could be found in literature in proposing robust alternatives, also with the function of pre-screening. Electrochemistry seems the best candidate for the development of an analytical option with comparable sensitivity, reduced analytical time and sample pretreatment and low cost. Especially, nano-engineered electrodes for cyclo-voltammetric analysis are acquiring great interest in literature thanks to tunable sensibility and selectivity[47, 48]. Unfortunately, catecholamines chemisorb and polymerize on metal and oxide electrodes quickly, making the device useless[49]. No traditional cleaning procedure can be adopted without altering the nano-engineered surface. Fouling is a great issue in term of cost per analysis. Covering the electrode by a homogeneous, nano-porous thin layer of photoactive titania makes the the surface photoactive. That is the first example in literature of self-cleaning nano-engineered electrodes for cyclic voltammetry[50] (Chapter 11). After the detection, also in simulated human serum and liquor, a fast and simple irradiation of the device under non-hazardous UV-A lamp degrades all the fouling on the surface without altering its features. The sensors turn back to its initial values of sensitivity. The sensor, after each UV treatment, recovers its pristine performance, with full

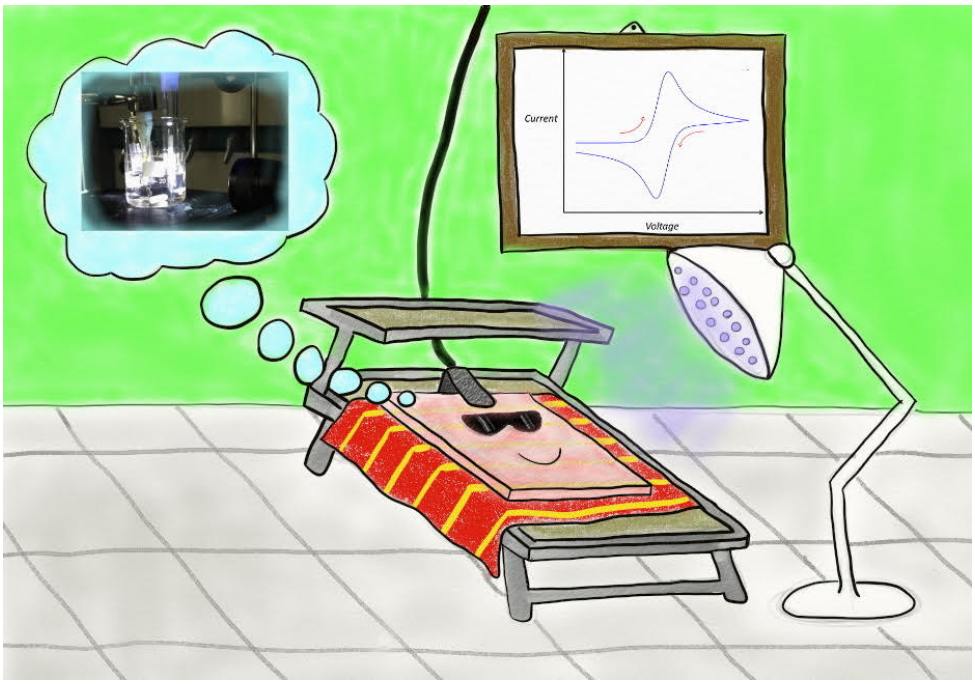

Figure 1.1: *Electrochemical sensors cleaned by light: a proof of concept for on site applications towards integrated monitoring systems[51].*

recovery in term of selectivity and sensitivity. Such electrodes reveal also high performances in term of selectivity and sensitivity towards dopamine, norepinephrine and serotonin. Cyclo voltammetric sensors with self-cleaning properties can be appealing also for environmental *in situ* detections, without the need to replace it after a while (Figure 1.1, ref.[51]). Irradiation trials were performed directly in the analytical mixture, showing high efficiency notwithstanding the liquid medium.

Eventually, a different approach to modify oxidic (and not only) surfaces is the creation of a homogeneous layer of Ag nano-particles by an innovative microwave procedure. That simple and accessible strategy allowed to produce plasmonic surfaces (thanks to the dimension and the homogeneity of the Ag particles) with countless applications[52, 53]. For example, in this Thesis, the layer will be shown to be a very active substrate for surface enhancement Raman spectroscopy (SERS). Thanks to the versatility of the synthetic method, all shapes and dimension can be covered. That makes it a perfect candidate for the production of new generation of SERS sensors.

In Appendix C, the reader can find many experimental information. While specific procedures are described chapter by chapter (sections *Specific procedures*), the reader can find methods, protocols and instrumentations used along all the Thesis, in the Appendix.

References

[1] E. Commission, HORIZON 2020, `http://ec.europa.eu/programmes/horizon2020/`.

[2] P. Leleux, J. Rivnay, T. Lonjaret, J.-M. Badier, C. Bnar, T. Herv, P. Chauvel, G. G. Malliaras, *Adv. Healthc. Mater.* **2015**, *4*, 142–147.

[3] X. Yang, J. Loos, S. C. Veenstra, W. J. H. Verhees, M. M. Wienk, J. M. Kroon, M. A. J. Michels, R. A. J. Janssen, *Nano Lett.* **2005**, *5*, 579–583.

[4] S. Goriparti, E. Miele, F. D. Angelis, E. D. Fabrizio, R. P. Zaccaria, C. Capiglia, *J. Power Sources* **2014**, *257*, 421 –443.

[5] K. Nakata, A. Fujishima, *J. Photochem. Photobio. C* **2012**, *13*, 169 –189.

[6] M. Callies, D. Quere, *Soft Matter* **2005**, *1*, 55–61.

[7] D. Qur, *Annu. Rev. Mater. Res.* **2008**, *38*, 71–99.

[8] A. Fujishima, X. Zhang, D. A. Tryk, *Surf. Sci. Rep.* **2008**, *63*, 515 –582.

[9] A. Fujishima, K Honda, *Nature* **1972**, *238*, 37–38.

[10] X. Ma, Y. Wu, Y. Lu, J. Xu, Y. Wang, Y. Zhu, *J. Phys. Chem. C* **2011**, *115*, 16963–16969.

[11] J. Lim, P. Murugan, N. Lakshminarasimhan, J. Y. Kim, J. S. Lee, S.-H. Lee, W. Choi, *J. Catal.* **2014**, *310*, 91 –99.

[12] S. S. Thind, G. Wu, A. Chen, *Appl. Catal. B* **2012**, *111 - 112*, 38 –45.

[13] S. Onclin, B. J. Ravoo, D. N. Reinhoudt, *Angew. Chem. Int. Edit.* **2005**, *44*, 6282–6304.

[14] Y. Paz, *Beilstein J. Nanotech.* **2011**, *2*, 845–861.

[15] L. Netzer, J. Sagiv, *J. Am. Chem. Soc.* **1983**, *105*, 674–676.

[16] K. Liu, M. Cao, A. Fujishima, L. Jiang, *Chem. Rev.* **2014**, *114*, 10044–10094.

[17] R. Barbey, L. Lavanant, D. Paripovic, N. Schwer, C. Sugnaux, S. Tugulu, H.-A. Klok, *Chem. Rev.* **2009**, *109*, 5437–5527.

[18] S. G. Boyes, A. M. Granville, M. Baum, B. Akgun, B. K. Mirous, W. J. Brittain, *Surf. Sci.* **2004**, *570*, 1 –12.

[19] O. Azzaroni, *J. Polym. Sci. Part A: Polym. Chem.* **2012**, *50*, 3225–3258.

[20] T. Chen, D. P. Chang, R. Jordan, S. Zauscher, *Beilstein J. Nanotech.* **2012**, *3*, 397–403.

[21] M. E. Welch, C. K. Ober, *J. Polym. Sci. Part B: Polym. Phys.* **2013**, *51*, 1457–1472.

[22] G. J. Dunderdale, J. R. Howse, J. P. A. Fairclough, *Langmuir* **2011**, *27*, 11801–11805.

[23] J. Cui, O. Azzaroni, A. del Campo, *Macromol. Rapid Commun.* **2011**, *32*, 1699–1703.

[24] G. J. Dunderdale, J. P. A. Fairclough, *Langmuir* **2013**, *29*, 3628–3635.

[25] M. Singh, O. Odusanya, G. M. Wilmes, H. B. Eitouni, E. D. Gomez, A. J. Patel, V. L. Chen, M. J. Park, P. Fragouli, H. Iatrou, N. Hadjichristidis, D. Cookson, N. P. Balsara, *Macromol.* **2007**, *40*, 4578–4585.

[26] C. R. Daniels, L. J. Tauzin, E. Foster, R. C. Advincula, C. F. Landes, *J. Phys. Chem. B* **2013**, *117*, 4284–4290.

[27] I. Tokareva, I. Tokarev, S. Minko, E. Hutter, J. H. Fendler, *Chem. Commun.* **2006**, 3343–3345.

[28] T. Chen, R. Ferris, J. Zhang, R. Ducker, S. Zauscher, *Prog. Polym. Sci.* **2010**, *35*, 94 –112.

[29] H. Ma, J. He, X. Liu, J. Gan, G. Jin, J. Zhou, *ACS Appl. Mater. Interfaces* **2010**, *2*, 3223–3230.

[30] H. C. McCaig, E. Myers, N. S. Lewis, M. L. Roukes, *Nano Lett.* **2014**, *14*, 3728–3732.

[31] C. Xu, X. Fu, M. Fryd, S. Xu, B. B. Wayland, K. I. Winey, R. J. Composto, *Nano Lett.* **2006**, *6*, 282–287.

[32] S. Kumar, Y. L. Dory, M. Lepage, Y. Zhao, *Macromol.* **2011**, *44*, 7385–7393.

[33] H. J. Snaith, G. L. Whiting, B. Sun, N. C. Greenham, W. T. S. Huck, R. H. Friend, *Nano Lett.* **2005**, *5*, 1653–1657.

[34] G. Gunkel, M. Weinhart, T. Becherer, R. Haag, W. T. S. Huck, *Biomacromol.* **2011**, *12*, 4169–4172.

[35] D. Falconnet, G. Csucs, H. M. Grandin, M. Textor, *Biomaterials* **2006**, *27*, 3044 –3063.

[36] S. Peng, B. Bhushan, *RSC Adv.* **2012**, *2*, 8557–8578.

[37] F. Zhou, W. T. S. Huck, *Phys. Chem. Chem. Phys.* **2006**, *8*, 3815–3823.

[38] S. Dai, P. Ravi, K. C. Tam, *Soft Matter* **2008**, *4*, 435–449.

[39] R. Fateh, R. Dillert, D. Bahnemann, *Langmuir* **2013**, *29*, 3730–3739.

[40] K. Reihs, A. Duparre, G. Notni, Substrate with a reduced light-scattering, ultraphobic surface and a method for the production of the same, CA Patent App. CA 2,409,959, **2001**.

[41] J. Meiser, D. Weindl, K. Hiller, *Cell Commun Signal* **2013**, *11*, 34.

[42] D. L. Robinson, A. Hermans, A. T. Seipel, R. M. Wightman, *Chem. Rev.* **2008**, *108*, 2554–2584.

[43] B. J. Venton, R. M. Wightman, *Anal. Chem.* **2003**, *75*, 414 A–421 A.

[44] A. Curulli, *Sensors* **2009**, *9*, 2437–2445.

[45] J. Segura-Aguilar, I. Paris, P. Muoz, E. Ferrari, L. Zecca, F. A. Zucca, *J. Neurochem.* **2014**, *129*, 898–915.

[46] K. Pacak, J. W. M. Lenders, G. Eisenhofer in *Pheochromocytoma*, Blackwell Publishing Ltd, **2008**, pp. 41–71.

[47] C. Brett, *Pure Appl. Chem.* **2001**, *73*, 1969–1977.

[48] C. Welch, R. Compton, *Anal. Bioanal. Chem.* **2006**, *384*, 601–619.

[49] J. Liebscher, R. Mrowczynski, H. A. Scheidt, C. Filip, N. D. Hadade, R. Turcu, A. Bende, S. Beck, *Langmuir* **2013**, *29*, 10539–10548.

[50] G. Soliveri, V. Pifferi, G. Panzarasa, S. Ardizzone, G. Cappelletti, D. Meroni, K. Sparnacci, L. Falciola, *Analyst* **2015**, *140*, 1486–1494.

[51] V. Pifferi, G. Soliveri, G. Panzarasa, S. Ardizzone, G. Cappelletti, D. Meroni, L. Falciola, *RSC Adv.* **2015**, *5*, 71210–71214.

[52] M. N. Nadagouda, T. F. Speth, R. S. Varma, *Acc. Chem. Res.* **2011**, *44*, 469–78.

[53] V. K. Sharma, R. a. Yngard, Y. Lin, *Adv. Colloid Interface Sci.* **2009**, *145*, 83–96.

Part I

Titanium dioxide doping and codoping

Chapter 2

Unraveling the cooperative mechanism of visible-light absorption in bulk N,Nb codoped TiO_2 nanopowders

Titanium dioxide has been the subject of extensive research in recent years due to its relevant photochemical and photophysical properties combined with its natural abundance, low cost and superior chemical and photo-stability[1]. The nanocrystalline TiO_2 applications are quite numerous and span from photocatalysis, self-cleaning and antifogging devices to solar energy conversion and photoelectrochemical water splitting[2–4].

Due to its wide band-gap (> 3 eV), however, the TiO_2 photoactivity is restricted to the UV-region, which represents only less than 5 % of the solar spectrum. Several approaches have been developed to promote the utilization of visible light ($\lambda > 400$ nm) by the TiO_2 -based materials. Two main different possibilities have been proposed depending on the final application, either doping by p-block nonmetal species (N, C, S, P etc.) or promoting the material by metal cations[5].

In the case of nonmetal species, the synthesis of N-doped TiO_2 has raised great interest and has become one of the most studied approaches to red shift the oxide light absorption[6, 7]. N-doping induces a visible light absorption by creating localized mid-gap states. It has been observed that both the structural and the electronic picture of these systems are largely affected by the conditions adopted for the sample synthesis and by the nature of the N source[8, 9]. Actually, these factors control the material microstructure, that in turn determines the concentration and nature of both extrinsic and intrinsic point defects. As for the latter, it is known that oxygen vacancies, $V_O^{\bullet\bullet}$, whose formation is favored by N doping[10], might reduce neighboring Ti ions and determine the formation of new gap states just below the conduction band (CB). It is believed that such defect-induced states could play a crucial role in enhancing the visible-light activity of N-doped TiO_2 [11–13]. However, such shallow mid-gap levels can also act as recombination centers for photogenerated charge carriers, lowering the quantum efficiency of the photo-induced process[11, 14]. Further, the limited structural stability of N-doped TiO_2 represents another unresolved issue[7, 15].

As for cationic dopants, the use of several metals of the first transition series has been proposed.

However, the enhanced absorption in the visible region has not always been accompanied by a significant improvement of the material photocatalytic performance. Rather, even detrimental effects were observed in some cases[16]. The doping effects are somehow different in the case of TiO_2 doped with high valence Sb(V) (d^{10}), Ta(V) (d^0) or Nb (V) (d^0) ions. The latter has been reported to promote both the photocatalytic activity and water splitting processes[17, 18], even when combined with other lower valence transition cations[19]. More importantly, the technological relevance of Nb-promoted TiO_2 materials goes beyond classical photocatalytical and photoelectrochemical applications, as they have recently raised significant attention for the development of transparent conductive oxides. Specifically, it has been reported that Nb-TiO_2 can show an electronic conductivity comparable to that of the classic transparent conductive systems (indium tin oxide, fluorine tin oxide), while maintaining optimal visible transparency[20, 21]. Such materials have received considerable attention also for the development of highly efficient photoanodes in dye-sensitized solar cells showing a reduced recombination loss and increased electron injection[22, 23].

The structural, electronic and defective properties of Nb-promoted TiO_2 systems play a major role in determining their final photoactivity. Two mechanisms have been proposed to account for the charge compensation of Nb^{5+} introduced in the TiO_2 lattice. One involves the creation of Ti^{3+} by excess electrons introduced by a mechanism of valence induction, while the other the creation of one Ti cation vacancy per four Nb introduced. Donor mid-gap states are usually quite deep within the gap, and they may be responsible for a faster electron-hole recombination[24]. Codoping is a possible way to make these states less deep and more shallow into the band gap. More specifically, compensating codoping of TiO_2 with nonmetals and transition metals is a highly promising way to generate second-generation photocatalysts, where the apparent band gap decrease occurs without increasing the electron-hole recombination rate[25–29]. Density functional theory (DFT) calculations have indeed shown a strong coupling between metals and N within the TiO_2 lattice, suggesting a possible increase in the photocatalytic performance of the material[7, 28, 30–32]. Marquez studied the structural and electronic properties of W, N co-doped titania observing enhanced photocatalytic properties[33]. Significant results have been reported also in the case of V, N and Fe, N titania systems[34, 35].

In this first part, the co-doping of non-metal (N) and metal elements will be investigated. In the Chapter 2, the role of N,Nb-codoping in the TiO_2 lattice will be analyzed; the electronic interaction between the oxide and the dopants and their synergistic effect will be studied. Chapter 3 will compare Nb,N-codoped samples with Ta,N-samples, analyzing also two distinct doping procedures and reporting their photocatalytic performances under UV and solar simulated light in the degradation of ethanol.

Studies concerning the co-promotion of TiO_2 by N and Nb species are scarce although the simultaneous presence of species might intrinsically help in compensating charge unbalance and eventually enhance the structure stability by inducing at the same time oxygen and Ti vacancies. The N,Nb-codoping of titania has been recently discussed in a theoretical study investigating its photoelectrochemical properties[24]. On the experimental side, Breault and Bartlett[36, 37] discussed heavily doped TiO_2 systems (defined by the authors as co-alloys). They showed that very large amounts of dopants (Nb contents up to 30 %) imply changes in the band edges that result in overall lower band gap materials. Keller et al.[18] prepared N,Nb co-doped titania nanotube arrays which show relevant visible light photoelectrochemical activity due to contents up to 15 % of Nb in the near-surface region. The only work relative to a conventionally N, Nb co-doped TiO_2 system is, to the best of our knowledge, the one by Lim et al.[38]. In this case the samples, prepared by a sol-gel procedure with $0.001 < \text{Nb/Ti molar ratio} < 0.03$, show N-Nb synergistic photocatalytic effects with respect to both the oxidation and the reduction of water pollutants.

The combination of Nb and N appears to be a novel and promising doping strategy to enhance the

Sample	**Nb/Ti nominal** % (molar)	**Nb/Ti EDX** % (molar)
T0	-	-
TNb_0.01	1.00	0.75
TNb_0.05	5.00	3.78
TN_0.01	-	-
TN_0.05	-	-
TNNb_0.005	0.50	0.31
TNNb_0.01	1.00	0.51
TNNb_0.05	5.00	2.15
TNNb_0.01_N_2	1.00	0.56

Table 2.1: *The nominal and experimental (EDX) Nb/Ti ratios of the synthesized samples.*

photoactivity of titania-based materials. However, the reasons underlying this evidence are still far to be fully understood. This chapter aims at bridging this gap. A possible electronic mechanism, where bulk Nb and N dopants cooperate synergistically, is proposed to account for experimental results. The compensating model for Nb/N titania codoping described above has already been put forward[24] but it has never been substantiated by a broad and thorough series of theoretical and experimental characterizations proving Nb lattice location and valence. This study is motivated by the superior photocatalytic performance of the co-doping with respect to each single doping solution.[38] More in detail, a series of N, Nb nanocrystalline titania samples, both mono- and co-doped, were synthesized by a sol-gel procedure. Crystallographic structure, local structure, microstructure and morphology of the powders were then probed at various length scales (from 10^{10} to 10^{6} m) by means of HR-XPRD, EXAFS, SEM, EDX and BET experiments. At the same time, DRS and EPR measurements provided information on the corresponding optical properties and defective features. Finally, periodic plane-wave DFT calculations were performed to supply a solid interpretative basis of the whole picture, explaining how different guest species and intrinsic point defects cooperate in determining the observed experimental response.

2.1 Results and discussion

The chemical composition of the samples was investigated by EDX analysis. The experimental Nb/Ti molar ratios are slightly lower than the calculated nominal ratios (Table 2.1), as commonly reported in the literature[37]. The nitrogen content needs instead a more detailed discussion. The very low N/Ti ratios adopted in these samples cannot be verified by EDX due to experimental limits. Indeed, previous studies have shown that the actual nitrogen content in TiO_2 lattice is generally much lower than the nominal amount[11, 14]. Nitrogen bulk quantification is quite a challenging task, since conventionally used techniques, such as X-ray photoelectron spectroscopy (XPS), provide information about the surface and near-subsurface composition of the oxide, which is greatly influenced by the presence of atmospheric contaminants (C, N and O)[8]. Previous studies on Nb-doped TiO_2 have also underlined other relevant discrepancies between bulk and surface compositions in such systems, such as a higher Nb content at the surface due to the occurrence of surface segregation phenomena[39]. Further, Bartlett and coauthors[36] reported by XPS the absence of any Ti^{3+} in heavily N,Nb-codoped samples, which was instead detected by EPR analyses. Being interested in the bulk effects of doping and codoping, we have chosen to rely on characterization techniques that are not merely surface sensitive, such EDX and EPR, to probe the composition and defective state of our samples.

Sample	Anatase	Brookite	α-NO_2
T0	0.6840(5)	0.316(1)	-
TN_0.05	0.6914(5)	0.309(1)	-
TNb_0.01	0.6929(5)	0.307(1)	-
TNNb_0.005	0.7179(4)	0.282(1)	-
TNNb_0.01	0.7698(4)	0.230(1)	-
TNNb_0.05	0.8065(3)	0.142(1)	0.052(1)
TNNb_0.01 N_2	0.7573(4)	0.243(1)	-

Table 2.2: *Phase composition of the materials investigated in the present study, as retrieved from Rietveld refinements of the HR-XRPD measurements. Numerical entries in this Table correspond to the graph shown in Figure 2.1b in the main text.*

2.1.1 Microstructure

Phase composition. Figure 2.1a shows the least squares fitting results *vs* the observed diffraction intensities for the undoped T0 specimen and for a series of mono- and co-doped nanopowders. Small fitting residuals are present in the diffractograms. These are due to the small inaccuracies of the final least-squares structural model in the description of profile asymmetry caused by axial beam divergence affecting low-order reflections. Also the highly defective nature of the nanostructured powders implies small anisotropies in the line profile broadening at higher angles. Nevertheless, the residuals are well-centered around the peaks and they average to zero, *i.e.*, cell parameters and main peak intensities are satisfactorily matched.

As we expected on the basis of our previous experience on similar materials[8, 11, 40] the major phase component is always TiO_2 -anatase (space group: $I4_1/amd$) with a non-negligible minority of brookite (Pbca), as it can be inferred from the peak at $2\theta \sim 10.0°$ originated from the (2 1 1) reflection of this phase. The most heavily codoped specimen (TNNb_0.05) shows in addition a small amount ($\sim$ 5 %, Table 2.2) of segregated α-NbO_2 oxide ($I4_1/a$)[41]. The segregation is clearly appreciable in the diffractogram from the secondary peak at $2\theta \sim 8.9°$, attributable to (4 0 0) and (0 4 0) equivalent reflections of the contaminating Nb oxide. Apart from α-NbO_2 oxide, no other crystalline phases were detected in our samples, since any attempt to add other Nb-containing structures to the model invariably led to the worsening of the least-squares fitting. The occurrence of surface segregation of Nb_xO_y is often reported at high Nb loadings[39, 42, 43] although the Nb content which determines such an effect and the obtained crystalline/amorphous phases strictly depend on the adopted synthetic conditions.

More quantitative information on the phase composition of the nanostructured powders is appreciable in Figure 2.1b, where the trend of the brookite content is shown as a function of the nominal doping extent. Interestingly, a single dopant species has a less appreciable effect on the brookite amount, that remains essentially unchanged ($\sim$ 31 %) on going from the undoped T0 reference material to the TNb_0.01 and TN_0.05 samples. On the contrary, the simultaneous presence of both N and Nb in the bulk structure invariably implies a significant decrease of the brookite phase, down to $\sim$ 14 % in the TNNb_0.05 material (green rhombi in Figure 2.1b). It is known that inclusion of the N dopant alone has a similar effect on the phase composition[8, 9], but the changes here observed occur at much lower dopant loadings. Moreover, the calcination conditions scarcely influence the final material composition, as the TNNb_0.01 samples bear an almost identical amount of brookite whether they are calcined in O_2 or N_2 (see the red triangle in Figure 2.1b). All these evidences imply that the observed changes are neither due to specific synthetic conditions nor are attributable to just one of the N, Nb guest species. Rather, the inclusion of both the dopants in the crystallographic structure should imply a strong thermodynamic driving force toward the

Sample	$< D_v >$			ϵ		
	anatase	brookite	α-NO_2	anatase	brookite	α-NO_2
T0	47(2)	44(4)	-	0.0204(3)	0.0115(7)	-
TN_0.05	46(2)	44(4)	-	0.0184(2)	0.0119(7)	-
TNb_0.01	48(2)	41(3)	-	0.0228(3)	0.011(1)	-
TNNb_0.005	44(2)	35(3)	-	0.0217(4)	0.013(1)	-
TNNb_0.01	32(1)	34(2)	-	0.0216(4)	0.009(1)	-
TNNb_0.05	25(1)	33(1)	29.2(8)	0.0166(4)	0.0241(3)	0.0208(5)
TNNb_0.01 N_2	27(1)	20.7(7)	-	0.0159(2)	0.007(1)	-

Table 2.3: *Average crystallite dimensions ($< D_v >$, Å), and lattice microstrain (ϵ, dimensionless) of the materials investigated, as retrieved from Rietveld refinements of HR-XRPD spectra. Both these quantities were estimated from the Williamson-Hall plot against h0l reflections up to* $\sin\theta/\lambda = 0.5$ $Å^{-1}$ *in resolution.*

formation of the anatase phase at the expense of brookite, as dopant-induced changes have appreciable effects even at very low loadings. Moreover, these evidences also suggest that guest species are most likely preferentially allocated into the anatase lattice.

Crystallite dimensions. The volume-weighted average crystallite sizes, $< D_v >$, of the two phases are quite similar (Figures 2.1c and 2.1d, Table 2.3). The presence of a single N or Nb dopant species does not affect at all $< D_v >$, that remains constant at $\sim$ 4.5 nm as in the bare T0 phase. On the contrary, both phases show a general tendency toward producing smaller crystallites when both N and Nb are introduced, even though only the changes affecting the anatase phase are statistically significant. The only exception is TNNb_0.01 N_2 (red triangle in Figure 2.1d), in which also the brookite phase is characterized by a significantly smaller crystallite average dimension than the O_2-treated analogue.

It is worth comparing the structural properties of the present series of co-doped samples with previous results on N-doped samples[8], which exhibited in this respect an opposite behavior. While the concomitant addition of N and Nb results in both an increase of the anatase content and a drop of its average crystallite dimension, N-doped materials showed an increase of both the anatase content and of the crystallite size at increasing (> 0.2) N/Ti nominal molar ratios[8]. A possible explanation of this contrasting behavior might be related to the nucleation and growth kinetics of the crystallization process. The observed codoping-induced strong thermodynamic bias toward anatase implies a large and negative free energy change associated to the appearing of the $I4_1/amd$ phase. The bias is larger when N and Nb concentration is increased. According to this scenario, the critical radii of anatase nuclei should become smaller[44] at increasing (N+Nb)/Ti molar ratios, assuming that the surface tension associated to the habit of anatase crystals does not change in bulk-doped samples with respect to the T0 reference. Therefore, we believe that nucleation should be faster in the codoped case than in single-doped TiO_2 :N materials and the crystallite average dimensions smaller as the N,Nb loading is raised.

Morphological features. Figure 2.2 reports the comparison among the adsorption isotherms of N_2, obtained in subcritical conditions, in the case of undoped TiO_2 and of the 1 % doped samples, both mono- and co-doped. All the samples show hysteresis loops characteristic of a mesoporosity.

In any case the presence of dopants induces a shift of the hysteresis loop to lower pressures indicating a decrease in the pore sizes, more so when Nb is present. The effect is even more conspicuous when higher Nb dopant contents are considered (Figure 2.2c). The effect of the sole N-doping seems almost negligible on the morphological features of TiO_2 , even when higher dopant contents are considered (Figure 2.2d). The presence of the sole Nb induces a small decrease in surface area (Table 2.4) and a relevant decrease

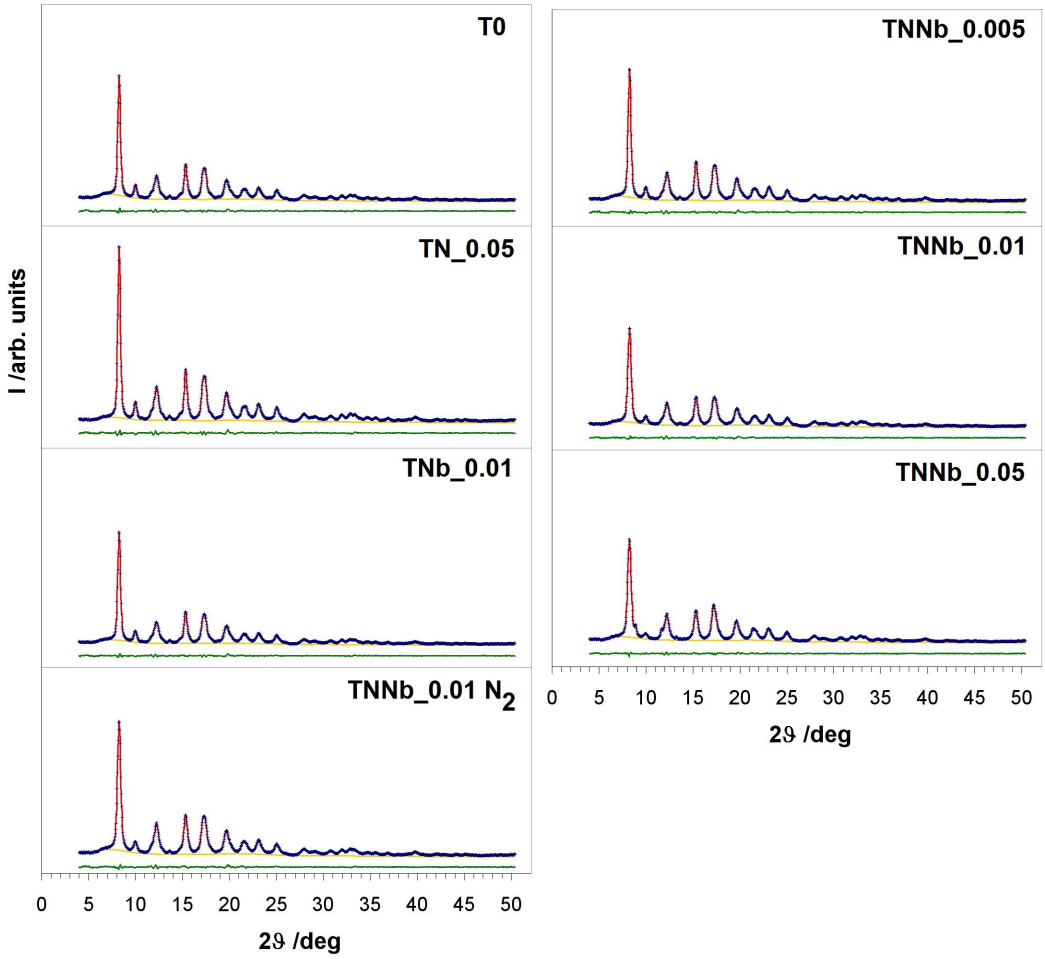

(a) Collected powder patterns (blue crosses). The least-square fitting curves are in red, the y_{obs}-y_{calc} point-by-point difference in green and the refined background function in yellow. Intensities are drawn on a common arbitrary scale.

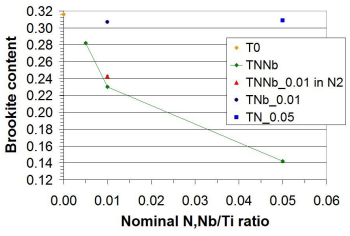

(b) Brookite content as estimated from the Rietveld refinement of the HR-XRPD data.

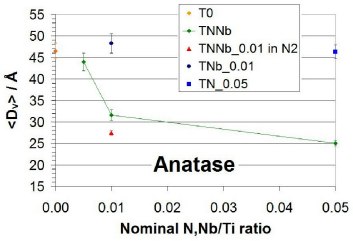

(c) Average volume-weighted crystallite dimensions of anatase phases as a function of the nominal doping extent.

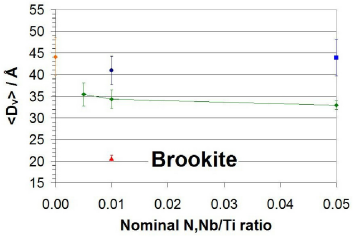

(d) Average volume-weighted crystallite dimensions of brookite phases as a function of the nominal doping extent.

Figure 2.1: *Phase and crystallite dimensions. Adapted with permission from C. Marchiori et al., J. Phys. Chem. C, 2014, Vol. 118, pp. 24152-64. Copyright 2015 American Chemical Society.*

Sample	$\mathbf{S}_{BET}$ $m^2\ g^{-1}$	$\mathbf{V}_{pores}$ $mL\ g^{-1}$	$\mathbf{E}_g$ eV
T0	129	0.293	3.16
TN_0.01	132	0.290	3.13
TN_0.05	123	0.293	3.09
TNb_0.01	119	0.166	3.04
TNb_0.05	113	0.097	2.96
TNNb_0.005	140	0.324	3.19
TNNb_0.01	161	0.223	3.11
TNNb_0.05	154	0.102	2.93
TNNb_0.01 N_2	166	0.256	3.09

Table 2.4: *Specific surface area (S_{BET}), total pore volume (V_{pores}) and apparent band gap (E_g) of the bare and doped samples.*

in the total pore volume (Figure 2.2e).

The presence of both dopants (TNNb_0.01) has a different effect with respect to the two single dopants (Figure 2.2a). The codoping supports an appreciable increase in surface area (about 30 % for both calcination atmospheres) while the total pore volume remains almost unchanged (Table 2.4). With respect to the undoped sample (T0), the pore sizes of the two codoped samples decrease (Figure 2.2e). This latter occurrence, together with their lower crystallite sizes (Figure 2.3a), can be the origin of the observed increase in surface area for the co-doped samples. The synergistic role played by the concomitant presence of both dopants is apparent also in the case of sample TNNb_0.05, which shows a larger surface area with respect to both undoped and single-doped samples (Figure 2.2). Once more, this is the joint result of smaller crystallites (Figure 2.3a) and smaller pores (Figure 2.2e).

The comparison among the three co-doped samples, (Figure 2.2b, and Table 2.4), shows that a progressive increase in surface area accompanies the parallel decrease in the crystallite sizes. In the case of TNNb_0.05 the relevant loss in pore volume partially smothers the surface area increase. It should be recalled that this sample shows also the occurrence, although to a limited extent, of NbO_2 segregation in the titania lattice.

SEM images (Figure 2.3) show that samples present aggregates at the micrometer scale. No well-formed crystal facets are clearly recognizable. Rather, the powders are organized at the mesoscale as syntherized grains made up by differently oriented crystallites. As for the series of co-doped TiO_2 :N,Nb, systems, the similar trend of the pore volume and the average crystallite dimensions suggests that most of the void space is due to inter-grain cavities and interstices.

2.1.2 Electronic structure

Bulk plane-wave DFT simulations are nowadays routinely employed to investigate the electronic properties of complex materials. DFT+U has proved to be appropriate to describe Nb anatase doping[45–47]. As for the present work, it is crucial to understand how the N and Nb co-dopants interact with each other and what is their cooperative effect, if any, on the predicted position of any gap state and the Fermi energies in the k-space. Experimental results (see Section 2.1.1) ensure that co-doping has a significant effect on the material microstructure. Thus, a comprehensive investigation of the electronic structure as a function of the doping scenario is mandatory to correlate the observed enhanced visible light absorption (see the following, Section 2.1.5) to compositional, crystallographic and morphological degrees of freedom. To this end, we chose to restrict our investigation to the anatase phase, as (i) diffraction

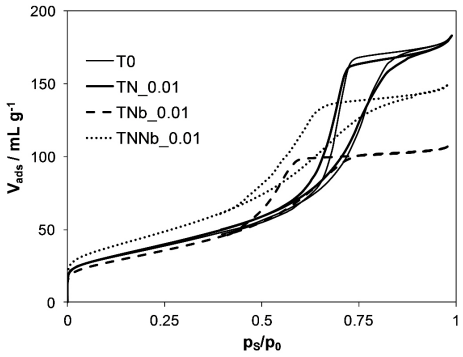

(a) Adsorption isotherms: comparison among undoped and 1%-doped and codoped systems.

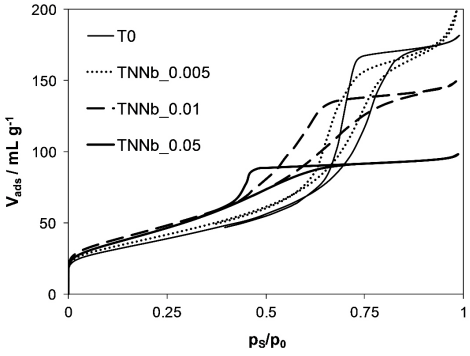

(b) Adsorption isotherms: comparison among the different N,Nb-codoped samples.

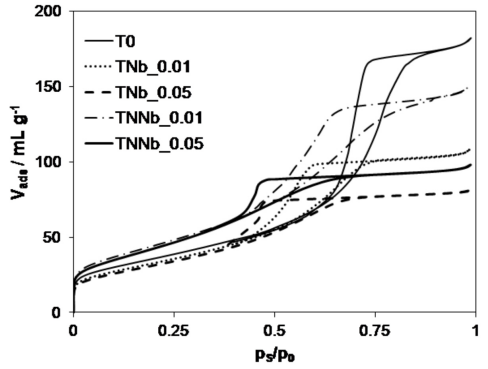

(c) Adsorption isotherms: comparison among N-doped and N,Nb-codoped systems.

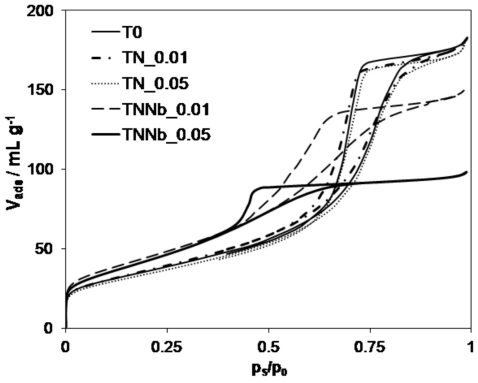

(d) Adsorption isotherms: comparison among Nb-doped and N,Nb-codoped systems.

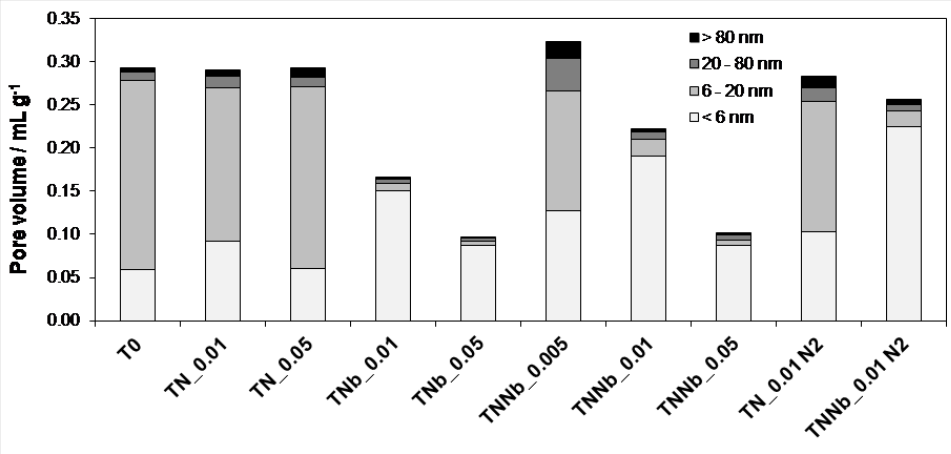

(e) Total pore volume distributions of undoped and doped samples.

Figure 2.2: *Surface area and pore analysis. Adapted with permission from C. Marchiori et al., J. Phys. Chem. C, 2014, Vol. 118, pp. 24152-64. Copyright 2015 American Chemical Society.*

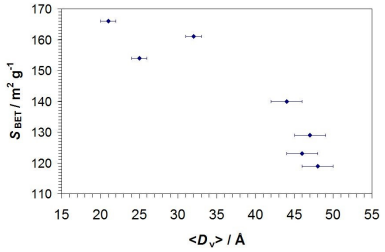

(a) Scatter plot for the average surface area *vs* average crystallite dimensions of the anatase phase ($< D_v >$).

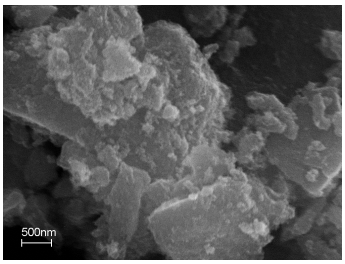

(b) SEM images of T0.

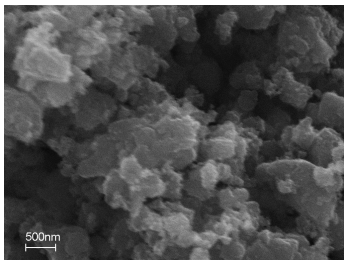

(c) SEM images of TNNb_0.005.

Figure 2.3: *Morphological characterization. Adapted with permission from C. Marchiori et al., J. Phys. Chem. C, 2014, Vol. 118, pp. 24152-64. Copyright 2015 American Chemical Society.*

experiments demonstrated that anatase is the prevailing phase in all the samples, and (ii) the brookite content diminishes as the N, Nb loading increases.

Our first-principle simulations show that Nb ions pull the Fermi Energy (FE) toward the conduction band (CB, Figure 2.4a SI and Table 2.5). It is worth noting that this is true for both interstitial and substitutional metal dopants, as electron-donor Nb species invariably create high-energy partially filled states in the CB proximity. In other words, Nb 4d orbitals mix well with Ti 3d ones and the excess electron formally reduce a Ti site to Ti^{3+}[45–50].

The picture becomes quite different when both N and Nb are simultaneously added to the anatase lattice (Figure 2.4b). As already calculated for N doping[9, 51], valence nitrogen states lie in the proximity of the valence band (VB). When Nb is placed as interstitial (Nb_i), the two guest species are electronically uncorrelated and the position of FE is again determined just by the shallow CB Nb states. Instead, when substitutional Nb is considered (Nb_s), an electron transfer to low-lying partially filled N states takes place and empties the Nb CB states. In the case of the interstitial Nb doping, there are more shallow CB states and any eventual electron transfer does not empty all of them. As a consequence, the FE abruptly shifts toward the VB (Figure 2.4b) only when the Nb doping is substitutive. This behavior implies that partial intrinsic charge compensation occurs when Nb goes in substitutional position. These conclusions are completely general and as a result, co-doping with substitutional Nb is advantageous with respect to mono-doping since the semiconductor characteristics are preserved thanks to charge balance[48]. In particular, they hold true independently by the location of the nitrogen atom (interstitial or substitutional). It is also important to stress that no defect clustering has been forced during the simulation, as no point defects were placed as close neighbors within starting unit cell geometries.

When an oxygen vacancy is included in the simulation of the co-doped lattice, the empty Ti^{3+} states near the CB become populated due to the electrons released to maintain charge neutrality. Therefore, FE invariably shifts toward CB, no matter the location of the guest species (see $Nb_x + N_y + V_O$ entries in Table 2.5, with x, y being either 's' or 'i'). Despite this apparent similarity, it should be stressed that the two doping models imply important differences, as the intrinsic Nb-N charge compensation is expected to occur in the Nb_s case, but not in the Nb_i one.

The lower panel of Figure 2.4b shows the effect of Ti vacancies on a $N_s + Nb_s$ co-doping scenario. The Ti vacancies shift the Fermi level toward the VB edge and populate the N electronic levels. Considering the differences in the charge compensation phenomena, either model (Nb_s, Nb_i) might imply a different mechanism through which the material will interact with UV-Vis photons. Therefore, understanding the actual nature (interstitial or substitutional) of Nb dopants is crucial to provide a solid interpretative basis for the experimental results. A possible strategy to achieve this goal consists in investigating the local

Sample	a	b	c	V	FE
Pure anatase	3.8554	3.8557	9.5575	142.04	1.077
Nbs	3.8547	3.8549	9.5774	142.27	2.968
Nbs + V_O	3.8544	3.8523	9.5827	142.24	2.962
Nbs + $2V_O$	3.8540	3.8497	9.5843	142.15	2.954
Nbi	3.8592	3.8672	9.5909	143.13	3.058
Nbi + V_O	3.8590	3.8618	9.6222	143.40	3.062
Nbi + $2V_O$	3.8565	3.8609	9.6240	143.36	3.074
Nbs + Ns	3.8530	3.8555	9.5857	142.37	1.610
Nbs + Ni	3.8540	3.8547	9.5907	142.48	1.762
Nbi + Ns	3.8574	3.8689	9.5930	143.09	3.052
Nbi + Ni	3.8582	3.8667	9.6082	143.36	2.846
Nbs + Ns + V_O	3.8586	3.8589	9.5757	142.59	2.943
Nbs + Ni + V_O	3.8576	3.8564	9.5799	142.51	2.868
Nbi + Ns + V_O	3.8626	3.8731	9.6023	143.52	3.025
Nbi + Ni + V_O	3.8602	3.8730	9.6285	143.84	2.851

Table 2.5: *Simulated cell edges, cell volumes and Fermi Energies (FE's) for various doping scenarios of anatase TiO_2 at the DFT+U GGA-PAW theory level. Units of measurement are Å, Å^3 and eV. The same crystallographic reference system has been employed throughout. Subscripts 's' and 'i' stand for 'substitutive' and 'interstitial' atoms, whereas V_O represents oxygen vacancies.*

coordination geometries around Nb metal centers.

2.1.3 Nature of point defects

No significant changes were detected in the Ti coordination geometry from Ti K-edge EXAFS spectra throughout the sample series, as expected from the very low dopant content. In the following discussion, we will focus on the average geometry around Nb dopants to find correlations among their local chemical environment and the simulated structural and electronic properties of the material described above.

Direct- and k-space fitting results for the Nb K-edge EXAFS data can be found in Figure 2.5. Table 2.6 compares the distances between Nb and its first and second nearest-neighbors as retrieved from DFT-optimized geometries and EXAFS fittings. For the sake of comparison, the crystallographic axial and equatorial Ti-O distances in the TiO_6 octahedral, as computed from the Rietveld refinement of T0 diffraction data, are 1.994(2) Åand 1.9298(4) Å, while the shortest Ti-Ti distance is 3.0310(2) Å. The same values as retrieved from high-resolution neutron diffraction data[52] are 1.9790(5) Å, 1.9340(1) Å, and 3.0394(< 1) Å, respectively.

As expected, DFT+U calculations show that when Nb enters the anatase lattice, the oxygen first-neighbors are significantly displaced toward longer bond distances with respect to the reference crystallographic anatase structure[52] due to the greater effective ionic radius of the dopant (Nb^{5+}: 0.64 Å, coordination VI,) with respect to Ti (Ti^{4+}: 0.605 Å, coordination VI)[53]. This is true when both interstitial and substitutional Nb atoms are considered (last rows of Table 2.6), even though DFT+U simulations predict greater d_{NbO} estimates for the interstitial case. However, the most significant difference between the two scenarios (Nb_s *vs* Nb_i) resides in the second-shell distances. If Nb goes interstitial, a peak around 2.6 Å would be expected in the Fourier Transform of the fine structure function. Instead, if Nb goes in substitutional position, the 2nd shell Nb-Ti distances should fall around 3.0 Å. Indeed, this is just the case when the theoretical outcomes are compared with phase-corrected Nb-Ti coordination distances as retrieved by EXAFS spectroscopy (Table 2.6, first 5 rows and Figure 2.5.a). Our results relative to both single Nb-doped and N,Nb-codoped TiO_2 are in agreement with EXAFS data reported by Bouchet and

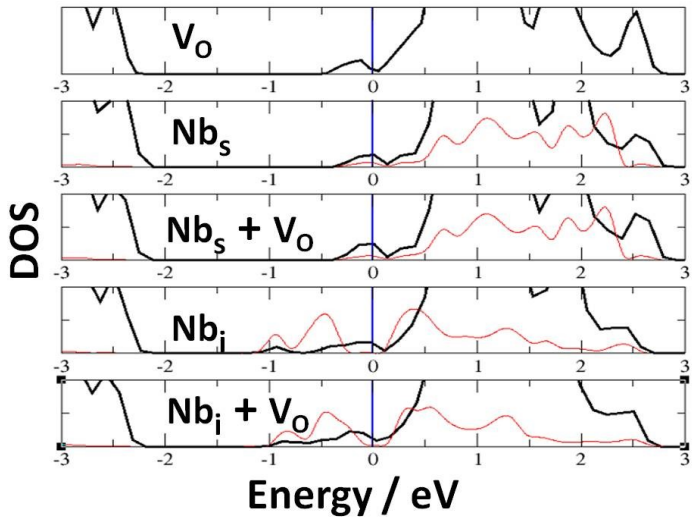

(a) Computed density of States (DOS) of TiO_2 -anatase for different doping scenarios (Nb/Ti = 1/54) involving the presence of oxygen vacancies, VO. Black curve: spin up. Red curve: spin down. 's' and 'i' subscripts describe the point defect type and stand for 'substitutional' and 'interstitial' species. The Fermi Energy (FE) is marked as a vertical line.

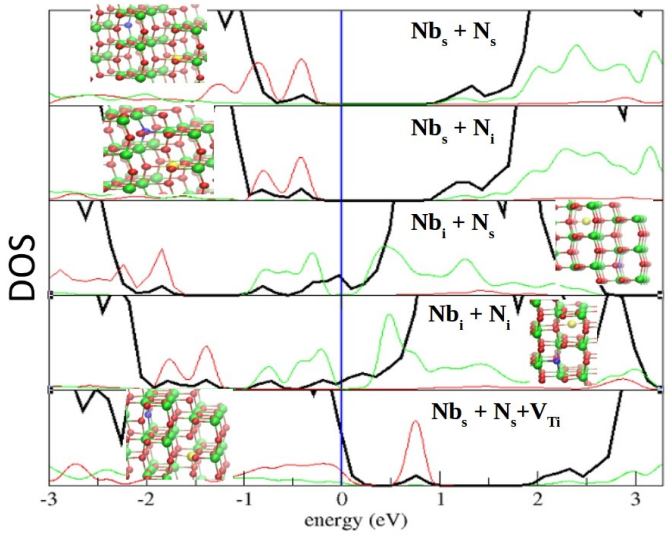

(b) Computed density of states (DOS) of TiO_2 -anatase for different doping scenarios (Nb,N,VTi/Ti = 1/54). Black curve: Total DOS. Red curve: Magnified partial DOS, projected on N atoms. Green curve: Magnified partial DOS, projected on Nb atoms. 's' and 'i' subscripts describe the point defect type and stand for 'substitutional' and 'interstitial' species. Insets: local geometries. Green atoms for Ti, red for O, blue for N, yellow for Nb. The Fermi Energy (FE) is marked as a vertical blue line .

Figure 2.4: *Density functional theory. Adapted with permission from C. Marchiori et al., J. Phys. Chem. C, 2014, Vol. 118, pp. 24152-64. Copyright 2015 American Chemical Society.*

Sample	$\mathbf{d}_{Nb-O}$ axial	$\mathbf{d}_{Nb-O}$ equatorial	$\mathbf{d}_{Nb-T}$
	EXAFS		
TNb_0.01	2.0(1)	1.98(5)	3.02(1)
TNNb_0.005	2.0(2)	1.98(8)	3.03(1)
TNNb_0.01	2.0(8)	2.0(4)	3.15(1)
TNNb_0.01 N_2	2(1)	2.0(7)	3.11(1)
TNNb_0.05	2.04(2)	1.96(1)	3.02(1)
	PAW-DFT		
Nb_s	2.0398(3)	1.969(1)	3.1376(2)
Nb_i	2.026(1)	2.128(1)	2.6535(3)
Nb_s+V_{Ti}^{2} 2.06(18)	1.99(6)	3.15(5)	

Table 2.6: *Comparison of the Nb-O and Nb-Ti phase-corrected distances as retrieved by EXAFS vs those predicted by DFT+U PAW optimizations. Values are expressed in Å. Estimated standard deviations of EXAFS results are given in parentheses. Undoped DFT+U axial distance average is 2.007(2) Å, the equatorial one is 1.9654(4) Å and the Ti-Ti one is 3.0698(3) Å.*

coauthors[54] in the case of single Nb-doped TiO_2 .

Theoretical calculations predict a greater percentage increment of the Nb-Ti second-shell distance with respect to the Nb-O first-shell ones. This is due to the greater repulsion between Nb^{5+} and Ti^{4+} with respect to the Ti^{4+} - Ti^{4+} second neighbors in the undoped TiO_2 . The first-shell oxygen atoms, in the case of Nb substitutional doping, are instead not as much affected since the greater attraction by Nb^{5+} with respect to Ti^{4+} is compensated by the greater Pauling radius of Nb^{5+}.

Unfortunately, the overall quality of the EXAFS fittings in terms of precision of the refined parameters is poor due to significant noise (see for example Figure 2.5). Nevertheless, the accuracy of the corresponding real-space refined parameters is satisfactory (Figure 2.5.a) and the latter are in fair agreement with theoretical estimates for substitutional Nb.

It should be noted that EXAFS-derived results are also compatible with a doping scenario where a titanium vacancy, $V_{Ti}^{''''}$, is added to the Nb_s model. This has been proposed to be the expected scenario when the TiO_2 -based phase is left free to equilibrate with high-activity O_2 species[55]. In the presence of this class of defects, PAW-DFT calculations predict, on average, statistically identical d_{TiO} bond lengths for the axial and equatorial ligands (last row in Table 2.6). Interestingly, the same holds true for most experimental estimates, even though the precision of the latter is generally too low to achieve sound conclusions on this issue.

Such a level of detail, however, can be reached by complementing information on the local coordination geometry available from EXAFS data with the long-range anisotropic strain affecting defective unit cells when the dopants are included in the lattice (Figure 2.7). The latter parameter can be computed from both HR-XPRD results and theoretical predictions, reported in details in Table 2.5. In general, lattice microstrain is defined as the elastic distortion of the unit cell with respect to an unstrained reference lattice. Operatively, to single out the role of N and Nb dopants, we employ a strain parameter $\epsilon_e = (l_e - l_{e0})/l_{e0}$, where l_e is the length of a symmetry-independent crystallographic cell edge (a or c), and l_{e0} has the same meaning in a suitable reference crystal structure without dopants included. The unit cell retrieved in the undoped T0 material and the PAW fully relaxed anatase lattice were chosen as references for the HR-XRPD and DFT methods, respectively. According to the expected highly defective nature of the nanoparticles, DFT simulations always took into account a single oxygen or titanium vacancy within the simulated lattice. If the microstrain along c, ϵ_c, is mapped against that along a or b, $\epsilon_{a,b}$, a two-

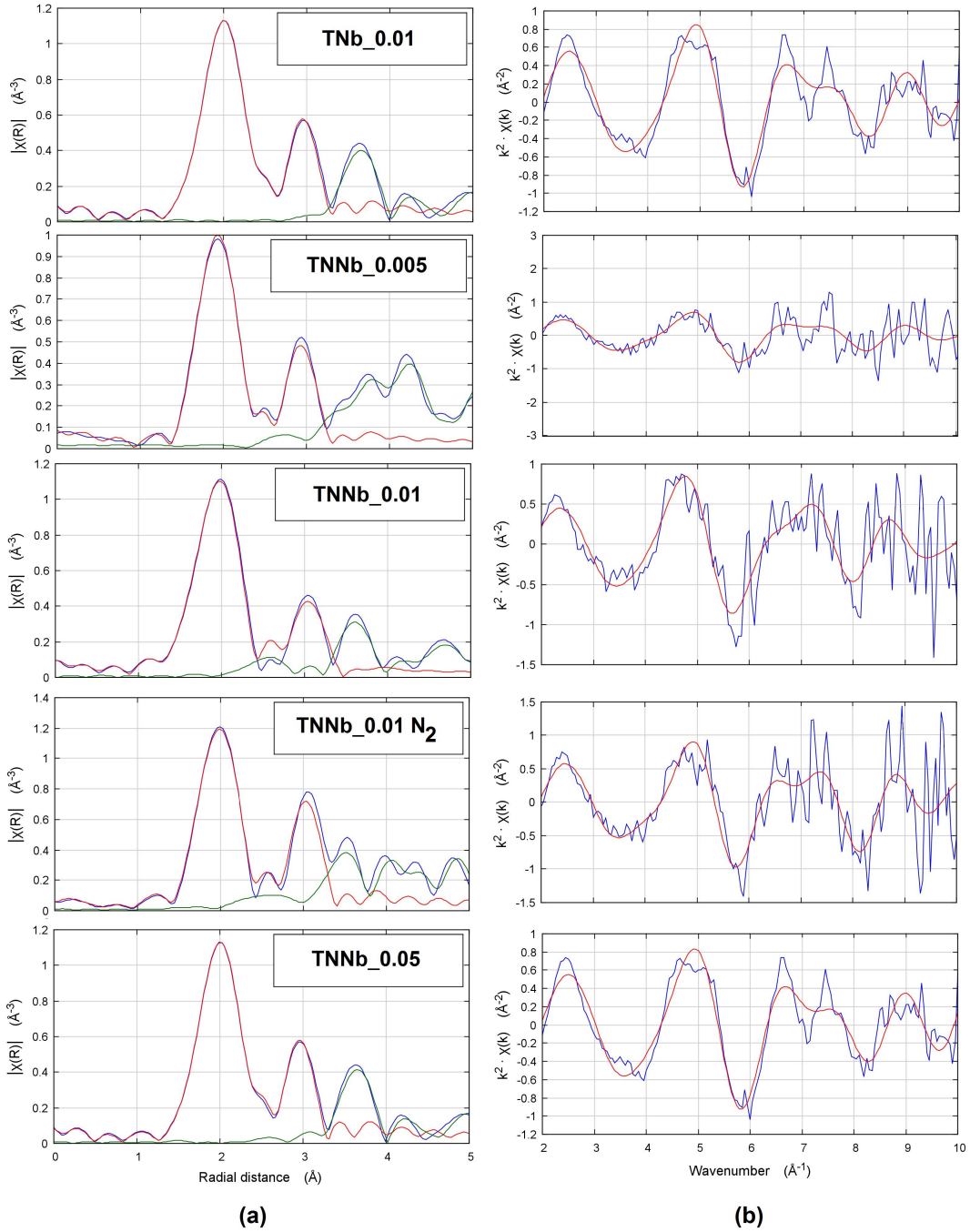

Figure 2.5: *Fitted magnitude of the forward EXAFS Fourier transform (left) and corresponding fitted k2-weighted Nb K-edge EXAFS spectra (right) of Nb-doped and N,Nb-codoped TiO_2 samples as a function of the doping extent. No phase-shifts were applied to the R-space curves. Blue curves: Experimental data; red curves: Least-squares fitting; green curves: Fitting residuals. Adapted with permission from C. Marchiori et al., J. Phys. Chem. C, 2014, Vol. 118, pp. 24152-64. Copyright 2015 American Chemical Society.*

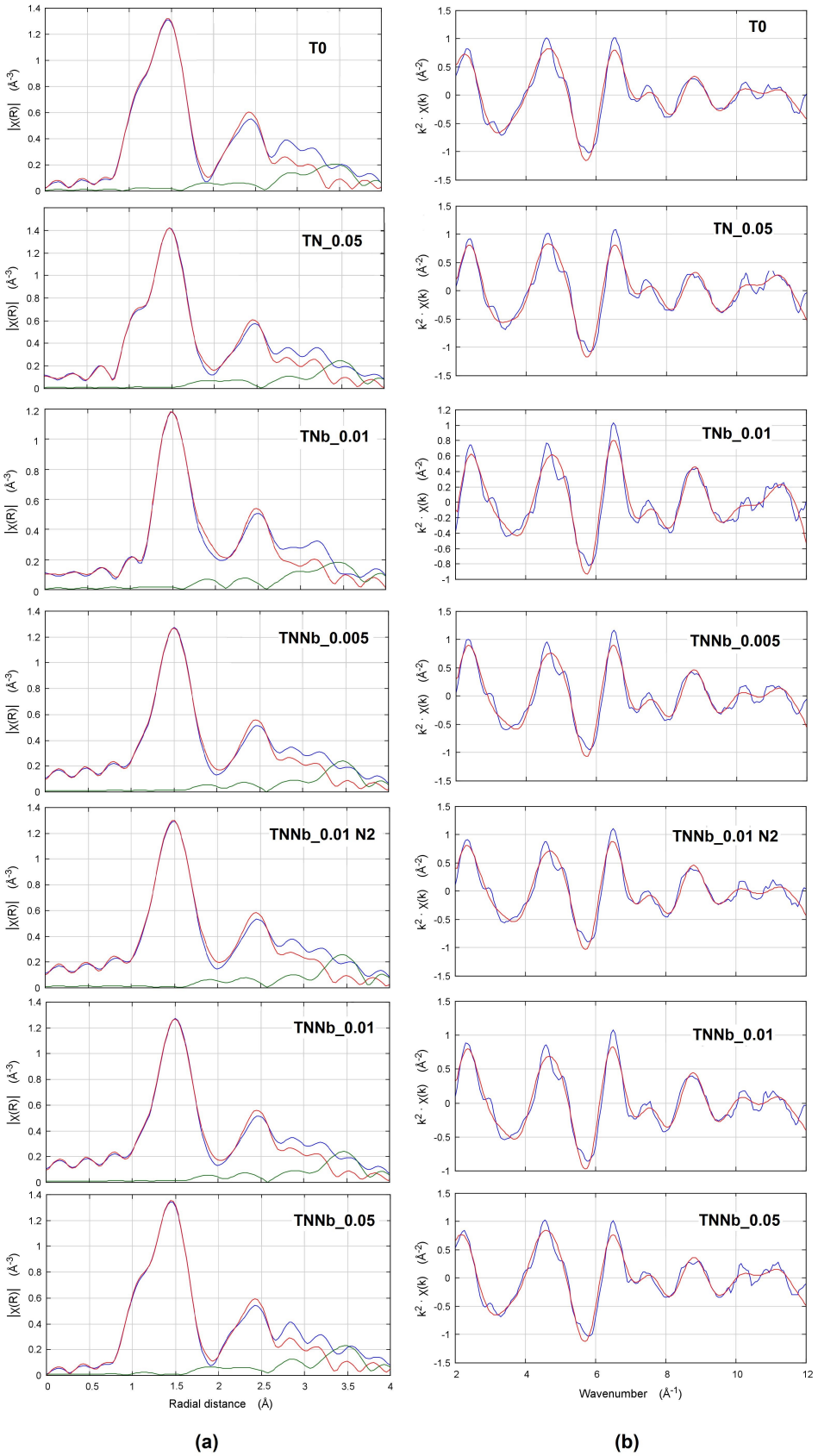

Figure 2.6: *Fitted magnitude of the forward EXAFS Fourier transform (left) and corresponding fitted k2-weighted Ti K-edge EXAFS spectra (right) of the samples as a function of the doping extent. No phase-shifts were applied to the R-space curves. Blue curves: Experimental data; red curves: Least-squares fitting; green curves: Fitting residuals. Adapted with permission from C. Marchiori et al., J. Phys. Chem. C, 2014, Vol. 118, pp. 24152-64. Copyright 2015 American Chemical Society.*

dimensional diagram is obtained that allows to disentangle the relative effect of individual point defects on anisotropic structural distortions (Figure 2.7a). When the cell edge distortions are due to interstitial Nb, they invariably fall in the upper-left part of the diagram ($\epsilon_c > 0.005$), whereas the distortions associated to substitutional Nb are significantly lower in magnitude. The presence of titanium vacancies further amplify this trend, with Nb_i models showing a considerable (up to ~ 0.009) strain along c no matter the nature (substitutional or interstitial) of the co-dopant nitrogen. On the other hand, very good agreement is found with the $Nb_s + N_s + VT_i$ model and most experimental estimates, as the latter always show small strain parameters (< 0.002, 0.001) for both the a and c symmetry-independent crystallographic directions. In any case, the very small distortions with respect to the dopant-free T0 material are clearly incompatible with the massive presence of interstitial Nb ions.

In conclusion, both the EXAFS and HR-XRPD results, when compared with the outcomes of first-principle simulations, provide compelling evidences that Nb enters in substitutional position within the materials here considered.

2.1.4 Analysis of paramagnetic centers

The undoped T0 sample is EPR silent at both room temperature and 77 K. On the contrary, when dopant are introduced, the 77 K spectra show several features (Figure 2.8a).

The TN_0.01 sample shows four narrow lines labeled by a star ($\star$) in Figure 2.8a. These features ($g_x = 2.066$, $g_y = 2.0054$, $g_z = 2.0040$, Ax $\sim$ Ay $\sim$ 3 G, Az $\sim$ 32.2 G), which are appreciable even at room temperature, have been already reported elsewhere[10, 14] and attributed to bulk nitrogen paramagnetic defects ($N_b^\bullet$). Further, six other lines can be detected at 77 K, labeled in Figure 2.8a as A, B, C, D, E and F. The features A and B ($g_x = 2.0082$, $g_y = 2.0118$, $g_z = 2.0285$) might be related to paramagnetic radical oxygen species[10, 56], while the lines C ($g_1 = 1.98$), D ($g_2 = 1.93$) and E ($g_3 = 1.96$) can be attributed to Ti^{3+} in different environments, analogously to what reported by the Giamello and coauthors[39, 57]. At last, the F line is characterized by an intensity comparable to that of the B line, and can be simulated by a symmetric line with g $\sim$ 2, attributable to F^+ paramagnetic defects, *i.e.* to almost free electrons trapped into oxygen vacancies. Previous studies reported the occurrence of F^+ defects in N-doped TiO_2 [14, 36].

The TNb_0.01 sample (Figure 2.8a) shows a much less intense EPR spectrum, in which only the A, B and C peaks can be appreciated. Therefore, only oxygen radical and Ti^{3+} species are appreciable in the Nb-doped sample. Several authors reported the occurrence of bulk Ti^{3+} species in Nb-doped TiO_2 [39, 43, 57], whose formation was attributed to a mechanism of valence induction. Our results therefore support the occurrence of the valence induction mechanism for at least a fraction of the excess electrons introduced by the Nb dopant, although it is not possible, on the basis EPR data, to confirm or exclude the occurrence of the charge compensation mechanism of Nb^{5+} involving titanium vacancies. Our DFT calculations support the hypothesis of Ti^{3+} formation in Nb-doped TiO_2 (Section 2.1.2), although EXAFS-derived results are also compatible with a doping scenario where titanium vacancies, V''''_{Ti}, are present.

The attribution of C, D and E lines to Ti^{3+} species is also supported by the fact that they cannot be detected at room temperature. Indeed, De Trizio *et al.*[43] reported that Ti^{3+} signals cannot be observed above 100 K due to the occurrence of carrier detrapping at elevated temperatures.

In the N,Nb-codoped samples (TNNb_0.01, Figure 2.8a), the most striking difference with respect to the TN_0.01 is that the E line, shown by the N-doped sample and attributed to Ti^{3+} ions, disappears in the N,Nb-codoped sample. The same comparison but at a higher dopant concentration (5 %) is reported

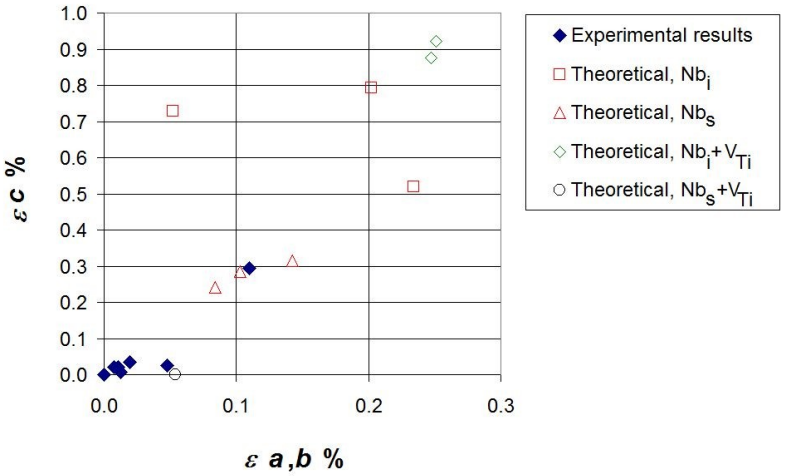

(a) Full rhombi: experimental results, as a function of Nb / N loadings (T0 is reported at the origin). Empty squares: DFT+U results, interstitial Nb. Empty triangles: DFT+U results, substitutional Nb.

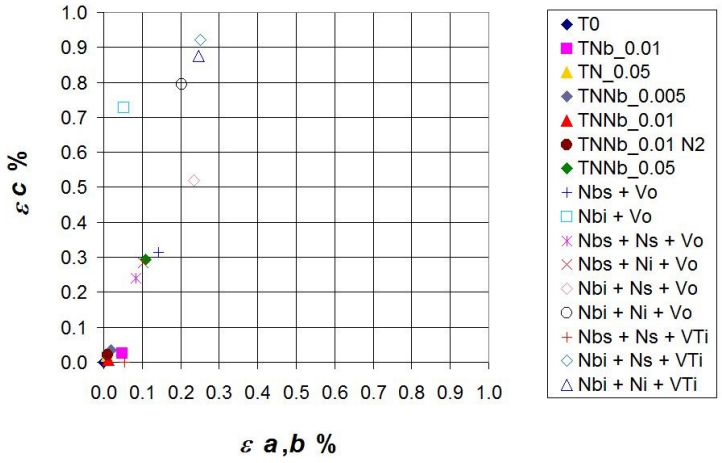

(b) Full dots: experimental results, as a function of the Nb doping loading. To the sake of comparison, the N-doped material TN_0.05 is also shown as a yellow triangle. Empty dots: DFT results, as a function of the doping scenario.

Figure 2.7: *Anisotropic cell strain as estimated by HR-XRPD and DFT+U methods with respect to the reference undoped anatase structure. Adapted with permission from C. Marchiori et al., J. Phys. Chem. C, 2014, Vol. 118, pp. 24152-64. Copyright 2015 American Chemical Society.*

in Figure 2.8b and it clearly shows that in the N,Nb-codoped sample the $Nb^{\bullet}$ pattern becomes by far less intense than the A,B pattern and the C, D and E features decrease or completely disappear.

Both observations (disappearance of Ti^{3+} and of N paramagnetic species in codoped samples) support the occurrence of charge compensation between Nb (acting as an electron donor) and N (acting as an electron acceptor) in the case of N,Nb-codoped samples, as predicted by our first-principle DFT calculations in the case of substitutional Nb doping. This latter evidence further confirms the hypothesis of substitutional Nb doping in our codoped samples. However, EPR spectra clearly show that such charge compensation phenomena are not complete, in agreement with previous reports by Bartlett and coauthors[36, 37].

It is noteworthy that in DRS spectra (see in the following, Section 2.1.5) the N,Nb-doped samples show systematically a larger absorption centered around 500 nm with respect to N-doped samples. Such a larger absorption might be related to an increased solubility of N in the host lattice as Nb incorporation increased[24]. Thus, although a larger amount of N-dopant is incorporated in the TiO_2 lattice in N,Nb-codoped samples, the occurrence of charge compensation between N and Nb results in a decrease of the N bulk paramagnetic species.

Figure 2.8c reports the comparison of three N,Nb-codoped samples with different nominal dopant contents (0.5-1-5 %). As above mentioned, the E line is absent from the EPR spectra of all the co-doped samples. We must outline that at high doping levels NbO_2 segregation can occur, as determined in the case of the TNNb_0.05 sample from XRD data. In this respect, it should be pointed out that TNNb_0.05 is the only sample showing a splitting of the C line, which might be related to the presence of Nb^{4+} ($g \sim 1.97$)[58].

2.1.5 Visible absorption properties

Comparing the DRS results of single doped N- or Nb-containing materials with the N,Nb-codoped ones provides hints on the mutual role of the guest species in determining the photoabsorption properties of the nanopowders.

Nb-doping gives rise to a red shift of the absorption edge (Figure 2.9a), which results in a reduction of the observed band gap of about 0.2 eV (Table 2.4, 4th column). Literature studies reported similar red shift effects for Nb-doped TiO_2 [38, 39] although in some cases a blue shift of the absorption edge was also reported[23, 38]. Such a blue shift effect is generally attributed to Burstein-Moss effect[43], in which the conduction band filling by 'extra' electrons due to Nb defects suppresses absorption at the band edge.

The situation is different in the case of N-doping. N-doped samples absorb in the visible region around 450-500 nm, but their absorption edge is comparable to that of undoped TiO_2 (Figure 2.9a). The visible light absorbance depends on the nominal nitrogen content of the material (Figures 2.9c and 2.9d), in agreement with previous reports[9, 10, 15, 38].

N,Nb-codoped materials show a combination of both effects. Comparing TN_0.05, TNb_0.05 and TNNb_0.05 samples (Figure 2.9a), the latter presents both a red shift of the absorption edge and a 'localized' absorption around 450 nm. The TNNb_0.05 sample shows indeed the lowest observed apparent band gap (2.93 eV *vs* 3.09 eV for TN_0.05) (Table 2.6, 4th column). Interestingly, the visible absorption at 450 nm is significantly more intense in the codoped sample than in the case of the corresponding N-doped sample. Both effects (red shift and absorption at 450 nm) are appreciable in the case of the codoped powder with the intermediate dopant content (TNNb_0.01), while at low N,Nb-content (TNNb_0.005) a blue shift of the absorption edge is instead observed (Figure 2.9b).

While the occurrence of the visible absorption of N-doped samples can be traced back to the formation

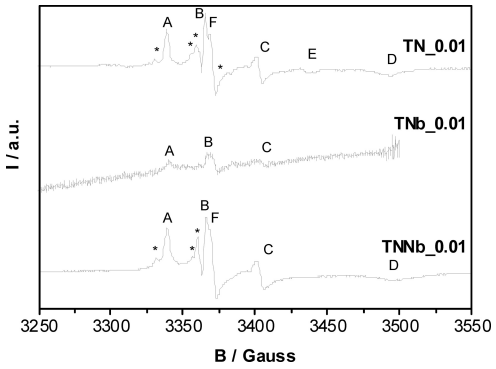

(a) TN_0.01, TNb_0.01 (multiplication factor: 3.6) and TNNb_0.01 (multiplication factor: 0.78).

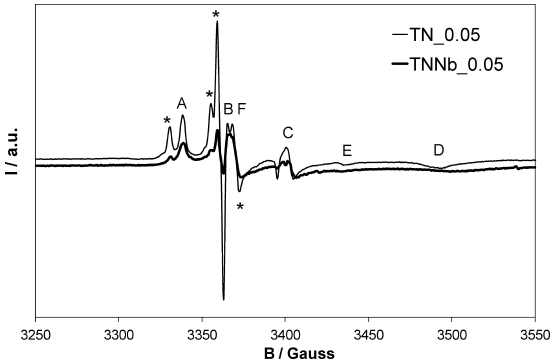

(b) TN_0.05 and TNNb_0.05.

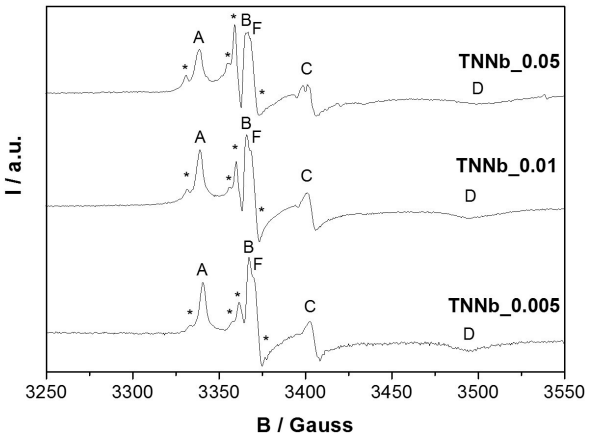

(c) TNNb_0.005 (multiplication factor: 0.88), TNNb_0.01 (multiplication factor: 1.04) and TNNb_0.05. The graphs are normalized with respect to the most intense peak.

Figure 2.8: *Experimental EPR spectra collected at 77 K. Adapted with permission from C. Marchiori et al., J. Phys. Chem. C, 2014, Vol. 118, pp. 24152-64. Copyright 2015 American Chemical Society.*

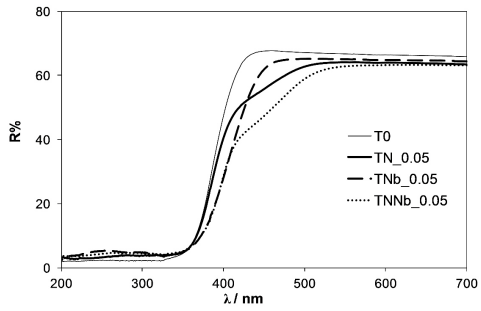

(a) Undoped and 5 % mono- and co-doped TiO_2 samples.

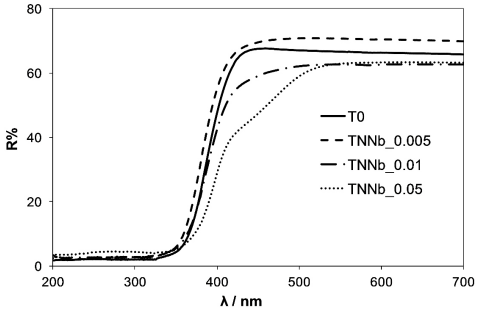

(b) Undoped and N,Nb-co-doped TiO_2 samples at different dopant contents.

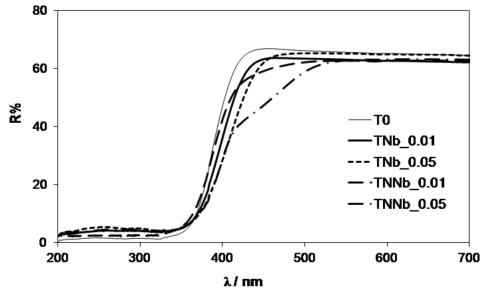

(c) Nb-doped and N,Nb-co-doped TiO_2 samples.

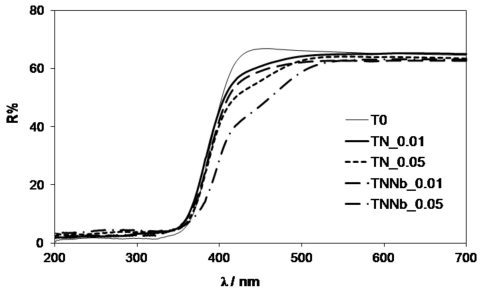

(d) N-doped and N,Nb-co-doped TiO_2 samples.

Figure 2.9: *DRS spectra of undoped and N,Nb-co-doped TiO_2 samples at different dopant contents. Adapted with permission from C. Marchiori et al., J. Phys. Chem. C, 2014, Vol. 118, pp. 24152-64. Copyright 2015 American Chemical Society.*

of shallow intra-gap states located above the valence band of TiO_2 [9, 40, 46] the red shift detected in Nb-doped systems can be related, on the grounds of theoretical calculations, to the formation of donor levels located close to the conduction band (see Section 2.1.2 above). Lim *et al.*[38] reported similar results in the case of N,Nb-codoped samples. They attributed the increased absorption around 450 nm to a higher effective concentration of N in the TiO_2 lattice, in accordance with theoretical calculations reporting that codoping with transition metals (Nb, Ta) might facilitate the enhancement of the concentration of p-type dopants (N and C) in the host lattice[24]. Our microstructural analysis (Section 2.1.1) supports this picture, but we go a step further by demonstrating that bulk electrons originating from Nb dopants can be localized onto N centers, making therefore available more charge density to be promoted into the CB upon visible-light photoexcitation.

2.2 Conclusion

In this chapter, a thorough multi-disciplinary investigation has been carried out on N, Nb co-doped multiphasic TiO_2 -based nanostructured materials. The effects of both mono- and co-doping with N and Nb on the electronic, crystallographic and morphological degrees of freedom of TiO_2 were studied through experimental (HR-XRPD, EXAFS, EDX, BET, SEM, EPR, DRS) and theoretical (plane-wave periodic DFT+U) methods. This joint experimental and theoretical approach has allowed, on one hand, to probe the materials (micro)structure at both the local and the long-range scale. On the other hand, it has resulted in the development of a solid first-principle interpretative basis for the observed light-induced responses as a function of the doping strategy.

We found that N, Nb species give rise to a significant synergism determining both intensive and

extensive properties of the nanopowders, while single N and Nb dopants are essentially ineffective at the very low (N, Nb/Ti $\leq$ 0.05) nominal loadings here employed. In particular, the contemporary presence of the two dopants implies a strong thermodynamic driving force toward the TiO_2 -anatase phase, that results in the growth of smaller crystallites and particles with higher surface areas than in the undoped material.

Most important, EXAFS, HR-XRPD and DFT simulations provide compelling evidence that in N,Nb-codoped TiO_2 Nb enters the anatase lattice in substitutional position, confirming what in the literature is generally empirically attributed on the grounds of considerations of the similar ionic radii of the two ions. We also demonstrated that, at variance with interstitial Nb, substitutional Nb can transfer an electron to low-energy valence states of the N co-dopant near the valence band. This intrinsic charge compensation mechanism is substantiated by EPR measurements, that show a neat reduction of the signal due to paramagnetic bulk N species when Nb is also present in the lattice and the systematic disappearance of the E peak attributed to Ti^{3+} species.

DRS measurements showed that N,Nb-codoped samples are subject to two distinct changes with respect to the undoped material, namely a slight shift of the band edge (either a blue or a red shift, depending on the dopant content) and an increased tendency to absorb visible photons in the region around 450-500 nm. We demonstrated that these two effects are individually due to Nb and N guests, respectively. When both the dopants are present in the lattice, the absorbance around $\sim$ 450 nm is significantly increased with respect to nitrogen-only containing nanopowders at comparable nominal N/Ti concentrations. DFT calculations provide a solid interpretative basis to this synergistic behavior. Niobium and nitrogen create shallow mid-gap states near the conduction and valence bands, respectively, determining an overall (slight) reduction of the band gap. At the same time, substitutional Nb ions transfer charge density to guest N, dampening bulk paramagnetism and injecting electrons in states near the top of the valence band. These electrons can in turn contribute to the light absorption process, therefore enhancing the DRS response.

The present work provides a comprehensive picture of how crystal structure, local coordination geometry, phase / defect composition and band structure are intertwined with each other in determining the structural properties and visible-light response of this class of important nanostructured materials.

2.3 Specific procedures

Nanopowder synthesis All reactants were purchased from Sigma Aldrich and were used without further purification. Doubly distilled water passed through a Milli-Q apparatus was used. Titania samples were prepared by a sol-gel synthesis using the following procedure. Titanium (IV) isopropoxide was dissolved in 2-propanol, using a molar ratio 1:5. Then, an aqueous solution of HCl was added dropwise under vigorous stirring (300 rpm), in order to obtain a H_2O : titanium (IV) isopropoxide molar ratio of 100 and final pH 3. The slurry was stirred for 90 min to complete the hydrolysis. Then, the solvent was completely removed by drying in oven at 80 $^{\circ}C$. The obtained powders were ground and calcined at 400 $^{\circ}C$ for 6 h in either O_2 or N_2 flux (9 NL h^{-1}). Nb-doped samples were obtained by adding $NbCl_5$ to the titanium (IV) isopropoxide solution, while Nb,N-codoped samples were synthesized using ammonium niobate(V) oxalate hydrate ($NH_4[NbO(C_2O_4)_2(H_2O)]\cdot nH_2O$) as a source of both N and Nb. This implies that codoped samples always nominally contain an equimolar quantity of both the N and Nb guest species. Undoped and N-doped samples were also synthesized, the latter using NH_4OH as precursor. Samples were denoted as TD1D2x, with D1 and D2 being the dopants and x the dopant/Ti nominal molar ratio (0.5-5 %). 'T0' represents the undoped TiO_2 reference. A N_2 mark distinguishes

the samples calcined in N_2 flux. Otherwise, it has to be intended that calcination was carried out in an O_2 atmosphere.

Materials characterization High-resolution X-ray powder diffraction (HR-XRPD) experiments were performed at the bending magnet BM01B station of the Swiss-Norwegian beamline at the European Synchrotron Radiation Facility (ESRF), in Grenoble, France. Data were collected from 4° to 50° in 2θ at 0.9°/min in Debye-Scherrer capillary geometry using Si-111 monochromated X-rays with λ = 0.50494(3) Å. The Rietveld method as implemented in the GSAS-EXPGUI program suite39-40 was utilized to fit experimental diffractograms. The Williamson-Hall method was applied to integral breadths of individual h0l reflections up to $\sin(\theta/\lambda) = 0.5$ Å^{-1} to estimate the average volume-weighted crystallite dimensions, $< D_v >$.

Extended X-ray Absorption Fine Structure (EXAFS). Thin tablets suitable for recording X-ray absorption spectra were prepared by pressing powder specimens. Samples intended for measurements at the Ti K edge were also carefully diluted in cellulose to avoid thickness effects. X-ray absorption curves were then collected around both Ti K and Nb K edges at room temperature at the BM01B beamline of ESRF. Ti spectra were recorded in transmission mode, while for Nb we had to resort to fluorescence mode as the signal in transmission geometry was partly contaminated by a spurious Bragg reflection due to the crystal monochromator. A Si (111)-monochromated beam was employed to probe the nanostructured samples in the 4.88 - 6.00 (Ti K edge) and 18.9 - 20.0 keV (Nb K edge) energy ranges. The Horae suite of programs, based on the IFEFFIT library, was used throughout data processing and fitting. The same multi-step fitting strategy was applied to extract information on the average coordination geometry around Ti. As for the spectra at the Nb K-edge, we considered as negligible the amount of dopant possibly present in the minority phase of brookite with respect to the major anatase one. Therefore, just the backscattering paths due to the anatase lattice were taken into account to model the average first and second coordination shells of the guest transition metal.

DFT modeling: spin-polarized calculations were performed with VASP suite of codes. The projector augmented wave (PAW) pseudopotentials were employed and the Perdew-Burke-Ernzerhof parametrization was utilized in generalized gradient approximation for the exchange-correlation potential. The energy basis cutoff was 400 eV and the optimizations were performed using the conjugate-gradient scheme until the change in total energy between successive steps was less than 0.001 eV and residual forces were below 0.01 (eV Å^{-1}). For Nb doping, agreement with experimental results was obtained using corrections for the self-interaction errors, such as the DFT+U approach. An effective on-site Coulombic interaction correction U (U=U'-J) was employed for the Ti 3d orbitals. The value of U = 3.3 eV was used because it has previously been shown to properly account for the electronic structure of the Ti 3d states. The reciprocal space was limited to the single Gamma point, given the 3x3x3 primitive supercell arrangement.

Further details about synthetic procedures and characterizations can be found in Appendix C.

References

[1] O. Carp, C. Huisman, A. Reller, *Prog. Sol. State Chem.* **2004**, *32*, 33 –177.

[2] X. Chen, S. S. Mao, *Chem. Rev.* **2007**, *107*, 2891–2959.

[3] A. Fujishima, X. Zhang, D. A. Tryk, *Surf. Sci. Rep.* **2008**, *63*, 515 –582.

[4] D. Meroni, S. Ardizzone, G. Cappelletti, M. Ceotto, M. Ratti, R. Annunziata, M. Benaglia, L. Raimondi, *J. Phys. Chem. C* **2011**, *115*, 18649–18658.

[5] F. Spadavecchia, G. Cappelletti, S. Ardizzone, M. Ceotto, M. S. Azzola, L. L. Presti, G. Cerrato, L. Falciola, *J. Phys. Chem. C* **2012**, *116*, 23083–23093.

[6] R. Asahi, T. Morikawa, T. Ohwaki, K. Aoki, Y. Taga, *Science* **2001**, *293*, 269–271.

[7] J. Zhang, Y. Wu, M. Xing, S. A. K. Leghari, S. Sajjad, *Energy Environ. Sci.* **2010**, *3*, 715–726.

[8] L. LoPresti, M. Ceotto, F. Spadavecchia, G. Cappelletti, D. Meroni, R. G. Acres, S. Ardizzone, *J. Phys. Chem. C* **2014**, *118*, 4797–4807.

[9] D. Meroni, S. Ardizzone, G. Cappelletti, C. Oliva, M. Ceotto, D. Poelman, H. Poelman, *Catal. Today* **2011**, *161*, 169–174.

[10] S. Livraghi, M. C. Paganini, E. Giamello, A. Selloni, C. D. Valentin, G. Pacchioni, *J. Am. Chem. Soc.* **2006**, *128*, 15666–15671.

[11] F. Spadavecchia, G. Cappelletti, S. Ardizzone, M. Ceotto, L. Falciola, *J. Phys. Chem. C* **2011**, *115*, 6381–6391.

[12] A. V. Emeline, V. N. Kuznetsov, V. K. Rybchuk, N. Serpone, *In. J. Photoen.* **2007**, *2008*, 1–19.

[13] H. Yates, M. Nolan, D. Sheel, M. Pemble, *J. Photochem. Photobio. A* **2006**, *179*, 213 –223.

[14] F. Spadavecchia, G. Cappelletti, S. Ardizzone, C. L. Bianchi, S. Cappelli, C. Oliva, P. Scardi, M. Leoni, P. Fermo, *Appl. Cat. B* **2010**, *96*, 314 –322.

[15] F. Spadavecchia, S. Ardizzone, G. Cappelletti, C. Oliva, S. Cappelli, *J. Nanopart. Res.* **2012**, *14*.

[16] S. Taylor, M. Mehta, A. Samokhvalov, *ChemPhysChem* **2014**, *15*, 942–949.

[17] A. Castro, M. Nunes, M. Carvalho, L. Ferreira, J.-C. Jumas, F. Costa, M. Florncio, *J. Solid State Chem.* **2009**, *182*, 1838 –1845.

[18] T. Cottineau, N. Bealu, P.-A. Gross, S. N. Pronkin, N. Keller, E. R. Savinova, V. Keller, *J. Mater. Chem. A* **2013**, *1*, 2151–2160.

[19] A. Kudo, R. Niishiro, A. Iwase, H. Kato, *Chem. Phys.* **2007**, *339*, 104 –110.

[20] Y. Furubayashi, T. Hitosugi, Y. Yamamoto, K. Inaba, G. Kinoda, Y. Hirose, T. Shimada, T. Hasegawa, *Appl. Phys. Lett.* **2005**, *86*, 252101.

[21] T. Hitosugi, N. Yamada, S. Nakao, Y. Hirose, T. Hasegawa, *Phys. Status Solidi* **2010**, *207*, 1529–1537.

[22] X. L, X. Mou, J. Wu, D. Zhang, L. Zhang, F. Huang, F. Xu, S. Huang, *Adv. Funct. Mater.* **2010**, *20*, 509–515.

[23] A. K. Chandiran, F. Sauvage, M. Casas-Cabanas, P. Comte, S. M. Zakeeruddin, M. Graetzel, *J. Phys. Chem. C* **2010**, *114*, 15849–15856.

[24] X. Ma, Y. Wu, Y. Lu, J. Xu, Y. Wang, Y. Zhu, *J. Phys. Chem. C* **2011**, *115*, 16963–16969.

[25] Z. Zhao, Q. Liu, *Cat. Lett.* **2008**, *124*, 111–117.

[26] A. T. Kuvarega, R. W. M. Krause, B. B. Mamba, *J. Phys. Chem. C* **2011**, *115*, 22110–22120.

[27] X. Wang, Y. Tang, M.-Y. Leiw, T.-T. Lim, *Appl. Catal. A* **2011**, *409410*, 257 –266.

[28] Y. Gai, J. Li, S.-S. Li, J.-B. Xia, S.-H. Wei, *Phys. Rev. Lett.* **2009**, *102*, 036402.

[29] S. S. Thind, G. Wu, A. Chen, *Appl. Catal. B* **2012**, *111 - 112*, 38 –45.

[30] W. Zhu, X. Qiu, V. Iancu, X.-Q. Chen, H. Pan, W. Wang, N. M. Dimitrijevic, T. Rajh, H. M. Meyer, M. P. Paranthaman, G. M. Stocks, H. H. Weitering, B. Gu, G. Eres, Z. Zhang, *Phys. Rev. Lett.* **2009**, *103*, 226401.

[31] P. Wang, Z. Liu, F. Lin, G. Zhou, J. Wu, W. Duan, B.-L. Gu, S. B. Zhang, *Phys. Rev. B* **2010**, *82*, 193103.

[32] M. E. Kurtoglu, T. Longenbach, K. Sohlberg, Y. Gogotsi, *J. Phys. Chem. C* **2011**, *115*, 17392–17399.

[33] A. M. Mrquez, J. J. Plata, Y. Ortega, J. F. Sanz, G. Coln, A. Kubacka, M. Fernndez-Garca, *J. Phys. Chem. C* **2012**, *116*, 18759–18767.

[34] D.-E. Gu, B.-C. Yang, Y.-D. Hu, *Catal. Commun.* **2008**, *9*, 1472 –1476.

[35] Y. Cong, J. Zhang, F. Chen, M. Anpo, D. He, *J. Phys. Chem. C* **2007**, *111*, 10618–10623.

[36] T. M. Breault, B. M. Bartlett, *J. Phys. Chem. C* **2012**, *116*, 5986–5994.

[37] T. M. Breault, B. M. Bartlett, *J. Phys. Chem. C* **2013**, *117*, 8611–8618.

[38] J. Lim, P. Murugan, N. Lakshminarasimhan, J. Y. Kim, J. S. Lee, S.-H. Lee, W. Choi, *J. Catal.* **2014**, *310*, 91 –99.

[39] J. Biedrzycki, S. Livraghi, E. Giamello, S. Agnoli, G. Granozzi, *J. Phys. Chem. C* **2014**, *118*, 8462–8473.

[40] M. Ceotto, L. L. Presti, G. Cappelletti, D. Meroni, F. Spadavecchia, R. Zecca, M. Leoni, P. Scardi, C. L. Bianchi, S. Ardizzone, *J. Phys. Chem. C* **2012**, *116*, 1764–1771.

[41] A. K. Cheetham, C. N. R. Rao, *Acta Crystallograph. B* **1976**, *32*, 1579–1580.

[42] S. Furukawa, T. Shishido, K. Teramura, T. Tanaka, *ACS Catal.* **2012**, *2*, 175–179.

[43] L. DeTrizio, R. Buonsanti, A. M. Schimpf, A. Llordes, D. R. Gamelin, R. Simonutti, D. J. Milliron, *Chem. Mater.* **2013**, *25*, 3383–3390.

[44] J. Mullin in *Crystallization (Fourth Edition)*, (Ed.: J. Mullin), Butterworth-Heinemann, Oxford, Fourth Edition, **2001**, pp. 216 –288.

[45] H. Anh Huy, B. Aradi, T. Frauenheim, P. Dek, *J. Appl. Phys.* **2012**, *112*, –.

[46] C. D. Valentin, G. Pacchioni, A. Selloni, *J. Phys. Chem. C* **2009**, *113*, 20543–20552.

[47] B. J. Morgan, D. O. Scanlon, G. W. Watson, *J. Mater. Chem.* **2009**, *19*, 5175–5178.

[48] R. Long, N. J. English, *Chem. Phys. Lett.* **2011**, *513*, 218 –223.

[49] D. Morris, Y. Dou, J. Rebane, C. E. J. Mitchell, R. G. Egdell, D. S. L. Law, A. Vittadini, M. Casarin, *Phys. Rev. B* **2000**, *61*, 13445–13457.

[50] T. Hitosugi, H. Kamisaka, K. Yamashita, H. Nogawa, Y. Furubayashi, S. Nakao, N. Yamada, A. Chikamatsu, H. Kumigashira, M. Oshima, Y. Hirose, T. Shimada, T. Hasegawa, *Appl. Phys. Exp.* **2008**, *1*, 111203.

[51] C. D. Valentin, E. Finazzi, G. Pacchioni, A. Selloni, S. Livraghi, M. C. Paganini, E. Giamello, *Chem. Phys.* **2007**, *339*, 44 –56.

[52] C. J. Howard, T. M. Sabine, F. Dickson, *Acta Crystallograph. Sect.* **1991**, *47*, 462–468.

[53] R. D. Shannon, *Acta Crystallograph. A* **1976**, *32*, 751–767.

[54] R. Bouchet, A. Weibel, P. Knauth, G. Mountjoy, A. V. Chadwick, *Chem. Mater.* **2003**, *15*, 4996–5002.

[55] M. K. Nowotny, L. R. Sheppard, T. Bak, J. Nowotny, *J. Phys. Chem. C* **2008**, *112*, 5275–5300.

[56] R. F. Howe, M. Gratzel, *J. Phys. Chem.* **1985**, *89*, 4495–4499.

[57] S. Livraghi, M. Chiesa, M. C. Paganini, E. Giamello, *J. Phys. Chem. C* **2011**, *115*, 25413–25421.

[58] J. Kiwi, J. Suss, S. Szapiro, *Chem. Phys. Lett.* **1984**, *106*, 135 –138.

Chapter 3

How the synthetic route affects the photocatalytic efficiency of Nb/Ta:N codoped TiO_2 nanomaterials

TiO_2 modification with transition metals (TMs) has been proposed to produce defects beneficial for visible light harvesting. In recent years, theoretical[1] and experimental[2–5] studies have proposed Niobium and Tantalum as efficient dopants, thanks to the favorable location of the electronic states created by their 4d and 5d orbitals. For instance, Wang et al.[3] prepared Ta-doped macroporous titania photocatalysts with superior performance in the degradation of 4-nitrophenol at high Ta:Ti molar ratios.

As discussed in the previous chapther, codoping by metal and nonmetal species has attracted much attention as a possible solution to optimize light absorption while preserving the quantum yield of titania. The simultaneous presence of electron donors (*e.g.*, a pentavalent metal like Nb or Ta) and acceptors (*e.g.*, N) might lead to charge compensation phenomena, possibly beneficial to the photocatalytic activity[6–8]. The theoretical study by Zhu et al.[9] underlined the positive effects of compensated codoping in Nb,N- and Ta,N-copromoted titania systems, such as an increased amount of nitrogen species entering the TiO_2 lattice. However, Ta- and Ta,N-codoped TiO_2 was investigated to a lesser extent than Nb- and Nb,N-codoped[10] titania. A very recent theoretical work by Liu and coworkers[11] showed how Ta ion is promoted as a lattice guest thanks to the compresence of a nonmetal species (sulfur). Obata et al.[12] first synthesized Ta,N-codoped films by magnetron sputtering, which showed enhanced photocatalytic activity under visible light. Furthermore, Wang et al.[13] demonstrated that even tri-doped Ta-N-F systems could be promising systems for visible-light applications. Based on EPR and XPS outcomes, they also found charge compensation effects and set an optimal Ta/Ti molar ratio as low as 1 %. A further test of the photocatalytic activity was provided by Gong et al.[14] for Ta,B-codoped TiO_2 , showing the beneficial effects of codoping with respect to single-doping in dye degradation tests. Consistently, other authors observed a better performance of co-promoted samples with respect to single-doped ones for photoelectrochemical water oxidation[15].

Given their proximity in the periodic table, a comparison between Nb- and Ta-containing TiO_2 nanomaterials is crucial to clarify what structure-properties relationships effectively contribute to determine a given photocatalytic performance. To the best of our knowledge, no previous experimental comparison between Nb,N- and Ta,N-codoped TiO_2 photocatalysts have been reported to date. The few works which compare Nb,N- and Ta,N-codoped titania are either theoretical [16, 17] or involve single-doping strategies

for electrochemical and DSSC applications[18–20].

This approach not only combines experimental characterizations and Density Functional Theory (DFT) simulations, but also investigates the role played by the synthetic route on the final photocatalytic performance. This issue has a paramount importance, although being seldom discussed in the literature. The synthetic procedure controls phase composition, crystallographic lattice distortions, nature and concentration of bulk defects, electronic band structure and surface properties, whose interplay determines crucial macroscopic properties such as the photocatalytic performance.

Among other synthetic approaches, the chapter will focus on bulk doping by classical sol-gel (sy) routes and post-synthesis impregnation (*im*), since these two techniques are among the most frequently employed in modern catalytic applications. While bulk doping generally leads to more homogeneous systems, impregnation is known to be a very effective method for the production of high performant catalysts[21].

In this Chapter, we compare the photocatalytic performance of TiO_2 single-doped and codoped nanomaterials as a function of the doping method (either *sy* or *im*). Niobium and tantalum were considered as TM dopants, while nitrogen was selected as a possible nonmetal co-dopant. The photocatalytic efficiency was tested toward the degradation of ethanol - a pollutant model system - under UV and simulated solar light irradiation in the gas phase. The photodegradation ability of the various materials was related to their structural, morphological and electronic properties at various length scales as investigated by XRPD, BET, XPS, DRS and EPR characterizations. Experimental results were also complemented by bulk plane-wave DFT simulations. A tentative structural / electronic model was then proposed to account for the observed differences in the photocatalytic performance between the *im* and *sy* sample series. Eventually, implications on the suitability of the im and sy synthetic routes on the engineering of more efficient titania photocatalysts are discussed.

3.1 Results

3.1.1 Microstructure

Figure 3.1 shows typical recorded X-ray diffractograms, together with the corresponding least-squares fittings, for the codoped samples TTaN(im), TNbN(im), TTaN(sy) and TNbN(sy).

As expected on the basis of the core synthetic procedure adopted[22–25], all the materials here investigated are biphasic, with anatase TiO_2 (space group: I41/amd) being always the major polymorph in the mixture and brookite (space group: Pbca) the minority one. When the two im and sy sample series are compared (Figure 3.1e), their trends as a function of the dopant are qualitatively similar. Nevertheless, im materials invariably bear a higher brookite content, while the sy ones are richer in anatase and, in general, more similar to the undoped T reference.

On average, the brookite content turns out to be as high as 43(2) % in impregnated specimens and 36(2) % in the sol-gel ones. Interestingly, Nb,N-codoping seems to somewhat (weakly) favor the anatase phase with respect to single-doped powders[23], while the contemporary presence of Ta and N in the lattice has just the opposite effect. This holds true no matter the dopant feeding method, even though changes in the brookite content are more evident in the sy nanostructured powders.

Also for what concerns the crystallite dimensions of the anatase phase (Figure 3.1f, left axis), the im samples are associated with a bit larger $< D_v >$ values (34(2) $Å^3$) than the sy ones (31(1) $Å^3$). However, there are neither striking nor systematic deviations with respect to the reference T material and differences in $< D_v >$ between the two series are scarcely significant from a statistical viewpoint. This

is even more true when the Williamson-Hall microstrain ϵ is taken into account (Figure 3.1f, right axis). Rather, sy and im samples always bear very similar ϵ values and just a tendency toward higher lattice strain in codoped samples, no matter the doping strategy, could be inferred from Figure 3.1f. In turn, this likely implies that both Nb- and Ta-based doping somewhat increase the average concentration of defects in the nanomaterials here studied. It should be also noted that Ta-containing materials invariably bear higher Willimson-Hall microstrain parameters than the Nb-containing ones. This could be likely related to the longer ionic radius of Tantalum (see below), which implies greater lattice distortions.

In general, microstructural results for Nb- and Nb,N-(co)doped anatase are similar to previous investigations on similar materials[23], as the presence of both dopants discourages the brookite formation and leads to smaller anatase crystallites. Probably, such a behavior can be traced back to the strong thermodynamic driving force toward the I41/amd phase, which results in smaller critical radii of the crystal nuclei and speeds up nucleation over the growth process[26]. However, this is no longer true when Tantalum is considered: Ta,N-codoping is associated with larger anatase crystallites and invariably imply $a \sim +5$ % increment in the brookite content (Figures 3.1e and 3.1f). Assuming the validity of the simple nucleation model above sketched, such a difference might be due to a lower ability of the tetragonal lattice in hosting the larger Ta^{5+} ions (for the sake of comparison, ionic radii of Ti^{4+}, Nb^{5+} and Ta^{5+} in 6-fold coordination[27] are 0.605 Å, 0.640 Å, and 0.780 Å).

More quantitative information on the amount of distortion to which the crystallographic long-range structure is subject upon doping can be obtained by following the changes of the anatase cell edges as a function of the dopant (Figure 3.2).

At the quite low nominal dopant concentration here employed (see above), the relative changes of the crystallographic anatase cell edges are generally immaterial in terms of their estimated standard deviations. More in details, both the c and the symmetry-equivalent a,b cell edges have length equal to those shown by the reference sample T within $\pm$ 0.1 %. The two codoped impregnated TNbN(im) and TTaN(im) samples are the only patent outliers, as they show a significant lengthening (up to $\sim +0.3$ %) of the $|c|$ vector module with respect to the reference compound.

In conclusion, the following take-home messages can be derived by our microstructural XRD analysis. First, the dopant feeding strategy mainly affects the phase composition, with im materials showing a higher brookite content than the sy ones. Second, other average microstructural parameters such as crystallite dimensions and microstrain, are very similar between the two sample series, with the im one possibly showing a small tendency toward larger $< D_v >$. Moreover, Ta-containing materials show higher microstrain, ϵ, than Nb-containing ones. Third, the crystallographic lattice parameters are scarcely affected by the dopant nature and the synthetic route, with the only exception of impregnated codoped materials, which undergo a $\sim +0.2, 0.3$ % increment of the cell along the unique axis. In general, structural distortions and compositional differences are enhanced by both Nb,N- and Ta,N-codoping, no matter how the dopants are added to the material, a fact that mirrors metal/non-metal synergic effects already detected in chapter 2.

3.1.2 Morphological features

The adsorption-desorption isotherms of N_2 in subcritical conditions of single- and codoped samples are reported in Figure 3.3. All the samples show hysteresis loops characteristic of a mesoporosity. The two doping approaches have markedly different effects on the morphological features of the resulting materials (Figures 3.3a and 3.3b).

As for sy materials, both doped and codoped samples generally show lower surface areas, together

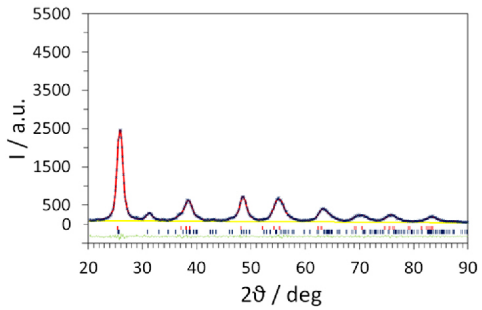

(a) XRPD of TNbN(sy).

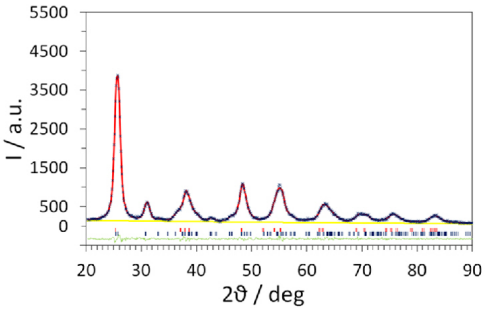

(b) XRPD of TNbN(im).

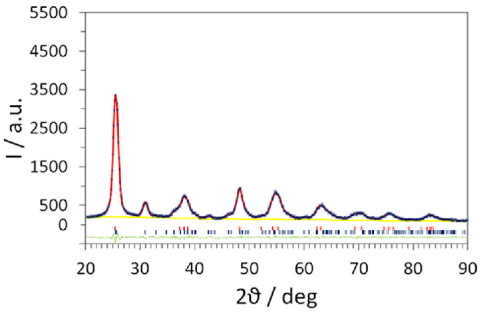

(c) XRPD of TTaN(sy).

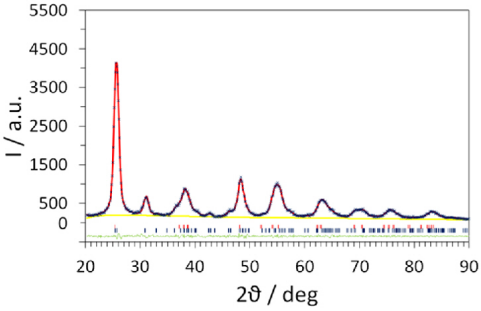

(d) XRPD of TTaN(im).

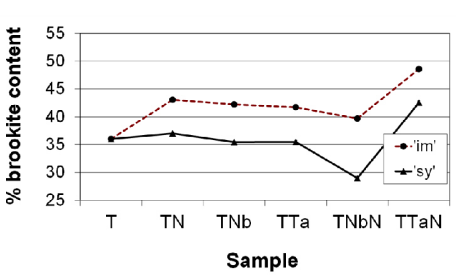

(e) Brookite content for the im (circles, dotted line) and sy samples (triangles, full line), as estimated from the Rietveld refinement against the XRPD data. The lines serve just as guides for the eye. The size of the symbols are roughly equal to the estimated standard deviation (e.s.d.).

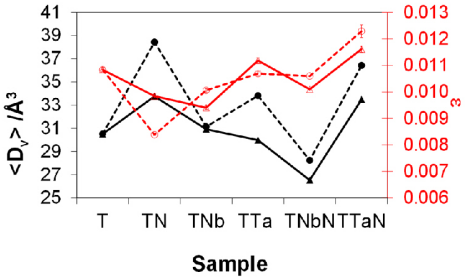

(f) Average volume-weighted crystallite dimensions of the anatase phase (left axis, full black markers) and lattice microstrain values (right axis, open red markers) as retrieved by the Williamson-Hall method from integral breadth of h0l reflections up to $2\theta = 55°$. Circles, dotted lines: im samples. Triangles, full lines: sy samples.

Figure 3.1: *Collected XRPD patterns (blue dots). The least-squares fitting curves are in red, the* y_{obs} - y_{calc} *point-by-point differences in green and the refined background function in yellow. Intensities are drawn on a common arbitrary scale. The diffractions for the anatase and brookite phases are shown as red and blue markers, respectively. Adapted with permission from L. Rimoldi et al., J. Phys. Chem. C, 2015, in press. Copyright 2015 American Chemical Society.*

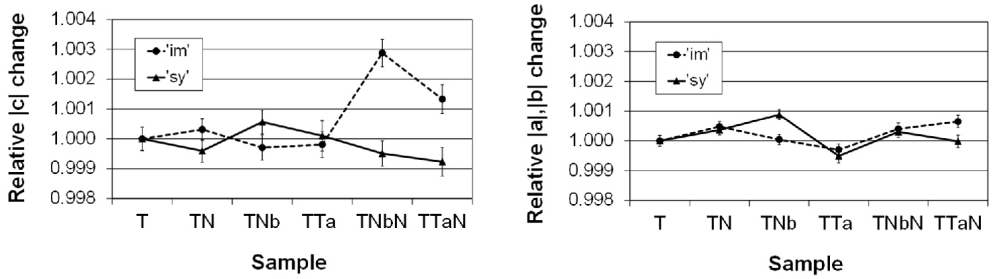

(a) c cell axe modulus. **(b)** a,b cell axe modules.

Figure 3.2: *Relative changes of the c and a,b cell axis modules throughout the im (circles, dotted line) and sy (triangles, full line) sample series with respect to the reference material T as a function of the dopant nature. Error bars correspond to 1 e.s.d. Adapted with permission from L. Rimoldi et al., J. Phys. Chem. C, 2015, in press. Copyright 2015 American Chemical Society.*

Sample	**BET** / $m^2\ g^{-1}$	$\mathbf{V}_{Pores}$ / $mL\ g^{-1}$	$\mathbf{D}_{BET}$ / nm
T	149	0.227	8.3
	Bulk synthesis		
TN(sy)	132	0.291	7.5
TNb(sy)	119	0.166	9.3
TNbN(sy)	161	0.223	8.2
TTa(sy)	135	0.187	10.6
TTaN(sy)	111	0.169	10.0
	Impregnation		
TN(im)	165	0.390	9.3
TNb(im)	133	0.328	10.4
TNbN(im)	150	0.268	7.7
TTa(im)	124	0.281	9.1
TTaN(im)	123	0.325	11.1

Table 3.1: *Specific surface area (S_{BET}), total pore volume (V_{pores}) and average grain diameter calculated from S_{BET} values (D_{BET}) for the doped and undoped samples of the two series.*

with a relevant decrease of the total pore volume (Table 3.1, Figures 3.3c and 3.3d), with respect to the reference T. Furthermore, the presence of either Nb or Ta species induces a shift of the hysteresis loop to lower pressures (Figure 3.3a), indicating a decrease in the average pore size. The shape of the hysteresis loop is also modified upon metal doping, becoming more typical of H_2 -type (bottleneck shape). On the contrary, N-doping has an almost negligible effect on the morphological features of TiO_2 , in agreement with previous reports[23].

The presence of both dopants has a different effect with respect to either single dopant. N,Nb-codoping results in an appreciable increase in surface area while the total pore volume remains unchanged, a fact that might be related to the smaller crystallites (Table 3.2, column 2-3) and smaller pores (Figure 3.3c). N,Ta-codoping gives rise instead to a decrease of the surface area, which may be traced back to the larger average pore size and bigger crystallites.

With respect to bulk doping, the impregnation method leads to higher total pore volumes and to larger average pore sizes (Figure 3.3d), although no clear trends can be appreciated by comparing the specific surface areas of the samples obtained by the two doping approaches. Furthermore, impregnation does not give rise to appreciable effects on the shape of the hysteresis loop of the adsorption/desorption isotherms (Figure 3.3b). *im* samples doped with Nb and Ta have lower surface areas with respect to the undoped reference, but have a higher total pore volume and larger pores, as appreciable from the shift

Sample	$< D_y >$ anatase	$< D_y >$ brookite	ϵ anatase	ϵ brookite
T	30.52(5)	30.39(6)	0.01083(8)	0.0107(1)
TN(sy)	33.8(1)	33.3(1)	0.00984(7)	0.0094(1)
TNb(sy)	30.93(4)	30.89(6)	0.00940(7)	0.0094(1)
TNbN(sy)	26.54(2)	26.46(6)	0.01010(5)	0.00997(7)
TTa(sy)	29.99(5)	29.81(7)	0.0112(1)	0.0110(1)
TTaN(sy)	33.49(8)	33.2(1)	0.0116(1)	0.0113(2)
TN(im)	38.44(3)	38.34(4)	0.00839(3)	0.00831(4)
TNb(im)	31.14(4)	30.99(6)	0.01006(7)	0.0099(1)
TNbN(im)	28.25(1)	28.26(1)	0.01060(1)	0.01061(1)
TTa(im)	33.82(5)	33.65(7)	0.01069(7)	0.0105(1)
TTaN(im)	36.4(2)	35.8(2)	0.0123(2)	0.0117(3)

Table 3.2: *Crystallite dimensions (Å) and microstrain parameters for the two phases. Both were calculated by Williamson-Hall equation applied to h0l reflections up to 55 deg in 2θ and are given with the values of standard deviations.*

of the hysteresis loop to higher pressures (Figure 3.3b). Finally, the addition of nitrogen, both in single- and codoped samples, seems to increase the surface area.

Figure 3.3e SI reports the trend between the experimental surface area and the average crystallite size ($< D_y >$) obtained by elaboration of X-ray powder diffractograms. As expected, a roughly inverse correlation between S_{BET} and $< D_y >$ can be envisaged. The only exception is the sample TN(im), which presents a large surface area together with the largest crystallite size. However, this specimen also bears the largest total pore volume (0.390 mL g^{-1}), which determines a significant increment of the corresponding surface area.

According to the following equation[28]:

$$S_{BET} = \frac{6 \cdot 10^{-4}}{\rho \, D_{BET}} \tag{3.1}$$

the BET surface area can be written as the total surface area of the powder population divided by the powder mass, where ρ is the density of the sample (4.9 g cm^{-3}). The factor 6 applies for spherical as well as for cubic particles. D_{BET} (Table 3.1, fourth column) could be therefore taken as a rough estimate of the average particle size in the assumption that both porosity and surface roughness are negligible. It can be observed that for all samples the D_{BET} value is larger than the crystallite data obtained from X-ray elaboration (Figure 3.1), possibly indicating the occurrence of aggregation phenomena among the crystallites.

3.1.3 Electronic structure

Figure 3.4a reports the electronic density of states (DOSs) of TM single-doped TiO_2 . Both substitutional and interstitial Ta-doping lead to quite different DOSs. In the case of substitutional doping (Figure 3.4a.a), the Fermi energy of the system lies at the bottom of the conduction band and the 5d states of the dopant are located deep into the conduction band. This opens the possibility for enhanced UV absorption. Instead, when Ta is located interstitially (Figure 3.4a.b), mid-gap states are injected into the band gap roughly at the bottom of the conduction band, as shown by the Ta 5d projected DOS.

Considering that the Fermi energy is in both cases just below the conduction band, it is possible to deduce that Ta acts in any case as an electron-donor. Taking into account that titania is highly

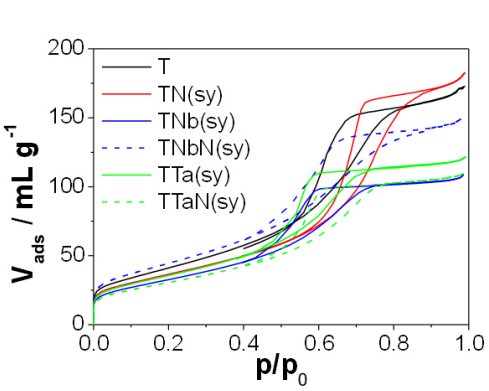

(a) Isotherms of the bulk doped samples.

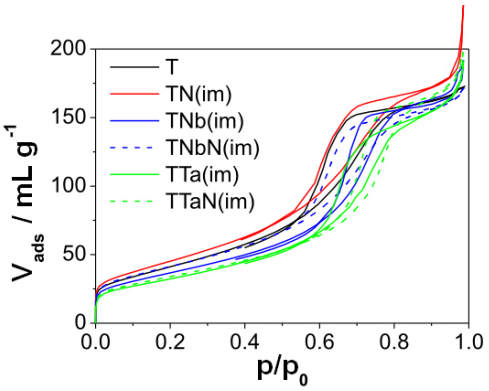

(b) Ishoterms of the impregnated samples.

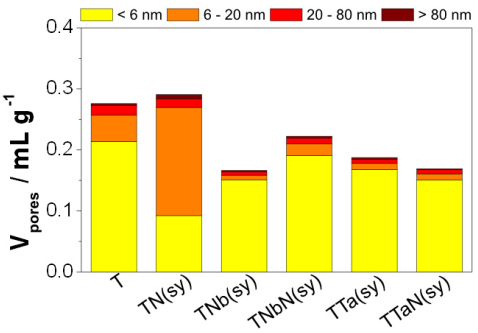

(c) Pore size distribution of the bulk doped samples.

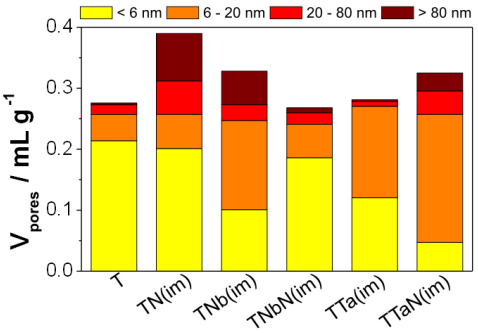

(d) Pore size distribution of the impregnated samples.

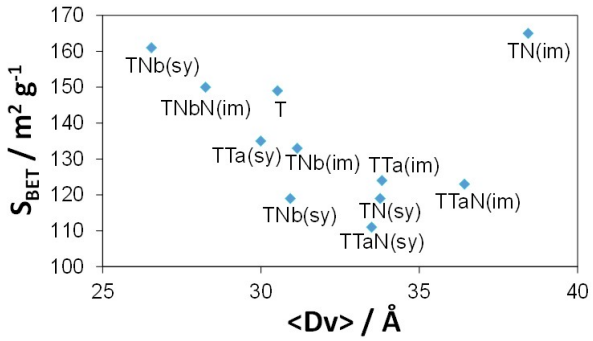

(e) Specific surface area values, S_{BET} *vs* X-ray crystallite dimensions $< D_v >$ of the different samples.

Figure 3.3: *Adsorptiondesorption N_2 isotherms in subcritical conditions and relative pore size disribution of doped sample with respect to the reference TiO_2 sample. Adapted with permission from L. Rimoldi et al., J. Phys. Chem. C, 2015, in press. Copyright 2015 American Chemical Society.*

defective[29–31], oxygen defective and Ta-doped supercells were simulated. Clearly, the vacancies act as electron donors and the Fermi energy is pinned at the bottom of the conduction band (Figure 3.4a.c,d). A comparison between these four panels shows that the Ta orbital location is left unchanged upon oxygen vacancy generation.

To better rationalize the experimental results, on the two lower panels (Figure 3.4a.e,f) the DOSs relative to Oxygen defective Nb substitutional and interstitial doping were reported. In the case of Nb dopant, Nb 4d orbitals act as electron donors as Ta 5d ones, but Nb states are just below the conduction band and potentially available for visible light excitation.

For sake of documentation both substitutional and interstitial TMs doping were reported. However, in the present case only substitutional doping is considered plausible. DFT+U calculations show that both Nb[29] and Ta are preferentially accommodated in substitutional Ti sites. The comparison of the crystallographic strains obtained by the XRD refinements and the DFT+U simulations (Figure 3.5), excludes the possibility for an interstitial TMs doping site.

Finally, the codoping scenarios were presented to complete the description of the experimental samples. To avoid rare configurations, the TM doping site was placed away from the Nitrogen one[23]. We have considered all possible substitutional and interstitial codoping combinations, even though, as stated above, the TM interstitial location is quite improbable. Figure 3.4b shows an electron transfer from the 5d Ta electronic states to the partially empty N orbitals located above the valence band, as it was reported also for the 4d Nb states (Figure 5 of ref. [23]). This electron transfer closes the electronic shell and shifts the Fermi energy toward mid-gap values. The occurrence of this phenomenon is confirmed by EPR experiments. Clearly, this charge compensation effect generates extra stability for the doping process and possibly enhances the photocatalytic performances.

3.1.4 Visible absorption properties

DRS results of single-doped and codoped samples provide direct insight into the mutual role of the guest species in modifying the photoabsorption properties of TiO_2 .

The undoped reference T has the characteristic absorption behavior of anatase TiO_2 , showing a band gap value of 3.2 eV. Bulk doping with either N or metal species (Figures 3.6a and 3.6b) gives rise to both an absorption in the UV region and to a visible sensitization of TiO_2 . N-doping causes a visible light absorption at 450-500 nm, in agreement with previous reports about TiO_2 doped with ammonia salts[7, 23, 32]. Such a localized visible light absorption can be traced back, on the grounds of DFT calculations, to the formation of shallow intragap states located above the valence band of TiO_2 [24]. Bulk doping with either Nb or Ta leads instead to a red shift of the absorption edge, which is comparable for both samples and results in a reduction of the observed band gap of about 0.1 eV (Table 3.3)[33]. Similar red shift effects have previously been reported for Nb-doped TiO_2 [7, 32, 34, 35] and can be attributed to the formation of donor levels located close to the conduction band of TiO_2 [9, 32] (see Figure 3.4a). With respect to Nb-doping, the Ta-doped sample shows also a broader absorption in the blue-green region, which can be attributed to the presence of the 5d state localized into the conduction band (Figures 3.4a.a and 3.4b.a). Interestingly, codoped samples display the characteristic features of the absorption spectra of both N- and Nb/Ta-doped samples. As reported previously15, N,Nb-codoping enhances the visible absorption at 450 nm with respect to nitrogen single-doped samples. Such an effect is even more marked in the case of the N,Ta-codoped sample. Theoretical calculations[9] have shown that transition metals (Nb, Ta) might facilitate the insertion of p-type dopants (N and C) in the TiO_2 lattice. Therefore, the observed enhanced visible absorption at 450 nm might be related to a higher amount of N entering the

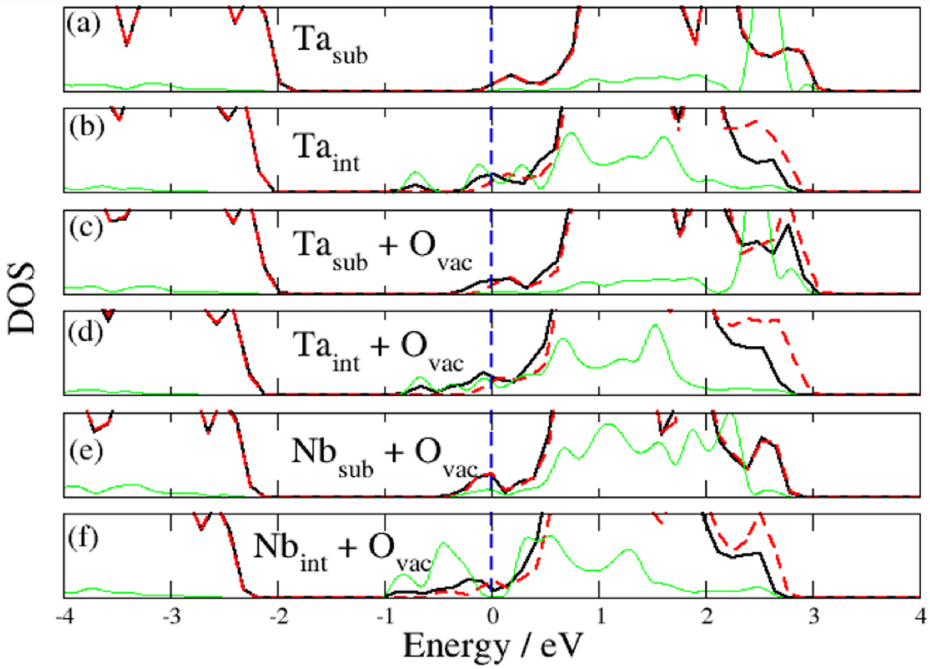

(a) PDOS for the Ta 5d or Nb 4d states (in green).

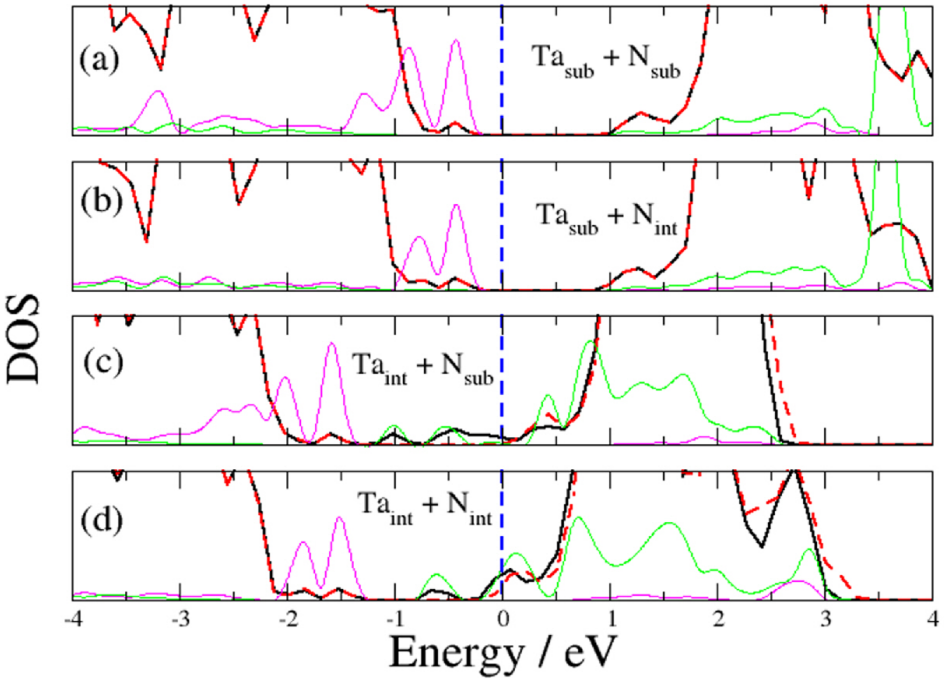

(b) Transition metal PDOS and pink for N PDOS (green line).

Figure 3.4: *Total spin-up (continuous black line) and spin-down (dashed red lines) DOSs. Adapted with permission from L. Rimoldi et al., J. Phys. Chem. C, 2015, in press. Copyright 2015 American Chemical Society.*

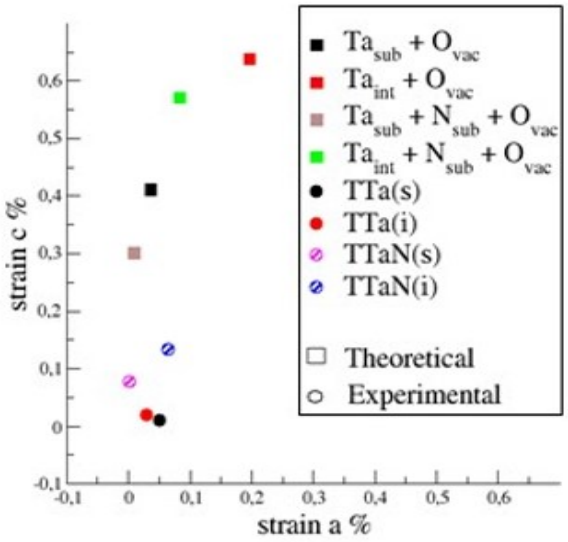

Figure 3.5: *Comparison between crystallographic and DFT+U simulation strains. Adapted with permission from L. Rimoldi et al., J. Phys. Chem. C, 2015, in press. Copyright 2015 American Chemical Society.*

Sample	**Band gap** / eV
T	3.23
TN(sy)	3.18
TNb(sy)	3.09
TNbN(sy)	3.13
TTa(sy)	3.16
TTaN(sy)	3.09
TN(im)	3.22
TNb(im)	3.22
TNbN(im)	3.22
TTa(im)	3.24
TTaN(im)	3.23

Table 3.3: *Band gap values obtained by Kubelka-Munk elaboration of DRS results.*

TiO_2 lattice in codoped samples.

The adopted doping strategy remarkably affects the optical properties of the resulting materials. DRS experiments show that impregnation with TMs (Nb, Ta) does not give rise to appreciable effects on the absorption features of TiO_2 (Figure 3.6b). In particular, no shifts of the absorption edge are observed upon either Nb- or Ta-doping with respect to the undoped reference. On the contrary, impregnated N atoms lead to a visible light absorption around 450 nm, which is fully comparable to what it is observed for bulk doped samples. It is noteworthy that impregnated codoped samples do not shift the absorption edge and the visible absorption localized around 450 nm has a lower intensity with respect to the N-doped sample.

3.1.5 Photocatalytic activity

The photocatalytic activity of the doped and codoped samples was tested toward the gas phase degradation of ethanol as a model volatile organic compound (VOC). Ethanol and its main degradation intermediate, acetaldehyde, are indeed important atmospheric and indoor pollutants[36–39]. During photocatalytic

tests, the concentrations of ethanol, acetaldehyde, and of the product of complete mineralization (CO_2) were monitored by a gas-chromatographic system (Figure 3.6c). Besides acetaldehyde, no other intermediate compounds were determined due to the difficulty in quantifying trace amounts. The carbon balance was always complete at the end of the reaction. Photocatalytic tests were carried out under both UV and simulated solar light irradiation (Appendix C). Photolysis tests under both irradiation sources showed negligible ethanol degradation.

Ethanol degradation was completed for all samples within 120 min of UV irradiation. Acetaldehyde showed the typical bell-shaped curve of a reaction intermediate (Figure 3.6c) and a significant degree of mineralization was obtained for all samples. Figures 3.6d and 3.6e compare the CO_2 formation for the bulk doped and impregnated samples, respectively, under UV irradiation. Bulk doping with either Nb or Ta has a clear detrimental effect on the TiO_2 photocatalytic behavior (Figure 3.6d). Conversely, nitrogen bulk doping gives rise to a very limited enhancement of the photocatalytic activity with respect to undoped TiO_2 . Interestingly, codoping with nitrogen significantly improves the performance of Nb- and Ta-doped materials, although they still remain less active than the nitrogen single-doped sample. Impregnated samples largely outperform their bulk doped counterparts under UV light. All impregnated samples are indeed more active than the undoped reference and give rise to complete mineralization of the pollutant in less than 120 min (Figure 3.6e), with the only exception of TNb(im) whose photocatalytic activity is comparable to that of the undoped reference. The most active sample is TTa(im), followed by TN(im), TTaN(im), TNbN(im) and TNb(im). Table 3.4.b (columns 2-3) reports the initial rates of ethanol degradation under UV light determined using the method of initial decay[32], and the CO_2 percentage after 60 min reaction time. The initial rates of ethanol degradation show the same trends in photocatalytic activity than the CO_2 formation percentage, although mineralization trends are, as expected, more evident.

The situation is quite different for simulated solar tests. For all samples, ethanol degradation was not completed under simulated solar irradiation during the reaction time (Figures 3.6f and 3.6g) and mineralization percentages were extremely low (Table 3.4.a,b, 5th column). Acetaldehyde was the main reaction product for all the tested samples. Figures 3.6f and 3.6g report the ethanol disappearance curves for bulk doped and impregnated samples, respectively, under simulated solar irradiation. As for the UV light tests, nitrogen bulk doped TiO_2 has a behavior similar to the undoped reference, while Ta-doping plays a detrimental role on the TiO_2 photocatalytic activity (Figure 3.6f). On the contrary, Nb-doped and codoped samples exhibit an enhanced photocatalytic performance with respect to the reference, with the codoped sample being the most active. These results are in agreement with the electronic structure calculations in Figure 3.4 and also with previous reports[6], showing improved photocatalytic activity of Nb,N-codoped samples under visible-light irradiation.

Strikingly, all the impregnated samples are less active than the undoped reference (Figure 3.6g), with the only exception of TNb(im) which still presents a comparable behavior with respect to the undoped TiO_2 . It is noteworthy that Ta-doped and codoped samples are the least active under solar irradiation.

3.1.6 EPR analyses

Several paramagnetic features, introduced by the dopants, can be appreciated in EPR spectra obtained at 77 K. Both the TN(sy) and TN(im) samples (Figure 3.7a) show four lines typical of bulk nitrogen paramagnetic defects. These features, labeled by a star (*) in Figure 3.7a ($g_x = 2.066$, $g_y = 2.0054$, $g_z = 2.0040$, $A_x \sim A_y \sim 3\ G$, $A_z \sim 32.2\ G$) have been previously described in the literature[30, 40]. Further, six other lines, labeled in Figure 3.7a as A, B, C, D, E and F, can be detected, in agreement with previous

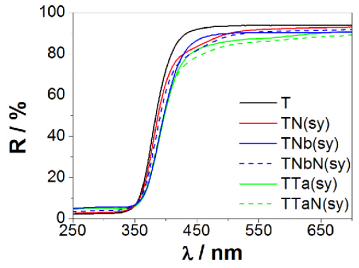

(a) Diffuse reflectance spectra (DRS) of bulk doped samples.

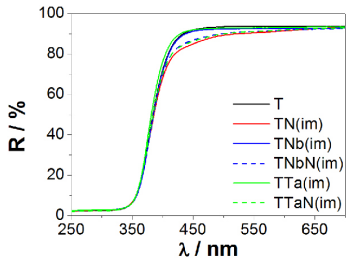

(b) Diffuse reflectance spectra (DRS) of impregnated samples.

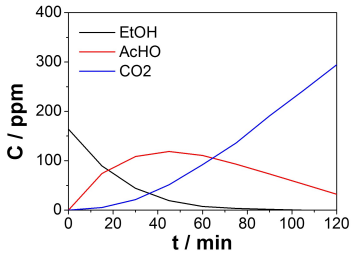

(c) The typical proceeding of ethanol degradation reaction.

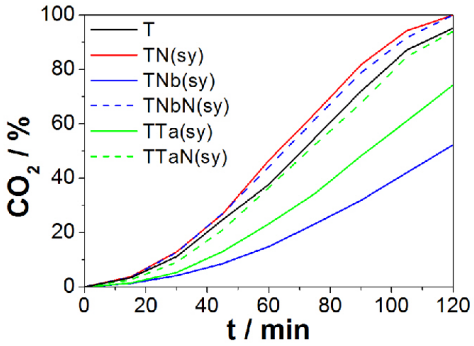

(d) Mineralization curves of bulk doped samples, under UV light irradiation.

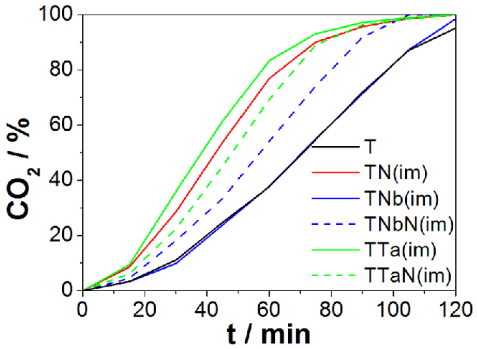

(e) Mineralization curves of impregnated samples, under UV light irradiation.

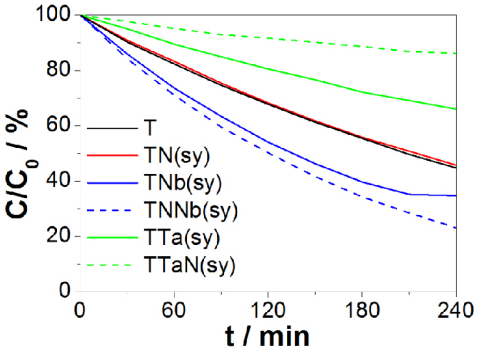

(f) Ethanol disappearance curves of bulk doped samples under simulated solar light irradiation.

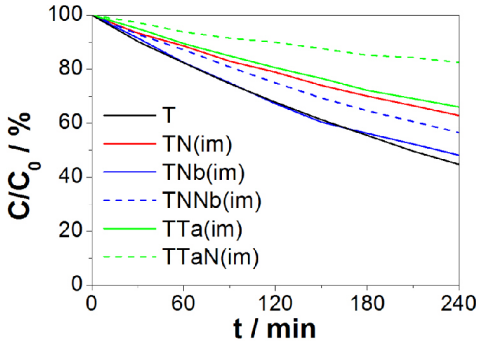

(g) Ethanol disappearance curves of impregnated samples under simulated solar light irradiation..

Figure 3.6: *UV-Vis spectroscopy and ethanol photocatalysis. Adapted with permission from L. Rimoldi et al., J. Phys. Chem. C, 2015, in press. Copyright 2015 American Chemical Society.*

Sample (a)	**UV $k_{pseudo-first-order}$** s^{-1}	**UV %CO_2** (t = 60 min)	**Solar $k_{pseudo-first-order}$** s^{-1}	**Solar %CO_2** (t = 210 min)
T	0.053	37.7	0.0021	0.6
TN(sy)	0.057	47.6	0.0031	1.1
TNb(sy)	0.039	14.8	0.0051	2.5
TNbN(sy)	0.056	44.4	0.0057	2.6
TTa(sy)	0.052	23.2	0.0009	0.3
TTaN(sy)	0.052	36.5	0.0007	0.3
Sample (b)	**UV $k_{pseudo-first-order}$** s^{-1}	**UV %CO_2** (t = 60 min)	**Solar $k_{pseudo-first-order}$** s^{-1}	**Solar %CO_2** (t = 210 min)
T	0.053	37.7	0.0021	0.6
TN(im)	0.060	80.6	0.0020	0.0
TNb(im)	0.051	37.9	0.0032	0.9
TNbN(im)	0.063	54.6	0.0023	0.7
TTa(im)	0.060	88.5	0.0018	0.5
TTaN(im)	0.066	74.6	0.0009	0.2

Table 3.4: *Kinetic constants and percentage of mineralization in UV and simulated solar tests for a) bulk doped samples and b) impregnated samples.*

work[23]. The features A and B ($g_x = 2.0082$, $g_y = 2.0118$, $g_z = 2.0285$) can be related to paramagnetic radical oxygen species[30, 41] while the lines C ($g_1 = 1.98$), D ($g_2 = 1.93$) and E ($g_3 = 1.96$) can be attributed to Ti^{3+} in different environments, analogously to what reported by other authors[34, 42]. It is relevant to observe that these three lines cannot be appreciated in room temperature spectra. This occurrence supports the attribution of these latter lines to Ti^{3+} species on the grounds of the reported disappearance of Ti^{3+} signals above 100 K due to carrier detrapping[35]. Line F, showing an intensity comparable to that of the B line, can be simulated by a symmetric line with $g \sim 2$, and can be attributed to F+ paramagnetic defects, which have already been reported in the case of N-doped TiO_2 [8, 23, 40].

TN(sy) and TN(im) have the same chemical nominal composition and indeed show the same EPR features. However, the same lines have different intensities in the two EPR spectra (Figure 3.7a). Specifically, we can compare the intensity ratio, R, between the most intense $N_b^\bullet$ (star-labeled) line and that of B, which is the most intense line due to oxygen radical species. This ratio is very different for the two spectra, being R(TN(sy)) ~ 0.44 and R(TN(im)) ~ 2.1. Furthermore, the E line attributed to Ti^{3+} is observed only in the case of TN(sy) but not in the case of N(im). The two adopted doping procedures apparently give rise to a different balance between paramagnetic defects.

The role played by the metal (Nb, Ta) in modifying N-induced defects can be now examined, starting from the codoped samples obtained by impregnation. Only oxygen radicals as well as F^+ and Ti^{3+} species (except for the one producing the E line) are appreciable in the TNbN(im) codoped sample (red in Figure 3.7b). Several authors reported the occurrence of bulk Ti^{3+} species also in Nb-doped TiO_2 [23, 34, 35] whose formation was attributed to a mechanism of valence induction[6, 9]. The disappearance of $N_b^\bullet$ paramagnetic species in the TNbN(im) sample supports the occurrence of charge compensation phenomena between Nb (acting as an electron donor) and N (acting as an electron acceptor), as already reported elsewhere[9, 23].

In the case, instead, of TTaN(im), the compensation mechanism is not as complete as for sample TNbN(im), since low intensity $N_b^\bullet$ lines add to the F^+ and Ti^{3+} paramagnetic species in the spectrum (Figure 3.7c). The intensity ratio R pertaining to TTaN(im) is about 0.21, to be compared with $R \sim 0$ for N,Nb-codoped, impregnated sample.

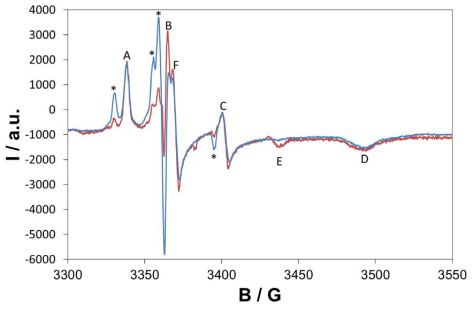

(a) Experimental EPR spectra of TN(sy) (red) and TN(im) (blue).

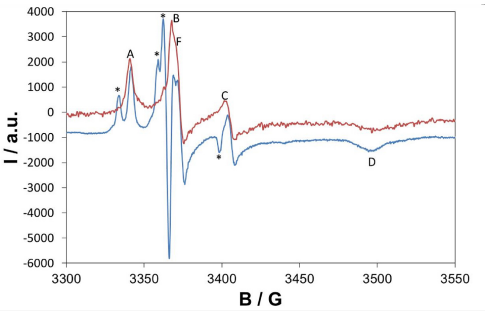

(b) Experimental EPR spectra of TNbN(im) (red) and TN(im) (blue).

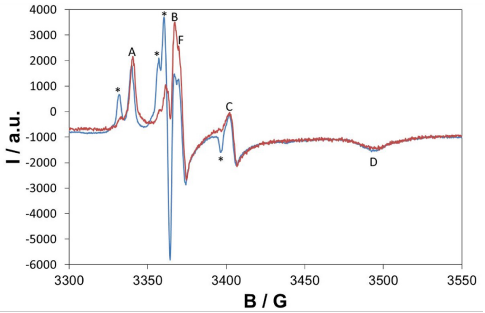

(c) Experimental EPR spectra of TTaN(im) (red) and TN(im) (blue).

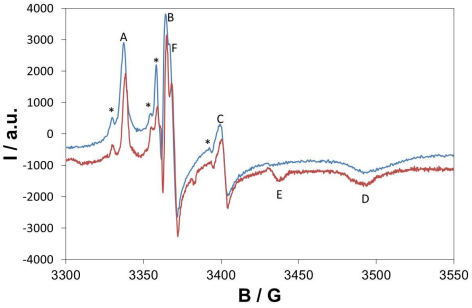

(d) Experimental EPR spectra of TNbN(sy) (blue) and TN(sy) (red).

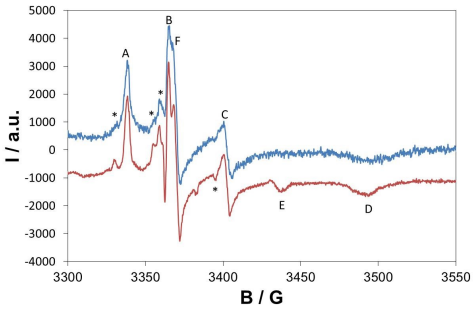

(e) Experimental EPR spectra of TTaN(sy) (blue) and TN(sy) (red).

Figure 3.7: *Experimental EPR spectra collected at 77 K. Adapted with permission from L. Rimoldi et al., J. Phys. Chem. C, 2015, in press. Copyright 2015 American Chemical Society.*

In the case of the codoped samples obtained by bulk synthesis (sy) the compensation effects are less significant than for the impregnated samples (Figure 3.7d). As for TNbN(sy), the only relevant effect due to the presence of the metal is the disappearance of the E line attributed to Ti^{3+} species while no other significant difference can be appreciated. The R value is around 0.47.

The picture is slightly different in the case of TTaN(sy) (Figure 3.7e). The R(TTaN(sy)) $\sim$ 0.25 ratio is almost half with respect to the value of TN(sy) and suggests that the compresence of Ta in the synthesis modifies the balance between $N_b^\bullet$ and of the oxygen-based radical species.

3.2 Discussion

XPS results are affected by a large noise, possibly due to the low amount of the provided dopants. However, as a general trend, they point out that im samples invariably bear an apparent higher amount

Sample	'im'	'sy'
TNb	0.14	0.03
TTa	0.06	0.01
TNbN	0.05	0.01
TTaN	0.02	0.01

Table 3.5: *Apparent concentrations of transition metal (TM) dopants within the im and sy nanostructured powders, as retrieved from the area ratios of the Nb/Ti and Ta/Ti XPS peaks and expressed as TM/Ti atomic ratios.*

of dopants with respect to the sy ones, as reported in Table 3.5. Figures 3.8a and 3.8b shows an assay of representative XPS spectra for the two guest metals.

This was quite an unexpected result, as the reaction mixtures were always fed with the same amount of precursor reagents within the experimental error. The two sample series were calcined under identical thermodynamic control conditions and non-volatile TM species should have been granted the same chances of entering the nanoparticles. Besides, no evidences of segregated Nb- and Ta-based phases were found by the XRD analysis (see Section 3.1.1). To explain the detected differences (Table 3.5), we hypothesize that im samples are less homogeneous than the sy ones. Actually, it is reasonable to assume that the distribution of point defects differs depending on the adopted doping procedure. In the sy case, guest ions are supplied when the TiO_2 crystalline phase is growing, and it is probable that they spread out quite uniformly throughout most of the anatase lattice structure[23]. On the contrary, in im materials the dopants are supplied after the bulk phases are formed and prior to the calcination step. With this procedure, the dopants must first diffuse through grain pores and interstitial voids to enter the crystallites. This diffusion needs to occur when the amorphous-to-crystalline transition is taking place. Consequently, a radial concentration gradient is set up within large aggregates of crystallites (grains), and the extrinsic impurities are more concentrated within crystallites near the boundaries and less at the core of each grain (Figure 3.8c). This defect modeling could explain the differences that we have detected in the XPS signals (Table 3.5). Indeed, higher concentrations of dopants in crystallites at the grain surface produce more intense signals, as less photoelectrons are available from inner crystallites. Actually, photoelectrons generated from regions buried in depth within the grain have a higher probability of being inelastically scattered prior to escaping from the surface.

The inelastic mean free path of the emitted photoelectrons associated with the characteristic kinetic energy of the Al Kα radiation (1.487 keV) here employed is $\sim$ 1-1.5 nm. Therefore, the expected sampling depth in our samples is $\sim$ 3-4.5 nm, which is comparable with the average crystallite diameters retrieved by powder XRD experiments for both the im and sy series (see Figure 3.1f and Table 3.2). In turn, this implies that, on average, each crystallite make available its whole volume as a photoelectron source. However, crystallites farther than $\sim$ 4.5 nm from the grain surface are essentially silent. Hence, the fact that im materials produce more intense Ta and Nb XPS peaks might imply that impregnated nanoparticles are more near-surface crystallites rich in extrinsic defects (Figure 3.8c).

It should be stressed, however, that it is the overall amount of defects in the host (intrinsic + induced) and guest (extrinsic) that determines the photocatalytic properties of these materials. In this respect, EPR provides accurate estimates of the ratios between paramagnetic host Oxygen species ($O^{\bullet}$) and guest $N_b^{\bullet}$ defects. When they are complemented with the experimental E_g's retrieved from DRS spectra (Section 3.1.4), it is possible to disentangle these two aspects, at least qualitatively (Figure 3.8d).

In Figure 3.8d, the two sample series show very different trends. For the im materials, the ratio among paramagnetic defects is high in TN and then undergoes an abrupt reduction when metal species

are also present, while the apparent band gap is invariant. Quantum mechanical calculations show that a reduction of the band gap is mostly associated with shallow mid-gap states created by oxygen vacancies[22]. Otherwise, E_g is expected to undergo a slight reduction in N (and TM,N co-)doped samples, as occupied valence N states lie just at the valence band edge (see also Section 3.1.3).

Combined EPR, DRS and DFT results provide compelling evidence that the im method does not change the concentration of host defects, *i.e.* the denominator in the $[N_b^\bullet]/[O^\bullet]$ ratio. The abrupt reduction of this ratio (Figure 3.8d, circles) can be explained by the reduction of the amount of paramagnetic $N_b^\bullet$ species, that in turn can be related to the occurrence of an internal electron transfer[23] from TM to N (see also Sections 3.1.3 and 3.1.6 above). When considering the sy samples, we observe a very different behavior (Figure 3.8d, triangles). First, the $[N_b^\bullet]/[O^\bullet]$ ratio is always low and constant, while E_g is systematically smaller than those of im materials. This latter evidence suggests that in these cases the concentration of host defects is always higher. This is also in accordance with the increased absorption efficiency detected for these powders in the visible range (Section 3.1.4).

These experimental results can be interpreted at the light of the measured photocalytic activity (see Section 3.1.5) of the two im and sy sample series. Under UV irradiation, im samples perform better than sy ones, with Ta-doped powders being significantly more efficient than the Nb-doped ones (Figures 3.6f and 3.6g). The first observation can be explained by invoking the anisotropic guest defect distribution at the mesoscale we have hypothesized, as near-surface crystallites should bear a higher amount of extrinsic guest species and are therefore expected to be more efficient in light harvesting. Also, the higher UV activity of Ta-doped specimens, can be traced back to the electronic states injected by Ta ions within the conduction band (see Section 3.1.3), since these orbitals improve the probability to allocate the photoexcited carries.

When subjected to simulated solar light irradiation, sy Nb,N-codoped and Nb-doped materials are the most active ones, while all the impregnated samples are even less performant than the undoped reference T (Section 3.1.5). It should be remarked that the spectrum of the solar lamp mostly bears longer-wavelength components, which penetrate more deeply than shorter UV ones. Therefore, it is reasonable that larger portions of the grains are involved in the process of creating photogenerated carriers. Consequently, differences in the defect distributions at the mesoscale (Figure 3.8c) are expected to be less important and the electronic structure, as resulting from the cooperative interplay between guest and host defects, becomes determinant. In general, the less defective im samples do not exploit any enhancement of the photocatalytic activity with respect to the T reference. Instead, the sy materials, which contain a higher amount of paramagnetic host defects (see above), does enhance the photocatalytic activity. This implies that a strict correlation exists, as expected, between such defects and the visible-light activity of the photocatalyst. At the same time, the synergic role of Nb and N codopants is confirmed, as the TNbN material is absolutely the best performing one. Also, sy Ta-doping performs worse than Nb-doping possibly because of kinetic effects. More specifically, an increased charge recombination is likely to occur since larger Ta^{5+} ions induce a bit higher lattice strain than the corresponding Nb^{5+}-containing materials (Figure 3.1f, Table 3.2), *i.e.* more lattice defects are present in Ta-doped systems. A too high defect concentration is detrimental to photocatalysis, as it favors recombination of the charge carriers[40]. It is also worth noting that the worst performing TTaN specimen is associated with the highest ϵ (Table 3.2) and to the lowest E_g (Figure 3.8d) estimates.

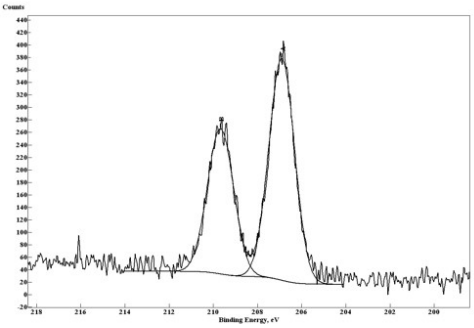

(a) XPS spectra of TNb(im) in the region of Nb. Fitting functions are also highlighted.

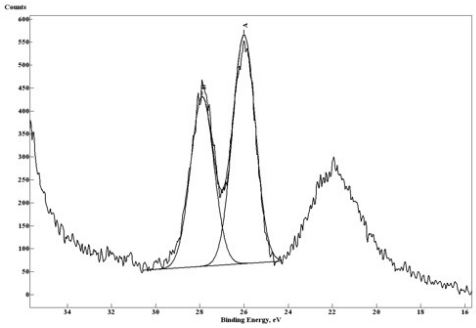

(b) XPS spectra of TTaN(im) in the region of Ta, respectively. Fitting functions are also highlighted.

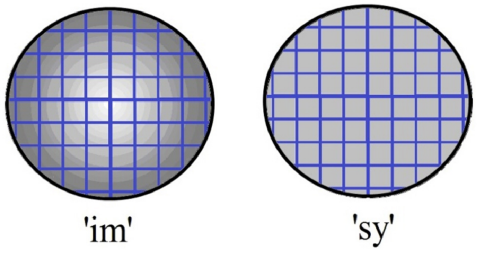

(c) A sketch of the mesoscale defect model proposed to explain compositional differences detected by XPS spectroscopy. The ellipsoids represent TiO_2 grains, small blue boxes (possibly) differently oriented crystallites and darker regions imply a higher concentration of extrinsic defects.

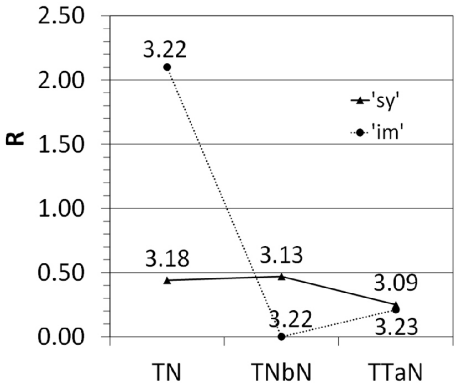

(d) EPR-derived $[Nb^{\bullet}]/[O^{\bullet}]$ ratios R for im (circles, dotted line) and sy (triangles, full line) TN, TNbN and TTaN materials. For each point, the band gap width in eV, as estimated through the Kubelka-Munk equation, is also shown.

Figure 3.8: *XPS analysis and defect scheme. Adapted with permission from L. Rimoldi et al., J. Phys. Chem. C, 2015, in press. Copyright 2015 American Chemical Society.*

3.3 Conclusion

In this work, a thorough multi-disciplinary experimental (XRPD, BET, XPS, DRS, EPR) and theoretical (plane-wave DFT) study was undertaken on both single-doped and codoped TM,N (TM = Nb, Ta) nanostructured TiO_2 materials. The photocatalytic performances of the synthesized powders were tested toward the gas phase degradation of ethanol under both UV and simulated solar light irradiation. This work mainly focused on relating the efficiency of the photocatalytic process to the synthetic route employed to feed titania nanocrystals with guest species, *i.e.* impregnation (im) *vs* bulk synthesis (sy).

The main absorption features of the im samples were found to be unchanged with respect to the undoped TiO_2 reference, whereas the sy ones show a significant apparent reduction of the band gap. Accordingly, upon solar light irradiation sy materials are the most active ones, while all the im samples perform worse than the undoped TiO_2 reference. These differences can be understood on the grounds of the different amount of host defects within the two sample series. Actually, sy materials are more defective, with the lattice microstrain of Ta-containing nanoparticles being always higher than the corresponding Nb-containing ones. In other words, the macroscopic photocatalytic activity in this energy range is mainly correlated with the presence of host defects. The more defective Ta-doped materials show worse performances due to a higher likelihood of charge recombination.

Under UV irradiation, the picture is very different. Here im samples perform better than sy ones, with Ta-doped powders being significantly more efficient than the Nb-doped ones. To account for this reversed behavior, we developed an anisotropic defect distribution model at the mesoscale. In few words, we observe that in im powders the crystallites near the grain surface bear a higher amount of guest species. Therefore, they are more efficient in light harvesting. Ta-doped specimens, on the other hand, degrade ethanol more efficiently than Nb-doped ones as guest Ta ions inject 5d-like states within the TiO_2 conduction band, enhancing the number of e^--h^+ pairs available to promote redox reactions at the grain surface.

3.4 Specific procedures

Samples preparation Two series of titania samples were synthesized, differing in the doping procedure: either addition during the sol-gel synthesis (sy) or impregnation (im). Each series consisted of five samples: N-doped (TN), Nb-doped (TNb), Ta-doped (TTa), Nb,N-codoped (TNbN) and Ta,N-codoped (TTaN) TiO_2 . The nominal dopant/Ti molar ratio was fixed at 1 %. Solutions of NH_4OH, $NbCl_5$ and $TaCl_5$ were employed as dopant precursors. For the TNbN specimens, the two dopants were provided at the same time by $NH_4[NbO(C_2O_4)_2(H_2O)]\cdot nH_2O$, whereas NH_4Cl and $TaCl_5$ were employed as precursors for the TTaN samples. (sy) or (im) symbols are added to the various sample labels to specify whether each specific material was respectively obtained either from the sy or the im procedure. An undoped titania sample (T) was also synthesized as a reference for both series.

The same sol-gel procedure was employed throughout as the basic synthetic route. More in detail, 0.063 mol of titanium(IV) isopropoxide was mixed with 24 mL of 2-propanol in order to obtain a molar ratio of 1:5. The solution was stirred for 10 min at 300 rpm. Then, 113 mL of a HCl aqueous solution at pH 3 was added drop-wise while stirring vigorously to obtain a final Ti/H_2O molar ratio of 1:100. The mixture was stirred continuously for 90 min to complete the hydrolysis. Then, the solvent was removed drying in oven at 80 $^\circ C$.

The first series (sy) of samples was prepared by adding the dopant precursors directly during the sol-gel synthesis in the 2-propanol solution. A NH_4OH solution was mixed to the aqueous solution for

the preparation of the N-doped (TN(sy)) sample. The powders were then dried in oven at 80 $^{\circ}C$ and calcined at 400 $^{\circ}C$ for 6 h in O_2 flux (9 NL h^{-1}).

The second series (im) of photocatalysts was prepared by suspending 1.5 g of the uncalcined powder in 15 mL of an ethanol:water (2:1) solution (or 15 mL of an aqueous solution for the TN(im) sample) containing the dopant precursors. After 90 min, the material was dried in oven at 90 $^{\circ}C$ and calcined at 400 $^{\circ}C$ for 6 h in O_2 flux (9 NL h^{-1}).

Photocatalytic activity tests All samples were tested under both UV and simulated solar irradiation (see Appendix C) in the gas phase photocatalytic degradation of ethanol, as a pollutant model for volatile organic compounds (VOCs). Photocatalytic tests were carried out in a previously described apparatus[43]. 50 mg of TiO_2 powder, drop casted on a 254 cm^2 Petri dish, were employed in conjunction with a starting ethanol concentration in the range 198-238 ppm. The disappearance of the pollutant molecule, the formation of the main intermediate (acetaldehyde) and its complete mineralization to CO_2 were monitored during photocatalytic tests by means of a gas-chromatographic system (Agilent 7890 equipped with DB-VAX and Porapak columns, two FID detectors and a methanator).

DFT modeling To simulate doped TiO_2 anatase, we performed DFT+U calculations[44] using VASP suite of codes[43]. The Projector augmented wave (PAW) pseudopotentials were employed42,44, considering the spin-polarization. The Generalized Gradient Approximation (GGA) was used[45] with the Perdew-Burke-Ernzerhof parametrization. A 3x3x3 anatase bulk supercell was built by reproduction of the primitive cell. Given the 162 atoms supercell, sampling was limited only around the point in reciprocal space. The energy cutoff was set at 400 eV. The conjugated gradient scheme was employed for optimization with a threshold for convergence equal to 0.001 eV for the change in total energy between two consecutive steps and 0.01 eV/Å for the forces. The question whether one should use DFT+U or hybrid functional for TMs doping and N codoping has been studied in details in literature[1, 16]. It has been found that in the case of Nb and Ta substitutional doping, both hybrid functional and DFT+U51 well reproduce the localized Ti^{3+} orbitals for rutile and the semi-metallic behavior for anatase. According to previous works on defective titania, we fixed the U parameter to be equal to 3.3 eV for the Ti 3d orbitals and checked that the Ti^{3+} induced by the Nb- and Ta-doping were at the conduction band edge, as in the case of previous theoretical calculations.

Further details about synthetic procedures and characterizations can be found in Appendix C.

References

[1] R. Long, N. J. English, *Chem. Phys. Lett.* **2009**, *478*, 175 –179.

[2] L. R. Sheppard, S. Hager, J. Holik, R. Liu, S. Macartney, R. Wuhrer, *J. Phys. Chem. C* **2015**, *119*, 392–400.

[3] C. Wang, A. Geng, Y. Guo, S. Jiang, X. Qu, *Mat. Lett.* **2006**, *60*, 2711 –2714.

[4] M. Altomare, K. Lee, M. S. Killian, E. Selli, P. Schmuki, *Chem. Europ. J.* **2013**, *19*, 5841–5844.

[5] S. M. Bawaked, S. Sathasivam, D. S. Bhachu, N. Chadwick, A. Y. Obaid, S. Al-Thabaiti, S. N. Basahel, C. J. Carmalt, I. P. Parkin, *J. Mater. Chem. A* **2014**, *2*, 12849–12856.

[6] J. Lim, P. Murugan, N. Lakshminarasimhan, J. Y. Kim, J. S. Lee, S.-H. Lee, W. Choi, *J. Catal.* **2014**, *310*, 91 –99.

[7] T. M. Breault, B. M. Bartlett, *J. Phys. Chem. C* **2013**, *117*, 8611–8618.

[8] T. M. Breault, B. M. Bartlett, *J. Phys. Chem. C* **2012**, *116*, 5986–5994.

[9] X. Ma, Y. Wu, Y. Lu, J. Xu, Y. Wang, Y. Zhu, *J. Phys. Chem. C* **2011**, *115*, 16963–16969.

[10] T. Cottineau, N. Bealu, P.-A. Gross, S. N. Pronkin, N. Keller, E. R. Savinova, V. Keller, *J. Mater. Chem. A* **2013**, *1*, 2151–2160.

[11] Q.-L. Liu, Z.-Y. Zhao, Q.-J. Liu, *Mater. Sci. Semicond. Pro.* **2015**, *33*, 94 –102.

[12] K. Obata, H. Irie, K. Hashimoto, *Chem. Phys.* **2007**, *339*, 124 –132.

[13] W. Wang, C. Lu, Y. Ni, M. Su, W. Huang, Z. Xu, *Appl. Surf. Sci.* **2012**, *258*, 8696 –8703.

[14] Y. Gong, C. Fu, L. Ting, J. Chenu, Q. Zhao, C. Li, *Appl. Surf. Sci.* **2015**, *351*, 746 –752.

[15] S. Hoang, S. Guo, C. B. Mullins, *J. Phys. Chem. C* **2012**, *116*, 23283–23290.

[16] J. Huang, S. Wen, J. Liu, G. He, *J. Nat. Gas Chem.* **2012**, *21*, 302 –307.

[17] W.-J. Yin, H. Tang, S.-H. Wei, M. M. Al-Jassim, J. Turner, Y. Yan, *Phys. Rev. B* **2010**, *82*, 045106.

[18] J. Liu, Y. Duan, X. Zhou, Y. Lin, *Appl. Surf. Sci.* **2013**, *277*, 231 –236.

[19] X. Liu, X. Wu, K. Scott, *Catal. Sci. Technol.* **2014**, *4*, 3891–3898.

[20] P. Mazzolini, P. Gondoni, V. Russo, D. Chrastina, C. S. Casari, A. L. Bassi, *J. Phys. Chem. C* **2015**, *119*, 6988–6997.

[21] A. Minguzzi, C. Locatelli, G. Cappelletti, C. L. Bianchi, A. Vertova, S. Ardizzone, S. Rondinini, *J. Mater. Chem.* **2012**, *22*, 8896–8902.

[22] M. Ceotto, L. L. Presti, G. Cappelletti, D. Meroni, F. Spadavecchia, R. Zecca, M. Leoni, P. Scardi, C. L. Bianchi, S. Ardizzone, *J. Phys. Chem. C* **2012**, *116*, 1764–1771.

[23] C. Marchiori, G. D. Liberto, G. Soliveri, L. Loconte, L. L. Presti, D. Meroni, M. Ceotto, C. Oliva, S. Cappelli, G. Cappelletti, C. Aieta, S. Ardizzone, *J. Phys. Chem. C* **2014**, *118*, 24152–24164.

[24] L. LoPresti, M. Ceotto, F. Spadavecchia, G. Cappelletti, D. Meroni, R. G. Acres, S. Ardizzone, *J. Phys. Chem. C* **2014**, *118*, 4797–4807.

[25] F. Spadavecchia, G. Cappelletti, S. Ardizzone, M. Ceotto, M. S. Azzola, L. L. Presti, G. Cerrato, L. Falciola, *J. Phys. Chem. C* **2012**, *116*, 23083–23093.

[26] J. Mullin in *Crystallization (Fourth Edition)*, (Ed.: J. Mullin), Butterworth-Heinemann, Oxford, Fourth Edition, **2001**, pp. 216 –288.

[27] R. D. Shannon, *Acta Crystallograph. A* **1976**, *32*, 751–767.

[28] S. Ardizzone, C. L. Bianchi, G. Cappelletti, S. Gialanella, C. Pirola, V. Ragaini, *J. Phys. Chem. C* **2007**, *111*, 13222–13231.

[29] Z. Zhao, Q. Liu, *Catal. Lett* **2008**, *124*, 111–117.

[30] F. Spadavecchia, G. Cappelletti, S. Ardizzone, M. Ceotto, L. Falciola, *J. Phys. Chem. C* **2011**, *115*, 6381–6391.

[31] H. Irie, Y. Watanabe, K. Hashimoto*, *J. Phys. Chem. B* **2003**, *107*, 5483–5486.

[32] D. Meroni, S. Ardizzone, G. Cappelletti, C. Oliva, M. Ceotto, D. Poelman, H. Poelman, *Catal. Today* **2011**, *161*, 169–174.

[33] V. N. Kuznetsov, N. Serpone, *J. Phys. Chem. C* **2009**, *113*, 15110–15123.

[34] J. Biedrzycki, S. Livraghi, E. Giamello, S. Agnoli, G. Granozzi, *J. Phys. Chem. C* **2014**, *118*, 8462–8473.

[35] L. DeTrizio, R. Buonsanti, A. M. Schimpf, A. Llordes, D. R. Gamelin, R. Simonutti, D. J. Milliron, *Chem. Mater.* **2013**, *25*, 3383–3390.

[36] H.-H. Nguyen, N. Takenaka, H. Bandow, Y. Maeda, S. De Oliva, M. Botelho, T. Tavares, *Atmos. Environ.* **2001**, *35*, 3075–3083.

[37] K.-D. Kwon, W.-K. Jo, H.-J. Lim, W.-S. Jeong, *Environ. Sci. Pollut. Res.* **2008**, *15*, 521–526.

[38] L. Brickus, J. Cardoso, F. De Aquino Neto, *Environ. Sci. Tech.* **1998**, *32*, 3485–3490.

[39] J. Gaffney, N. Marley, *Atmos. Environ.* **2009**, *43*, 23–36.

[40] F. Spadavecchia, G. Cappelletti, S. Ardizzone, C. L. Bianchi, S. Cappelli, C. Oliva, P. Scardi, M. Leoni, P. Fermo, *Appl. Cat. B* **2010**, *96*, 314 –322.

[41] R. F. Howe, M. Gratzel, *J. Phys. Chem.* **1985**, *89*, 4495–4499.

[42] S. Livraghi, M. Chiesa, M. C. Paganini, E. Giamello, *J. Phys. Chem. C* **2011**, *115*, 25413–25421.

[43] G. Kresse, J. Hafner, *Phys. Rev. B* **1994**, *49*, 14251–14269.

[44] S. L. Dudarev, G. A. Botton, S. Y. Savrasov, C. J. Humphreys, A. P. Sutton, *Phys. Rev. B* **1998**, *57*, 1505–1509.

[45] J. P. Perdew, Y. Wang, *Phys. Rev. B* **1992**, *45*, 13244–13249.

Part II

Wettability modulation of oxide surfaces

Chapter 4

Silanes: wettability and polar momenta

Organosilanes have attracted great attention in the last few years due to their ability to functionalize oxide surfaces, such as native metal oxides, silica, titana and conductive oxides. The control of those reactions has allowed to easily tune the physico chemical properties of surfaces, with incredible flexibility and effectiveness. The modification of friction, wettability[1], capacitance[2], permeability are only few of the many advances connected with such layers. They have found promising applications in several different fields, ranging from everyday life products (like commercial wall coatings and anti-corrosion layers) to the more technological and futuristic uses (microfluidics[3] and microelectronics, they act as lithographic coatings[4], binders for nano-objects and bio-macromolecules, up to insulating parts in transistor technology and active sensing probes). Organosilane derivatives in the presence of water molecules tend to undergo condensation reaction with hydroxyl groups at the oxide surface and/or with other organosilane molecules[1]. The most commonly studied molecules, trifunctional alkylsilanes ($RSiX_3$ where X can be -Cl, -OEt or -OMet), can give rise to a number of possible surface structures, both 2-D (self-assembly monolayer, SAM) and 3-D arrangement[5]. The obtained layer structure crucially depends on the deposition conditions, chemical architecture of the siloxane, nature and chemistry of the substrate.

In this second part of the thesis, the properties of silanes will be studied as hydrophobizing agents for oxide surfaces, particularly on SiO_2 and TiO_2 . While in this Chapter 4, the wettability properties of the bare siloxanes will be studied with respect to the polar momenta of the molecules, in Chapter 5, two selected molecules will be grafted on a smooth silica surface to assembly a monolayer by chemical vapor deposition (CVD) technique. Chapter 6 will compare distinct oxide substrates with different morphologies and chemical natures(TiO_2 and SiO_2), with the final aim to obtain superhydrophobic surfaces; two different funtionalization procedures will be compared, CVD and wet impregnation (WI). Eventually, in Chapter 7, the wet impregnation technique will be exploited to obtain organic/TiO_2 hybrid coatings with superhydophobic/oleophobic properties; here, the photoactivity of TiO_2 will be investigated as an effective lithographic tool to produce superhydro-phobic/philic patterns.

Silane hydrophobizing agents find many applications in formulation technology, in which they are used directly in the formulation or as hydrophobizing agents for oxide fillers of hydrophobic and self-cleaning coating and paints. From this, the understanding of the wettability properties of the molecules themselves, and the ability to correlate hydrophobizing properties and the molecular structure, are crucial. In this contest, the surface and interfacial energy are important parameters for the control of practical

applications such as spinning, polymer adhesion, stability of dispersions, wetting of solids, and spreading on solid surfaces.[6]

In this chapter, the SFEs of both commercial and laboratory-made siloxane thin layers deposited by spin coating onto glass supports are evaluated. The effects of the presence of fluorinated groups in the siloxane chains with regards to the final wetting features of the siloxane films are investigated in detail. Experimental static contact angle data, elaborated by empirical models (Zisman, EOS, OWRK) and wetting envelope (WE) graphs, allow the prediction and understanding of the wetting behaviors toward the most common solvents. All the elaborations were extended also to literature compounds[7, 8], in order to produce a series of films with increasing SFE. Theoretical calculations employing semi-empirical Hamiltonians and force-field potential investigations are performed. Specifically, long-range dipole electrostatic interactions allow us to develop a molecular picture about the interactions originating the interfacial surface energy changes. This novel combined approach could lead to the design of tailored siloxane structures and the ensuing tuning of the surface features of a material[9].

4.1 Results and discussion

4.1.1 Wetting behavior of bare siloxane layers

The siloxanes dissolved in an alcoholic matrix, were spin-coated on a glass slide in order to obtain homogeneous layers, after the controlled evaporation of the solvent. This procedure is generally adopted to provide a stable and reproducible coating[10, 11], easy to use in the common practice[12, 13]. Actually, it is a procedure comparable to the coating methods adopted in industrial applications[14]. By this procedure, silane molecules are expected to give rise to a quite random multi-layer, due to the thickness of a few micrometers of the film. Figure 4.1 shows the adopted siloxanes in comparison with literature examples.

The surface roughness of the siloxane films was evaluated by AFM images in tapping mode. Figure 4.2a shows Si-Alk film, as a representative layer; average roughness recorded was 6.9 nm (R_{RMS}, 50x50 μm area). Moreover, cracks, voids and protrusions, which might influence the static contact angle measurements, are not appreciable.

The surface free energy (SFE) values and the relative disperse and polar components of the siloxane-coated glasses were firstly calculated by using Owens, Wendt, Rabel and Kaelble (OWRK) (see Appendix B). Figure 4.3a shows the linear trends of the data relative to the three adopted siloxanes, characterized by good correlation coefficient and relatively low errors in the intercept and slope; the extrapolated results are reported in Table 4.1. The Table reports also, for the sake of comparison, the calculated SFE values of two silanes taken from the literature[7], showing opposite polar and disperse components.

Si-Ph, Si-biPh, and TESU exhibit the highest SFE (around 40 (mN m^{-1})); among the different silanes, the variation of the disperse component is not large, while their polar component shows larger variation in the following sequence: OTS < Si-Alk < Si-Ph < Si-biPh < TESU. In order to rationalize these results, geometric and electrostatic properties of the above mentioned molecules were calculated in the gas phase, that is, for each single molecule at a time. The module of the dipole moment vectors, reported in the last column of Table 4.1, shows the same trend as the experimental polar components.

In the Zisman method (see Appendix B and Ref. [15, 16]), the SFE value can be approximated to the critical surface tension, extrapolating at $\cos\theta = 1$ the linear trend of a plot $\cos\theta$ *vs* γ_{lv} of several test liquids. However, when this model is applied to polar surfaces, the obtained SFE is inaccurate and

Name	Acronym	Formula
Bare silane molecules		
Octadecyltrichlorosilane	OTS[a]	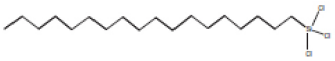
Isooctyltriethoxysilane SILRES® BS 1701	Si–Alk	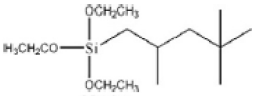
Triethoxy(phenyl)silane	Si–Ph	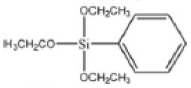
Diethoxy(diphenyl)silane	Si–biPh	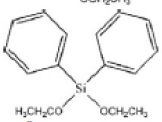
11-(triethoxysylil)undecanal	TESU[a]	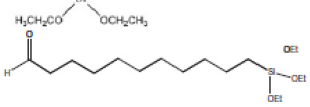
Fluorinated compounds		
1H,1H,2H,2H-perfluorodecyltrichlorosilane	FDTS[a]	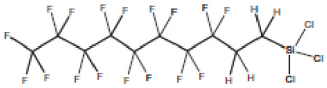
Phenyltris(trifluoroethoxy)silane	Si–Ph(F)	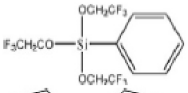
Diphenylbis-(trifluoroethoxy)silane	Si–biPh(F)	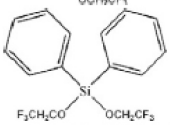
n-Perfluoroeicosane	Alk(F)*	

Figure 4.1: *Adopted compounds.(a) molecules from refs.[7] and [8].Reprinted from J. Coll. Inter. Sci., Vol. 389, G. Cappelletti et al., Wettability of bare and fluorinated silanes: A combined approach based on surface free energy evaluations and dipole moment calculations, pp. 284-91, Copyright 2015, with permission from Elsevier.*

Siloxane film	OWRK			Zisman	EOS	μ /D
	γ_s /mN m^{-1}	γ_s^p /mN m^{-1}	γ_s^d /mN m^{-1}	γ_{crit} /mN m^{-1}	γ_s /mN m^{-1}	
OTS[a]	23.50 ± 0.05	5.43 ± 0.01	18.07 ± 0.05	20.03 ± 0.03	24 ± 1	2.14
Si-Alk	31 ± 2	6 ± 1	25 ± 1	33 ± 5	23 ± 4	2.71
Si-Ph	42 ± 4	12 ± 1	30 ± 3	41 ± 5	33 ± 5	3.82
Si-biPh	42 ± 6	18 ± 3	24 ± 3	35 ± 8	38 ± 3	4.50
TESU	40.89 ± 0.03	25.12 ± 0.01	15.77 ± 0.03	26.37 ± 0.03	32 ± 2	6.01
Si-Ph(F)	28 ± 2	2 ± 1	26 ± 1	-	-	1.51
FDTS	13.5 ± 0.1	2.28 ± 0.07	11.22 ± 0.09	-	-	1.79
Si-biPh(F)	33 ± 4	10 ± 2	23 ± 3	-	-	2.60
Alk(F)	6.7	1.2	5.5	-	-	0.31

Table 4.1: *SFE values by Owens, Wendt, Rabel and Kaelble (OWRK), Zisman and Equation of State (EOS) methods and dipole moments by theoretical calculations for silane films.*

physically meaningless. Furthermore, the application of Zisman method is possible only for low-energy surfaces[15, 16]. Figure 4.3b shows the application of this model to the tested siloxane films, and the calculated critical surface tensions are reported in Table 4.1. In the case of the TESU molecule, showing the highest polar component, the concordance between the Zisman and the OWRK values is very poor, whereas the consistency is quite good for all the other silanes.

The results (Table 4.1) obtained by Neumann method (see Appendix B) suggest that Si-biPh, Si-Ph, and TESU layers present the highest energy properties with respect to the alkyl ones, in agreement with what obtained by OWRK method.

To better enlighten the wettability behavior of the siloxane films toward solvents other than water, wetting envelope (WE) elaborations (Figures 4.2b and 4.2c) were performed by reversing the equation adopted by OWRK method and introducing the disperse and polar components of the solid SFE. By plotting γ_{lv}^{p} *vs* γ_{lv}^{d}, a bow-shaped curve is produced for $\cos\theta = 1$ ($\theta = 0$, complete wetting, bold line in Figure 4.2b), which starts at the origin, attains a maximum value and then returns to the x-axis. The area enclosed within this curve is the wetting envelope or wetting range; all liquids whose surface tension data lie within this enclosed area will wet the corresponding film. Figure 4.2b shows, as an example, the case of Si-Ph. Similarly, lines for higher contact angles (θ = 20 - 80°) can be drawn. Hence, the wettability of a given film by particular liquids can be read off from their position in the wetting envelope diagram; the points of water, glycerol, ethylene glycol, and toluene are plotted in the Si-Ph WE graph. The value for toluene lies within the wetting area; this means that toluene is expected to wet the layer. Indeed, the experimental contact angle for the Si-Ph is very small ($\theta < 5°$). In contrast, the other tested solvents lie outside the envelope and they should therefore not wet the film. It is worth pointing out that the measured CA values for the different solvents closely trace out the WE prediction for all the considered silanes. This plot confirms that the adopted OWRK model describes well the current systems. This implies that the radii of the Van der Waals interactions of the elements in the silane layers and of the wetting liquid molecules are of the same order[17].

Besides, the WE elaboration allows an easy determination of the layer wettability toward both tested and several other common solvents, whose polar and disperse components are known. Figure 4.2c shows the comparison of the wetting threshold contours of the three representative silane films with respect to liquids belonging to distinct families characterized by different polar and disperse fractions of surface tension: EG/water mixtures (2-9), aliphatic (18-23), aromatic (28, 29, 33) and chlorinated (25, 26, 30, 31) solvents, alcohols (11-17), formamide (8), Dimethyl sulfoxide (DMSO) (34), dioxane (24), diiodomethane (32), and so on. This comprehensive plot leads us to conclude that the SFE generally increases as the degree of arylation increases, because the phenyl groups confer increase polarizability (see the polar component of the SFE and the dipole moments, Table 4.1). Thus, some solvents (such as cyclopenthanol, dichloroethane, and benzyl alcohol) can completely wet the Si-Ph and Si-biPh surfaces in contrast to the SiAlk one. The figure shows also the distribution of the polar and disperse components of the surface tension of solvents belonging to the same family, that is, 1-7 ethylene glycol/water (EG/W) mixtures and 11-16 alkyl and aryl alcohols with increasing chain lengths. In the case of the EG/W mixtures, the disperse component is comparable, while the polar term increases progressively from pure EG to water. *Vice versa* in the case of the alcohols, the polar component is fixed at around 5 (mN m^{-1}) while the disperse term varies from 15 to 25 (mN m^{-1}).

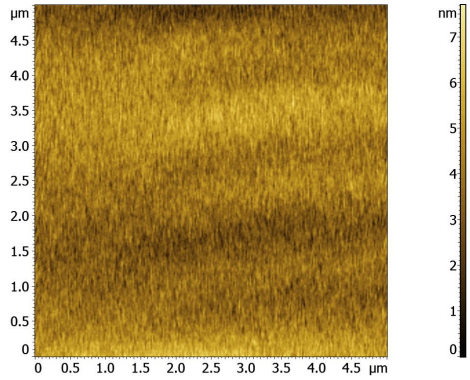

(a) AFM topography picture of Si-Alk deposited on glass slide.

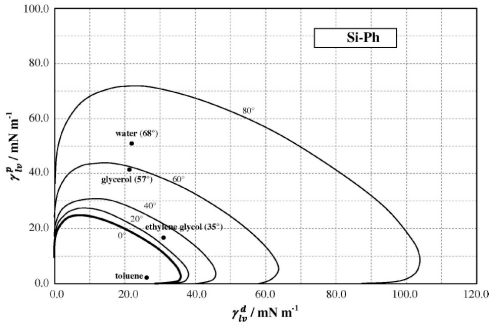

(b) Wetting envelopes for the Si-Ph siloxane film.

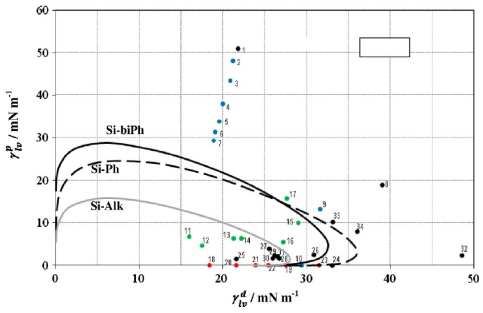

(c) Comparison between the WEs curves for the laboratory made siloxanes.

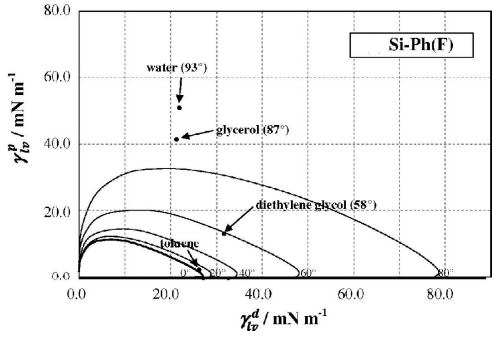

(d) Wetting envelopes for the Si-Ph(F) siloxane film.

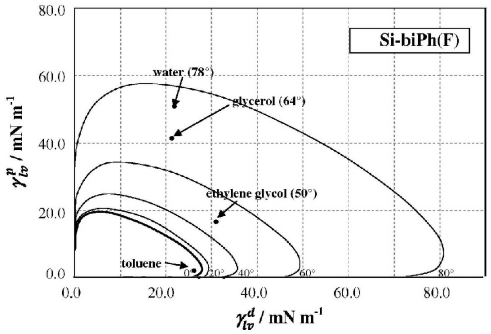

(e) Wetting envelopes for the Si-biPh(F) siloxane film.

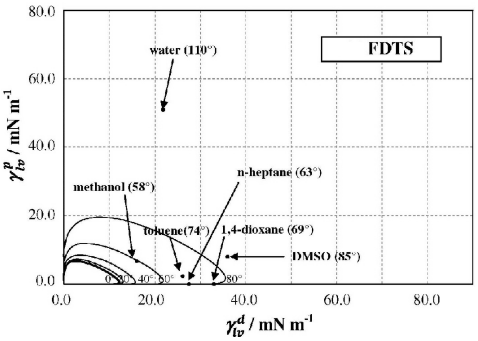

(f) Wetting envelopes for the FDTS siloxane film.

Figure 4.2: *Atomic force microscopy analysis and wetting envelopes curves. Reprinted from J. Coll. Inter. Sci., Vol. 389, G. Cappelletti et al., Wettability of bare and fluorinated silanes: A combined approach based on surface free energy evaluations and dipole moment calculations, pp. 284-91, Copyright 2015, with permission from Elsevier.*

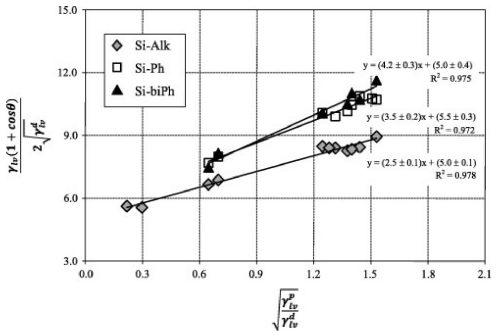

(a) OWKR elaboration for all the laboratory-made unfluorinated siloxane films.

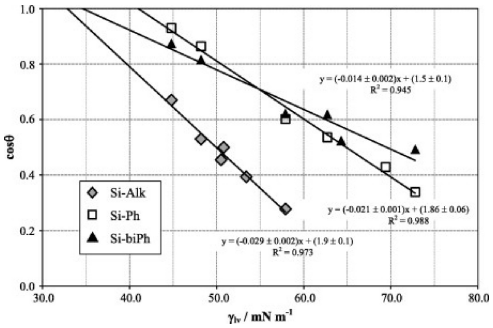

(b) Zisman plot for all the laboratory-made unfluorinated siloxane layers.

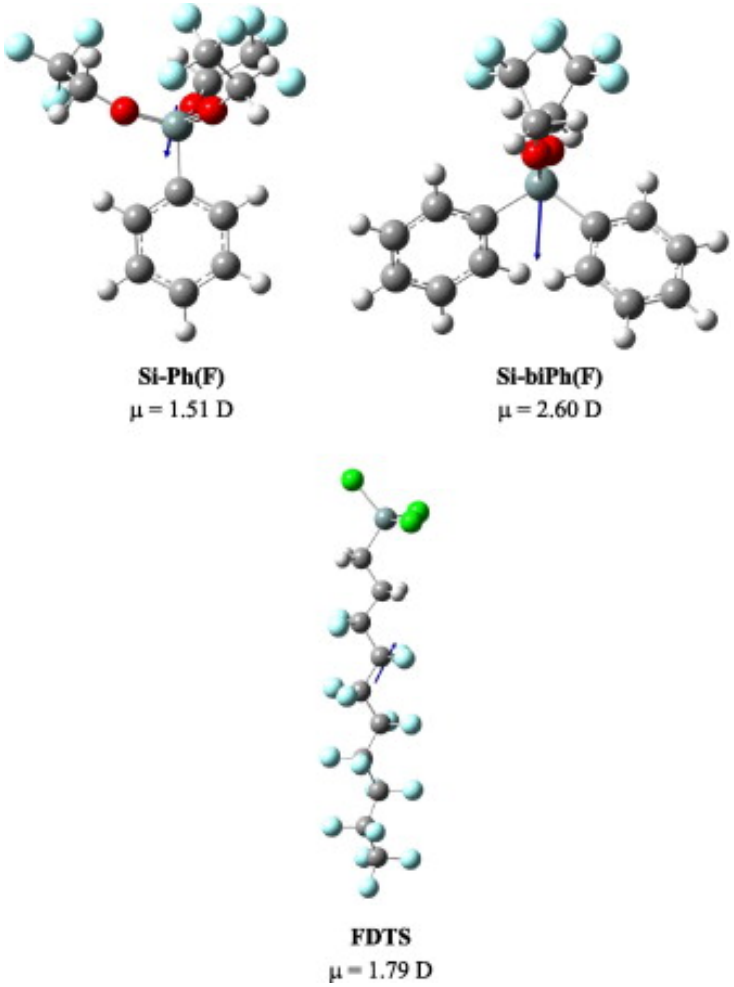

(c) Calculated dipole moments for SiPh(F), SibiPh(F), and FDTS.

Figure 4.3: *Surface free energy and momenta calculation of miscellaneous samples. Reprinted from J. Coll. Inter. Sci., Vol. 389, G. Cappelletti et al., Wettability of bare and fluorinated silanes: A combined approach based on surface free energy evaluations and dipole moment calculations, pp. 284-91, Copyright 2015, with permission from Elsevier.*

4.1.2 The role of fluorinated CF_3 groups

Fluorine-based molecules are traditionally characterized by scarce wettability and extremely low surface energy, because of the high ionization potential of fluorine and its low polarizability. It is our goal to develop a molecular insight into these properties both from an experimental and theoretical point of view.

Here, all laboratory-made fluorinated siloxane molecules, Si-Ph(F) and Si-biPh(F), are synthesized by substituting the methyl end groups with fluorinated ones. For the sake of comparison, literature data referring to a linear alkyl fluoride silane (FDTS) [7] and a totally F-substituted alkane (Alk(F)) [8] are also analyzed.

Experimental SFE data by the OWRK model are reported in Table 4.1. The elaborations of the CA data by Zisman and EOS methods give for all fluorinated molecules not fully satisfying results (data not reported). In order to appreciate the effect produced in the silanes by the fluorination, theoretical calculations of dipole moment vectors of the gas phase are performed for all the fluorinated molecules and reported in Table 4.1 and in Figure 4.3c (selected images). In Figure 4.3c, the moment vectors for each molecule are reported as arrows whose length is proportional to the module and show the same trend for the polar component of the surface free energy (Table 4.1, 3rd column). In the case of SiPh(F) and SibiPh(F), dipole module is about halved under fluorination. The complete agreement between the sequence of the gas-phase dipole moment and the polar component allows us to consider the OWRK model as an acceptable representation of the fluorinated systems.

To further analyze the fluorinated silanes wettability features, WE curves are shown in Figures 4.2 (4.2d, 4.2e and 4.2f): in the case of the aryl compounds, the WE elaborations closely follow the experimental contact angles (Figures 4.2d and 4.2e). Instead, in the case of FDTS, the curves result compressed and experimental contact angles deviate from the expected values and do not respect the wettability sequence obtained by the empirical laws (such as OWRS) described above (see *e.g.*, water and glycerol).

Also in the case of the totally fluorinated alkane Alk(F), the agreement between the experimental CAs[8] for water and CH_2I_2 (the only two CAs present in the paper) and their relative position in the WE area is very poor. The discrepancies shown in Figure 4.2f for FDTS can arise from the fact that the Fowkes' assumptions[17] embedded in the OWRK equation are not fully satisfied. Apparently, in the case of the aryl molecules, the aromatic rings dominate the interactions with the solvents and the fluorination of the ethoxy groups does not appreciably change the features of the interface zone; instead, the geometrical size of the long CF_2 chain of FDTS appear not to be of the same order of the solvent radius, so that the distance between the interacting volume elements is not comparable, as assumed in the model.

Therefore, the fluorination of the CH_3 and/or CH_2 groups in different matrices leads to effects which are the function of: (i) the position of the fluorine in the molecule, (ii) the orientation of the molecule, and (iii) the nature of the functional group exposed at the interface, interacting with the polar/apolar solvents.

4.2 Conclusion

The present results show the strong correlation between the wettability features of each siloxane, both bear and fluorinated ones, and their alkyl, aryl substitution and especially the position of fluorinated end groups. Both laboratory experiments and literature data are analyzed. General trends hold for any system allowing us to draw general considerations. The gas-phase theoretical dipole moment calculations closely follow the trend of the relative polar component of the SFE obtained by OWRK model for all molecules.

A fine investigation of the wettability by WE elaboration, instead, suggests that the theoretical prediction may fail depending on the specific chemical/geometrical features of the interfacial contact. This latter occurrence may become significant in the case of the interaction between long fluorinated chains and the solvent.

On the grounds of these considerations, it seems possible to build modified siloxanes with higher or lower SFE, whose wetting character can change dramatically. Such capability to tune the SFE of thin films would have important implications in a large number of applicative areas.

4.3 Specific procedures

The adopted silanes (Figure 4.1) are commercial (SILRES® BS 1701), laboratory-made molecules (triethoxy(phenyl)silane and dimethoxy(diphenyl)silane) and taken from the literature (Octadecyltrichlorosilane (OTS), 11-(triethoxysylil)undecanal (TESU))[7]. SILRES® BS 1701 (named Si-Alk in the following) is a commercial mixture of isomeric octyltriethoxysilanes (*Wacker Chemie AG*), containing isooctyltriethoxysilane as the main component. Triethoxy(phenyl)silane and diethoxy(diphenyl)silane (named SiPh and SibiPh, respectively) were obtained in laboratory following a synthetic route, already reported in literature[10].

The results concerning fluorinated molecules are both taken from the literature (1H,1H,2H,2H-perfluoro decyltrichloro silane (FDTS) and n-perfluoroeicosane (Alk(F))) [7] and [8] and synthesized in laboratory (phenyltris(trifluoroethoxy)silane and diphenylbis-(trifluoroethoxy)silane).

The siloxane depositions were performed on glass slides. Substrates were cleaned via sonication in acetone, isopropyl alcohol, and deionized water for 5 min to remove organic contamination. The siloxane layers were deposited by spin coating (2000 rpm, 500 (rpm s^{-1}) for 20 s) from a 40% siloxane solution in isopropyl alcohol and dried in vacuum oven at 40 $°C$ and 400 mbar. The silane-clad substrates were not cleaned after deposition.

All dipole moment calculations (gas phase) were performed at a semi-empirical level with the PM6 Hamiltonian (Gaussian09 package) in the vacuum for the most stable conformation, as located with Molecular Mechanics techniques and MMFFs force field with a stochastic Monte Carlo analysis of the potential energy surface. All PM6 minima were characterized as such by performing a vibrational analysis[10].

Further details about synthetic procedures and characterizations can be found in Appendix C.

References

[1] S. Onclin, B. J. Ravoo, D. N. Reinhoudt, *Angew. Chem. Int. Edit.* **2005**, *44*, 6282–6304.

[2] S. A. DiBenedetto, A. Facchetti, M. A. Ratner, T. J. Marks, *Adv. Mater.* **2009**, *21*, 1407–1433.

[3] N. G. Batz, J. S. Mellors, J. P. Alarie, J. M. Ramsey, *Anal. Chem.* **2014**, *86*, 3493–3500.

[4] Y. Lu, S. Sathasivam, J. Song, C. R. Crick, C. J. Carmalt, I. P. Parkin, *Science* **2015**, *347*, 1132–1135.

[5] A. Y. Fadeev, T. J. McCarthy, *Langmuir* **2000**, *16*, 7268–7274.

[6] R. Menescal, R. West, C. Murray, *Macromol.* **1991**, *24*, 329–330.

[7] D. Janssen, R. D. Palma, S. Verlaak, P. Heremans, W. Dehaen, *Thin Solid Films* **2006**, *515*, 1433 –1438.

[8] T. Nishino, M. Meguro, K. Nakamae, M. Matsushita, Y. Ueda, *Langmuir* **1999**, *15*, 4321–4323.

[9] G. Cappelletti, S. Ardizzone, D. Meroni, G. Soliveri, M. Ceotto, C. Biaggi, M. Benaglia, L. Raimondi, *J. Coll. Inter. Sci.* **2013**, *389*, 284 –291.

[10] D. Meroni, S. Ardizzone, G. Cappelletti, M. Ceotto, M. Ratti, R. Annunziata, M. Benaglia, L. Raimondi, *J. Phys. Chem. C* **2011**, *115*, 18649–18658.

[11] C. Reich, L. Andruzzi, *Soft Matter* **2010**, *6*, 493–500.

[12] D. Meroni, S. Ardizzone, G. Cappelletti, C. Oliva, M. Ceotto, D. Poelman, H. Poelman, *Catal. Today* **2011**, *161*, 169–174.

[13] P. Chatterjee, S. Hazra, H. Amenitsch, *Soft Matter* **2012**, *8*, 2956–2964.

[14] P. N. Manoudis, I. Karapanagiotis, A. Tsakalof, I. Zuburtikudis, C. Panayiotou, *Langmuir* **2008**, *24*, 11225–11232.

[15] H. Fox, W. Zisman, *J. Coll. Science* **1952**, *7*, 428 –442.

[16] H. Fox, W. Zisman, *Journal of Colloid Science* **1952**, *7*, 109 –121.

[17] F. M. Fowkes, *Indust. Engin. Chemistry* **1964**, *56*, 40–52.

Chapter 5

Alkylsilane SAM by chemical vapor deposition

As described in the previous chapter, the great interest in silane molecules from an applicative point of view has been highly connected to the reactivity of hydroxy groups at the oxide surfaces. Notably, such molecules, in proper conditions, are able to self-organize at the interface to form an ordered monolayer; that, described for the first time by Prof. J. Sagiv in 1983[1], was named self-assembled monolayer (SAM). Later, such behavior was observed for many different molecules (thiol on Au[2], phosphonate on oxides[3] ...), paving the way for applications in many different fields. In recent years, self-assembled monolayers on silicon oxide have reached a high level of sophistication and have been combined with various lithographic patterning methods to develop new nanofabrication protocols and biological arrays[4–7]. Microelectronic, transistor fabrication, solar cells, drug delivery are only few of many fields in which those systems are being involved[8, 9]. Nanoscale control over surface properties is of paramount importance to advance from 2D patterning to 3D fabrication([7], see Chapters 11 and 9).

Two approaches have been commonly employed in the deposition of alkylsilane films on oxide surfaces: wet procedure (or wet impregnation[1, 10], see Chapters 6 and 7) and vapor-phase methods[11, 12]; both have advantages and disadvantages. Although the wet approach has been the most extensively studied, it is neither environmentally friendly nor industrially viable because of generation of significant amounts of solvent waste (for smooth films, commonly used solvents are bicyclohexane[10], tolune,[13]...)[14]. Compared to the wet approach, there have been relatively few reports of vapor-phase deposition methods (chemical vapor deposition, CVD) for alkylsilane deposition, although the vapor-phase approach has been reported to yield alkylsilane films with comparable quality. In fact, CVD requires a tricky set-up and are strongly related to the vapor pressure of the functionalizing molecules. Recent studies have focused on the role played by the water content[15] and surface hydration of the oxide substrate on the final layer quality; the control of such parameter in vapor-phase are much easier, without the requirement of specific instrumentation.

In this chapter, a simple procedure of chemical vapor deposition is adopted to functionalize silica substrates with two different trifunctional alkylsilanes. Triethoxysilanes with different linear chains were employed, comparing fluorinated and unfluorinated molecules. The effect of the functionalization temperature (70-150 $^{\circ}C$) was investigated in detail. An original combination of characterization techniques was used to provide a complete picture of the alkylsilane layer structure. Next to FTIR and CA analysis, electrochemical characterizations (cyclic voltammetry and impedance spectroscopy) proved to be a pow-

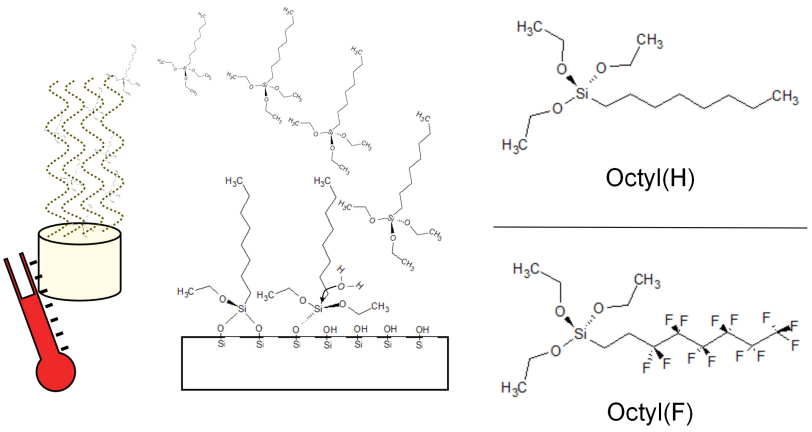

Figure 5.1: *Schematic of the CVD functionalization and formula of the two adopted molecules. Adapted with permission from G. Soliveri et al., J. Phys. Chem. C, 2015, Vol. 119, pp. 15390-400. Copyright 2015 American Chemical Society.*

erful tool to assess the defectiveness of the alkylsilane layers, while solid state nuclear magnetic resonance (NMR) provided a molecular insight into the grafting mode of the alkylsilane molecules on the surface.

5.1 Results and discussion

5.1.1 Chemical vapor deposition

In chemical vapor deposition, the functionalizing molecules were vaporized at different temperatures and collected on the silica substrates. As commonly known, water molecules are generally strongly physisorbed at the oxide surface; those reacts with the siloxane, making it highly active with regard to the hydroxil groups at the oxide interface (See Figure 5.1). We adopted 3 hours time of vapor/solid contact, on the ground of experimental and literature results[11, 12, 15]. In the cooling step, the unreacted vaporized siloxane condenses on the surface. Sonication in toluene is generally advised to remove the excess. Now, the film is robust and hard for a long period of time.

Two distinct siloxanes were tested in order to study the influence of the chain chemistry: triethoxy(octyl)silane (named Ocyl(H), Figure 5.1) and 1H,1H,2H,2H-perfluorooctyltriethoxysilane (named Octyl(F), Figure 5.1). In this chapter, the samples functionalized by Octyl(H) will be named H_(temperature of CVD), while he samples functionalized by Octyl(F), F_(temperature of CVD).

5.1.2 Contact angle and surface free energy

Contact angle measurement is one of the most commonly employed techniques to assess the quality of alkylsilane layers. After pretreatment, the water contact angle (θ_w) of the bare surface of the silicon wafer (covered by a native layer of SiO_2) is close to 0°. The superhydrophilicity of the clean Si surface is related to its surface hydroxylation. After functionalization with Octyl(H), the interface turns hydrophobic. Literature has widely reported the correlation between θ_w and the formation of a complete alkylsilane monolayers; that is connected to highest contact angle because of the exclusive interaction of the methyl and methylene groups with the solvent. Sugimura *et al.*[12] reported $\theta_w \approx 105-107°$ as the optimum for that family of alkylsilanes.

Figure 5.2a shows the θ_w of the functionalized surfaces with Octyl(H) at different temperatures. The bell shaped curve has a maximum at 100 $°C$. The maximum contact angle ($\theta_w \approx 107°$) is in full agreement with literature results about complete monolayers. The contact angle varies sharply by

changing the deposition conditions: at the highest tested deposition temperature, a water contact angle much lower than 90° was detected.

The implications of the wetting features of the functionalized surface on its structure are more clearly appreciable when the surface free energy (SFE) is considered. Among all literature models[16–18], the Owens-Wendt-Rabel-Kaelble (OWRK) method[19] was considered the most accurate one for the aim of the present work. A clear picture of the thermodynamic and the approximations behind the determination of those values are described in Appendix B. The γ_s^p and γ_s obtained for the surfaces functionalized by Octyl(H) at different temperatures are reported in Figure 5.2b. While the γ_s^d values show a limited variation with respect to the functionalization temperature, the γ_s^p changes dramatically as a function of deposition conditions. It is noteworthy that $\gamma_s^p \approx 0$ at 100 $^\circ C$, *i.e.*, no polar groups are present at the surface. On the grounds of considerations about the physical meaning of γ_s^p, the formation at 100 $^\circ C$ of a complete monolayer can thus be suggested. Such hypothesis is supported also by AFM topography and phase images (Figures 5.2e and 5.2f) showing the occurrence of a smooth and homogeneous surface. At higher deposition temperatures, polar groups are appreciable at the interface ($\gamma_s^p \neq 0$), which implies the occurrence of either an incomplete coverage of the silica surface or the presence of disordered and multilayer structures.

A completely different picture emerges from the contact angle measurements of surfaces modified with the fluorinated analogue (Figure 5.2c). The substrates, functionalized at temperatures ranging from 70 $^\circ C$ to 150 $^\circ C$, showed θ_w values comparable within the experimental error. The observed water contact angles were close to 117° for all the samples, irrespectively of the functionalization temperature. The obtained values are comparable to literature reports of similar compounds[11, 20–23]. The SFE components reflect the change in wettability of the fluorinated chain: the polar component is almost zero and the disperse component is significantly reduced with respect to the unfluorinated analogue. Interestingly, the functionalization temperature seems to play a negligible role on the wetting features of Octyl(F) films. Considering the macroscopic scale of the technique, other characterization approaches are required to probe the layer quality at the molecular scale.

5.1.3 Electrochemical measurements

Alkyl chain layers are dielectric in nature due to the large gap between the highest occupied molecular orbital (HOMO) and the lowest unoccupied molecular orbital (LUMO)[24]. As a result, they behave as electronic insulators, they can work as an ionic barrier, and depending on the nature of the terminal group, might behave as an ideal capacitor[23]. Electrochemical techniques have been utilized to study the insulating properties of alkylsilane monolayers at oxide surfaces, such as indium tin oxide[15, 25, 26], and SiO_2/Si[27, 28]. The electrochemical properties have been correlated to the eventual presence of pinholes and structural defects within the monolayer. Here, electrochemical techniques were used to evaluate the barrier properties of the chemical vapor deposited alkylsilane layers, studying the effect of the deposition temperature and of the fluorination of the alkyl chain. Cyclic voltammetry (CV, Figure 5.3a and 5.3b) was employed to calculate the capacitance of the organic layer at the electrode surface (capacitor)[15, 27] (Table 5.1). The measured capacitance is a combination of the support and film capacitances; the former can be assumed to be invariant.

In the Octyl(H) set, H_100 shows the highest capacitance, followed by H_80, while H_150 displays a capacitance one order of magnitude lower (Table 5.1 column 2). These results closely mirror the bell-shaped curve obtained by contact angle measurements. In the case of fluorinated precursor, the highest capacitance was obtained for F_90, followed by F_80. F_100 and F_70 showed similar capacitances, while

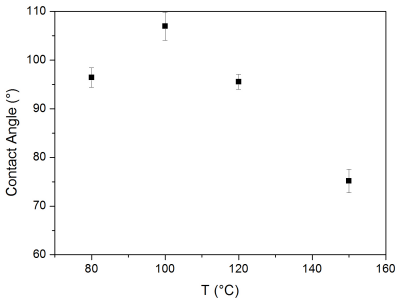

(a) Water contact angle *vs* temperature of CVD: Octyl(H).

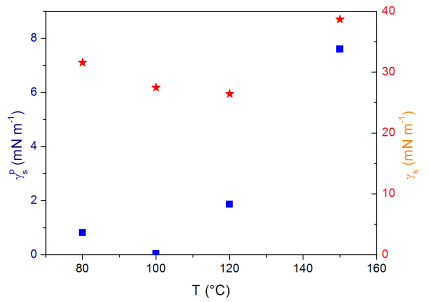

(b) Polar and total SFE *vs* temperature of CVD: Octyl(H).

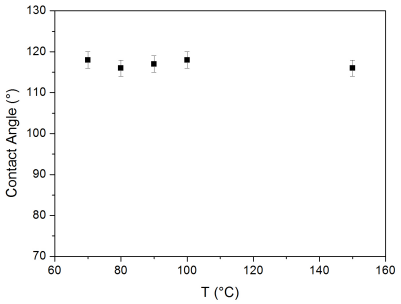

(c) Water contact angle *vs* temperature of CVD: Octyl(F).

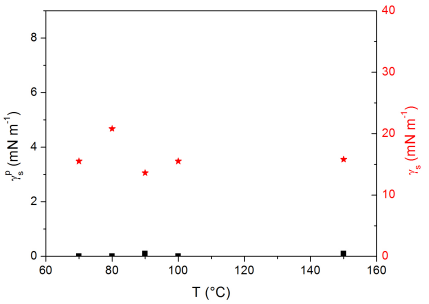

(d) Polar and total SFE *vs* temperature of CVD: Octyl(F).

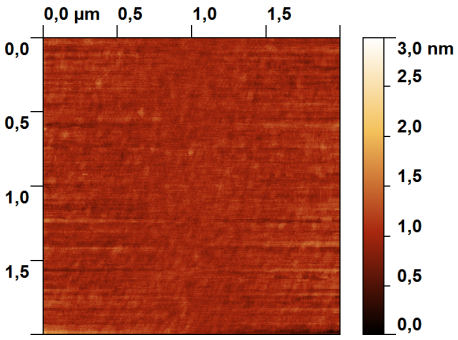

(e) AFM topography image of H_100.

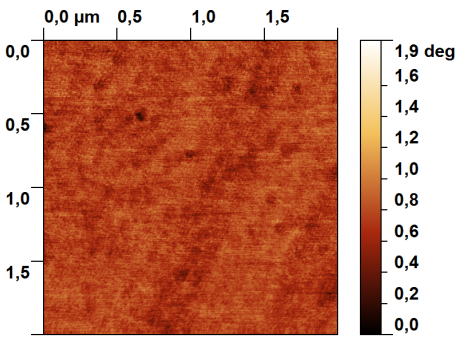

(f) AFM phase image of H_100.

Figure 5.2: *Effect of functionalization temperature on the wetting features and AFM images. Adapted with permission from G. Soliveri et al., J. Phys. Chem. C, 2015, Vol. 119, pp. 15390-400. Copyright 2015 American Chemical Society.*

F_150 had the lowest value. Electrochemical impedance spectroscopy (EIS) was chosen to further study the insulating and barrier properties of the alkylsilane layer by investigating the ionic permeation of an inert electrolyte in a wide frequency range (0.1 - 65000 Hz). EIS data were fitted using an electrical equivalent circuit (Figure 5.3g), often employed for these organic layers[26, 28]; it was composed by a parallel combination of a double layer capacitance, C_{dl}, and a charge transfer resistance to ionic permeation, R_{ct}, in series with the solution resistance, R_Ω, and with a constant phase element, denominated CPE_{pol}, corresponding to the film polarization capacitance. The R_{ct} parameter provides the resistance offered by the film toward the electron transfer across the electrode-electrolyte interface. Higher R_{ct} are correlated with stronger inhibition of electron transfer (due to the presence of the alkylsilane layer)[27]. The constant phase element CPE_{pol} allowed us the evaluation of the alkylsilane layer dielectric behavior and, indirectly, the homogeneity of the layer: a CPE frequency exponent α equal to 1 corresponds to a pure capacitor (*i.e.*, defect-free layer), whereas an α value of 0.5 corresponds to a diffusion element (*i.e.*, a defective layer)[26].

Complex plane plots for all the tested samples show the typical trend related to that equivalent circuit (Figure 5.3c and 5.3d): a semicircle at high frequencies followed by a straight line with different slopes at low frequencies. The parameters obtained by the equivalent circuit fitting procedure of EIS data are reported in Table 5.1 (columns 3-5).

Film capacitance values (Table 5.1 column 4) are consistent with those obtained from cyclic voltammetry (Table 1 column 2), following the same trend, and are coherent with values previously reported in the case of unfluorinated and fluorinated silanes[15, 28].

In the case of Octyl(H) (Figure 5.3c), H_100 shows the highest charge transfer resistance, measured from the semicircle diameter, which is indicative of a low ionic permeability of the electrolyte in the organic structure. The R_{ct} values strongly decrease for H_80 and H_150, revealing a more disordered and non uniform layer, where the electrolyte can permeate. Moreover, while the semicircle is complete for H_100 and H_80, it is not for H_150, reflecting a lower homogeneity of the layer for the latter. These results were corroborated by Bode plots (Figure 5.3e), which show a deviation at medium frequencies in the case of H_150, ascribable to a diffusion component due to ionic permeation. Consistently, an α value closer to unity was obtained for H_100, indicating a pure capacitive-like behavior for this system, typical of a very flat and homogeneous film.

In the case of Octyl(F) (Figure 5.3d), F_90 showed the highest charge transfer resistance and value, in agreement with capacitance results. The system behaves as a pure capacitor; only the beginning of the semicircle is visible. This behavior can be observed exclusively for F_90, while the other samples show a consistent decrease in charge transfer resistances and α values(Table 5.1). F_70 and F_80 show similar α and R_{ct} values. However, with respect to F_70, F_80 presents a higher capacitance, a complete semicircle and a Bode plot (Figure 5.3f) without the diffusion component. The highest temperatures (100 $°C$ and 150 $°C$) lead to the lowest charge transfer resistances, capacitances and α values, as well as incomplete semicircles and diffusion components in Bode plots.

5.1.4 FTIR spectroscopy

Spectroscopic characterizations were resorted to study the functionalization process at the molecular level. FTIR specrtoscopy provided information about the extent of the functionalization and about the surface hydroxylation before and after the functionalization.

Figure 5.4g reports the FTIR spectrum of the starting material. The following spectral features can be appreciated:

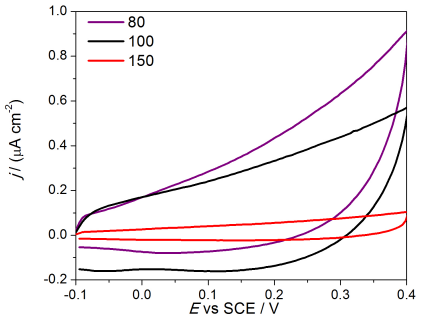

(a) Cyclic voltammograms of H_ samples.

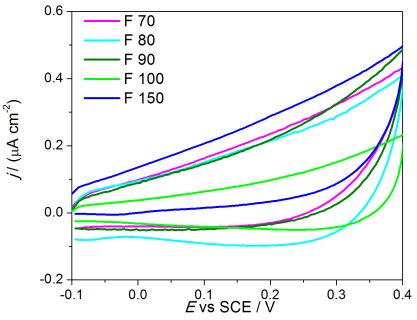

(b) Cyclic voltammograms of F_ samples.

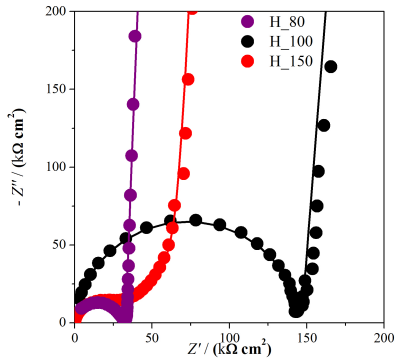

(c) Complex plane plot with fitted data for Octyl(H) samples at different deposition temperatures.

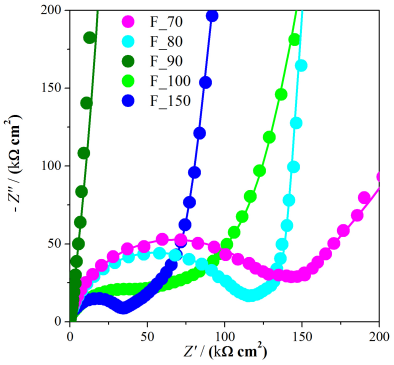

(d) Complex plane plot with fitted data for Octyl(F) samples at different deposition temperatures.

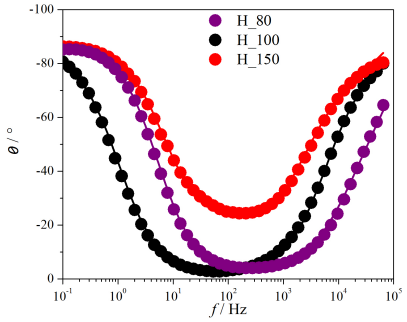

(e) Bode plots with fitted data for Octyl(H) samples at different deposition temperatures.

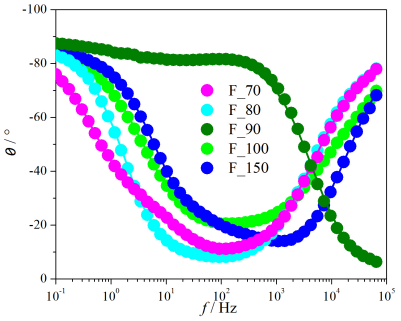

(f) Bode plots with fitted data for Octyl(F) samples at different deposition temperatures.

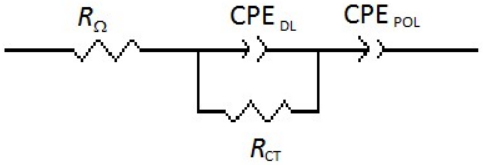

(g) Equivalent circuit used to fit impedance spectra.

Figure 5.3: *Electrochemical characterization. Adapted with permission from G. Soliveri et al., J. Phys. Chem. C, 2015, Vol. 119, pp. 15390-400. Copyright 2015 American Chemical Society.*

Sample	C μF cm^{-2}	R_{ct} kΩ cm^2	CPE_{pol} μF cm^{-2} s$^{\alpha-1}$	α
H_80	1.19	34.36	1.36	0.87
H_100	1.25	147.39	1.64	0.91
H_150	0.32	29.45	0.60	0.60
F_70	0.43	129.04	1.06	0.84
F_80	0.75	108.19	1.52	0.86
F_90	0.79	145.08	2.17	0.92
F_100	0.41	54.33	0.66	0.72
F_150	0.33	31.53	0.73	0.70

Table 5.1: *Cyclic voltammetry and impedance data.*

- OH-stretching vibration of free surface hydroxyl groups in the 3700-3750 cm^{-1} spectral range;
- A broad band in the 3700-3000 cm^{-1} spectral range due to OH-stretching vibration of hydroxyl groups mutually interacting by hydrogen bonding;
- A typical component located at $\sim$ 1630 cm^{-1} characteristic of the in plane HOH bending mode of undissociated water molecules, which is normally indicated as spectroscopic partner of the broad envelope;
- Three broad bands, located in the 2100-1750 cm^{-1} spectral region, attributed to Si-O-Si overtones typical of the silica matrix.

The differential FTIR spectra relative to the samples functionalized with Octyl(H) are reported in Figure 5.4a, 5.4b and 5.4c. After the functionalization process with Octyl(H), the following spectral features are clearly detectable:

- In the 3000-2850 cm^{-1} spectral region a clear envelope, made up of three sharp components, ascribable to the CH stretching bands of all CH_n containing species;
- Their bending counterparts being normally located in the 1500-1350 cm^{-1} spectral region;
- A specific component located at $\sim$ 1680 cm^{-1} ascribable to the CO group present in the Octyl(H) agent[29], which might be indicative of an incomplete substitution of the ethoxy groups;
- Negative peaks for both the OH stretching vibration interacting by hydrogen bonding and HOH of undissociated molecular water occurs (Figure 5.4a). The loss of silanol groups upon functionalization with organofunctional alkoxysilanes has been reported previously12 and may be partly related to the formation of Si-O-Si bonds between the surface and alkylsilane molecules, as supported by NMR results.

The temperature of the functionalization treatment has mainly an effect on the peak intensity. The bands ascribable to CH functionalities decrease at functionalization temperatures higher than 100 $^{\circ}C$. Moreover, in the temperature range from 80 to 120 $^{\circ}C$, the peaks associated with silanols interacting by hydrogen bonding and undissociated molecular water become less intense. These aspects closely mirror solid state NMR results and will be discussed in detail therein. Figures 5.4d, 5.4e and 5.4f report the FTIR differential spectra relative to samples functionalized with Octyl(F).

After functionalization with Octyl(F) the following spectral features are clearly detectable, apart from those already described for the pristine silica system and described above:

- CH stretching bands in the 3000-2850 cm^{-1} spectral region, due to the CH_n groups present in the functionalizing agent, with their spectroscopic bending counterpart located in the 1500-1350 cm^{-1} spectral region;
- A specific component located at $\sim$ 1680 cm^{-1} ascribable to the CO group present in the Octyl(F) agent.
- Negative peaks are observed for both the OH stretching vibration interacting by hydrogen bonding and HOH of undissociated molecular water. However, in this case a much lower dependence of the peak intensity on the deposition temperature is appreciable.

Unfortunately, the detailed inspection of the region located at $\nu < 1200$ cm^{-1} was not feasible to highlight the various C-F modes which characterize the functionalizing agent, due to the presence of the cut-off typical of all silica-based systems.

Similarly to the case of the Octyl(H), the functionalization temperature strongly affects the intensity of the peaks related to the alkylsilane layer, as clearly seen in Figure 5.4e for the ν_{CH}. However, in this case the maximum intensity of the ν_{CH} peaks is reached at 90 $°C$.

5.1.5 Solid state NMR

Solid-state NMR has emerged as an important tool to study organic molecules chemisorbed at the oxide surface and to obtain structural information concerning hybrid materials. This technique provides spectroscopic evidence for the presence of organic moieties in the materials, confirms their chemical structure and investigates the characteristics of the attachment bonds.

It is well-known that siloxane derivatives bind to oxide surfaces, such as SiO_2, via Si-O-Si bonds resulting from the condensation between Si and -OR and surface -OH groups and from the coordination of the silyl oxygen to a surface Si atom; this leads to a variety of mono-, bi-, and tridentate-binding modes (see below). ^{29}Si and ^{13}C solid state MAS NMR can provide relevant information about the changes taking place at the silica surface upon functionalization[30–33], *e.g.* changing the temperature of the treatment. Notwithstanding the powerful of this technique, only scarce studies are present in literature[34].

All the ^{29}Si NMR spectra display two sets of signals, the first between -85 and -110 ppm (Q^n signals) and the second one between -50 and -70 ppm (T^{n*} signals). The former can be related to the unsubstituted silica surface, while the latter can be assigned to the Si atoms covalently bound to the alkylsilane molecules. Figure 5.6c shows as a representative example that the Q^n and T^{n*} signals of H_150 are composite peaks, showing three resolved resonances. This suggests the co-presence of several Si species with different chemical structures. The same species are present in all other spectra. The peak resolution is not high because the shift between the peaks is small and the width is large. However, we were able to determine the different components by a deconvolution program. On the basis of literature studies[34–37], we can assign the three high-field resonances (at -93/94, -101 and -108/110 ppm) to geminal silanols Q^2 [($\equiv$SiO)$_2$ Si(OH)$_2$], single silanols Q^3 [($\equiv$SiO)$_3$SiOH)] and alkoxysilane groups Q^4 [($\equiv$SiO)$_4$Si)], respectively. Instead, the low-field resonances (at -51, -59 and -69 ppm) can be related to silicon atoms in position [($\equiv$SiO)SiR(OH/Et)$_2$] (denominated as T^{1*}), [($\equiv$SiO)$_2$Si(OH/Et)R] (T^{2*}) and [($\equiv$SiO)$_3$SiR] (T^{3*}), respectively. A fitting analysis was performed using Lorentzian and Gaussian curves to deconvolute the components and determine the relative ratio of the coexisting structures (Figure 5.6c).

Figure 5.5a reports the ^{29}Si spectra of H_80, H_100 and H_150 samples, compared to the spectra of unfunctionalized silica. The signal of the starting compound (-28 ppm) is not appreciable from the

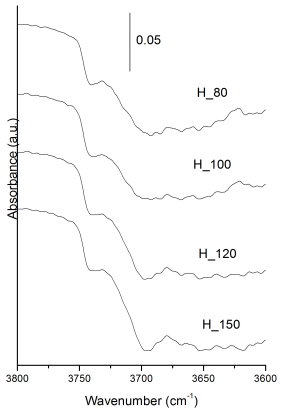

(a) Octyl(H), 3800-3600 cm^{-1} spectral range.

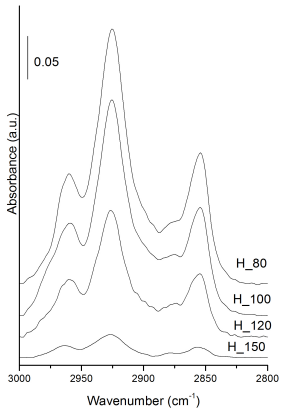

(b) Octyl(H), 3000-2800 cm^{-1} spectral range.

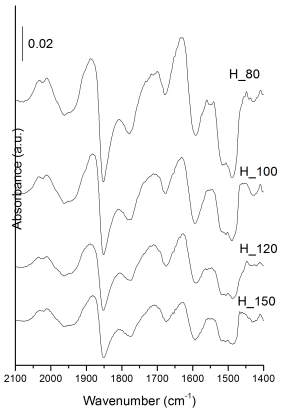

(c) Octyl(H), 2100-1400 cm^{-1} spectral range.

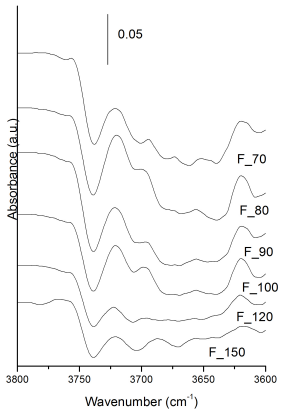

(d) Octyl(F), 3800-3600 cm^{-1} spectral range.

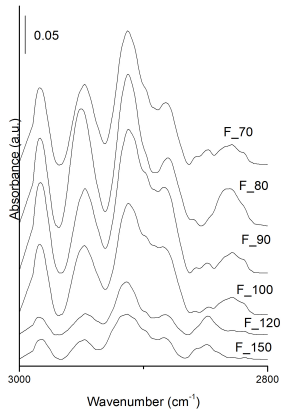

(e) Octyl(F), 3000-2800 cm^{-1} spectral range.

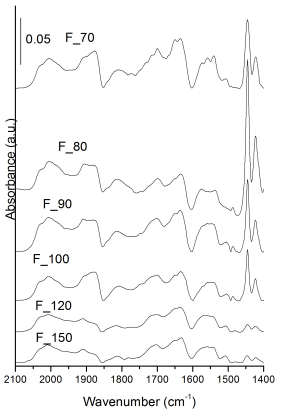

(f) Octyl(F), 2100-1400 cm^{-1} spectral range.

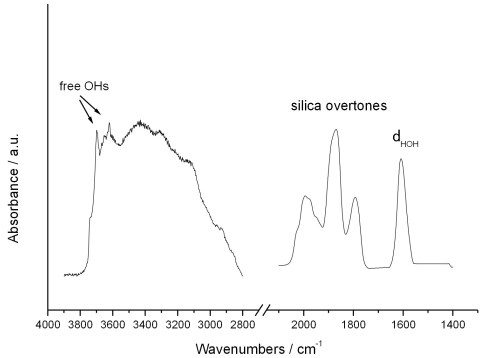

(g) FTIR spectrum of the unfunctionalized silica.

Figure 5.4: *Differential absorbance FTIR spectra obtained by subtracting the curve of the pristine samples from those of samples functionalized and the pristine one (g). Adapted with permission from G. Soliveri et al., J. Phys. Chem. C, 2015, Vol. 119, pp. 15390-400. Copyright 2015 American Chemical Society.*

Sample	SiO_2		Octyl(H) 80 °C		100 °C		150 °C	
	δ /ppm	%	δ /ppm	%	δ /ppm	%	δ /ppm	%
Q^2	-93.3	33	-94.0	34	-93.3	21	-93.4	11
Q^3	-101.0	51	-101.3	46	-101.6	59	-101.7	68
Q^4	-109.4	16	-108.4	20	-109.9	20	-110.0	21
T^1	-	-	-49.6	16	-50.9	32		-
T^2	-	-	-59.0	62	-59.6	54	-62.7	54
T^3	-	-	-69.7	22	-69.0	15	-68.0	46

Table 5.2: *^{29}Si CP/MAS NMR chemical shifts and relative percentages for the proposed Si structures of the unfunctionalized and Octyl(H) functionalized samples.*

spectra, confirming the absence of unbound Octyl(H) molecules. The ratio between the two signals depends on the functionalization temperature: the T/Q ratio of H_80 and H_100 is very similar (1/3.0 and 1/2.8, respectively), while it decreases up to 1/4 for the H_150 samples. This behavior is indicative of a different functionalization degree of the samples. Table 5.2 reports the peak position and content of the different structures for unfunctionalized silica and H_80, H_100 and H_150 samples.

The deconvolution analysis reveals that the relative content of the Q components varies as a function of the functionalization temperature. While the Q^4 component remains essentially unchanged, the Q^2 resonance, assigned to single silanols, tends to decrease at increasing functionalization temperatures, whereas the Q^3, relative to germinal silanols, shows an opposite trend. The disappearance of single silanols as a result of the functionalization with Octyl(H) is supported by FTIR results (Subsection 5.1.4).

The T^{1*}, T^{2*} and T^{3*} signals, relative to substituted alkylsilane derivatives, correspond to structures containing respectively one, two and three Si-O-Si bonds with either the silica surface or neighboring alkylsilane molecules. Although we cannot distinguish between the last two situations, an alkylsilane molecule cannot form three Si-O-Si bonds with the surface due to steric reasons.

The H_80 and H_100 samples present all three T^{n*} resonances, whereas H_150 shows only T^{2*} and T^{3*} signals. High temperatures seem thus to favor lateral polymerization. ^{13}C MAS NMR spectra of H_80 (a), H_100 (b) and H_150 (c) (Figures 5.5b, 5.5c and 5.5d), performed in the same experimental conditions, show a decrease of the signal to noise ratio (S/N) passing from (a) (S/N) equal to (27/1) to (b) (S/N), (10/1) and c) (S/N) (7/1). These results, along with T:Q ratios determined by ^{29}Si spectra, support a higher functionalization degree at 80-100 °C with respect to 150 °C. Such findings are in agreement with FTIR data showing a decrease of the alkyl chain content at increasing functionalization temperature.

^{13}C NMR spectra present well defined peaks, which can be readily assigned for comparison with the Octyl(H) spectrum obtained in homogeneous solution: 12.6 ppm ($\underline{CH_3}$ and $\underline{CH_2}Si$), 22.6 ppm ($\underline{CH_2}CH_3$ and $\underline{CH_2}CH_2Si$), 29.9 ppm ($\underline{CH_2}CH_2CH_2CH_3$ and $\underline{CH_2}CH_2$ CH_2Si) and 32.3 ppm ($CH_2CH_2CH_3$ and $CH_2CH_2CH_2CH_2Si$). The low intensity or complete absence of the ethoxy group signal (58.0 and 16.0 ppm) supports a high substitution degree of the ethoxy group during the functionalization process for all samples. The presence of unhydrolyzed alkoxy groups on the alkylsilanes could sterically hinder dense monolayer formation[15].

The samples functionalized by the Octyl(F) show ^{29}Si spectra similar to corresponding compounds functionalized with the unfluorinated analogue. In the same way, ^{29}Si NMR spectra of Octyl(F) derivatives (Figure 5.6a) are characterized by the presence of T^{n*} and Q^n species, which are as well strongly affected by the functionalization temperature. Indeed, the T/Q ratio reaches a maximum for the sample

Sample	SiO_2		Octyl(F) 70 °C		80 °C		90 °C		100 °C		150 °C	
	δ /ppm	%	δ /ppm	%	δ /ppm	%	δ /ppm	%	δ /ppm	%	δ /ppm	%
Q^2	-93.3	33	-93.5	34	-93.0	36	-93.5	30	-93.0	28	-93.6	36
Q^3	-101.0	51	-101.5	49	-101.2	44	-101.7	48	-101.6	50	-101.3	44
Q^4	-109.4	16	-109.6	17	-109.6	20	-109.7	22	-108.0	22	-108.6	20
T^1	-	-	-53.0	29	-54.0	11	-51.5	13	-	-	-	-
T^2	-	-	-59.9	71	-61.0	58	-59.8	62	-58.0	68	-59.0	85
T^3	-	-	-	0	-69.0	31	-69.6	25	-70.0	32	-70.0	15

Table 5.3: *^{29}Si CP/MAS NMR chemical shifts and relative percentages for the proposed Si structures of the unfunctionalized and Octyl(F) functionalized samples.*

F_90 (1/1.5) and decreases at higher temperatures (1/3.0 and 1/7.3 for F_100 and F_150, respectively).

Such observation is in agreement with the trend observed in the S/N ratio of ^{13}C NMR spectra, performed in the same experimental conditions. The S/N increases raising the functionalization temperature up to 90 °C, while at higher values the S/N ratio decreases. Figure 5.6b shows the trend of ^{13}C NMR spectra, from 70 up to 150 °C. Moreover, in the case of Octyl(F), the temperature effect appears to be more critical with respect to the unfluorinated analogue. Indeed, the optimal functionalization temperature seems a narrow range centered at 90 °C: above and below this value the ^{13}C NMR spectra show a relevant S/N decrease.

^{13}C NMR spectra show the following resonances: 1.9 ppm ($\underline{CH_2}Si$), 24.2 ppm ($\underline{CH_2}CH_2Si$), 11.9 and 118.0 ppm ($\underline{CF_2}$ and CF_3). The peaks at 58.0 and 16.0 ppm can be attributed to a 10-20% residual ethoxy group, in agreement with FTIR findings.

A deconvolution analysis was carried out on T^{n*} and Q^n signals of ^{29}Si NMR spectra, in order to estimate the amount of the different species (Table 5.3). As for the unfluorinated analogue, the ^{29}Si NMR spectra show that the alkylsilane polymerization degree increases with the functionalization temperature, leading to higher T^{3*} and lower T^{1*} contents. On the contrary, the functionalization temperature does not significantly modify the ratio among the Q components. Such evidence suggests a lower degree of covalent bonding with the silica surface in the case of fluorinated alkylsilane.

5.2 Conclusion

The chemical vapor deposition of triethoxy(octyl)silane and of its fluorinated analogue on silica substrates was studied by a combination of surface, electrochemical and spectroscopic characterization techniques. The influence of the functionalization temperature was studied. The different techniques were able to provide a coherent picture of the alkylsilane layer structure as a function of the deposition conditions.

In both cases the influence of the temperature during the CVD functionalization showed a bell-shaped curve, in which wetting, electrical and molecular proprieties displayed a maximum at average values. Spectroscopic investigation (especially solid state NMR) provided a clear picture of the silane organization at the interface, proving, for example, that higher functionalization temperatures increase the lateral polymerization across the alkylsilane layer. Undesired self-polymerization of the alkylsilane molecules before vaporization might concur to reduce the functionalization degree at high temperatures[14, 15] along with effects on the surface hydration[14].

All those informations will be crucial in the next chapter, where this technique (in comparison with traditional wet impregnation) is adopted for the study of super-hydrophobic, self cleaning surfaces.

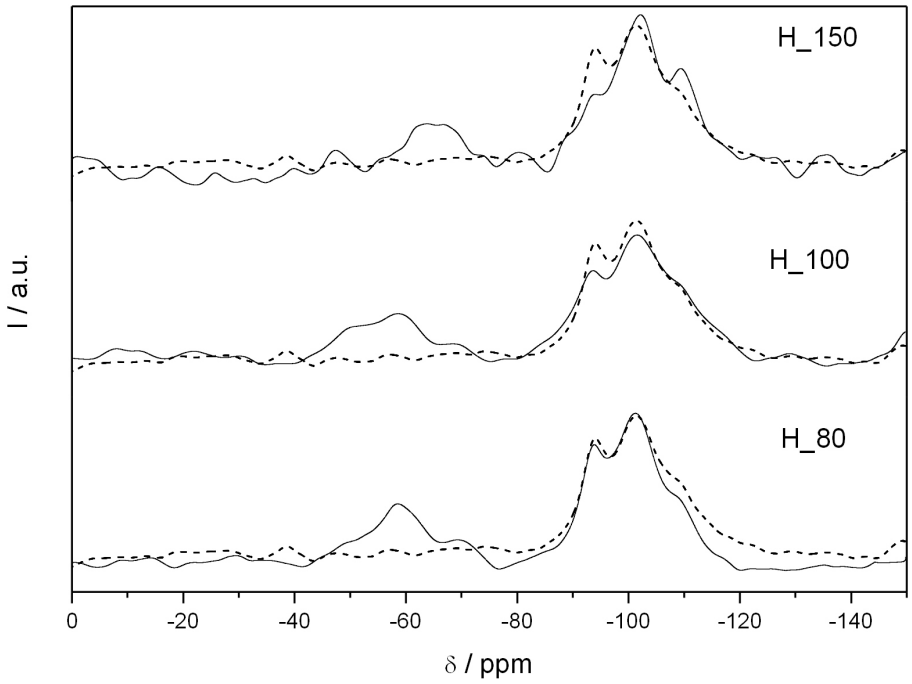

(a) ^{29}Si CP/MAS NMR spectra of Octyl(H) samples (solid lines). The spectrum of unfunctionalized SiO_2 is reported as a reference (dashed line).

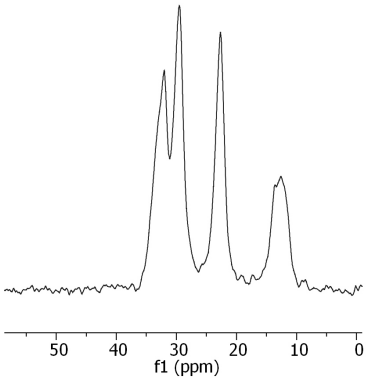

(b) ^{13}C CP/MAS NMR spectra of H_80.

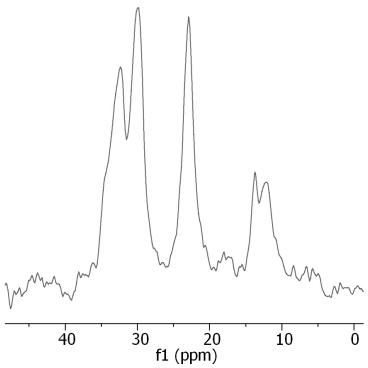

(c) ^{13}C CP/MAS NMR spectra of H_100.

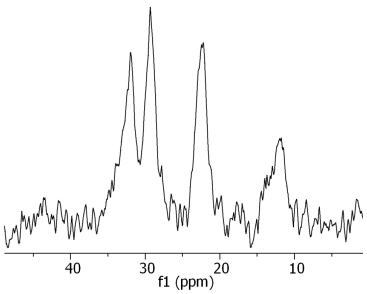

(d) ^{13}C CP/MAS NMR spectra of H_150.

Figure 5.5: *NMR analysis on Octyl(H) samples. Adapted with permission from G. Soliveri et al., J. Phys. Chem. C, 2015, Vol. 119, pp. 15390-400. Copyright 2015 American Chemical Society.*

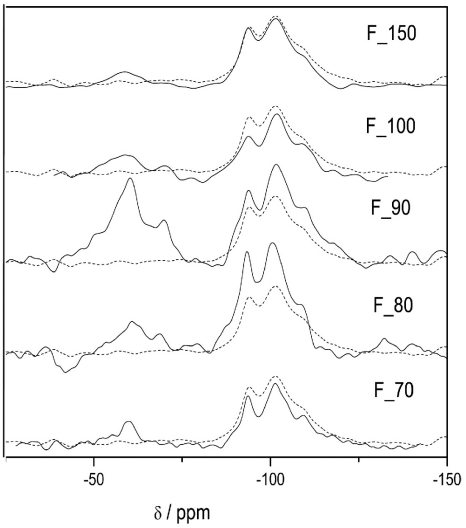

(a) ^{29}Si CP/MAS NMR spectra of Octyl(F) functionalized samples (solid lines). The spectrum of unfunctionalized SiO_2 is reported as a reference (dashed line).

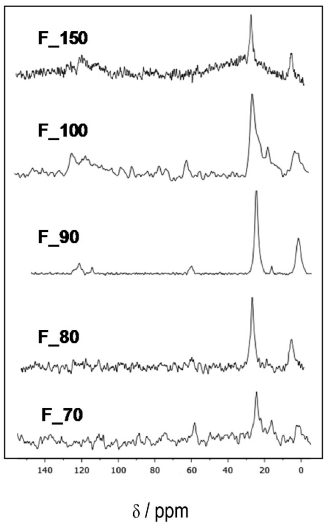

(b) ^{13}C CP/MAS NMR spectra of Octyl(F) derivatives in the temperature range $70 - 150\ ^{\circ}C$.

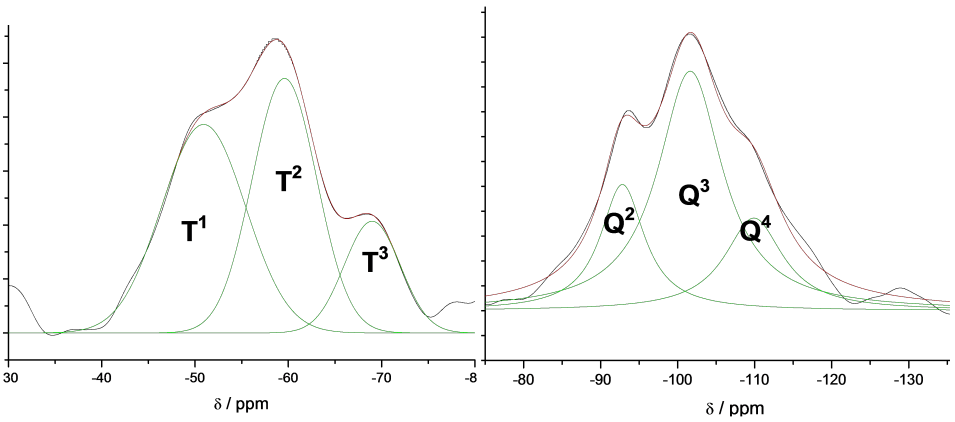

(c) Fitting analysis of the T and Q signals of a representative sample.

Figure 5.6: *NMR analysis on fluorinated samples. Adapted with permission from G. Soliveri et al., J. Phys. Chem. C, 2015, Vol. 119, pp. 15390-400. Copyright 2015 American Chemical Society.*

5.3 Specific procedures

Two different kinds of trifunctional alkylsilanes were investigated in this chapter: Triethoxy(octyl)silane (named Ocyl(H)) and 1H,1H,2H,2H-perfluorooctyltriethoxysilane (named Octyl(F)), both purchased from Sigma Aldrich. The alkylsilane structures are reported in Figure 5.1. The substrate was n-type Si(100) (3-6 (Ω cm), Ultrasil Corporation), having a native oxide layer $\approx$1.5 nm thick. Due to experimental limits, solid state magic angle spinning nuclear magnetic resonance (MAS NMR) and Fourier transform infrared (FTIR) spectroscopies were carried out on SiO_2 powders (Sigma-Aldrich).

Electrochemical characterizations were carried out using a PGStat potentiostat/galvanostat equipped with FRA module (Methrom, Autolab). Measurements were recorded in a standard three electrode cell, using a saturated calomel, a Pt wire and a functionalized Si wafer electrode as reference, counter and working electrodes, respectively. Cyclic voltammetry (CV) was performed in 0.1 M $NaClO_4$ aqueous solution, scanning the potential in the range 0.1 V / + 0.4 V. Electrochemical impedance spectroscopy (EIS) was performed at three different potentials, - 0.1 V, + 0.1 V and + 0.25 V, in the same conditions of CV, in the frequency range 0.1-65000 Hz with amplitude 0.01 V.

Further details about synthetic procedures and characterizations can be found in Appendix C.

References

[1] L. Netzer, J. Sagiv, *J. Am. Chem. Soc.* **1983**, *105*, 674–676.

[2] A. Ulman, *Chemical Reviews* **1996**, *96*, 1533–1554.

[3] W. Gao, L. Dickinson, C. Grozinger, F. G. Morin, L. Reven*, *Langmuir* **1996**, *12*, 6429–6435.

[4] S. Hoeppener, R. Maoz, J. Sagiv, *Nano Lett.* **2003**, *3*, 761–767.

[5] C. Haensch, S. Hoeppener, U. S. Schubert, *Chem. Soc. Rev.* **2010**, *39*, 2323–2334.

[6] G. Panzarasa, G. Soliveri, K. Sparnacci, S. Ardizzone, *Chem. Commun.* **2015**, *51*, 7313–7316.

[7] S. Onclin, B. J. Ravoo, D. N. Reinhoudt, *Angew. Chem. Int. Edit.* **2005**, *44*, 6282–6304.

[8] A. Kumar, H. A. Biebuyck, G. M. Whitesides, *Langmuir* **1994**, *10*, 1498–1511.

[9] J. C. Love, L. A. Estroff, J. K. Kriebel, R. G. Nuzzo, G. M. Whitesides, *Chem. Rev.* **2005**, *105*, 1103–1170.

[10] D. Meroni, S. Ardizzone, U. Schubert, S. Hoeppener, *Adv. Funct. Mater.* **2012**, *22*, 4376–4382.

[11] A. Hozumi, K. Ushiyama, H. Sugimura, O. Takai, *Langmuir* **1999**, *15*, 7600–7604.

[12] H. Sugimura, A. Hozumi, T. Kameyama, O. Takai, *Surf. Interface Anal.* **2002**, *34*, 550–554.

[13] N. Rozlosnik, M. C. Gerstenberg, N. B. Larsen, *Langmuir* **2003**, *19*, 1182–1188.

[14] F. Zhang, K. Sautter, A. M. Larsen, D. A. Findley, R. C. Davis, H. Samha, M. R. Linford, *Langmuir* **2010**, *26*, 14648–14654.

[15] R. D. Lowe, M. A. Pellow, T. D. P. Stack, C. E. D. Chidsey, *Langmuir* **2011**, *27*, 9928–9935.

[16] H. Fox, W. Zisman, *J. Coll. Science* **1952**, *7*, 428 –442.

[17] S. Wu, *J. Adhesion* **1973**, *5*, 39–55.

[18] D Li, A. Neumann, *J. Coll. Interf. Sci.* **1992**, *148*, 190 –200.

[19] D. K. Owens, R. C. Wendt, *J. Appl. Polym. Sci.* **1969**, *13*, 1741–1747.

[20] K. Wu, T. C. Bailey, C. G. Willson, J. G. Ekerdt*, *Langmuir* **2005**, *21*, 11795–11801.

[21] S Kobayashi, T Nishikawa, T Takenobu, S Mori, T Shimoda, T Mitani, H Shimotani, N Yoshimoto, S Ogawa, Y Iwasa, *Nature Mater.* **2004**, *3*, 317–322.

[22] G.-Y. Jung, Z. Li, W. Wu, Y. Chen, D. L. Olynick, S.-Y. Wang, W. M. Tong, R. S. Williams, *Langmuir* **2005**, *21*, 1158–1161.

[23] O. Zenasni, A. C. Jamison, T. R. Lee, *Soft Matter* **2013**, *9*, 6356–6370.

[24] S. A. DiBenedetto, A. Facchetti, M. A. Ratner, T. J. Marks, *Adv. Mater.* **2009**, *21*, 1407–1433.

[25] A. Muthurasu, V. Ganesh, *J. Coll. Interf. Sci.* **2012**, *374*, 241 –249.

[26] H. Hillebrandt, M. Tanaka*, *J. Phys. Chem. B* **2001**, *105*, 4270–4276.

[27] *Surf. Sci.* **2007**, *601*, 2983 –2993.

[28] H. Einati, A. Mottel, A. Inberg, Y. Shacham-Diamand, *Electrochimica Acta* **2009**, *54*, 6063 –6069.

[29] *Introduction to Infrared and Raman Spectroscopy (Third Edition)*, (Eds.: N. B. Colthup, L. H. Daly, S. E. Wiberley), Academic Press, San Diego, Third Edition, **1990**.

[30] F. Milanesi, G. Cappelletti, R. Annunziata, C. Bianchi, D. Meroni, S. Ardizzone, *J. Phys. Chem. C* **2010**, *114*, 8287–8293.

[31] D. Meroni, S. Ardizzone, G. Cappelletti, M. Ceotto, M. Ratti, R. Annunziata, M. Benaglia, L. Raimondi, *J. Phys. Chem. C* **2011**, *115*, 18649–18658.

[32] G. Soliveri, R. Annunziata, S. Ardizzone, G. Cappelletti, D. Meroni, *J. Phys. Chem. C* **2012**, *116*, 26405–26413.

[33] A. Ciogli, P. Simone, C. Villani, F. Gasparrini, A. Lagan, D. Capitani, N. Marchetti, L. Pasti, A. Massi, A. Cavazzini, *Chemistry A European Journal* **2014**, *20*, 8138–8148.

[34] G. Soliveri, D. Meroni, G. Cappelletti, R. Annunziata, V. Aina, G. Cerrato, S. Ardizzone, *J. Mater. Sci.* **2014**, *49*, 2734–2744.

[35] S. Huh, H.-T. Chen, J. W. Wiench, M. Pruski, V. S.-Y. Lin, *Angew. Chem. Int. Edit.* **2005**, *44*, 1826–1830.

[36] D. Kovacek, Z. Maksic, S. Elbel, J. Kudnig, *J. Mol. Struct.* **1994**, *304*, 247 –254.

[37] J. Kujawa, W. Kujawski, S. Koter, A. Rozicka, S. Cerneaux, M. Persin, A. Larbot, *Coll. Surf. A* **2013**, *420*, 64 –73.

Chapter 6

Organic/inorganic hybrids for superhydrophobic coatings

The growing attention in the direction of self-cleaning and anti-fouling materials has emphasized the importance of super-hydrophobic surfaces. Those form a water contact angle of more than 150°, with no adhesion with respect to the surface; water droplets roll away with almost null friction. From thermodynamic evaluation and laboratory tests, the presence of an air cushion between the surface and the liquid are described (see Appendix B). The presence of such cushion requires, apart chemically apolar surfaces, a controlled morphology with a peculiar roughness between nano and micro scale[1, 2].

In the specific case of oxidic materials functionalized by organic moieties, the wetting features are the result of a complex balance among several aspects: the morphology of the substrate[3–5], the interactions between the surface and the organic moieties[6] and the orientation/packing of the molecules in the hydrophobic layer[7, 8]. The morphology of the surface plays a crucial role as the presence of micro- and nano-roughness may definitely change the wetting pattern, *e.g.* from hydrophobic to superhydrophobic[1]. Such results are obtain in this chapter comparing coating obtained by nano- and micro-structured powers, previously functionalized by a commercial hidrophobizing siloxane (SILRES 1701, Waker Chemie, identified as Si-Alk in Chapter 4). On the grounds of their highly applicative interest, oxide substrates with different chemical nature (SiO_2 and TiO_2) are tested.

Although the features of the substrate may affect the surface wettability, the procedure of functionalization may produce relevant modifications on the final performance of the material[4, 9]. Here, two relevant techniques are adopted: wet impregnation and chemical vapor deposition. As described in the previous chapter, while wet impregnation procedure has been mostly adopted (for compatibility with almost all siloxanes and simple procedures)[10], the vapor-phase reaction is generally less sensitive to variations in humidity and reagent purity than the solution-phase method, thus resulting in more reproducible hydrophobing layers[11–15].

The obtained hybrids are characterise for their morphology (dynamic light scattering, DLS, and scanning electron microscopy, SEM), their wettability (static and dynamic contact angle measurements, CA) and for the features of the hydrophobing layer by using Fourier transform infrared spectroscopy and solid-state nuclear magnetic resonance (NMR).

6.1 Results and discussion

6.1.1 Oxide particles morphology

The three selected samples show different morphological features. S-6 sample is a silica powder characterised by a specific surface area of ≈ 6 (m^2 g^{-1}). The silica powder is compared with two different TiO_2 samples, a commercial and a laboratory-made one. The commercial sample T-3 is composed by rutile, a phase composition suggesting a high-temperature preparation procedure, and, consequently, presents a very low-surface area (≈ 3 (m^2 g^{-1})). The laboratory-made sample (T-216) is instead composed by 60% anatase and 40% brookite, two polymorphs usually obtained by calcination at mild temperatures, thus exhibiting a high-specific surface area (≈ 216 (m^2 g^{-1})). The particle size distributions of the selected oxides were analysed using dynamic light scattering (DLS). Figure 6.1a shows that all oxides are polydispersed, presenting at least two distinct size populations. S-6 and T-3 are largely micrometric, although they exhibit a small but significant fraction of nanometric aggregates. The laboratory-made sample T-216 is the most polydispersed, showing three distinct populations in both nanometric and micrometric range.

The morphology of the particles deposited by spin-coating on a glass substrate was determined using SEM analysis (Figures 6.1b,6.1c and 6.1d). For all samples, SEM images show inhomogeneous distribution with different degrees of aggregation between the primary particles. The size of the aggregates observed in SEM images are well correlated with the particle size determined in suspension by DLS (Figure 6.1a(inset), column 4). However, larger agglomerates (in the micrometre scale) are formed by all samples during the particle deposition, probably triggered by the solvent evaporation. Further, the particle size distributions obtained using SEM images have a limited statistical significance given the very low number of particles that can be measured in each image. The laboratory-made oxide T-216 (Figure 6.1d) exhibits a much lower tendency to form large agglomerates during solvent evaporation, resulting in a much smaller particle size range.

6.1.2 FTIR spectroscopy

FTIR spectroscopy was resorted in order to study the functionalization of the oxide surface by the addition of siloxane molecules. As described before, two different functionalization procedures were adopted. The vapor phase deposition was obtained as widely described in the previous chapter; in this specific case, the powders were previously suspended in i-propanol, spin-coated on a glass support and put in the CVD chamber. The wet impregation technique follows a procedure previously developed in the group[8, 16], that newly has adopted i-propanol as solvent. Such solvent is benign and green, but also has high vapor pressure; that allowed fast drying of the powder. Unfortunately, as all the alcoholic media, the solvent generally contains significant amount of water that strongly reacts with siloxane molecules. Furthermore, the polarity of the solvent itself slow down the reactivity of the -OH group at the surface. Such problems can be overpassed, carefully choosing the silane molecule and utilizing a high surface area / porosity substrate, with great abundance of -OH reactive groups.

Figures 6.2a and 6.2b reports the FTIR spectra of the two most representative samples (S-6 and T-216, respectively) before and after the functionalisation with the hydrophobing agent. In the case of sample T-3, the amount of grafted siloxane is very low, so that the relative bonds are scarcely appreciable.

Concerning the two pristine samples (see spectra a, dashed lines, in both sections), the following features can be appreciated in the 3900-1350 cm^{-1} range:

- The OH-stretching vibration of free surface hydroxyl groups, located at ≈ 3700 and ≈ 3690 cm^{-1} for S-6 and T-216 samples, respectively;

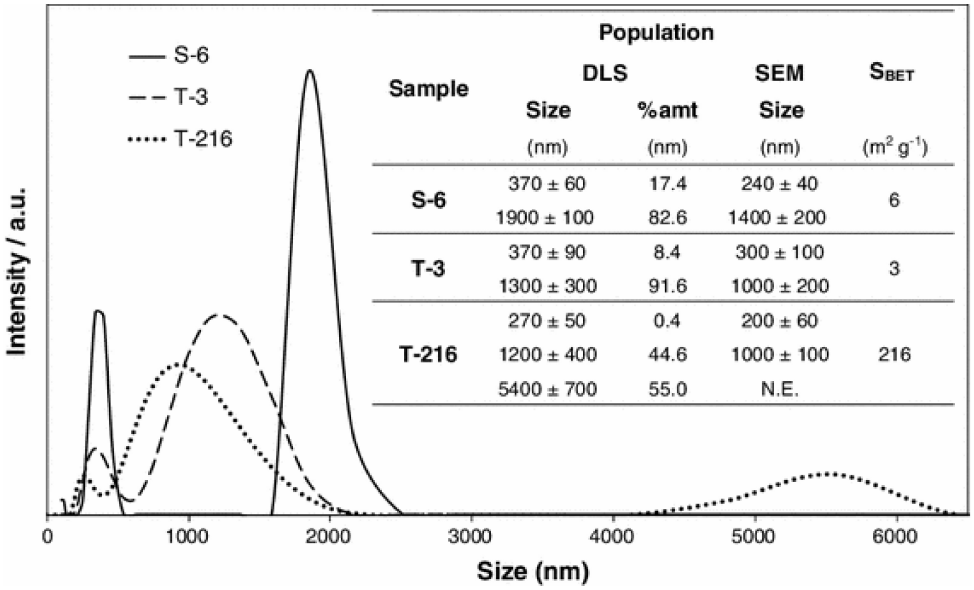

Sample	Population DLS Size (nm)	DLS %amt (nm)	SEM Size (nm)	S_{BET} ($m^2 g^{-1}$)
S-6	370 ± 60	17.4	240 ± 40	6
	1900 ± 100	82.6	1400 ± 200	
T-3	370 ± 90	8.4	300 ± 100	3
	1300 ± 300	91.6	1000 ± 200	
T-216	270 ± 50	0.4	200 ± 60	216
	1200 ± 400	44.6	1000 ± 100	
	5400 ± 700	55.0	N.E.	

(a) Particle size distribution curves (intensity vs. particle diameter) of the three oxide powders determined using DLS analysis. Inset particle size distribution [average size and relative amount (%amt) of the different size populations] obtained by means of DLS (2nd and 3rd column), SEM analyses (4th column), and specific surface area using BET analysis (5th column) of the different oxides.

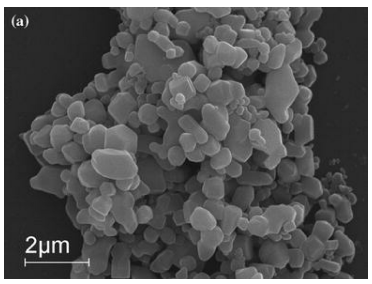

(b) SEM imagines of the oxide particles T-3.

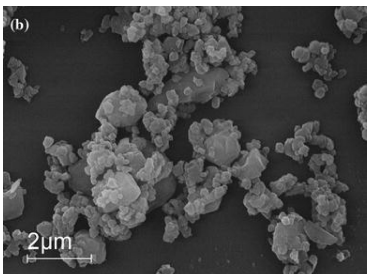

(c) SEM imagines of the oxide particles S-6.

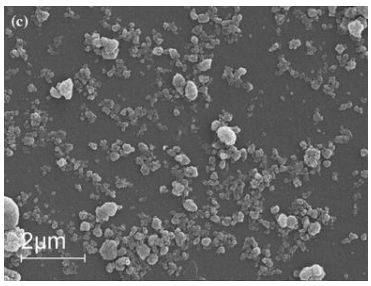

(d) SEM imagines of the oxide particles T-216.

Figure 6.1: *Morphological characterizations[4].*

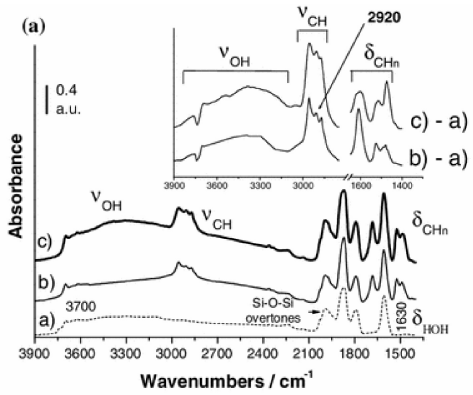

(a) FTIR spectra, in the 3900-1350 spectral range of S-6 pristine (dashed line, spectrum a) and either functionalised via WI (thin solid line, spectrum b) or CVD (thick solid line, spectrum c). Inset: differential FTIR spectra: the (ba) trace refers to a differential absorbance spectrum obtained by subtracting curve a) (pristine samples) from curve b (WI functionalised samples); the ca trace refers to a differential absorbance spectrum obtained by subtracting curve (a) (pristine samples) from curve c) (CVD functionalised samples).

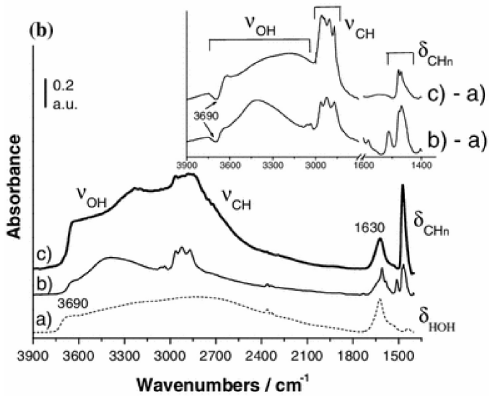

(b) FTIR spectra, in the 3900-1350 spectral range of T-216 pristine (dashed line, spectrum a) and either functionalised via WI (thin solid line, spectrum b) or CVD (thick solid line, spectrum c). Inset: differential FTIR spectra: the (ba) trace refers to a differential absorbance spectrum obtained by subtracting curve a) (pristine samples) from curve b (WI functionalised samples); the ca trace refers to a differential absorbance spectrum obtained by subtracting curve (a) (pristine samples) from curve c) (CVD functionalised samples).

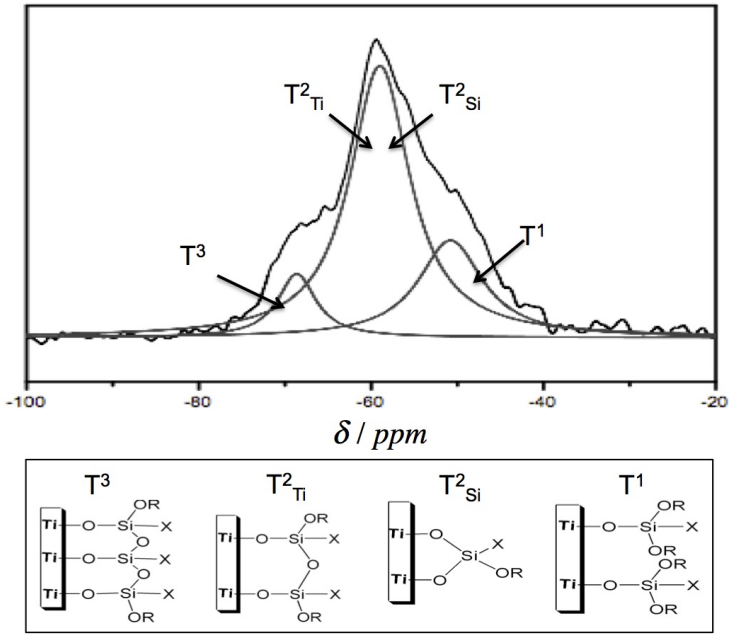

(c) Fitting analysis of the ^{29}Si NMR spectra of siloxane-TiO_2 composites.

Figure 6.2: *FTIR anlaysis and NMR schematic[4].*

- A broad band in the 3700-3000 cm^{-1} spectral range originating from the OH-stretching vibration of hydroxyl groups interacting by hydrogen bonding;
- The spectral component located at $\approx$ 1630 cm^{-1} is due to the in-plane HOH-bending mode of undissociated water molecule present at the sample surface;
- Only in the case of the S-6 sample, there are three additional bands in the 2100-1700 cm^{-1} region that, on the grounds of the literature [22, 24] and of the spectral behavior, can be attributed to SiOSi combination (overtones) modes, typical of the silica matrix.

After the functionalization with both procedures (WI, lines b, and CVD, line c), some important spectroscopic changes are evident for both samples:

- Sharp bands appear in the 2900-2700 cm^{-1} region, which can be assigned to ν_{CH}-stretching modes on the basis of the spectral position and the literature data;
- At lower frequencies (1700-1350 cm^{-1} spectral range), the bands of the bending δ_{CH} counterparts of the above-described stretching modes of all CH-containing species are evident.

The above-described spectral changes that occur after the functionalization for both samples, are better visible in the (b-a) and (c-a) traces (see insets of Figures 6.2a and 6.2b), which represent the difference obtained by subtracting the background spectrum of pristine oxide (S-6 or T-216) from that of the functionalized samples (with both procedures, *i.e.* WI and CVD methods), respectively. By the detailed inspection of these differential spectra, it is worth noting the following:

- A negative peak appears, located at $\approx$ 3700 cm^{-1} (sharp) and $\approx$ 3690 cm^{-1} (broad) for S-6 and T-216 functionalized samples, respectively. Negative peaks are indicative of species (or groups of species) that have been consumed upon functionalization. This experimental evidence confirms that the hydrophobing agent is present on the surface of the examined samples and interacts with it through the OH species. The shape of this negative peak is related to the type(s) of OH groups present on either silica or titania matrices: on the basis of both their spectral behavior and literature data, these components are ascribable to free OH groups coordinated to surface Me^{n+} (*i.e.* Si^{4+} or Ti^{4+}) cations. In particular, in the case of the S-6 samples, these OH species are coordinated to only one silicon ion, thus representing a terminal position, whereas in the case of the T-216 materials, the broadness of the envelope indicates that different contributions may be present, *i.e.* OH groups can be coordinated either to one titanium ion or bridged to two of them.
- Also positive peaks appear: these are due to the species which form on the surface after the functionalization procedures. They can be represented by both OH groups interacting by hydrogen bonding, in the 3700-3000 cm^{-1} spectral range, and CH groups, whose modes lie in the 2900-2700 and 1700-1350 cm^{-1} regions. As for the former envelope, its relative intensity, if compared to that exhibited by the ν_{C-H} modes, is much higher in the case of the T-216 samples rather than in the case of the S-6 ones (see the insets of Figures 6.2a and 6.2b).

Thus, FTIR spectra confirm the successful functionalization of both samples with both procedures (WI and CVD). In the case of sample T-3, differential spectra show that the grafting process may occur by the same mechanism as for T-216. The much lower intensity of the siloxane-related bands, in particular of the ν_{C-H}, may be traced back to the much lower surface area, the presence of the rutile polymorph and the scarce surface hydroxylation. The same effect is observed using NMR (see Subsection 6.1.3). The semi-quantitative differences observed in the ν_{C-H} and δ_{C-H} bands (namely, differences in the intensity

of the peaks) obtained with the two functionalization procedures represent an indication of a different structure of the adsorbed layer. In particular, as for what concerns the SiO_2 systems, films obtained by the CVD procedure exhibit a more ordered character than those obtained by the WI approach: this can be inferred by the detailed inspection of the ν_{C-H}-stretching region around 2910-2930 cm^{-1} (see the inset in Figure 6.2a). In fact, in the case of the CVD films a specific ν_{C-H} component located at ≈ 2920 cm^{-1} is more evident than in the case of the WI sample. On the basis of the spectral behavior of this species and of literature data for similar systems[17], this component is ascribable to the formation of ordered aggregates of grafted molecules. On the other hand, in the case of the TiO_2 systems, the situation is less clear, since the spectral patterns in the ν_{C-H}-stretching region are more complicated, preventing us from drawing reliable assignments. These differences will be confirmed and better explained by the solid-state NMR spectroscopy study, as reported in the following.

6.1.3 Solid state NMR

As well described in Chapter 5, solid state NMR is a critical tool to invetigate the chemisorbed layer from a molecular point of view. The present spectroscopic study, performed by ^{13}C and ^{29}Si solid-state MAS NMR, investigates the attachment modes of the siloxane to the oxide surface and demonstrates that the oxide materials were well functionalized.

The ^{13}C spectra of all compounds (reported in Figures 6.3a, 6.3b, 6.3c, 6.3d) show resonances in agreement with those observed in homogeneous solution of the corresponding precursor. All ^{13}C spectra provide clear evidence that the materials have been functionalized as expected. The marked differences among the spectra will be commented below.

The ^{29}Si resonances were attributed on the grounds of the literature[8, 18, 19]. The Figures 6.3e, 6.3f, 6.3g and 6.3h report the ^{29}Si MAS NMR spectra of the siloxane-oxide hybrids. The absence, in the ^{29}Si spectra, of the signal relative to the siloxane-starting compound (≈ -28 ppm), confirms the successful functionalization of all materials and the absence of unbound siloxane molecules. Also in this case, as by FTIR analyses, the two titania samples show completely different behavior. The ^{29}Si signals of T-3 samples are not sufficiently intense even to be appreciable and are, therefore, not further discussed.

The ^{29}Si spectra concerning the SiO_2 samples (Figures 6.1b and 6.3g) show two well differentiated set of signals, already discussed in Chapter 5. The ^{29}Si high-field resonances, observed around -85 and -110 ppm, are at positions typical of silicon groups Q^4 [siloxane, $(\equiv SiO)_4\underline{\mathbf{Si}}$], Q^3 [single silanol, $(\equiv SiO)_3\underline{\mathbf{Si}}OH$] and Q^2 [geminal silanol, $(\equiv SiO)_2\underline{\mathbf{Si}}(OH)_2$] relative to the starting silica material unsubstituted, as reported in the literature[20, 21]. The low-field resonances (around -50 and -70 ppm) represent silicon atoms in position $(\equiv SiO)_2\underline{\mathbf{Si}}(OH)R$ and $(\equiv SiO)_3\underline{\mathbf{Si}}R$ which are denoted T^{2*} and T^{3*}, respectively, in other words, they can be related to the surface silicon atoms bounded to the siloxane molecules. Therefore, the T^{2*} and T^{3*} resonances confirm the existence of a covalent linkage between the organic group and the silica surface. The ratio between the areas of the two resonance sets largely differs, depending on the functionalization method, showing that the material obtained following the CVD procedure was far more functionalized than the WI one.

Also the ^{13}C MAS NMR spectra of these SiO_2 compounds, functionalized by the two methods, show marked differences. While the spectrum of the WI sample (Figure 6.3a) reveals only two unresolved and very broad signals (width at half height $\Delta\nu_{1/2} = 20$ ppm), the CVD sample shows well defined and sharp peaks (Figure 6.3c), which are indicative of a more ordered layer. As a matter of fact, in an ordered layer, chains tend to align and pack together as a result of Van der Waals forces, causing a lack of mobility and for the steric hindrance a minor number of possible conformations, decreasing the line width. The ^{13}C

	T-216 CVD			T-216 WI		
	δ /ppm	%	$\Delta\nu_{1/2}(Hz)$	δ /ppm	%	$\Delta\nu_{1/2}(Hz)$
T^1	51	47	982	51	39	949
T^2_{Si}/T^2_{Ti}	59	39	656	59	48	699
T^3	68	14	692	68	13	610

Table 6.1: *Relative percentages of the different T^x structures and width at half height ($\Delta\nu$ 1/2) of each resonance obtained by the fitting analysis of the ^{29}Si NMR spectra of the T-216 samples.*

NMR spectrum reported allows us to appreciate the well resolved resonances of the ethoxy group, methyl (58 ppm) and methylene (17 ppm) carbons, which are instead overlapped to the alkyl chain carbons in all others samples. The low intensity of the ethoxy group signals supports, in the case of SiO_2 functionalized by CVD, the high-substitution degree of the ethoxy group during the functionalization process.

Concerning TiO_2 samples, a single signal in the range -50/-60 ppm (Figures 6.3f and 6.3h) was observed in the ^{29}Si spectra, corresponding to silicon atoms involved in Si-O-Si and Si-O-Ti bonds between the siloxane molecules and the TiO_2 surface. This signal shows three resolved resonances, suggesting the co-presence of silicon species with different chemical structures. The relative percentages of the coexisting structures of silicon sites were obtained by deconvolution of DP MAS spectra. The fitting analysis, performed with Gaussian curves, and the structures related to the different components are reported in Figure 6.2c.

From literature data previously reported for silicon atom coordination[8, 16, 22], the three different resonances at -51.0, -59.0, and -68 ppm, can be attributed to different structures depending on the attachment modes of the siloxane molecule to the TiO_2 surface, respectively, named T^1, T^2 and T^3. In the T^1 structure, the siloxane moieties are bound to the oxide surface only by one Si-O-Ti bond. While in the T^2, the Si atom has two Si-O-Si/Si-O-Ti bonds and one residual OH/OR group. In this case, there are two possible different structures, not discriminated by ^{29}Si NMR: they result from either siloxanes making two Ti-O-Si bonds with the TiO_2 surface (T^2_{Ti}) or siloxanes making one Ti-O-Si bond with the TiO_2 and one Si-O-Si bond with a neighboring siloxane group (T^2_{Ti}). In the T^2 structure, the siloxanes form one Si-O-Ti bond with the titania surface and two Si-O-Si bonds with adjacent siloxane moieties.

Table 6.1 reports the amounts of the different T^x structures and the width at half height ($\Delta\nu_{1/2}$) of each resonance obtained by the fitting analysis of the ^{29}Si NMR spectra of siloxane-TiO_2 samples. It appears that the T^2 component is prevalent in the case of the sample from WI, in agreement with previous results[8]. On the other hand, the T^1 structure is prevalent in the CVD sample. This difference in behavior can be ascribed to different mechanisms working in the formation of the siloxane layer, during CVD and WI procedures. It is in fact often reported that in liquid phase methods, siloxane tends to condense into flat aggregates in solution which subsequently adsorb onto the substrate[10]. The absence of this pre-polymerization step in vapor phase techniques (siloxane olygomers have lower vapor pressure than monomers) is in agreement with studies reporting that polymerization of silane molecules could be reduced in layers deposited by the vapor phase methods[14, 23].

6.1.4 Wetting properties

Film roughness dramatically alters the wetting features of a surface. Depending on the roughness degree of a surface, a Wenzel[24] or CassieBaxter[25] state can be obtained, resulting in completely different observed behavior (See Appendix B). In a film composed of particles, the resulting surface roughness can be expected to be linked to the size and morphology of the employed particles and to their degree of

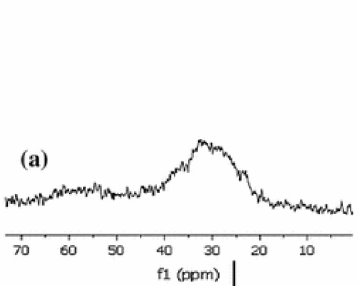

(a) ^{13}C MAS NMR spectrum: S-6 from WI.

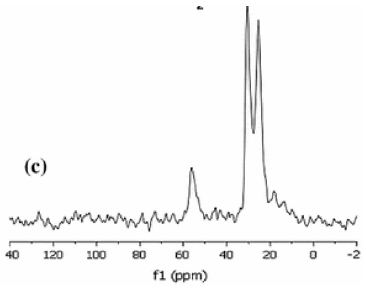

(b) ^{13}C MAS NMR spectrum: T-216 from WI.

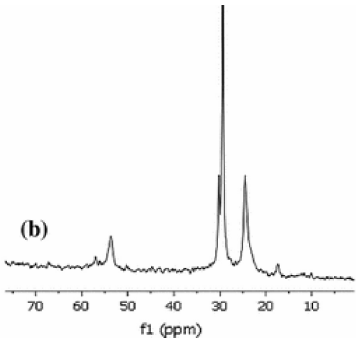

(c) ^{13}C MAS NMR spectrum: S-6 from CVD.

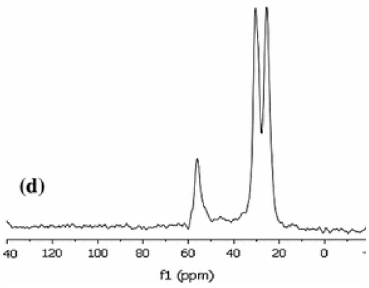

(d) ^{13}C MAS NMR spectrum: T-216 from CVD.

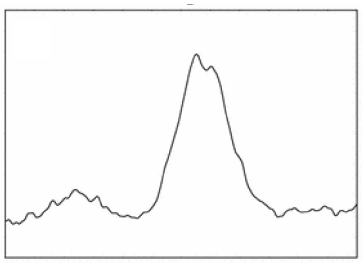

(e) ^{29}Si CP/MAS NMR spectrum: S-6 from WI.

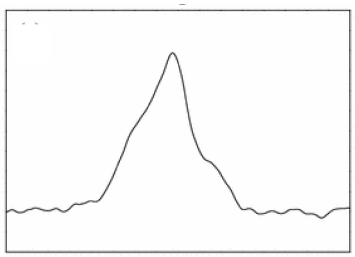

(f) ^{29}Si CP/MAS NMR spectrum: T-216 from WI.

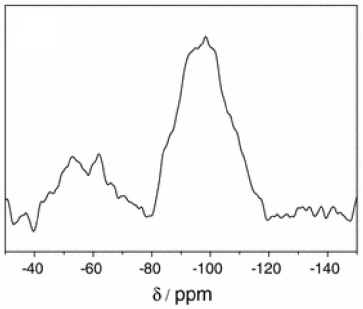

(g) ^{29}Si CP/MAS NMR spectrum: S-6 from CVD.

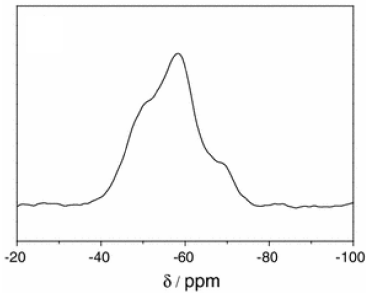

(h) ^{29}Si CP/MAS NMR spectrum: T-216 from WI.

Figure 6.3: *Solid state NMR[4].*

Sample	CVD		WI	
	θ_a	$\Delta\theta$	θ_a	$\Delta\theta$
S-6	147 ± 2	< 5	118 ± 4	40
T-3	123 ± 4	34	101 ± 6	44
T-216	> 150	< 5	> 150	< 5

Table 6.2: *Water advancing contact angles (θ_a) and contact angle hystereses ($\Delta\theta$) of the oxide films functionalised using CVD and WI*

agglomeration. A textured topography showing a multi-scale (micro and nanometric) roughness, similar to that of lotus leaves, has proven to be necessary to impart stable superhydrophobic properties[26].

Before functionalisation, bare oxide films showed hydrophilic to superhydrophilic properties ($\approx 0°$). Instead, all functionalized films exhibit a hydrophobic behavior, although largely different wetting properties are appreciable among the different oxides and functionalization methods. Comparing the effect of the oxide type (Table 6.2), T-216 is the only oxide that gives superhydrophobic coatings upon functionalization by both methods. In fact, T-216 films exhibit low-CA hysteresis $\Delta\theta_w$ and water CAs higher than 150°. NMR spectra of the T-216 samples functionalized by CVD and WI were indeed remarkably similar, showing only a minor difference in the relative percentages of the T^1 and T^2 structures. These evidences are to be related to the texture/morphology of the pristine particle composing the layer. In the case of T-216, the specific surface area of the pristine particles is very large and the size distribution of the particles broad. On the contrary, the other TiO_2 powder, T-3, is the only one among the studied oxides that never gives rise to superhydrophobic coatings. T-3 samples, produced by both functionalization methods, exhibit a Wenzel-type wetting behavior, characterized by large CA hysteresis and moderate water CA values ($\ll 150°$). The low intensity of siloxane peaks observed in both FTIR and NMR spectra, show that the degree of functionalization for T-3 is very low by both adopted procedures. Although S-6 sample has a similar surface area to T-3, it shows much better performances, showing a behavior close to superhydrophobicity when functionalized by CVD method. Indeed, the relative intensity exhibited by the ν_{CH} modes and by OH groups interacting by hydrogen bonding suggests a larger functionalization of the SiO_2 system with respect to TiO_2 , especially in the case of the CVD samples. S-6 shows the largest gap in the CA values between CVD and WI methods in agreement with the relevant differences observed in ^{29}Si and ^{13}C solid-state NMR spectra.

Comparing the two functionalization methods, it can be appreciated that CVD is the most efficient in imparting hydrophobicity as it results in water CAs 20°- 30° higher than those of WI samples. This phenomenon could possibly be explained on the grounds of NMR and FTIR data. In the case of SiO_2, a higher degree of functionalization was determined for the CVD sample on the grounds of ^{29}Si NMR, accompanied by well defined and sharp ^{13}C NMR peaks.

6.2 Conclusion

The role played by the adopted functionalisation procedure of different oxides by siloxane was investigated in detail. Both a wet impregnation and a CVD method were employed to highlight possible effects on the features of the resulting organic/inorganic hybrids. By solid-state NMR and FTIR, the occurrence of chemisorption bonds between the organic moieties and the inorganic substrate were observed in any condition. The effects of both particle morphology and siloxane layer features on the wetting behavior were studied.

By comparing the spectroscopic analyses, silica (S-6) sample presents much larger functionalisation

degree than the titania sample with comparable specific surface area (T-3), resulting in a more hydrophobic wetting behaviour by both procedures. It has been reported that higher ionic character of the Ti-O bond with respect to Si-O, ascribable to the different electronegativities of the two atoms, may affect the interaction with an adsorbate[6].

Among the three different oxides, only the laboratory-made titania (with high polydispersity in the nanometric/micrometric range) gave rise to a Lotus leaf effect, apart from the functionalization technique utilized. The resulting hierarchical topography of the substrate surface is thought to be beneficial in order to obtain a stable super-hydrophobic behavior[26]. Different results were instead achieved for micrometric titania and silica, which presented critical differences by changing the functionalisation technique. On the ground of these results, a deep investigation of such T-216 functionalized by siloxans with different properties will be carried out in the next Chapter.

The dissimilarity between the two techniques has been well investigated by means of ^{29}Si and ^{13}C solid-state NMR and FTIR analyses. The use of CVD results in higher hydrophobicity for all the samples analysed, deriving from a larger functionalisation. Furthermore, the observed variation in the relative weight of the siloxane attachment modes, resulting from the fitting of ^{29}Si CP-MAS NMR spectra, suggests the occurrence of a different functionalisation mechanism in the two cases. The lower degree of cross-linking observed in the case of CVD on T-216 (prevailing T^1 component in NMR spectra) can be traced back to the absence of a pre-polymerisation step in solution. This latter step is critically affected by the water content of the solvent. Thus, CVD is inherently less dependent on parameters such as the quality of the silane and the solvent-siloxane interactions. The vapour deposition, although less investigated in literature, seems to create better functionalised films, and could be identified as a possible replacement to the classical reaction in high-anhydrous and apolar conditions. This could be a great advantage in some applications that need a good quality of the hydrophobing layer without the use of environmentally unfriendly solvents.

6.3 Specific procedures

The adopted hydrophobing agent is SILRES BS 1701 (Si-Alk in Table 4.1, Chapter 4, produced and commercialised by Wacker Chemie AG). Three different kinds of particles, characterized by different compositions and surface areas, were employed. The samples are named according to the following notation: a letter identifying the nature of the oxide (S for silica, T for titania) and a number specifying the sample-specific surface area. The adopted SiO_2 sample (named S-6) was a silica powder from Sigma Aldrich. Two different TiO_2 samples were employed: one commercial (T-3), purchased from Sigma Aldrich; and one laboratory-made (T-216), prepared by a sol-gel synthesis using the procedure reported in Appendix C.

Further details about synthetic procedures and characterizations can be found in Appendix C.

References

[1] D. Qur, *Annu. Rev. Mater. Res.* **2008**, *38*, 71–99.

[2] M. Callies, D. Quere, *Soft Matter* **2005**, *1*, 55–61.

[3] D. M. Spori, T. Drobek, S. Zrcher, M. Ochsner, C. Sprecher, A. Mhlebach, N. D. Spencer, *Langmuir* **2008**, *24*, 5411–5417.

[4] G. Soliveri, D. Meroni, G. Cappelletti, R. Annunziata, V. Aina, G. Cerrato, S. Ardizzone, *J. Mater. Sci.* **2014**, *49*, 2734–2744.

[5] G. Soliveri, R. Annunziata, S. Ardizzone, G. Cappelletti, D. Meroni, *J. Phys. Chem. C* **2012**, *116*, 26405–26413.

[6] Y. Paz, *Beilstein J. Nanotech.* **2011**, *2*, 845–861.

[7] D. M. Spori, N. V. Venkataraman, S. G. P. Tosatti, F. Durmaz, N. D. Spencer, S. Zrcher, *Langmuir* **2007**, *23*, 8053–8060.

[8] D. Meroni, S. Ardizzone, G. Cappelletti, M. Ceotto, M. Ratti, R. Annunziata, M. Benaglia, L. Raimondi, *J. Phys. Chem. C* **2011**, *115*, 18649–18658.

[9] G. Soliveri, V. Pifferi, R. Annunziata, L. Rimoldi, V. Aina, G. Cerrato, L. Falciola, G. Cappelletti, D. Meroni, *J. Phys. Chem. C* **2015**, *119*, 15390–15400.

[10] S. Onclin, B. J. Ravoo, D. N. Reinhoudt, *Angew. Chem. Int. Edit.* **2005**, *44*, 6282–6304.

[11] M. Zhu, M. Z. Lerum, W. Chen, *Langmuir* **2012**, *28*, 416–423.

[12] A. Hozumi, K. Ushiyama, H. Sugimura, O. Takai, *Langmuir* **1999**, *15*, 7600–7604.

[13] H. Sugimura, A. Hozumi, T. Kameyama, O. Takai, *Surf. Interface Anal.* **2002**, *34*, 550–554.

[14] H. Sugimura, T. Moriguchi, M. Kanda, Y. Sonobayashi, H. M. Nishimura, T. Ichii, K. Murase, S. Kazama, *Chem. Commun.* **2011**, *47*, 8841–8843.

[15] H. Sugimura, T. Hanji, K. Hayashi, O. Takai, *Adv. Mater.* **2002**, *14*, 524–526.

[16] F. Milanesi, G. Cappelletti, R. Annunziata, C. Bianchi, D. Meroni, S. Ardizzone, *J. Phys. Chem. C* **2010**, *114*, 8287–8293.

[17] T. Vallant, J. Kattner, H. Brunner, U. Mayer, H. Hoffmann, *Langmuir* **1999**, *15*, 5339–5346.

[18] S. Huh, H.-T. Chen, J. W. Wiench, M. Pruski, V. S.-Y. Lin, *Angew. Chem. Int. Edit.* **2005**, *44*, 1826–1830.

[19] D. Kovacek, Z. Maksic, S. Elbel, J. Kudnig, *J. Mol. Struct.* **1994**, *304*, 247 –254.

[20] A. Puglisi, R. Annunziata, M. Benaglia, F. Cozzi, A. Gervasini, V. Bertacche, M. C. Sala, *Adv. Syn. Catal.* **2009**, *351*, 219–229.

[21] S. Huh, J. W. Wiench, J.-C. Yoo, M. Pruski, V. S.-Y. Lin, *Chem. Mater.* **2003**, *15*, 4247–4256.

[22] J. Kujawa, W. Kujawski, S. Koter, A. Rozicka, S. Cerneaux, M. Persin, A. Larbot, *Coll. Surf. A* **2013**, *420*, 64 –73.

[23] T. Moriguchi, K. Murase, H. Sugimura, *Coll. Surf. A* **2008**, *321*, 94 –98.

[24] R. N. Wenzel, *Ind. Engin. Chem.* **1936**, *28*, 988–994.

[25] A. B. D. Cassie, S. Baxter, *Trans. Faraday Soc.* **1944**, *40*, 546–551.

[26] M. Nosonovsky, B. Bhushan, *Curr. Opin. Colloid Interface Sci.* **2009**, *14*, 270 –280.

Chapter 7

Self-cleaning TiO_2 coating and photo-lithography

Nano-structured titanium dioxide/siloxane hybrid coatings were discussed in the previous chapter as an effective self-cleaning water repellent surface. Furthermore, the well-known photo-activity of crystalline titania makes these hybrid ideal substrates for many more applications. Under UV-irradiation, the formation of electron-hole pairs turns the TiO_2 highly reative with respect to the adsorbates. Especially, organic adsobate molecules can be mineralized by direct oxidation, by holes, or through secondary reaction with $OH^{\bullet}$ and $O_2^{\bullet}$ (produced by reaction of the surface with atmospheric H_2O and O_2). So, when active titania functionalized by siloxanes is irradiated under near-UV light, the organic moieties are oxidized, changing the chemistry of the surface, and thus its phisico chemical properties[1]. Especially, this chapter is focused on the modulation of wettability features of a rough titania surface. By controlling the time and the condition of irradiation, a partial degradation of the organic chains (of the siloxanes) can be obtained; that is correlated with intermediate contact angle. Superhydrophobic surfaces bear relevance to numerous applications like self-cleaning, protection of outdoor cultural heritage, anticorrosion coatings, and biomaterials[2–5]. In several instances, however, the wettability of a material should be tuned to some predetermined level without reaching superhydrophobic conditions. For example, the maximum adsorption of proteins, as well as cell adhesion and growth, is observed on a moderate hydrophilic surface with a water CA around 60°[6].

Further, the tuned localization of pristine/degradated siloxane patches on a surface may control numerous physico chemical properties of a system, *e.g.*, the condensation of water from the gas phase[7], the controlled adsorption of metal ions[8], or the transport of electrolytes and gas bubbles into interfaces such as porous environments or complex flow networks[9–11]. Such pattern can also be the pillar for the selective grown of supra-molecular 3D structure, (as it will be shown in Chapter 9). Photolithography is one of the most advanced patterning techniques employed to obtain controlled localized hydrophobic/hydrophilic patches. Photochemical patterning without the use of the expensive photoresist can be performed by irradiating a self-assembled monolayer with ultraviolet (UV) light with a wavelength shorter than 185 nm; however, this approach is limited to specific functional groups and under constrained environments[12]. In contrast, photoactive semiconductors can be directly patterned by selective oxidation, supported by the photocatalyst itself, of chemisorbed hydrophobic monolayers in the presence of a patterning mask. This surface modification technique, besides bearing straightforward applications for offset printing and printed-circuit boards, may offer the starting point for additional functionalization

of the underlying material[8, 13]. One of the aims of the work described in this chapter is to test the photocatalytic lithography efficiency of the synthesized films.

Furthermore, compared to the previous chapter, different silanes were tested in order to impart, in addiction to superhydrophobicity, oleophobic properties. As a matter of fact, while the control of the wettability by water has been extensively studied in the literature, the preparation of oleophobic surfaces is by far less investigated, despite the numerous, economically relevant, potential applications in fields such as crude oil transfer, fluid power systems, antifouling materials, and also in several energy storage systems[14].

Notwithstanding the very relevant applicative impact of nano-TiO_2 films with tunable wettability for both water and nonaqueous solvents, only very few recent works deal with this topic[15–19]. Most of these works[16, 18, 19] rely on complex multistep synthetic procedures, often limited to a special kind of substrate: Wang *et al.*[16] obtained engineered oleophobic TiO_2 surfaces by a complex procedure implying a combination of anodization of a Ti foil and laser technology; Kim *et al.*[19] modified metal Ti foils by electrochemical etching and hydrothermal processes; Zhang and coauthors[18] obtain titania/single-walled carbon nanotube composites by complex processes.

Here, the T-216 (described in Chapter 6) were tested with the respect to three different silane hydrophobizing molecules, fluorinated and unflourinated: triethoxy(octyl)silane (named Ocyl(H), Figure 5.1, Chapter 5), 1H,1H,2H,2H-perfluorooctyltriethoxysilane (named Octyl(F), Figure 5.1) and triethoxy(octadecyl)silane (named OcDe(H), Figure 7.1a). Wet impregnation (WI) in benign solvent (like i-propanol) was chosen as the effective technique to compare those distinct siloxanes; vapor phase approach is not adequate for the comparison becouse of the large difference in vapor pressure of the studied siloxane (especially for OcDe(H)). The structure of the functionalizing layer and the attachment modes of Si atoms at the TiO_2 surface are analyzed by combining data of solid-state nuclear magnetic resonance (NMR) analyses with SFE and CA measurements by several solvents. Eventually, patterned structures with tunable hydrophobic and oleophobic patches are obtained by photocatalytic lithography. The resulting wetting contrast is exploited to obtain a site selective adsorption of a dye molecule.

7.1 Results and discussion

7.1.1 Nano-TiO_2 composites: synthesis and characterization

As discussed in the previous chapter, the features of the particles must be carefully tailored due to the key role played by the layer morphology on the wettability of the film. High water/alkoxide ratio and the solvent/water ratios (100 and 20, respectively) were used to provoke an extensive hydrolysis of the alkoxide, favoring nucleation *vs* particle growth, in order to produce small crystallites and, consequently, large particle surface area[20, 21]. The ensuing thermal treatment was performed to promote the crystallinity of the oxide, which is fundamental to obtain a good photocatalytic activity. The final product shows a nanocrystalline structure with a controlled enrichment in anatase and brookite (75% anatase and 25% brookite, Figure 7.1b). The concomitant presence of different polymorphs is thought to enhance the photocatalytic activity of the oxide by reducing the recombination rate of the photogenerated electrons and holes[22]. Moreover, this composite structure may provide random exposure of facets affecting the in-homogeneity of the texture and thus its wetting properties.

Confirming the data presented in the previous chapter, film morphology was studied by means of AFM. The AFM 3D (Figure 7.1c) image of the bare TiO_2 film shows the complete coverage of the glass substrate by the titania film. The surface presents a multiscale roughness, due to the presence of both

Siloxane film	OWRK - siloxane films		
	γ_s /mN m^{-1}	γ_s^p /mN m^{-1}	γ_s^d /mN m^{-1}
Octyl(H)	44	11	33
Octyl(F)	22	5	17
OcDe(H)	46	6	40

Table 7.1: *SFE values for the siloxane films (polar and disperse component) by OWRK model.*

nanometric particles and micrometric aggregates. The average roughness was 150 nm (RMS).

No effects are introduced in the structural features of TiO_2 by siloxane addition, with respect to both the polymorphs enrichment and the crystallite size, as it can be seen comparing XRPD spectra before and after functionalization (Figure 7.1b). The functionalization by the organic molecules affects instead the specific surface area of the particles and their porosity. The oxides modified by the two siloxanes bearing a C8 chain show a decrease in the surface area by about 80% with respect to the bare oxide, this decrease being mainly the result of the loss in pore volume (Figures 7.1d and 7.1f). In the case of functionalization by OcDe(H), the surface area drops severely, and it is reduced to a few square meters per gram. The N_2 adsorption isotherms of the siloxane-clad samples, obtained in subcritical conditions, are reported in Figure 7.1e. Figure 7.1d reports the elaboration in the reciprocal BET coordinates of the adsorption isotherms of N_2, obtained in subcritical conditions. By elaborating the isotherms data on the grounds of the BJH model, the mesopore size distribution can be obtained (Figure 7.1f). A marked decrease of the pore volume, especially concerning the smallest mesopores, can be appreciated for the Octyl(H) siloxanes, while the decrease becomes dramatic in the case of the OcDe(H) alkyl chain siloxane. The alkyl chains may bend and spread shielding to much larger oxide patches than those pertaining to their projected co-area. Further, the loss of accessibility of the smallest pores of the particles supports the hypothesis of the presence of relevant tail-tail networks, more so in the case of the OcDe(H) compounds. These latter considerations are in full agreement with solid-state NMR data, reported in the following, which suggest in the case of OcDe(H) functionalized samples a very compact and ordered structure.

7.1.2 Wettability features

Before considering the wettability of the nano-TiO_2 -siloxane composites, the surface features of the bare siloxanes deposited onto smooth glass slides were investigated, following the procedure reported in Chapter 4. According to Owens and Wendts approach[23], the measurement of CAs of test liquids, with known surface tension and relative components, enables the determination of SFE, as the sum of polar and disperse parts (Appendix B). Table 7.1 reports the total SFE and relative polar and disperse components obtained for the present siloxanes. Nonfluorinated molecules (Octyl(H) and OcDe(H)) show similar SFE values but a different polar/disperse component ratio; the weight of the disperse component increases with increasing the length of the alkyl chain. The fluorinated compound (Octyl(F)), instead, exhibits the lowest total SFE and an almost halved disperse component with respect to the corresponding unfluorinated compound (Octyl(H)), in agreement with the expected weak dispersive interactions of fluorocarbons[24, 25]. The different component partition appears directly by the comparison of the water and CH_2I_2 CAs (Octyl(H): θ_w 67°, $\theta_{CH_2I_2}$ 39°; Octyl(F): θ_w 92°, $\theta_{CH_2I_2}$ 75°); the CA increases in passing from the nonfluorinated to the fluorinated molecules, especially for the non-aqueous solvent.

For rough surfaces, the simple picture represented by Young's relation[26] fails. For very rough hydrophobic surfaces, air pockets remain trapped in the network created by the hydrophobic posts, as

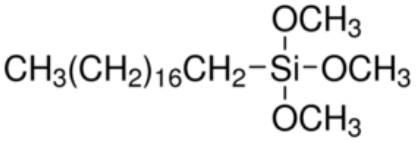

(a) triethoxy(octadecyl)silane (named OcDe(H)).

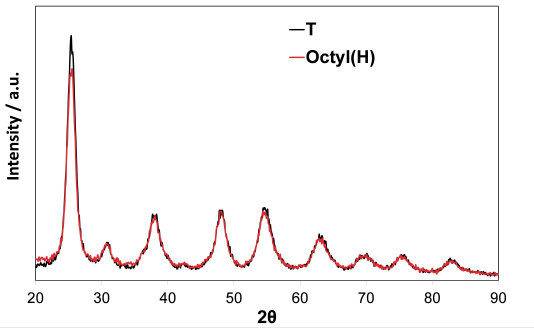

(b) X-ray powder diffraction spectra of the bare and Octyl(H) TiO_2 powder .

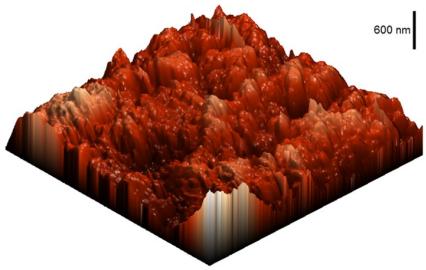

(c) AFM 3D image (5 x 5 μm^2) of a TiO_2 film..

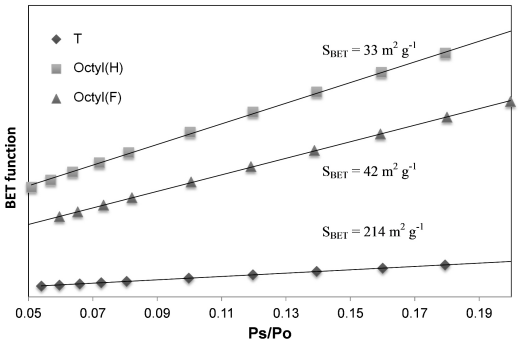

(d) Elaboration of adsorption isotherms of N_2 in subcritical conditions by reciprocal BET coordinates.

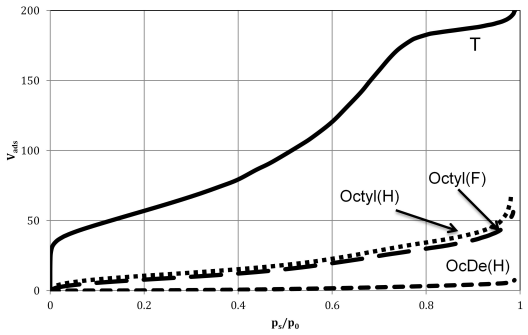

(e) Adsorption isotherms of N_2 in subcritical conditions.

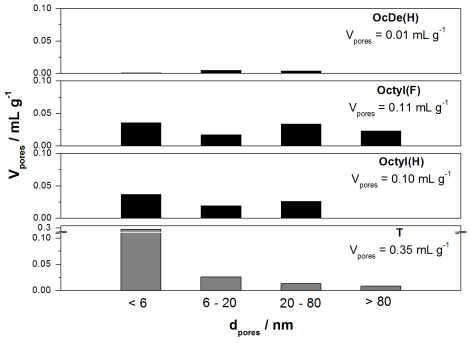

(f) Total pore volume distribution obtained by N_2 adsorption/desorption in subcritical conditions.

Figure 7.1: *Adapted with permission from G. Soliveri et al., 2012, Vol. 116, pp. 26405-13. Copyright 2015 American Chemical Society.*

Siloxane	CAs over siloxane-TiO_2 composites (°)					
	water		glycerol	EtGly	CH_2I_2	toluene
	θ_{avg}	$\Delta\theta$	θ_s	θ_s	θ_s	θ_s
Octyl(H)	> 150	< 5	150	110	97	0
Octyl(F)	> 150	< 5	142	108	> 133	53
OcDe(H)	> 150	< 5	139	114	75	0

Table 7.2: *Contact angle values for different solvents over the siloxaneTiO_2 composite films.*

proposed in the Cassie-Baxter model[27]. The resulting material shows superhydrophobic behavior (See Appendix B).

For all the present TiO_2 -siloxane composites, the measurement of the water CA was not straightforward; because of the enhanced water repellency, water drops bounced and rolled off the layers. Even performing the measurements by rising, very slowly, the support up to the contact with the pendant drop, the simple detachment of the drop from the tip produced, almost invariably, rolling off of the drop. In Table 7.2, the values of water CAs are, in any case, reported as larger than 150°, with very low measured hystereses ($< 5°$), indicating the occurrence of superhydrophobic surfaces. The Cassie-Baxter state is generally attributed to rough surfaces bearing hierarchical structures due to multiscale roughness. This is the case of the present layers as shown by the AFM image (Figure 7.1c) where a random roughness is produced by the aggregation of the primary nanometric particles. Random roughness at multiple length scale can be expected to be more hydrophobic than surfaces bearing regularly spaced hydrophobic posts[28].

Toluene CAs are close to 0° for all the substrates apart from composites of Octyl(F). Octyl(F) is the only siloxane exhibiting a good degree of oleophobicity, giving CAs of 53° for toluene. In the case of this composite, the measurement of the CA of CH_2I_2 drops presented the same difficulties as for water CAs. Again, CH_2I_2 drops roll off the surface making the direct measurement difficult. Angles larger than 135° could be measured by keeping the tip of the needle inside the drop. This condition, together with the high density of the liquid, produced, however, an increased flattening of the drop profile.

Interestingly, the wetting properties toward polar solvents (water, glycerol, and ethylene glycol) do not change significantly between Octyl(F) and the other siloxane composites (Octyl(H) and OcDe(H)). This behavior could be traced back to the surface energy components of the different siloxanes (Table 7.1). While the polar SFE component of Octyl(F) is almost identical to those of Octyl(H) and OcDe(H), the disperse component is almost halved. Hence, we can propose that the ability of Octyl(F) to interact with polar solvents remains unchanged (in polar solvents, the CA is mostly the result of polar interactions between liquid and surface), whereas totally apolar solvents, such as toluene and CH_2I_2, give much higher CAs because of the lower ability of the surface to give disperse interactions. For instance, CH_2I_2 CA over Octyl(H) is more than 20° larger than on OcDe(H).

7.1.3 Solid state NMR

Here, ^{13}C and ^{29}Si solid-state CP/MAS NMR are used to investigate the different behavior and reactivity toward the nano-TiO_2 surface of siloxanes with different organic chains. As already discussed in the previous chapters (and in Appendix C), the ^{29}Si resonances were assigned following previous reports in the literature[2, 29, 30], while those of ^{13}C were referred to the solution spectra of the corresponding unbound precursors. In the case of the Octyl(F) derivative, the structure is also confirmed by the correct integral ratio between hydrogen and fluorine carbons.

Substrates	Octyl			Octyl(F)			ODS		
	δ *ppm*	%	$\Delta\nu_{1/2}$ *Hz*	δ *ppm*	%	$\Delta\nu_{1/2}$ *Hz*	δ *ppm*	%	$\Delta\nu_{1/2}$ *Hz*
T^1	-51	25	895	-	-	795	-	30	497
T^2_{Si} / T^2_{Ti}	-59	65	839	-52	64	1334	-58	66	767
T^3	-69	10	532	-60	36	1157	-68	5	397

Table 7.3: *^{29}Si CP/MAS NMR chemical shifts, relative percentages and $\Delta\nu_{1/2}$ (Hz) for the proposed Si structures of the three different hydrophobizing molecules. The powders analysed were T300-Octyl-WI33, T300-Octyl(F)-WI33, T300-ODS-WI33*

^{29}Si CP/MAS NMR spectra confirm the absence of physisorbed/excess siloxane molecules, which would result in a separate sharp peak shifted in the direction of the unbound molecules. Figure 7.2a shows the solid-state ^{29}Si CP/MAS NMR spectra of the present TiO_2 hybrids; in these compounds, the ^{29}Si resonances are in the chemical shift region of siloxane groups (-40 to -80 ppm). The shape of the peaks of the three compounds is markedly different. Three well resolved resonances are appreciable in the case of the ^{29}Si spectrum of OcDe(H) (Figure 7.2a), suggesting the co-presence of silicon species with different chemical structures. This behavior characterizes also the Otlyl(H) spectrum, though with a minor signal resolution. Instead, in the case of Octyl(F), the line width becomes too large to recognize the three components; the distinctive feature of this compound is the presence on the silicon chain of fluorine atoms instead of hydrogen, and this, increasing the relaxation rate, broadens the signal.

The fitting analysis of the ^{29}Si NMR signals was performed in order to recognize the relative percentages of the coexisting structures as previously reported in Chapter 6. From data previously reported in the literature for silicon atom coordination, the lower field resonances at 51.0 and 50.0 ppm of Octyl(H) and OcDe(H) samples, respectively, can be attributed to a T^1 structure in which only one ethoxy group has been removed by the Ti-O-Si bond formation; the structures containing only one residual OH (OR) group (T^2) show the resonances at 59.0 and 58.0 ppm for the Octyl(H) and OcDe(H), respectively. Two different T^2 structures are possible: a siloxane forming two bonds with the titania surface (T^2_{Ti}) and a siloxane forming one bond with the titania and one with a neighboring siloxane molecule (T^2_{Si}). The technique does not allow us to identify separately the two structures.(38) Finally, the ^{29}Si resonances at 69.0 for octyl and 68.0 ppm for octadecyl derivatives can be related to siloxanes in which all the three ethoxy groups are substituted in the functionalization reaction, with the formation of SiOSi bonds between adjacent siloxane molecules (T^3 structure).

Relatively to the Octyl(F) sample, we found small chemical shift differences in the resonance of T^2 (-52.0 ppm) and T^3 (-60.0 ppm), with respect to the other studied compounds, and the absence of the T^1 structure; the presence of the fluorine atoms on the silicon chain gives rise to these $\Delta\delta$ variations, shifting the ^{29}Si NMR signal downfield with respect to two other compounds (see Table 7.3), this behavior can be ascribed to the larger local electron density of the fluorine atom with respect to the hydrogen one. There is a clear correlation between the F electronegativity and the induced shift, the fluorine being the most electronegative substituent.

For all the studied TiO_2 hybrids, the ^{13}C MAS NMR spectra reveal that the signals of the methyl and methylene carbons, ascribable to the ethoxy groups on the silicon, have a very low intensity, confirming their high substitution degree during the Ti-O-Si bond formation and, consequently, the prevalence of the T^2 and T^3 structures in comparison to the T^1 one. The relative percentages of the different T^x structures present in each compound together with the width at half height ($\Delta\nu_{1/2}$) of the signal are reported in Table 7.3. The data show that, in all cases, the T^2 component is prevalent (64-66%), although a relevant

presence of T^1 structures can be appreciated in the unfluorinated samples (25-30%). A relevant difference can be appreciated in the case of the octyl(F) compound, in which the T^1 structure is absent and the T^3 component is more abundant. These effects could be possibly related to the different reactivity of the organic molecule inducing a higher prepolymerization of the siloxane in solution before attaching to the oxide. The withdrawing effects of F and O seem to play an important role in events of prepolymerization in solution.

The line width values of the ^{29}Si signals relative to the three proposed structures (T^1, T^2, and T^3) are very different and can provide information about the dynamic processes in the materials. For all compounds, the T^3 structure, being the more strained and more ordered structure, shows the smallest value of $\Delta\nu_{1/2}$ in comparison with the corresponding T^1 and T^2. The OcDe(H) shows, without doubts, the sharper peaks, the $\Delta\nu_{1/2}$ being 497, 767, and 397 Hz for T^1, T^2, and T^3, respectively. In this case, in agreement with the literature, the chains tend to align and pack together as a result of van der Waals forces; this causes a lack of mobility, and for steric hindrance, a minor number of possible conformations, decreasing the line width. These conclusions fully agree with the data of specific surface area of the hybrids, presented above. In the case of OcDe(H), the specific surface area dropped to a few square meters, mainly due to the total loss of porosity ensuing, in turn, to tail-tail networks. An opposite behavior is found, instead, for the fluorinated Octyl(F) sample, where the fitting analysis reveals large $\Delta\nu_{1/2}$ values, up to 1334 and 1157 Hz for T^2 and T^3, respectively. In this case, the presence of the fluorine atoms on the chain may alter the relaxation rate of the material by increasing the mobility for electrostatic repulsion between the chains, thus supporting a larger conformational freedom. These latter data are consistent with SFE results, which showed (Table 7.3) the lowest disperse component for the fluorinated compound.

7.1.4 Self-cleaning and photocatalytic lithography

The remarkable differences observed in the structure and wetting behavior of the tested siloxanes can be exploited to obtain valuable materials for applications such as self-cleaning. Figure 7.2c shows the comparison between the self-cleaning behavior of pristine TiO_2 , OcDe(H), and Octyl(F) layers with respect to dye stains either dissolved in water (methyl orange) or in CH_2I_2 (methylene blue). In the case of the pristine TiO_2 layer (Figure 7.2c(a,d)), the two drops spread out, and the stains are not significantly removed by washing the layer by water or CH_2I_2. The OcDe(H) (Figure 7.2c(b,e)) is highly hydrophobic but not oleophobic; consequently, it shows self-cleaning properties only with respect to the water-soluble dye, while the CH_2I_2 dye stains the film. The Octyl(H) behaves in the same way as OcDe(H). The Octyl(F) layer (Figure 7.2c(c,f)) is not wet by either of the two dye solutions, the drops roll off the surface without leaving any trace.

The semiconductor nature of TiO_2 allows the wettability of the hybrid layers to be modulated by photocatalytic lithography[31]. However, the photoactivity of TiO_2 does not reduce the durability of the samples under environmental light since room-light lamps only emit a very small amount of UV light: the present samples have proved to be stable for several months in a well lighted laboratory.

The Octyl(H) film, covered by a paper mask (Figure 7.2b), is irradiated with UV light for 1 h. The organic chains attached to the film area not protected by the mask are photocatalytically decomposed. The areas covered by the mask remain superhydrophobic, whereas the CAs for the irradiated areas decrease due to the surfacing of the pristine oxide. The boundary between the hydrophobic and hydrophilic regions is highlighted by the use of a water-soluble dye, methyl orange (Figure 7.3).

The studies relative to the variation of the CA *vs* time under UV-A radiation permitted us to optimize

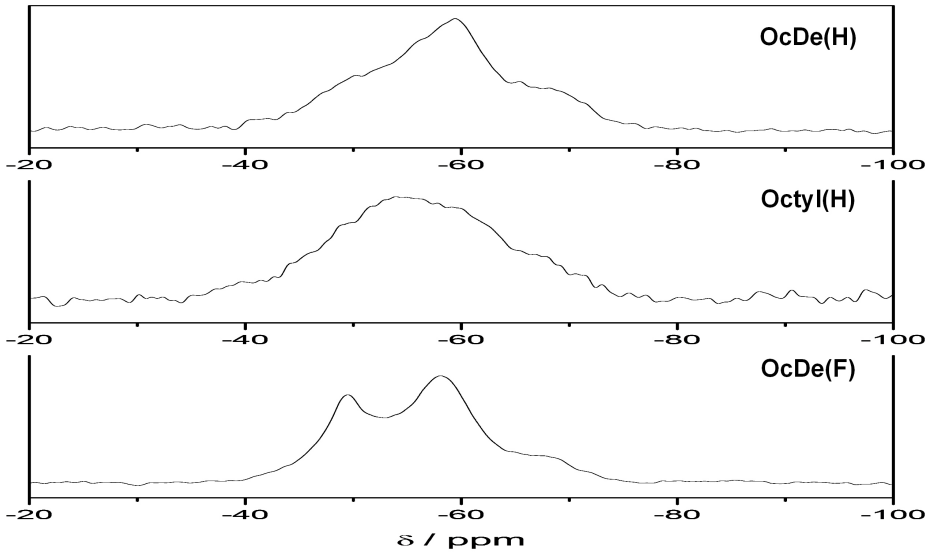

(a) ^{29}Si CP/MAS NMR spectra of OcDe(H), Octyl(H), and Octyl(F).

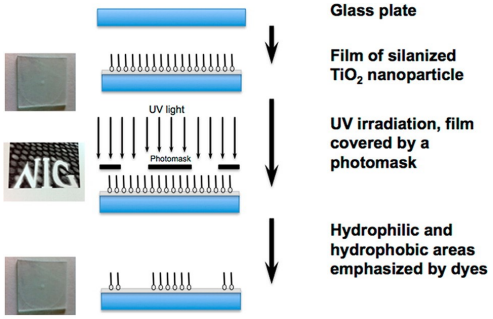

(b) Schematic representation of the photocalatlytic lithography process.

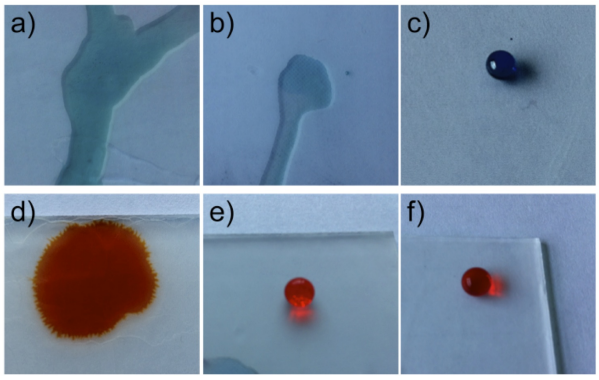

(c) Self-cleaning tests on (a,d) pristine TiO_2 , (b,e) OcDe(H), and (c,f) Octyl(F) layers with respect to dye stains either dissolved in water (methyl orange, MO) or in CH_2I_2 (methylene blue, MB).

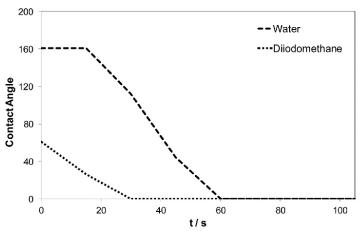

(d) Variation of water and CH_2I_2 static CAs over the time of irradiation under UV-A lamp, for Octyl(H) layer.

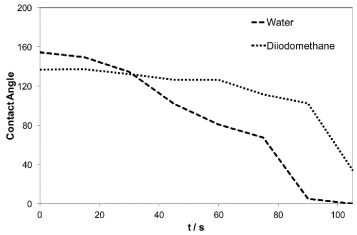

(e) Variation of water and CH_2I_2 static CAs over the time of irradiation under UV-A lamp, for Octyl(F) layer.

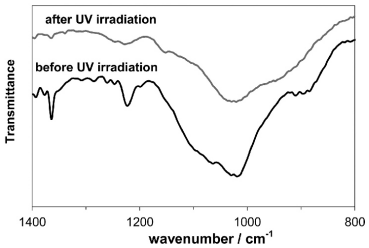

(f) FTIR spectrum of Octyl(H), before and after irradiation by UV light for 1 h.

Figure 7.2: *Adapted with permission from G. Soliveri et al., 2012, Vol. 116, pp. 26405-13. Copyright 2015 American Chemical Society.*

the exposure time in order to obtain a high contrast. Figure 7.2d and 7.2e report the variation of water and CH_2I_2 static CAs over the time of irradiation under UV-A lamp, for Octyl(H) (Figure 7.2d) and Octyl(F) (Figure 7.2e) layers, respectively. It is noteworthy that the behavior of the two hybrids is highly different, not only with respect to oleophobic performances, but also concerning the hydrophobicity. The Octyl(F) appears to be, as a whole, more stable under UV light. Furthermore, the behavior of CH_2I_2 CA in the two cases is completely different. The film covered by Octyl(H) shows a steep fall to oleophilicty, while in the case of Octyl(F), the repellency for CH_2I_2 is more permanent than hydrophobicity; this may be due to a different degradation way of the two layers.

FTIR measurements were performed to enlighten the presence of surface functionalizing groups. Figures 7.2f reports the comparison between the FTIR spectra of the Octyl(H) hybrid in two different conditions: as-prepared (black curve) and after being submitted to the photocatalytic lithography experiment (gray curve). The spectrum of the bare TiO_2 layer has been previously subtracted. The presence of siloxane gives rise to strong bands in the 800-1400 cm^{-1} and 2800-3000 cm^{-1} regions. Absorption peaks at 919-926 cm^{-1} are generally attributed in the literature to stretching vibrations of the Ti-O-Si bond[32, 33], while Si-O-Si stretching vibrations may occur from around 950 to 1150 cm^{-1}, overlapping the region of Si-O-C linkages (1090-1050 cm^{-1}). The peak at 1028 cm^{-1}, that could be attributed to the bending vibration of Ti-O-Si, is shifted at higher wavenumber after UV irradiation, probably because of the restoration of Ti-O-H bonds on the photodegradated film[34]. All bands relative to the siloxane molecule in the photocatalytically lithographed sample appear to be less intense than in the case of the fresh sample, suggesting a partial degradation of the organic molecules upon UV irradiation. However, while the bands relative to the Ti-O-Si and Si-O-Ti are still evident, peaks attributable to Si-C and C-H linkages (1126-1372 cm^{-1} and 2800-3000 cm^{-1}) are almost absent. The peaks associated with adsorbed water increase as a consequence of the disappearance of the hydrophobic siloxane monolayer. This observation may suggest that the photo-oxidation starts attacking the more external alkyl chains, while the polar Si-O-Ti and Si-O-Si bonds are less modified. An indirect oxidation mechanism involving $OH^{\bullet}$ radicals has been proposed as the dominant one for the degradation of monolayers attached at titanium dioxide. An indirect mechanism may, in our case, support the larger stability of the Octyl(F) molecule during the photocatalytic lithography experiments as shown in Figures 7.2d and 7.2e since the higher degree of polymerization of the Octyl(F) monolayer may result in a more difficult penetration of oxygen-containing species to the TiO_2 surface and thus in a slower oxidation kinetics. In addition, the strength of the C-F bonds, which are generally associated with strong chemical resistance, could contribute to the higher resistance toward oxidation.

7.2 Conclusion

In this chapter, wet impregnation was used to compare three distinct siloxanes (with different chemical nature), chemisorbed at laboratory-made TiO_2 nanoparticles, tuned to obtain superhydrophobic coatings. The use of siloxanes with fluorinated alkyl chains allowed the development of coatings that present, apart super hydrophobicity, oleophobic properties; that is extremely appealing from an applicative point of view.

The presence of the partially fluorinated chain relevantly modifies the attachment modes of the siloxane at the oxide surface. By solid-state ^{29}Si CP MAS NMR, the silicon atoms appear to be involved in one, two, or three bonds. For the unfluorinated hybrids, the prevalent structure is T^2 in which silicon is bound with two groups, either -O-Ti or the neighboring -O-Si groups. Furthermore, the increase in the length of the alkyl chain (from C8 to C18) provides ordered packing of the molecules with less degree of freedom.

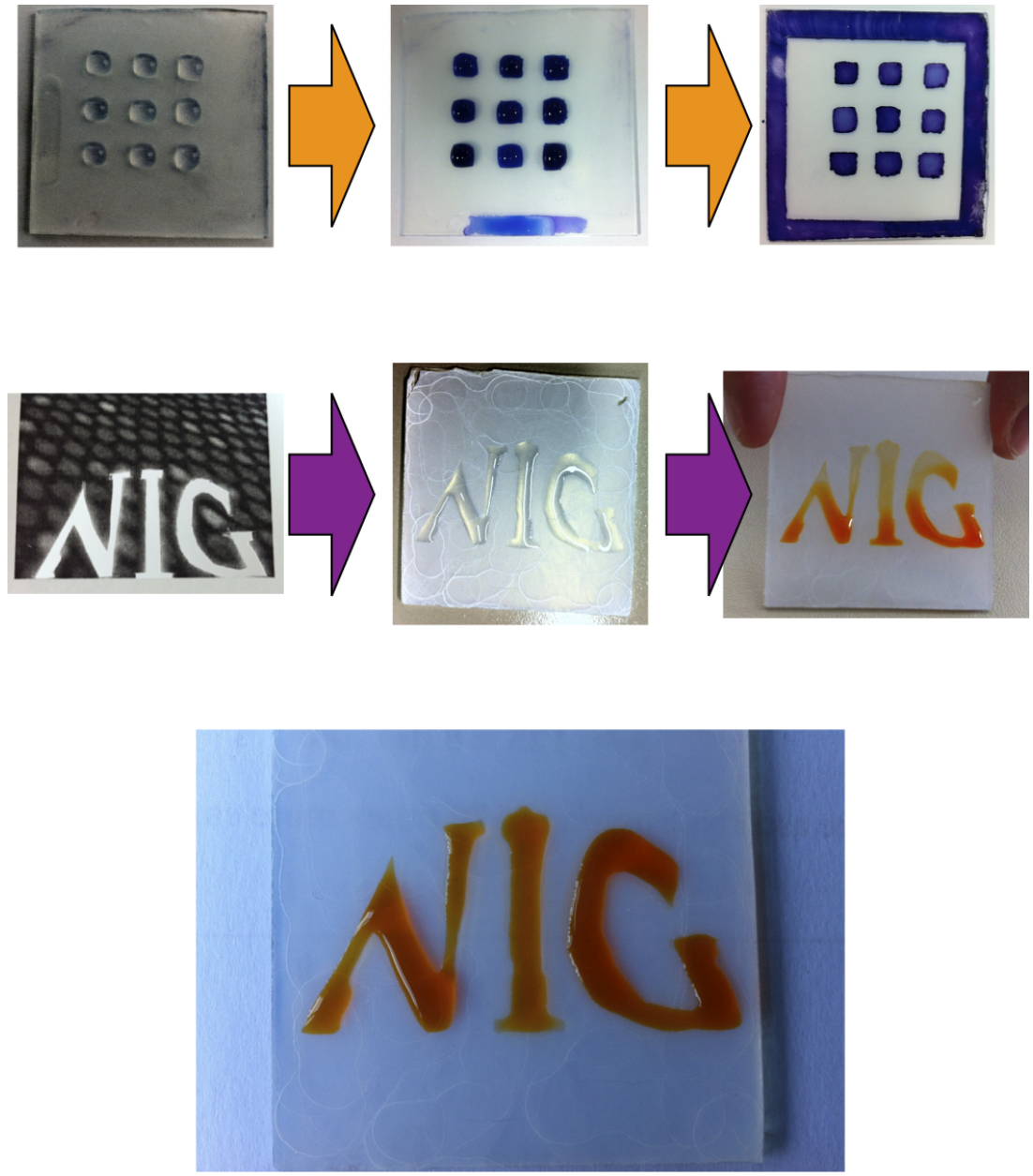

Figure 7.3: *Photo-catalytic lithography, step by step.*

This latter result of NMR analysis perfectly fits in the picture obtained by SFE determinations of the bare siloxanes, which indicated a larger disperse component for the C18 molecule. In the case of the fluorinated hybrids, the NMR picture appears to be appreciably modified, the siloxane adopting, preferentially, a polymeric organization with a prevailing T^3 structure and no T^1 component. The polymeric nature of the film, in the case of the fluorinated molecules, imparts strengthened stability to these hybrids, even when irradiated under direct UV irradiation, as shown by photocatalytic lithography experiments.

The semiconductor nature of the chosen crystalline oxide film, also promoted by its composite structure, reducing electrons and holes recombination, permits to obtain patterned surfaces by photocatalytic lithography, showing tunable degrees of hydro- and oleophilicity. Using the present approach, patterned surfaces with a superhydrophobic/superhydrophilic and oleophobic/oleophilic contrast can be obtained; the behavior critically depends to the type of siloxane employed. Such patterned surfaces are exploited to obtain the site selective adsorption of a dye. This approach can be utilized as well to obtain complex, hierarchical structures in which metal nanoparticles, polymers, or biological molecules could be site selectively attached to the surfaces.

7.3 Specific procedures

The adopted siloxanes were commercial products by Sigma Aldrich: trimethoxy(octadecyl)silane (OcDe(H)), triethoxy(octyl)silane (Octyl(H)), and 1H,1H,2H,2H-perfluorooctyl-triethoxysilane (Octyl(F)).

Self-cleaning tests, by methyl orange (dissolved in water) and methylene blue (dissolved in CH_2I_2), were performed on the titania films, prepared as reported in Appendix C. The siloxane-TiO_2 composite films were photocatalytically[35] litographed by irradiating with an iron halogenide lamp (Jelosil HG 500), emitting in the UV-A (see spectrum in Appendix C), in the presence of paper mask onto the TiO_2 film. The time of irradiation depended on the nature of the siloxane molecules. The irradiated areas could be wetted by water or CH_2I_2, and so colored by water or CH_2I_2 soluble dyes. The kinetics of the photodegradation of the siloxane on the TiO_2 was studied. During 2 h, the loss of hydrophobicity and oleophobicity was investigated by the CA variation of water and diiodomethane, respectively. In addition, the functionalized TiO_2 before and after UV irradiation was analyzed by Fourier transform infrared spectroscopy (FTIR) using a Jasco 4200 spectrometer, accessorized by attenuated total reflectance (ATR) module.

References

[1] A. Fujishima, X. Zhang, D. A. Tryk, *Surf. Sci. Rep.* **2008**, *63*, 515 –582.

[2] D. Meroni, S. Ardizzone, G. Cappelletti, M. Ceotto, M. Ratti, R. Annunziata, M. Benaglia, L. Raimondi, *J. Phys. Chem. C* **2011**, *115*, 18649–18658.

[3] P. Manoudis, I. Karapanagiotis, A. Tsakalof, I. Zuburtikudis, B. Kolinkeov, C. Panayiotou, *Appl. Phys. A* **2009**, *97*, 351–360.

[4] H.-C. Liao, C.-H. Lee, Y.-C. Ho, M.-H. Jao, C.-M. Tsai, C.-M. Chuang, J.-J. Shyue, Y.-F. Chen, W.-F. Su, *J. Mater. Chem.* **2012**, *22*, 10589–10596.

[5] K. Liu, M. Cao, A. Fujishima, L. Jiang, *Chem. Rev.* **2014**, *114*, 10044–10094.

[6] Q. Liang, Y. Chen, Y. Fan, Y. Hu, Y. Wu, Z. Zhao, Q. Meng, *Appl. Surf. Sci.* **2012**, *258*, 2266 –2269.

[7] M. Järn, F. J. Brieler, M. Kuemmel, D. Grosso, M. Lindn, *Chem. Mater.* **2008**, *20*, 1476–1483.

[8] D. Meroni, S. Ardizzone, U. Schubert, S. Hoeppener, *Adv. Funct. Mater.* **2012**, *22*, 4376–4382.

[9] S. Ardizzone, C. Bianchi, G. Cappelletti, M. Ionita, A. Minguzzi, S. Rondinini, A. Vertova, *J. Electroanal. Chem.* **2006**, *589*, 160 –166.

[10] H. Su, T. Wang, S. Zhang, J. Song, C. Mao, H. Niu, B. Jin, J. Wu, Y. Tian, *Sol. State Sci.* **2012**, *14*, 677 –681.

[11] Y. Shi, S. Cheng, S. Quan, *J. Power Sources* **2012**, *209*, 130 –140.

[12] Y. Paz, *Beilstein J. Nanotech.* **2011**, *2*, 845–861.

[13] G. Panzarasa, G. Soliveri, K. Sparnacci, S. Ardizzone, *Chem. Commun.* **2015**, *51*, 7313–7316.

[14] M. Dahbi, D. Violleau, F. Ghamouss, J. Jacquemin, F. Tran-Van, D. Lemordant, M. Anouti, *Ind. Engin. Chem. Res.* **2012**, *51*, 5240–5245.

[15] E. Sawada, H. Kakehi, Y. Chounan, M. Miura, Y. Sato, N. Isu, H. Sawada, *Composites B* **2010**, *41*, 498 –502.

[16] D. Wang, X. Wang, X. Liu, F. Zhou, *J. Phys. Chem. C* **2010**, *114*, 9938–9944.

[17] J. Yang, Z.-Z. Zhang, X.-H. Men, X.-H. Xu, *J. Disp. Sci. Tech.* **2011**, *32*, 485–489.

[18] M. Zhang, T. Zhang, T. Cui, *Langmuir* **2011**, *27*, 9295–9301.

[19] H. Kim, K. Noh, C. Choi, J. Khamwannah, D. Villwock, S. Jin, *Langmuir* **2011**, *27*, 10191–10196.

[20] T. Boiadjieva, G. Cappelletti, S. Ardizzone, S. Rondinini, A. Vertova, *Phys. Chem. Chem. Phys.* **2004**, *006*, 3535–3539.

[21] R. Penn, J. F. Banfield, *Geochimica et Cosmochimica Acta* **1999**, *63*, 1549 –1557.

[22] D. Meroni, S. Ardizzone, G. Cappelletti, C. Oliva, M. Ceotto, D. Poelman, H. Poelman, *Catal. Today* **2011**, *161*, 169–174.

[23] D. K. Owens, R. C. Wendt, *J. Appl. Polym. Sci.* **1969**, *13*, 1741–1747.

[24] G. Cappelletti, S. Ardizzone, D. Meroni, G. Soliveri, M. Ceotto, C. Biaggi, M. Benaglia, L. Raimondi, *J. Coll. Inter. Sci.* **2013**, *389*, 284 –291.

[25] S. Lee, J.-S. Park, T. R. Lee, *Langmuir* **2008**, *24*, 4817–4826.

[26] T. Young, *Phil. Trans.* **1805**, *95*, 65–87.

[27] A. B. D. Cassie, S. Baxter, *Trans. Faraday Soc.* **1944**, *40*, 546–551.

[28] D. Öner, T. J. McCarthy, *Langmuir* **2000**, *16*, 7777–7782.

[29] S. Huh, H.-T. Chen, J. W. Wiench, M. Pruski, V. S.-Y. Lin, *Angew. Chem. Int. Edit.* **2005**, *44*, 1826–1830.

[30] D. Kovacek, Z. Maksic, S. Elbel, J. Kudnig, *J. Mol. Struct.* **1994**, *304*, 247 –254.

[31] K. Nakata, A. Fujishima, *J. Photochem. Photobio. C* **2012**, *13*, 169 –189.

[32] P. Xu, H. Wang, R. Tong, R. lv, Y. Shen, Q. Du, W. Zhong, *Polym. Degrad. Stab.* **2006**, *91*, 1522 –1529.

[33] G. Mink, I. Bertti, L. Nmeth, G. Gti, M. Mohai, T. Szkely, *Surf. Inter. Anal.* **1988**, *12*, 262–268.

[34] H. Haick, Y. Paz, *J. Phys. Chem. B* **2003**, *107*, 2319–2326.

[35] S. Ardizzone, C. L. Bianchi, G. Cappelletti, A. Naldoni, C. Pirola, *Envir. Sci. Tech.* **2008**, *42*, 6671–6676.

Part III

Titanium dioxide thin films

Chapter 8

Electrochemically assisted deposition of titania films

In the recent years, transparent oxide films have been extensively investigated for numerous applications. The tuning of mechanical, optical and electrical properties represents a must in many different fields, from electronics to building material manufacture, to optics. In this contest, titanium dioxide, thanks to its unique properties (described before and in Appendix A), is acquiring a leading position in the development of present and future technologies, like smart widows[1], anti-fogging mirrors[2], optically transparent electrodes[3] and solar cells[4, 5]. Recently, TiO_2 based photoactive layers have been also intensively studied due to their vast potential market in fields like photocatalytic environmental remediation, indoor air purification and water disinfection[6–12].

The availability of film with highly desirable technological properties, like smoothness, full transparency and robustness, will drive to the use of such layers for more sophisticate applications with critical impact to everyday life[13]. Exploiting the semiconductor nature of the TiO_2 , proof of concept self-cleaning SERS active sensors[14] or nano-structurated lithographic protocols[8] are only few of the most recent reports that will bring dramatic advances in many different fields connected to everyday life (analytical chemistry, bio-medicine, electronics, etc.)[15].

This third part will show the last three years work about the development of a synthetic procedure for the facile production of a transparent, smooth, robust and photoactive TiO_2 thin film and their tremendous impact in fields such as electrochemistry and polymer brushes science. Chapter 8 will describe the development of a method for the synthesis of TiO_2 thin films supported on inorganic substrates, their morphological, optical and electronic characterizations, their photoactivity and proof of concept applications in self-cleaning surfaces and photo-electro polymerization. In the Chapter 9, advanced lithographic techniques using TiO_2 will be shown, from the formation of hydrophobic/hydrophilic micrometric patterns till the rise of 3D complex polymer brush structures, by the innovative use of direct and remote photocatalysis. In Chapter 10, the challenge of the TiO_2 layer grown on an organic macromolecular substrate will be dealt with; the critical issue of self-cleaning in polymers for the building industry forces us in this direction. Eventually, Chapter 11 will detail the engineering of an electroanalytical sensor for the determination of neurotransmitters in real matrices; such sensor, covered by an *ad hoc* TiO_2 layer, pioneers the field of self-cleaning electrodes for cyclovoltammetric analysis.

Transparent crystalline TiO_2 films may be obtained by rather complex techniques requiring expensive equipments, such as magnetron sputtering[16], atomic layer deposition[17], or ion engineering meth-

ods[18]. Other techniques, like dip coating[19], layer-by-layer deposition[20], Langmuir-Blodgett deposition[21] and spin-coating[22, 23], often used in literature because of their simplicity, have several limitations, such as the limited number of operational parameters that can be modified to tailor the film properties and their inadequacy to produce continuous large-area films or cover non-flat surfaces.

In this chapter, a novel approach for the deposition of transparent TiO_2 films, based on the electrochemically assisted deposition of a titania sol onto inert substrates, is reported. Films obtained by the adopted procedure were closely compared with the dip coated ones obtained on the same substrates and using the same sol. First, the morphological, optical, and mechanical properties of the resulting films were investigated. Then, the photoactivity of the film was proved by degradation tests of VOCs and simultated dry stain. Eventually, the versatility of the technique is employed to obtain materials with largely different applications concerning, on one side, the modulation of the surface wettability and on the other side, photo-electrochemical applications. Furthermore, a deep investigation of the applicability of such layer in photo-catalytic lithography will be described in the next chapter.

8.1 Results and discussion

8.1.1 Synthesis procedure and characterization

The sol synthesis and film deposition are fast and facile, and can be performed under laboratory conditions without any control of the humidity (see Appendix C). Several tests were performed modulating the acid content of the sol. The reported conditions (0.11 H^+/Ti molar ratio) give rise to a sol that remains stable and transparent for several weeks, whereas both higher and lower acidity conditions determine lower stability of the sol. The film formation takes place by migration and deposition of either soluble titania clusters or, more probably, of oxide nuclei that are positively charged due to the acidic conditions adopted during the sol preparation (TiO_2 isoelectric point in water is around 6). In this respect, the cell geometry was optimized to obtain a homogeneous film by employing two Ti electrodes with a suitable orientation and distance from the film support. With respect to traditional electrodeposition [24], in the present case the film formation does not occur onto the electrodes, but onto an inert (*i.e.* uncharged) substrate, which could thus be either conductive or un-conductive. Moreover, the adopted technique does not require any expensive equipment and the final film thickness and morphology can be controlled by varying the working parameters. A calcination treatment was performed after the film deposition to improve the mechanical robustness and film adhesion to the substrate. Furthermore, the calcination promotes the complete removal of the organic species present in the sol and promote the crystallinity grow (see below).

The resulting films are transparent and homogeneous (Figure 8.1). Optical microscopy reveals that the TiO_2 films deposited on glass substrate by electroassisted deposition are far more uniform and defect-free than films obtained by dip coating into the same titania sol (Figure 8.2a, 8.2b). Moreover, cyclic voltammograms show that the dip coated sample presents a higher resistivity (Figure 8.2c). Indeed, the film preparation procedure is known to influence the conductivity of thin films by influencing the density of crystallographic defects and grain barriers[26]. On the grounds of the presented characterizations, dip coating seems to lead to much more heterogeneous and less transparent films.

Grazing angle XRD (Figure 8.1d) revealed pure anatase film, with an average crystallite dimension of 17 nm. That is in agreement to the findings of Violi et al.[27] who obtained highly crystalline anatase for dip coated films from ethanol based sols.

Film morphology was investigated by SEM and AFM analyses on a two-layer substrate. Atomic force

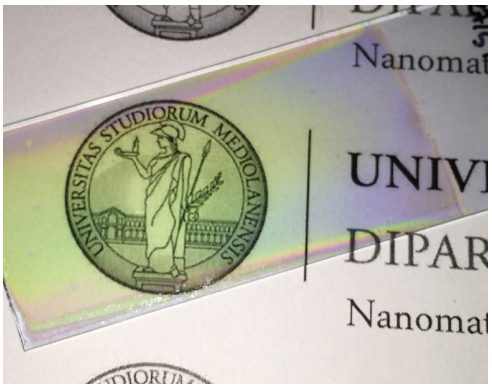

(a) Photo of the transparent film.

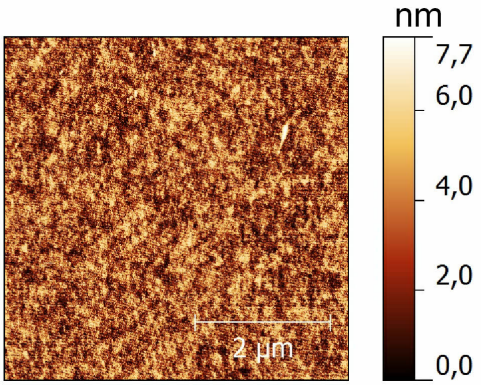

(b) Atomic force microscophy, tapping mode.

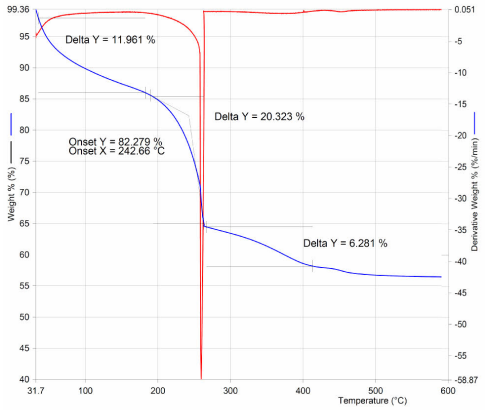

(c) Thermgravimetric analysis of the sol.

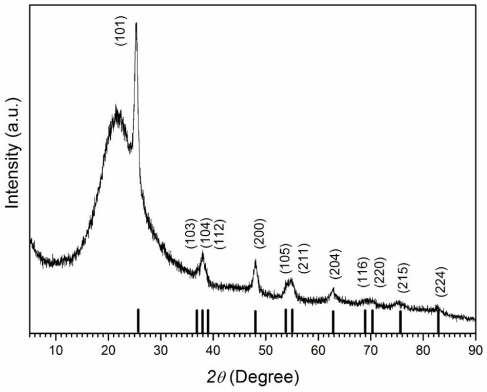

(d) X-ray diffractio analysis, grazing angle.

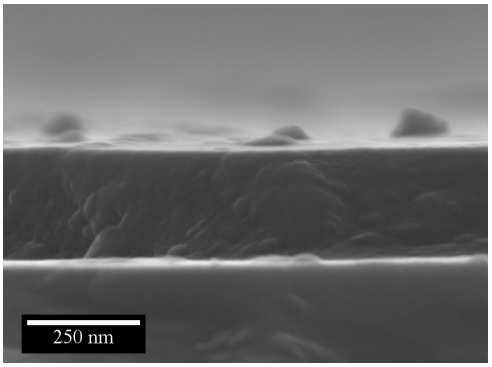

(e) Scanning electrom microscophy, cross section.

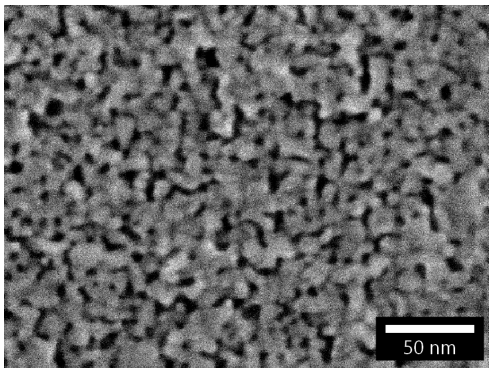

(f) Scanning electron microscophy, top view.

Figure 8.1: *Characterization of 2-layer titania film supported on glass[25].*

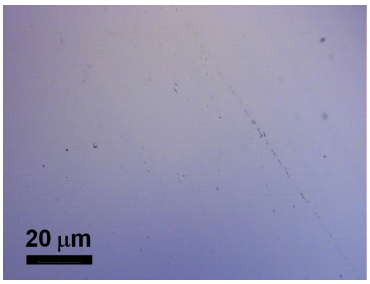

(a) Optical microscope images of TiO_2 films deposited by electrochemically assisted process.

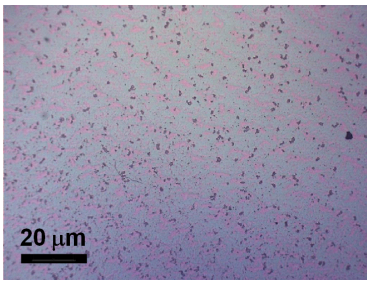

(b) Optical microscope images of TiO_2 films deposited by dip coating.

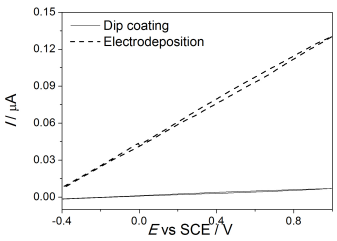

(c) Comparison of electroassisted deposition and dip coating on glass laminas: cyclic voltammograms at 50 mV s^{-1}.

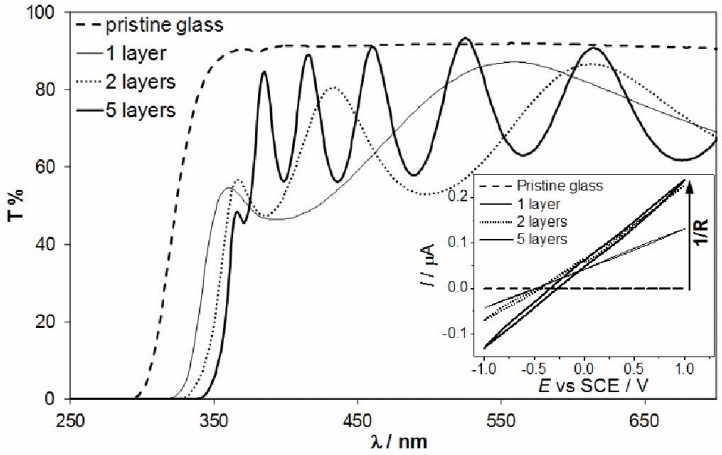

(d) UV-visible spectra and cyclic voltammograms at 50 (mVs^{-1})(inset) of the pristine glass and TiO_2 films as a function of the number of layers.

Figure 8.2: *Electrochemically assisted deposition vs dip coating and number of layers[25].*

TiO_2 layers	Ave. Trasm.	Hardness	Adhesion
1	71 %	3H-4H	0
2	78 %	4H-5H	0
5	75 %	4H-5H	0

Table 8.1: *TiO_2 film properties: average transmittance in the 400-800 nm range, hardness according to the Wolff Wilborn test (hardness increasing going from 8B to 10H) and adhesion (0 stands for top adhesion, 5 stands for poor adhesion).*

microscopy picture (Figure 8.1b) shows smooth film, with a RMS roughness of about 0.6 nm. SEM top analysis on sample areas of the layer demonstrated that the TiO_2 layer is smooth, homogeneous and completely free of cracks. At higher magnification (Figure 8.1f), the surface seems to have a(n expected) porosity, with average pore diameter between 5 and 15 nm. The effect of the number of layers on the film morphology was also studied. The film thickness could be evaluated by cross section images. In order to determine the thickness of the central part of the layer, the film and its support were broken in half and cross-section images were taken of the two portions. In the case of the 2-layer film, a uniform thickness of around 200 nm was determined (Figure 8.1e).

All obtained films are highly transparent as verified by UV-visible spectroscopy. The average transmittance in the visible region layers is about 75% (compared with 92% of pristine glass used as a support, Figure 8.2d). The UV-visible spectra present clear interference fringes between 350 and 700 nm, which are a characteristic feature of transparent thin films. They indicate that uniform and highly transparent films were formed onto the glass substrates[18]. The adsorption edges of the TiO_2 films were around 350-380 nm and are shifted to higher wavelengths with increasing the number of layers due to a quantum size effect related to the increasing number of calcination steps. Another effect related to the increasing number of layers was the decrease in film resistance, evaluated by cyclic voltammograms (Figure 8.2d, inset). Films showed good electrochemical stability as they remain unaltered after 100 consecutive cycles.

In real life applications, films may need to survive harsh conditions, hence robustness are required. The films exhibit excellent chemical and mechanical stability. The deposited layers, actually, resist unaltered to prolonged sonication in several solvents (water, alcohols, apolar solvents) and show a good resistance towards sand abrasion. Wolff Wilborn tests were performed on the grounds of ISO 15184 standard (see Appendix C), regarding the determination of film hardness for coatings: in this test, the hardness is classified with a scale of 8B to 10H. For all the present samples, the hardness is high (H type) and it remains high and invariant after the deposition of the second layer (Table 8.1). Hardness values for thin films, obtained by the present standard procedure, are not frequently reported in the literature. The only data on comparable systems are those reported by Kesmez et al.[11] in the case of silica-titania coatings. The films, obtained under variable conditions, showed hardness values in the range 5B-3H, in any case lower than the present ones. Adhesion quality was determined according to ISO 2049 (see Appendix C), by crisscrossing the layer with a razor blade in order to form small squares to which an adhesive tape was then pressed and removed applying a constant force under an angle of 60°. The tests show optimal adhesion of the present titania films since no appreciable detachment of the TiO_2 layers from the substrate could be appreciated. Both the monolayer and the multilayers performed equally well as far as adhesion is concerned (Table 8.1).

8.1.2 Photoactivity and photocatalysis

Photo-induced superhydrophilicity The semiconductor features of titania promote a photo-induced superhydrophilic transition of the layers upon irradiation. Figure 8.3a shows the variation of the water contact angle on the TiO_2 films *vs* the irradiation time under simulated solar light. Before irradiation the TiO_2 surface exhibits the expected hydrophilicity, with water contact angles of about 30°. Upon simulated solar irradiation, after only 20 minutes, the contact angle drops to zero, the water spreading uniformly over the surface. The mechanism for this process was first proposed by Fujishima *et al.*[28, 29] and attributed to the reconstruction of the surface hydroxyl groups ensuing the formation of oxygen vacancies at the surface of the semiconductor upon illumination. The motivation behind this effect is still under discussion (See Appendix A and [6]). It can be underlined that the present superhydrophilic transition is particularly fast, even if compared to similar trends obtained under UV irradiation[30, 31]. This fact, besides evidencing the high photo-activity of the material under solar irradiation, allows to assess the absence, at the surface of the film, of residual organic impurities from the synthesis. In fact, the presence of organic adsorbates is reported to severely slow down the superhydrophilic transition for titania[9].

The observed superhydrophilicity of the present films, produced very fast and even under solar light, could be exploited to obtain antifogging surfaces in which moisture or water spread evenly, without forming droplets which might impair the visual clarity.

Degradation of dry stains The degradation of long chain organic moieties (Octyl(H), Figure 5.1, Chapter 5) adsorbed at the photocatalyst surface was carried out to simulate the removal of stains by fingerprints/oily liquids. Here, siloxanes were selected as model compounds, also due to their capability of forming stable and chemisorbed bonds with oxides[32, 33]. Homogeneous and reproducible siloxane layers were deposited onto the transparent films via chemical vapor deposition, as reported in Appendix C.

The degradation of the organic moieties was monitored by measuring the water contact angle as a function of irradiation time (Figure 8.3b). The photocatalytic degradation of siloxane molecules leads to the formation of more hydrophilic moieties, by progressively oxidizing the terminal part of the alkyl chain, resulting in a decrease of the observed water contact angle[34–36]. When the siloxane degradation is completed, the superhydrophilic behavior of the pristine oxide is restored. Figure 8.3c reports the water contact angle images of the siloxane treated TiO_2 layers before and after UV irradiation, along with the correspondent FTIR curves. Prior to light irradiation, strong bands in the 2800-3000 cm^{-1} region are appreciable, which can be attributed to the stretching vibrations of C-H bonds of the grafted siloxane molecules[37]. On the contrary, after light irradiation, these bands are completely absent, supporting the complete degradation of the siloxane organic chain. The effect of UV and simulated solar irradiation were compared. Interestingly, the complete degradation of the siloxane layer takes place in a very short reaction time for both UV and simulated solar irradiation (Figure 8.3b). The present materials thus exhibit substantial self-cleaning properties even in indoor irradiation conditions.

Degradation of volatile organic compounds (VOCs) Ethanol was selected as model VOCs to test the photocatalytic activity, with respect to air remediation, of the present titania layers. Ethanol is an important atmospheric pollutant, whose emissions are rising owing to the increasing relevance of biofuel usage[38]. Moreover, ethanol emissions lead to an increase in the atmospheric levels of acetaldehyde[38, 39], its main degradation intermediate, which is a far more toxic compound and contributes to ozone pollution[40, 41]. Ethanol emissions may thus impact the ozone-forming potential of the atmosphere and have been reported to be precursor to secondary aerosols[40]. Moreover, acetaldehyde and ethanol

are among the most significant indoor VOCs. Ethanol is one of the main components of detergents and other household products[42, 43]. Acetaldehyde indoor concentration derives from both ethanol degradation and from its direct released by several indoor sources (building materials, hardwood, plywood, laminate floorings, adhesives, paints and solvents, smoking, household products, and the use of un-vented fuel-burning appliances)[44]. During the gas-phase photocatalytic degradation of ethanol, several intermediates, besides the most abundant acetaldehyde, have been identified in the literature: formaldehyde, formic and acetic acid[45, 46]. In the present chapter, the disappearance of ethanol, the parallel formation of acetaldehyde and the final formation of CO_2, as the result of complete mineralization, were followed during the photocatalytic tests, by means of a gas-chromatographic system. The carbon balance was always complete at the end of the reaction. No other intermediate, besides acetaldehyde, was analyzed due to the difficulty in quantifying trace amounts. Reactions were performed under both UV and simulated solar light irradiation.

Under UV irradiation (Figure 8.3e), the ethanol degradation is accomplished in 75 minutes while its complete mineralization, implying the formation and subsequent oxidation of acetaldehyde to CO_2, requires 120 min. Acetaldehyde concentration has the typical dependence with time expected for a reaction intermediate, going from zero to a maximum value and again to zero. Figure 8.3d reports also the trend observed under simulated solar irradiation. A reaction route implying the intermediate formation of acetaldehyde is appreciable, although the reaction does not reach completion in the investigated reaction time. However, the mineralization percentage is high, reaching 87% after 210 minutes (Figure 8.3f). Table 8.2 (2nd and 3rd columns) shows the initial rates determined using the method of initial decay[45] for the present laminas under UV and solar irradiation and the CO_2 percentage after 120 min reaction time. Standard deviations were obtained by comparing 5 independent experiments: $\sigma(r_{EtOH}) = 0.2$ $(mgL^{-1}min^{-1})$; $\sigma(\%CO_2) = 0.6\%$. The table reports also the data relative to the same reaction, performed by using as active material, the well-known reference photocatalyst P25 (Evonik). In this latter case, spin-coated films were prepared starting from dispersions of the powder in $i-PrOH$ and by matching the geometric area of the support and the TiO_2 mass with those of the electrodeposited layers. The electrodeposited films seem to exhibit a faster ethanol degradation and better mineralization with respect to P25 under both irradiation sources (Figure 8.3f). However, a direct comparison cannot be made due to the inherent differences in the nature of deposited films and powders, since the latter tend to agglomerate giving rise to inhomogeneous films.

The photocatalyst deactivation in time represents a major concern for the commercial application of self-cleaning/photocatalytically active materials. Piera and coauthors studied in detail the deactivation of TiO_2 films during the photocatalytic gas phase degradation of ethanol[46]. They found that the presence of water and of carbonaceous species, produced upon ethanol mineralization, cause the deactivation of the photocatalyst. Catalyst deactivation seems to be related to reactant adsorption capability, since in the case of P25 a very relevant loss of ethanol adsorption (43%) was observed after the first photocatalytic run, even in the case in which no organic species are left in the gas phase[46]. In the present case, the used laminas were first employed in a second degradation run without any regeneration treatment and the photocatalytic activity appeared to be invariant within the experimental error. In the case of P25 Evonik the same procedure lead to a loss of activity of about 8% after one single run. Further the electrodeposited laminas were submitted to repeated photocatalytic tests (7 tests without any regeneration of the photocatalyst) under UV light finding a total loss of activity of 7%. These results can be considered to be very satisfying also taking into account the very large ethanol amount adopted in the experiments in comparison with the potential indoor pollution by ethanol.

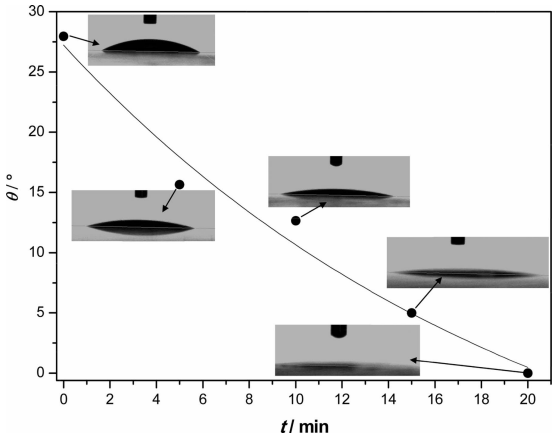

(a) Water CAs of bare TiO_2 film as a function of the irradiation time of solar irradiation.

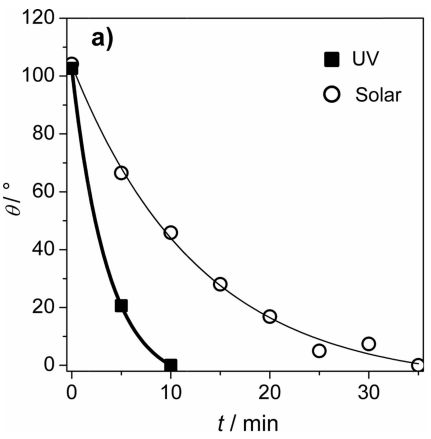

(b) Photocatalytic degradation of octylsilane grafted to TiO_2 film.

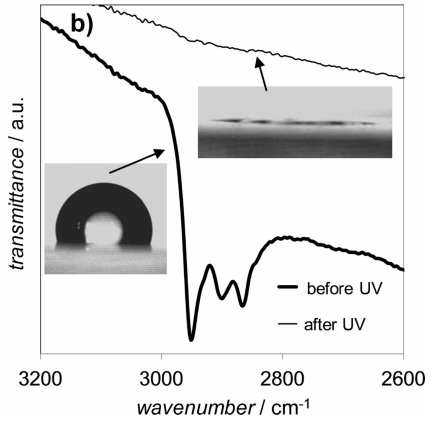

(c) Octylsilane grafted on TiO_2 film before and after irradiation: wCA and FTIR.

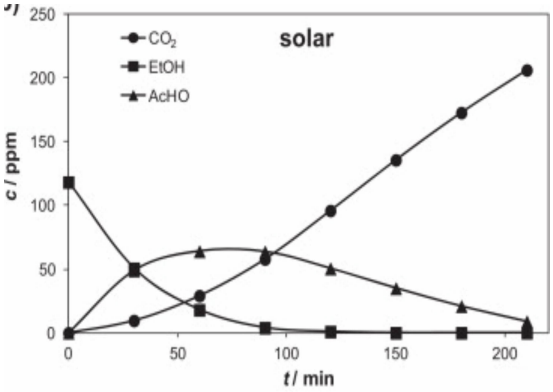

(d) Ethanol, acetaldehyde and CO_2 concentration tests of 2-layer TiO_2 film under solar irradiation.

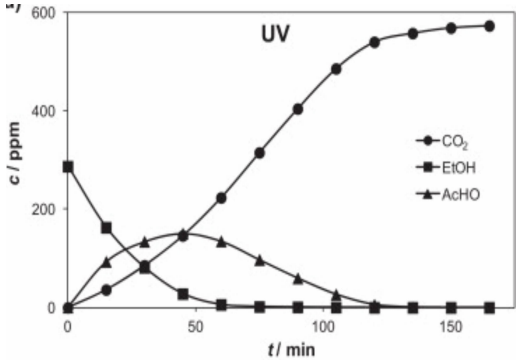

(e) Ethanol, acetaldehyde and CO_2 concentration tests of 2-layer TiO_2 film under UV irradiation.

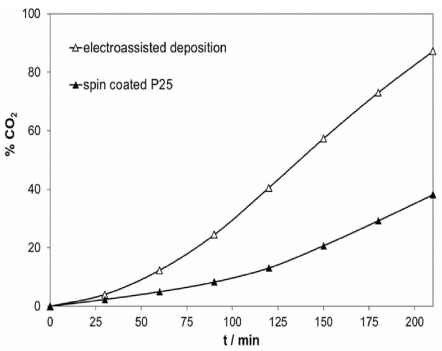

(f) Photocatalytic tests: comparison between 2-layer TiO_2 film and P25.

Figure 8.3: *Photoactivity of TiO_2 films. Reprinted from Catalysis Today, Vol. 230, A. Antonello et al., Photocatalytic remediation of indoor pollution by transparent TiO_2 films, pp. 35-40, Copyright 2015, with permission from Elsevier.*

		$\mathbf{r}_{EtOH}$**(t=30 min)** $mgL^{-1}min^{-1}$	$\mathbf{\%CO_2}$**(t=120 min)** $mgL^{-1}min^{-1}$
Dark adsorption		0.7	0.4
UV	Photolysis	0.3	6.3
	Electroass. Dep.	6.9	94.0
	P25	5.9	70.3
Solar	Electroass. Dep.	2.3	40.5
	P25	1.9	13.1

Table 8.2: *Initial rate of ethanol degradation (r_{EtOH}) and percentage of complete mineralization after 120 min ($\%CO_2$) of the photocatalytic tests under UV and simulated solar irradiation for films by electroassisted deposition and by deposition of a commercial P25 powder. Data relative to dark absorption and UV photolysis tests are also reported. Standard deviation of r_{EtOH}=0.2 (mg L^{-1} min^{-1}) and of $\%CO_2$=0.6. Photolysis under solar irradiation was not appreciable.*

8.1.3 Further application

The possibility to obtain homogeneous transparent films onto several kinds of technologically relevant substrates was exploited to produce advanced materials for widely different innovative applications. Here, we present applications related, on one hand, to the modulation of the surface wettability and, on the other hand, to the photoelectrochemical response of the TiO_2 layers.

Wettability modulation The wetting properties of the present layers can be modulated over a wide range, from high hydrophilicity to enhanced water and oil repellency, obtaining materials exhibiting either antifogging or antistain properties. The semiconductor character of TiO_2 leads to interesting properties such as its UV-induced superhydrophilicity[6]. Such films show marked superhydrophilic properties. For instance, Figure 8.4a presents the results obtained on a 2-layer TiO_2 deposited onto a glass support. Before UV irradiation, the TiO_2 surface exhibits ordinary hydrophilicity, with water contact angles around 40° (Figure 8.4a(I) and inset). Instead, after UV irradiation, the water spreads evenly across the surface (II). The photo-induced superhydrophilic conversion was observed to reach completion (water contact angle no more measurable) after less than 15 minutes at a UV light intensity of 30 ($mW\ cm^{-2}$). No change in color was observed even after prolonged UV irradiation. This characteristic of our films was exploited to obtain antifogging surfaces (III, IV). The fogging of surfaces like mirrors and glass occurs when humid air cools down on these surfaces, forming water droplets of micrometer to millimeter size. These droplets scatter, reflect, or refract light randomly, thus impairing the visual clarity (III). When a superhydrophilic surface is exposed to moist air, the water droplets spread forming a very thin layer that evaporates quickly (IV). Instead, if the amount of water is larger, then it forms a sheet-like layer (II). In both cases, visual clarity is markedly improved with respect to ordinary hydrophilic surfaces.

On the other hand, our TiO_2 films can be used to enhance the water/oil repellency of technologically relevant underlying materials, upon functionalization with siloxanes. As shown previously, siloxanes are able to form durable bonds with oxide surfaces, leading to the formation of an organic layer that effectively modulates the oxide wetting properties[32–34]. Here, the case of an Al foil is presented due to the relevant concern connected to the protection from corrosion of light metal alloys (*e.g.*, Al and Mg alloys) with alternative chromate-free coatings[47, 48]. A fluorinated siloxane (Octyl(F), Figure 5.1, Chapter 5) was employed to functionalize a TiO_2 film deposited onto a roughened Al lamina (Figure 8.4b II, IV). By comparison, the case of a bare Al lamina functionalized by Octyl(F) is reported (I, III). The functionalized materials were tested for their anti-stain properties with respect to dye solutions in aqueous or apolar solvent. In these tests, a drop of liquid was placed over the surface (I, II), then the substrate was tilted

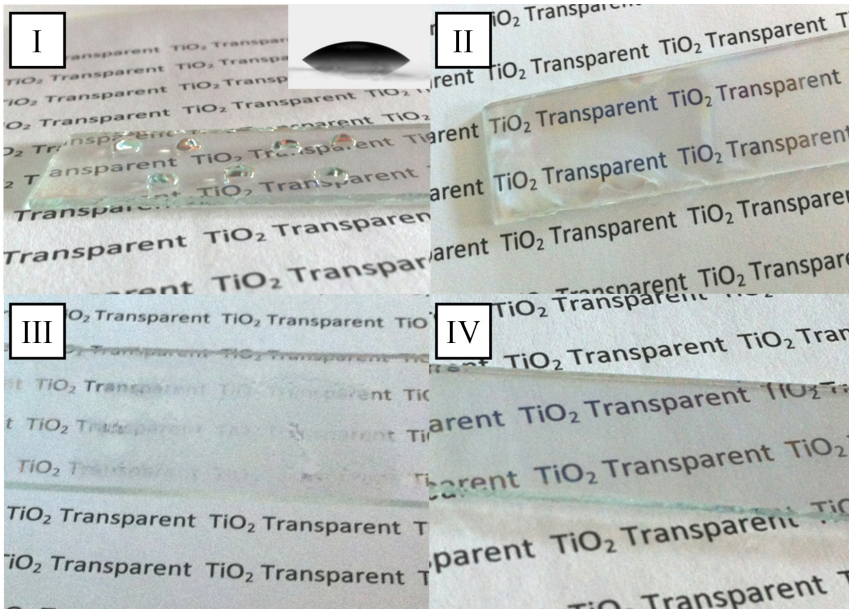

(a) Pristine wettability (I), UV-induced superhydrophilicity (II) and antifogging properties (III, IV) of TiO_2 films on glass: water droplets/condense on the films before (I, III), and after (II, IV) UV irradiation. Inset: water contact angle on TiO_2 films before UV irradiation.

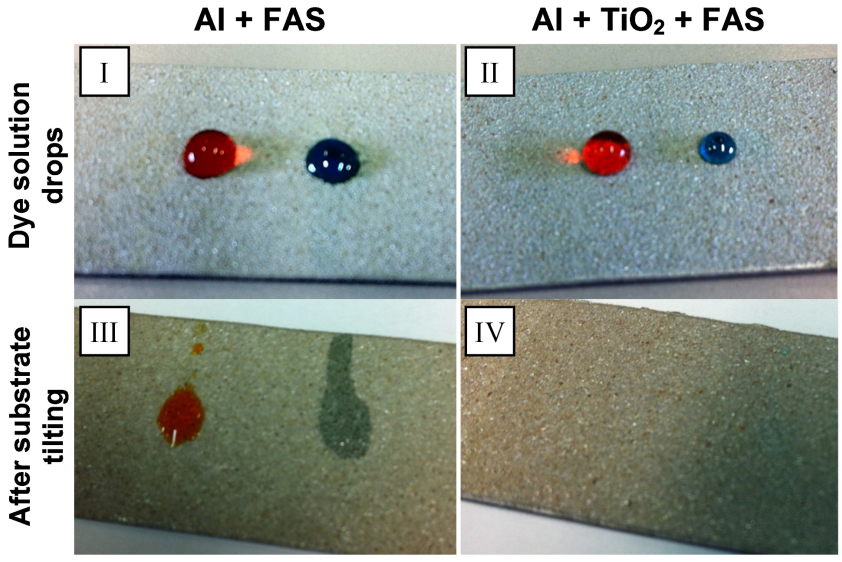

(b) Antistain tests with respect to dye solutions (methyl orange in water and methylene blue in CH_2I_2) performed on a rough Al lamina treated with Octyl(F) (I, III), and on the same substrates coated with TiO_2 and functionalized with Octyl(F) (II, IV).

Figure 8.4: *Wettability modulation[25].*

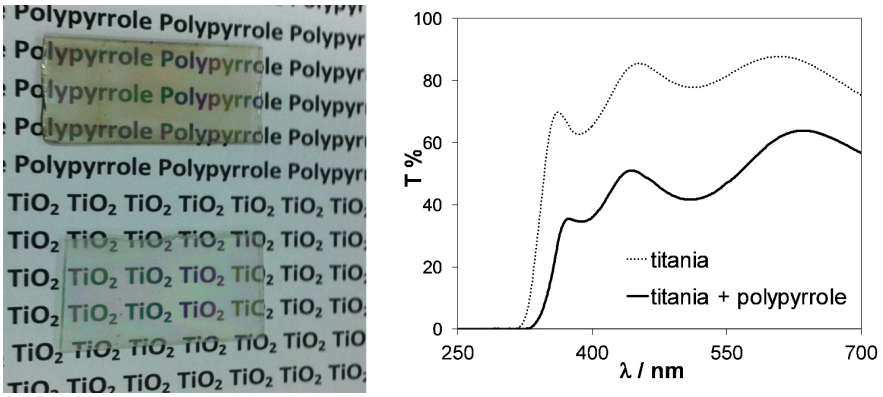

(a) Bare and polypyrrole-coated TiO_2 films on glass, photo.

(b) Bare and polypyrrole-coated TiO_2 films on glass, UV-visible spectra.

Figure 8.5: *Photoelectrochemical applications[25].*

to remove the droplet (III, IV). In the case of the bare Al substrate functionalized with Octyl(F), no antistain properties were observed since both test liquids stained the surface (III). The situation changed completely when the Al lamina was coated by a TiO_2 film prior to the functionalization with Octyl(F). In this case, the combined action of the texture of the film and of the features of the functionalizing molecule induced excellent antistain properties with respect to both test liquids (IV). The TiO_2 layer provides both a nanometer scale roughness, which is essential to impart efficient and stable antistain properties[49], and a good surface hydroxylation, necessary to give rise to a uniform and dense siloxane monolayer.

Photoelectrochemical applications A further field of great interest, due to its important application, is the photo-electrochemistry. Here, the TiO_2 thin film, exploiting its photocatalytic activity under UV irradiation, was used to activate the synthesis of conductive polymers. TiO_2 films on inert, unconductive glass substrate were adopted to induce the photoelectrochemical polymerization of conductive polymers, such as polypyrrole (PPy). The production of TiO_2 PPy composites on transparent conductive supports by either electro or photopolymerization has been reported in the literature [1, 50, 51] for applications such as hole transporting materials in dye-sensitized solar cells[52]. In the present work, the conduction features of this TiO_2 films allowed the deposition of the polypyrrol even in the absence of a conductive support. Pyrrole was photoelectrochemically polymerized on 2- and 5-layer TiO_2 films, obtaining very similar results. The reported results are relative to 2-layer TiO_2 films. Polypyrrole formation is evident, since after deposition, the film acquires a brownish color (Figure 8.5a), observed also by UV-Visible spectroscopy (Figure 8.5b), although the film preserves its transparency. Moreover, the adsorption of monomer was separately investigated, excluding that it could cause differences in color and in the UV-Vis data. Photo and electrochemical polymerization were also studied separately to demonstrate the efficiency of the combined process. In particular, the electrochemical polymerization gives no clear change in film color and in UV-Vis spectrum, while films obtained by photopolymerization have a less intense color than those obtained by photoelectrochemical polymerization. In conclusion, a synergistic effect occurs in the combined process, leading to more continuous and homogeneous polymer surfaces[50, 51].

8.2 Conclusion

A simple fabrication procedure of TiO_2 transparent films based on electrochemically assisted deposition was demonstrated. This deposition procedure can be applied to manifold substrate shapes and types, both the conductive and nonconductive. The obtained films exhibited homogeneous morphology, smoothness, high transparency, and good mechanical properties, thus representing promising materials for real life applications exploiting the TiO_2 semiconductor properties. A very fast light-induced superhydrophilicity is observed even under solar irradiation, which could be exploited for efficient antifogging mirrors or lenses. The titania layers showed excellent photocatalytic activity in both tested systems under UV and simulated solar irradiation, giving rise to the complete mineralization of VOCs and the removal of adsorbed stains. The presented stable and transparent TiO_2 layers thus represent promising materials for photocatalytic windows and coatings. With respect to classical commercial nano-powders, the present robust films allow to overcome the health concerns associated with volatile nanostructured materials.

Moreover, antistain surfaces were successfully obtained upon functionalization of the TiO_2 film by siloxanes. The successful modulation of the wetting properties of the obtained films bears relevance to several fields, such as the protection against corrosion of metals and alloys and in the antifouling of electrode/sensor surfaces. The TiO_2 activity was also exploited to fabricate TiO_2 -polypyrrole composite materials by a photo-electrochemical polymerization of pyrrole onto the titania films.

The next chapters are going to relate the applicability of such versatile procedure; the most recent successes in the using those TiO_2 thin films will be described further on, in fields ranging from lithography to sensoring.

8.3 Specific procedures

Characterization Film morphology was analyzed by optical microscopy (Nikon Eclipse MA200).

Electron microscopy pictures in figure 8.1f was performed by Jeol JSM 7600f Schottky Field Emission Scanning Electron Microscope, while figure 8.1e was performed by LEO 1530 Gemini (Zeiss) scanning electron microscope with InLense detector.

The film chemical and mechanical stabilities were evaluated by both prolonged sonication in several solvents (water, ethanol, acetone) and also by sand abrasion with quartz sand (150 m) according to a literature procedure[53].

Cyclic voltammetry (CV) was performed using a μ-Autolab III potentiostat/galvanostat (Ecochemie, The Netherlands). The electrochemical cell was composed by a saturated calomel (reference electrode, RE), a Pt-wire (CE), and a TiO_2 transparent glass (WE). Voltammograms were recorded between 0.4 and 1.2 V (at a scan rate of 50 (mV s^1)) in deaerated 0.2 M KNO_3.

Photocatalytic tests The photocatalytic activity of the films was tested towards two different photocatalytic systems: the gas phase degradation of ethanol and the degradation of siloxane layers adsorbed at the film surface. All photocatalytic tests were carried out both under UV (Jelosil HG500, Appendix C) and simulated solar irradiation (Lot Oriel, Appendix C).

The degradation of long chain organic moieties adsorbed at the photocatalyst surface was carried out to simulate the staining by fingerprints/oily liquids. Homogeneous and reproducible siloxane layers (SILRES 1701) were deposited on the TiO_2 surface via chemical vapor deposition adopting the procedure reported in Appendix C (100 $°C$). The degradation of the organic moieties was monitored by measuring the water contact angle as a function of time of light irradiation (Halogen lamp). The functional groups present

at the TiO_2 surface were investigated before and after the light irradiation by Fourier transform infrared (FTIR) spectroscopy using a Jasco 4200 spectrometer equipped with an attenuated total reflectance (ATR) module.

The gas-phase photocatalytic tests were carried out at 40 $°C$ in a 7 L Pyrex glass cylindrical reactor equipped with a quartz window, filled with a 80:20 N_2:O_2 dry atmosphere. Tests under UV irradiation were performed using two-layer films adopting an irradiated film area of 60 cm^2 (equivalent to 3 mg TiO_2), while 80 cm^2 (equivalent to 4 mg TiO_2) was used during solar tests. Ethanol was injected using a microsyringe into the reaction chamber up to an initial concentration of 275 ppm for tests under UV light or 140 ppm for solar tests. After the pollutant injection, the system was held in the dark for an equilibration time of 20 min. Both the disappearance of the pollutant molecule, the formation of the main intermediate (acetaldehyde) and its complete mineralization to CO_2 were followed during photocatalytic tests, by means of a gas-chromatographic system (Agilent 7890, equipped with a DB-VAX and a Porapak column, two FID detectors and a methanator). Dark adsorption tests and photolysis tests in the absence of photocatalyst were carried out.

For the sake of comparison, the activity of Evonik P25 was tested for the same gas-phase photocatalytic test. Films were deposited by spin-coating from the powder dispersions in i-PrOH and were not calcined prior to use, obtaining layers with geometric surface areas and TiO_2 mass comparable to those of TiO_2 transparent layers.

Applications The wetting properties of TiO_2 films deposited onto aluminum foils roughened by sand blasting, were modulated by functionalization with 1H,1H,2H,2H-perfluorooctyl-triethoxysilane (Figure 5.1, Chapter 5). The surface functionalization with the fluoroalkylsilane molecule was carried out by chemical vapor deposition described in Appendix C (100 $°C$). Antistain tests of the functionalized surface were performed with respect to dye solutions in aqueous and CH_2I_2 solvents using a procedure previously described[34].

Polypyrrole films were deposited onto the TiO_2 layers starting from a solution containing KCl 0.1 and 0.1 M in the monomer, using a photoelectro polymerization (20 consecutive CV cycles at 50 (mV s^{-1}) under UV illumination). The UV source was an iron halogenide lamp (Jelosil HG500, Appendix C).

Further details about synthetic procedures and characterizations can be found in Appendix C.

References

[1] D. Kowalski, P. Schmuki, *Chem. Commun.* **2010**, *46*, 8585–8587.

[2] K. Hashimoto, H. Irie, A. Fujishima, *Japanese J. Appl. Phys.* **2005**, *44*, 8269.

[3] Y. Furubayashi, T. Hitosugi, Y. Yamamoto, K. Inaba, G. Kinoda, Y. Hirose, T. Shimada, T. Hasegawa, *Appl. Phys. Lett.* **2005**, *86*, 252101.

[4] M. Faustini, L. Nicole, C. Boissire, P. Innocenzi, C. Sanchez, D. Grosso, *Chem. Mater.* **2010**, *22*, 4406–4413.

[5] E. L. Unger, E. Ripaud, P. Leriche, A. Cravino, J. Roncali, E. M. J. Johansson, A. Hagfeldt, G. Boschloo, *J. Phys. Chem. C* **2010**, *114*, 11659–11664.

[6] A. Fujishima, X. Zhang, D. A. Tryk, *Surf. Sci. Rep.* **2008**, *63*, 515 –582.

[7] V. A. Ganesh, H. K. Raut, A. S. Nair, S. Ramakrishna, *J. Mater. Chem.* **2011**, *21*, 16304–16322.

[8] K. Nakata, A. Fujishima, *J. Photochem. Photobio. C* **2012**, *13*, 169 –189.

[9] R. Fateh, R. Dillert, D. Bahnemann, *Langmuir* **2013**, *29*, 3730–3739.

[10] H. Yaghoubi, N. Taghavinia, E. K. Alamdari, *Surf. Coatings Tech.* **2010**, *204*, 1562 –1568.

[11] O. Kesmez, H. E. Camurlu, E. Burunkaya, E. Arpac, *Sol. Energ. Mat. Sol. C.* **2009**, *93*, 1833 –1839.

[12] T. A. Gad-Allah, F. H. Margha, *Mater. Res. Bull.* **2012**, *47*, 4096 –4100.

[13] G. Soliveri, V. Pifferi, G. Panzarasa, S. Ardizzone, G. Cappelletti, D. Meroni, K. Sparnacci, L. Falciola, *Analyst* **2015**, *140*, 1486–1494.

[14] R. Alam, I. V. Lightcap, C. J. Karwacki, P. V. Kamat, *ACS Nano* **2014**, *8*, 7272–7278.

[15] K. Liu, M. Cao, A. Fujishima, L. Jiang, *Chem. Rev.* **2014**, *114*, 10044–10094.

[16] C. H. Heo, S.-B. Lee, J.-H. Boo, *Thin Solid Films* **2005**, *475*, 183 –188.

[17] L. K. Tan, M. K. Kumar, W. W. An, H. Gao, *ACS Appl. Mater. Inter.* **2010**, *2*, 498–503.

[18] M. Takeuchi, M. Anpo in *Environmentally Benign Photocatalysts*, (Eds.: M. Anpo, P. V. Kamat), Nanostructure Science and Technology, Springer New York, **2010**, pp. 301–317.

[19] Q.-C. Xu, D. V. Wellia, M. A. Sk, K. H. Lim, J. S. C. Loo, D. W. Liao, R. Amal, T. T. Y. Tan, *J. Photochem. Photobio. A* **2010**, *210*, 181 –187.

[20] E. Pl, D. Sebk, V. Hornok, I. Dkny, *J. Colloid Interf. Sci.* **2009**, *332*, 173 –182.

[21] M. Szekeres, O. Kamalin, R. A. Schoonheydt, K. Wostyn, K. Clays, A. Persoons, I. Dekany, *J. Mater. Chem.* **2002**, *12*, 3268–3274.

[22] S. Lee, D. H. Kim, J. Y. Kim, H. S. Jung, H. Shin, K. S. Hong, *Electrochem. Commun.* **2012**, *15*, 29 –33.

[23] T. Tatsuma, K. Suzuki, *Electrochem. Commun.* **2007**, *9*, 574 –576.

[24] Y. Lai, Y. Tang, J. Gong, D. Gong, L. Chi, C. Lin, Z. Chen, *J. Mater. Chem.* **2012**, *22*, 7420–7426.

[25] G. Maino, D. Meroni, V. Pifferi, L. Falciola, G. Soliveri, G. Cappelletti, S. Ardizzone, *J. Nanopart. Res.* **2013**, *15*, 2087.

[26] K. Ellmer, *Nature Photon.* **2012**, *6*, 809–817.

[27] I. L. Violi, M. D. Perez, M. C. Fuertes, G. J. Soler-Illia, *ACS Appl. Mater. Inter.* **2012**, *4*, 4320–4330.

[28] R. Wang, K. Hashimoto, A. Fujishima, M. Chikuni, E. Kojima, A. Kitamura, M. Shimohigoshi, T. Watanabe, *Adv. Mater.* **1998**, *10*, 135–138.

[29] A. Fujishima, X. Zhang, *C. R. Chim.* **2006**, *9*, 750–760.

[30] M. Takeuchi, K. Sakamoto, G. Martra, S. Coluccia, M. Anpo, *J. Phys. Chem. B* **2005**, *109*, 15422–15428.

[31] M. Miyauchi, A. Nakajima, A. Fujishima, K. Hashimoto, T. Watanabe, *Chem. Mater.* **2000**, *12*, 3–5.

[32] D. Meroni, S. Ardizzone, G. Cappelletti, M. Ceotto, M. Ratti, R. Annunziata, M. Benaglia, L. Raimondi, *J. Phys. Chem. C* **2011**, *115*, 18649–18658.

[33] F. Milanesi, G. Cappelletti, R. Annunziata, C. Bianchi, D. Meroni, S. Ardizzone, *J. Phys. Chem. C* **2010**, *114*, 8287–8293.

[34] G. Soliveri, R. Annunziata, S. Ardizzone, G. Cappelletti, D. Meroni, *J. Phys. Chem. C* **2012**, *116*, 26405–26413.

[35] N. Herzer, J. Van Schaik, S. Hoeppener, U. Schubert, *Adv. Funct. Mater.* **2010**, *20*, 3252–3259.

[36] Y. Paz, *Beilstein J. Nanotech.* **2011**, *2*, 845–861.

[37] D. Meroni, S. Ardizzone, U. Schubert, S. Hoeppener, *Adv. Funct. Mater.* **2012**, *22*, 4376–4382.

[38] H.-H. Nguyen, N. Takenaka, H. Bandow, Y. Maeda, S. De Oliva, M. Botelho, T. Tavares, *Atmos. Environ.* **2001**, *35*, 3075–3083.

[39] R. Pal, K.-H. Kim, Y.-J. Hong, E.-C. Jeon, *J. Hazard. Mater.* **2008**, *153*, 1122–1135.

[40] V. Naik, A. Fiore, L. Horowitz, H. Singh, C. Wiedinmyer, A. Guenther, J. De Gouw, D. Millet, P. Goldan, W. Kuster, A. Goldstein, *Atmos. Chem. Phys.* **2010**, *10*, 5361–5370.

[41] J. Gaffney, N. Marley, *Atmos. Environ.* **2009**, *43*, 23–36.

[42] L. Brickus, J. Cardoso, F. De Aquino Neto, *Environ. Sci. Tech.* **1998**, *32*, 3485–3490.

[43] K.-D. Kwon, W.-K. Jo, H.-J. Lim, W.-S. Jeong, *Environ. Sci. Pollut. Res.* **2008**, *15*, 521–526.

[44] C. Marchand, B. Bulliot, S. Le Calv, P. Mirabel, *Atmos. Environ.* **2006**, *40*, 1336–1345.

[45] D. Meroni, S. Ardizzone, G. Cappelletti, C. Oliva, M. Ceotto, D. Poelman, H. Poelman, *Catal. Today* **2011**, *161*, 169–174.

[46] E. Piera, J. Aylln, X. Domnech, J. Peral, *Catal. Today* **2002**, *76*, 259–270.

[47] G. Song, *Adv. Engin. Mater.* **2005**, *7*, 563–586.

[48] M. W. Kendig, R. G. Buchheit, *Corrosion* **2003**, *59*, 379–400.

[49] M. Nosonovsky, B. Bhushan, *Curr. Opin. Colloid Interface Sci.* **2009**, *14*, 270 –280.

[50] N. C. Strandwitz, Y. Nonoguchi, S. W. Boettcher, G. D. Stucky, *Langmuir* **2010**, *26*, 5319–5322.

[51] J. Kawakita, M. Weitzel, *J. Nanosci. Nanotech.* **2011**, *11*, 2937–2943.

[52] R. Cervini, Y. Cheng, G. Simon, *J. Phys. D* **2004**, *37*, 13.

[53] X. Deng, L. Mammen, H.-J. Butt, D. Vollmer, *Science* **2012**, *335*, 67–70.

Chapter 9

Advanced patterning techniques: photocatalytic lithography and polymer brushes

The word lithography is abundantly used both in scientific and everyday life. That is connected to a wide range of technological and scientific uses, at many different length-scales, from the newspaper printing[1], to micro-electronics, up to the most modern nano-fabrication techniques for biomedical and optoelectronic applications[2, 3]. Many different substrates have been lithographied (photoresists, polymers, metals, oxides...) but, for sure, self-assembled monolayer (SAM) (on silicon wafer, gold, ect.) has been the best platform to test the limit of lithography in the direction of nano[4, 5]. Furthermore, these systems often are the foundation for bottom-up fabrication, with the prospect of complex 3D structures[6, 7].

As mentioned before, SAMs are not merely a passivating coating at a material surface, *e.g.* layers to provide anti-corrosion (electrical passivation[8], see Chapter 5) or self-cleaning features[9, 10] (see Chapters 4, 6 and 7); they form ordered molecular structures that can be exploited as reactive centers and, consequently, ordered pillars for the design of complex 3D frameworks[6]. The criticalness and the importance of managing such techniques have been underlined in recent reports. For example, Leggett *el al.* [11] pressed the criticalness of the protein and cells hierarchical adsorption on nanostructured patterns both for high-tech bio-sensor synthesis and the fundamental understanding of the interaction between cells/tissue and neuronal connections. In elecrocheistry, Yang *et al.*[12] used L-cysteine self-assembled monolayer to make a gold electrode selective to dopamine in a ascorbic acid solution. In this contests, silane molecules have been largely utilized thanks to the ability to form flexible and ordered monolayers, strongly chemisorbed at the surface, with high physical and chemical resistance[13]. Literature reports many different uses of silanes in lithography. After patterning, the patches can act as a mask for wet chemical etching to fabricate inorganic micro/nanostructures [11] of high applicative relevance (on, for example, Si substrates[14, 15], in order to create metal/plasmonic structure[16]), or can selectively favor/prevent the adsorprion of metal/oxide NPs (as a template for Pd adhesion and subsequent electroless deposition of ZnO[17], or the selective growth of titania[18]), or can act as reactive linkers for bottom-up macromolecular fabrication (see further on).

Generally adopted techniques to obtain such patterns concern photolithography (high energetic radiation, laser, etc.; shifting a collimate beam or by a mask), ion and electron beam lithography, μ-contact lithography, nanoimprinting lithography, scanning probe lithography and dip-pen nanolithography[13].

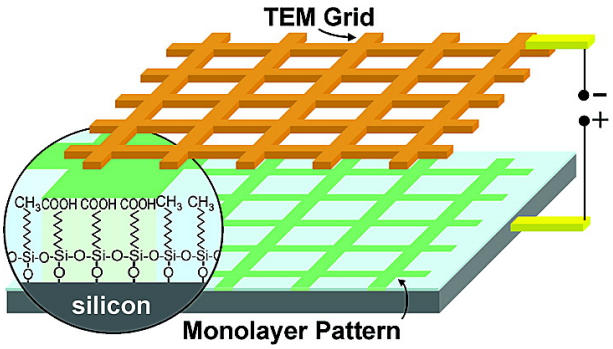

Figure 9.1: *Schematic of the stamp lithography. Reprinted with permission from S. Hoeppener et al., Nano Lett., 2003, Vol. 3, 761-7. Copyright 2015 American Chemical Society.*

Each of those techniques have advantages and disadvantages. When a very small scale (10-1000 nm) is required with good resolution, drawbacks like expensive and hazardous instrumentations, slow processes and small areas processability occur. In 2003, S. Hoeppener *et al.*[19, 20] firstly reported an innovative approach that selectively electro-oxidizes surfaces of siloxane self-assembled monolayer / silicon wafer(SW). Before that, the electro-oxidation lithography in the micrometric scale had been obtained by scanning probe techniques, which need extremely slow and complex instrumentation[4, 21]; large scale applications are prevented. The *stamp lithography* was born; applying a bias voltage between the OTS functionalized silicon wafer and a conductive mask (Cu TEM grid), the pattern could be obtained. The negative potential applied to the mask allowed the oxidation of the C18 top chain (presumably, to -COOH), forming the longed-for hydrophilic/phobic pattern. Such technique, well pictured in Figure 9.1, could be, in principle, applied only trough a conductive surface. On the grounds of the well described importance of titanium dioxide and its peculiar characteristics, the application of stamp lithography was evaluated of great importance for the realization of hydrophobic/philic patterns. In order to succeed, in this chapter, the conductivity of the titania layer is increased using indium tin oxide conductive glass (ITO) as a substrate for the TiO_2 thin film deposition.

If the substrate is not conductive at all, further strategies must be considered. Crystalline titanium dioxide is ubiquitously claimed as photocatalyst[22]. When its surface is irradiated at certain wavelengths, electron-hole pairs formation occurs. Holes are powerful oxidants, electrons are good reducing agents and both rapidly react directly or indirectly with adsorbates. If the titania surface, functionalized by an organic monolayer (like the alkylic tails of silanes), is irradiated in the near UV-region, quickly, the organic moieties mineralize. To pattern photoactive a titanium dioxide surface, the most direct way is, definitively, the irradiation of the pre-functionalized substrate through a mask. This process was well investigated by Prof. Fujishima and his group ([22] and references therein). The irradiation power, wavelength, humidity and time must be finely tuned, *ad hoc* for each surface and coating[23]. In fact, the production of secondary oxidative radicals, well reported in literature, could compromise the resolution of the lithography by lateral oxidation[24, 25].

Lithography exploiting TiO_2 / SAMs has already been described for many different applications, ranging from 2D modification (that exploits the hydropbobic/phylic contrast) up to the building up of complex 3D structure, like selective growth or adsorption of bio-molecules, cells, tissue, etc[26]. Here, the application of photocatalytic lithography on polymer brushes is reported for the first time. Polymer brushes are surface-tethered, highly-stretched polymer chains. They exhibit excellent robustness and well-organized chain conformation, which endow superior control over several surface properties as morphology, grafting density and chemical composition[27–29]. Patterned polymer brushes[30, 31] are versatile building blocks for micro-fabrication and controlled assembly of small particles[32], sensors/biosensors and actuators[33–41], drug delivery systems[42], electronic devices[43], anti-biofouling coatings[44], biocompatible

scaffolds[45]. In general they are efficient means to confer smart, stimuli-responsive behavior to surfaces and interphases[46–48].

By a combination of lithographic tools and surface-initiated polymerization (grafting-from, as opposed to grafting to which relies on adsorption of preformed polymer)[49, 50] micro- and nanoscale-complex architectures can be readily built from suitable self-assembled monolayers (SAMs)[51–54]. If they are composed by polymerization initiators, chains can grow directly from them. Eventually, if the SAMs are patterned, patterned polymer brushes will be obtained.

The expertise to master the patterning[55] is crucial in order to realize devices with applications ranging from biotechnology[56] to electronics[57]. Patterning has been accomplished using colloidal lithography[58, 59], micro-contact printing[60, 61], electron beam lithography[62], scanning probe[63] or near field lithography[64], conventional photolithography (with the use of photoresists[65, 66]) and SAM photolithography[66, 67]. The latter, as previously discussed, requires high-intensity UV sources[32, 68–70] (*e.g.* deep-UV, vacuum-UV)[71, 72] or highly focused beams (UV-lasers)[73].

There is a significant demand for more affordable and facile lithographic techniques, which should update the present technologies[74] to reliably pattern polymer brushes at the wafer scale[75] with high resolution micrometric and sub-micrometric features. Here, for the first time, this challenge can be successfully addressed by taking advantage of titanium dioxide photocatalytic properties. Up to now, that technique has been used mostly to build hydrophilic/hydrophobic patterns[1, 76].

Direct photocatalytic lithography could play a crucial role for innovation in the field of polymer brushes micro-lithography. Nevertheless, the need of a TiO_2 layer or, in general, of a photoactive substrate is limiting for many applications. Notwithstanding the smoothness, the transparency, the hardness and the biocompatibility of the titania layer, its photocatalytic properties could not be desired for some applications. The necessity to graft brushes directly onto a specific surface or onto substrates that cannot withstand thermal treatments (needed for the development of titania photoactivity) could occur. We found in remote photocatalysis a powerful solution for this general problem. The group of Fujishima, first, reported that the photooxidation of organic molecules can take place not only on the direct titanium dioxide surface but also on substrates placed at relatively considerable distances (up to 500 μm) from it[22, 77]. The mechanism of remote photocatalysis had been highly controversial until Kubo et al.[78] demonstrated that H_2O_2 molecules, which are generated at the photocatalyst surface from atmospheric water and oxygen, migrate in the surrounding air and are cleaved to HO$\bullet$ radicals in the exposed areas of the target surface. Such mechanism is particularly useful to explain the high resolution pattern obtained. Highly oxidative radical species form only in the irradiated areas, avoiding lateral oxidation due to migration[79, 80]. Remote oxidation of organic contaminants, alkylsiloxane and thiol SAMs, polymers and metals have been reported[23, 81], especially oriented to the generation of superhydrophilic/superhydrophobic patterns[80]. Here, for the first time, we describe the successful application of remote photocatalytic lithography for the realization of patterned polymer brushes. This is potentially a universal approach, able to generate high resolution patterns on any kind of substrate. In order to obtain a good resolution, avoiding effects connected to the titania substrate morphology and light scattering ability, the quality of the photoactive layer is critical. The titania film obtained by electrochemically-assisted deposition developed in Chapter 8 seems the ideal candidate for this goal.

In this chapter, modern concepts of micro and nano-lithography are exploited to obtain high resolution 2D patterning, a critical step in the direction of complex 3D supramulecolar structure design. While in the first part of this chapter, facile and not-hazardous lithographic methods are transferred to TiO_2 thin film as a valuable platform for many different applications, then, the titania photocatalytic properties are exploited. Both direct and remote approaches are used to pattern, in principle, any kind of surfaces.

Stamp lithography and photocatalytic lithography shape micrometric hydrophobic/hydrophilic patches, patterning SAM alkyl silanes (see Chapters 5 and 7). In this contest, we demonstrate the possibility to pattern different kind of self-assembled monolayers, including initiators for ATRP polymerization. The patterned initiator layers can be amplified by polymerization in patterned polymer brushes.

9.1 Results and discussion

9.1.1 Micrometric lithography on TiO_2 thin films

OTS monolayer on SiO_2 and TiO_2 Silicon wafer (SW) and titanium dioxide thin films, synthesized by the electrochemical assisted deposition (previously described in Chapter 8) both on glass and on indium thin oxide coated glass (ITO), were functionalized by a monolayer of octadecyl-trichlorosilane (OTS, Figure 4.1, Chapter 4) following a consolidate literature procedure (wet procedure in bicyclohexyl, BCH)[4]. After pre-treatment in plasma, different times of immersion in the functionalization mixture were tested, in order to reach a good quality layer. The best values were obtained after 2-3 minuts for SW and 15 minutes for TiO_2 . While TiO_2 requires longer time of immersion, the OTS layer is generally more reproducible; functionalized SW substrates, occasionally, show (by AFM analysis) the presence of small particles (5-10 nm, risen from the silane polymerization) at the surface. After functionalization, the substrates were sonicated in toluene, to remove the not chemisorbed OTS and some of the silane particles.

The quality of the silane layer was evaluated, for each sample, by water CA measurements, AFM and FTIR (transmission or reflectance mode for SiO_2 and TiO_2 , respectively). The first evidence of a good quality layer is the water contact angle up to 105-107°[82]. By tapping mode AFM, topography pictures reveal the presence of nanoparticles or other undesirable nano-objects, while phase analysis could reveal an island-like structure of the monolayer, related to a partial coverage of the surface. FT-IR measurements, additionally, confirmed the formation of an ordered monolayer. Peak positions of the -CH_2- stretching are revealing of the quality of the layer. Values close to 2917 and 2849 cm^{-1} are correlated to the formation of an ordered and well packed monolayer[4]. Figure 9.2 reports a satisfactory example of OTS monolayer on TiO_2 thin film.

Stamp lithography Stamp lithography was obtained both on silicon wafer and on TiO_2 (supported on ITO), following the procedure reported by Hoeppener *et al.*[19]. A TEM grid was used as the stamp, while the electric connection between the grid and the potentiostat was made by an Al foil. While the procedure was fast and quite simple in the case of SW, TiO_2 required more time, more trials, and, eventually, the procedure was less reproducible. SW coated by OTS was treated by 30 V for 10 s. After that period of time, any difference could be observed by naked eye. By condensing atmospheric humidity on the surface, by cooling the sample by a Peltier plate, the pattern became visible. Once the sample was back at lab temperature, the grid pattern was disappeared. The AFM pictures obtained in contact mode revealed a presence of the well defined pattern (Figures 9.3a and 9.3b). Especially, lateral force images clearly show the friction contrast between the tip and the surface moving along the different patches. That is generally explained as a sharp variation of polarity, correlated to a change in the chemical composition of the surface.

As previously discussed, the stamp lithography on TiO_2 was more tricky. The 200 nm semiconductor layer with 3.2 eV bad gap, compared to a p-type silicon, make the two substrates highly different in term of layer conductivity. Furthermore, due to the synthetic procedure adopted, the TiO_2 layer presents

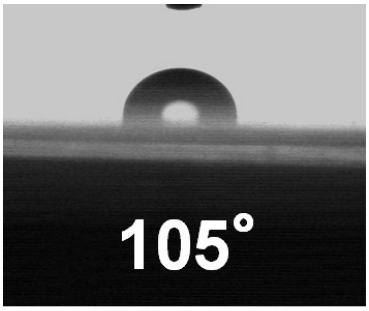

(a) Water contact angle mesurements.

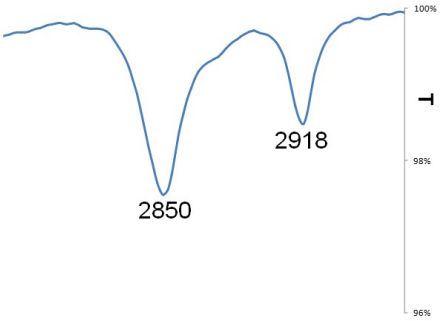

(b) FTIR reflectance analysis.

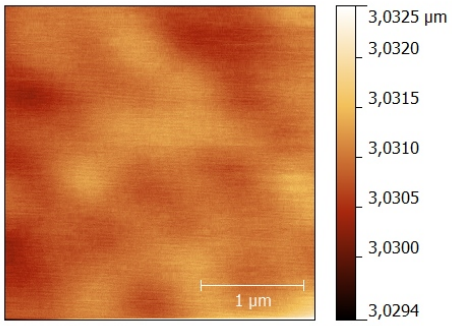

(c) AFM topography picture, tapping mode.

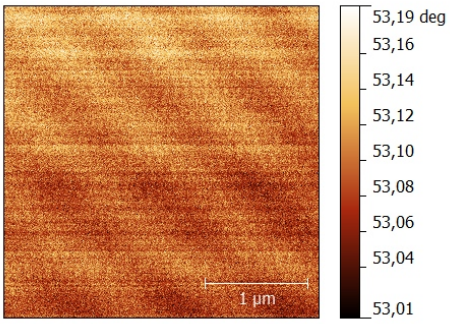

(d) AFM phase picture, tapping mode.

Figure 9.2: *OTS self assembled monolayer on TiO_2 thin film. Characterization of the film.*

more inhomogeneities and cracks (and pores) that allowed current preferential ways. Such local high current paths short-circuited the system and burned the surface. Although, good results were obtained applying a bias voltage of 10 V for 5 s (Figure 9.3c). As for SW, the pattern was visible only after condensation of atmospheric humidity (Figure 9.3d); quite good lateral resolution was observed by AFM pictures (topography and lateral force, Figures 9.3e and 9.3f).

Photocatalytic lithography In the study of patterning methods on TiO_2 thin film, further approaches were studied. Especially, photocatalytic lithography seems the most effective approach, exploiting the photo-activity of titania. As discussed in the introduction, many reports have shown the use of titania film, synthesized by different methods (most of them are physical methods), to selectively mineralize organic adsorbent when UV-irradiated through a photo-mask[22, 83]. The formation of electron-hole pairs and their direct or indirect (formation of radicals) reactions with the adsorbates, selectively tune the properties of the surface. Compared to previous discussion in Chapter 7, here, thank to the smoothness of the film and fine tuning of the experimental layout, micrometer resolutions were reached.

As shown in Figure 9.4a, a nickel grid was used as a proof of concept mask. A magnet was placed under the TiO_2 sample; thanks to the ferromagnetic properties of Ni, the grid strongly adheres at the surface. Furthermore, a quartz glass covered the sample, to fix the grid. A black open box protected the sample from lateral irradiation. After 25 minutes of irradiation, the organic moieties on the irradiated areas were presumably mineralized and the patches became hydrophilic. Again, a pattern was visible after humidity condensation (Figures 9.4b and 9.4c); in the present case (compared stamp lithography), the hydrophilic/phobic pattern was specular. AFM pictures (contact mode, lateral friction, Figures 9.4d, 9.4e and 9.4f) revealed very high lateral resolution (less then 5 μm) and a great reproducibility on all the

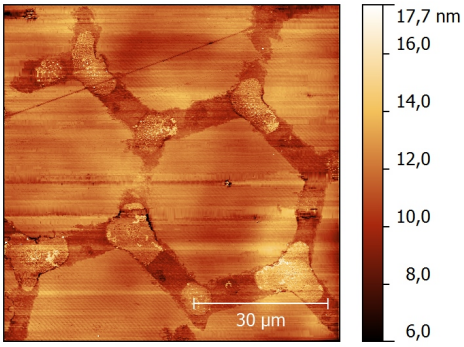

(a) Stamp lithography on silicon wafer. AFM topograpy picture, contact mode.

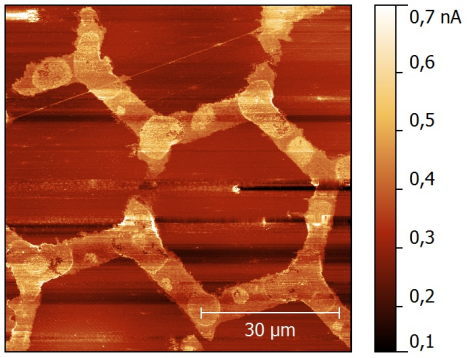

(b) Stamp lithography on silicon wafer. AFM lateral force picture, contact mode.

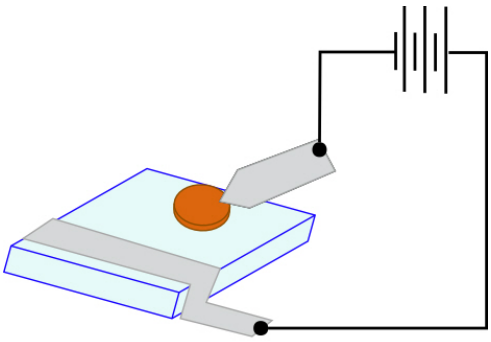

(c) Stamp lithography on TiO_2 thin film. Schematic.

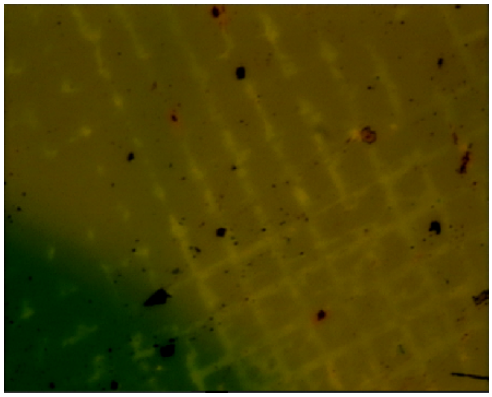

(d) Stamp lithography on cooled TiO_2 thin film. Optical microscopy picture.

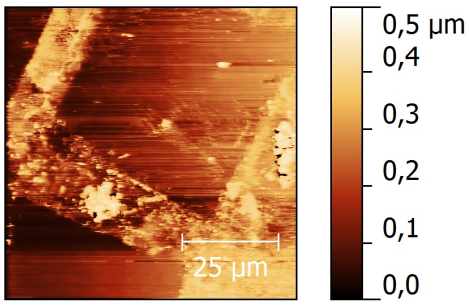

(e) Stamp lithography on TiO_2 thin film. AFM topograpy picture, contact mode.

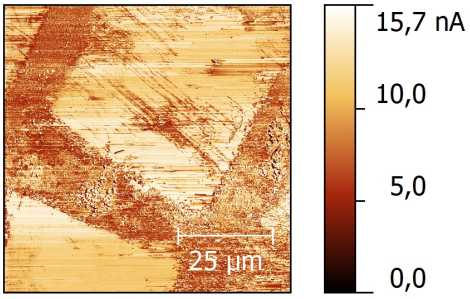

(f) Stamp lithography on TiO_2 thin film. AFM lateral force picture, contact mode.

Figure 9.3: *Stamp lithography on silicon wafer and TiO_2 thin film.*

areas covered by the grid. No good topography pictures could be obtained due to the small difference in hight between irradiated and not-irradiated areas. It is noteworthy that longer time of irradiation showed lateral oxidation effect, and a consequent loss in the resolution.

To prove the versatility of the technique, the specular pattern can be obtained. As shown in Figure 9.5a, the Ni grid can be fixed at the TiO_2 surface by the magnet and put in a metal evaporator. The TiO_2 /OTS sample was covered by an Al thin layer, except for the areas covered by the grid. After grid removal, the sample was irradiated under the UV lamp. The Al-layer protected the siloxane from oxidation. The Al can be removed by soft scrubbing with acetone. As shown by optical microscopy and AFM pictures (Figures 9.5b, 9.5c, 9.5d and 9.5e), the resolution of the patterning was totally comparable with that described in the previous paragraph.

9.1.2 Patterning of polymer brushes made easy using titanium dioxide

Direct approach Patterning of SAM, as discussed in the introduction, can be the basis for 3D micro and nano-fabrication. Here, the first work about patterned polymer brushes exploiting photo-catalytic lithography is reported. The TiO_2 films were deposited both on glass and silicon wafer to answer specific characterization requirements of over-built polymer brushes. Films showed the typical increase in hydrophilicity upon exposure to 365 nm UV radiation due to enhanced hydroxyl surface termination (see Chapter 8). This phenomenon was exploited to improve chemisorption of the atom transfer radical polymerization (ATRP) initiator (3-(2-bromoisobutyramido)propyl)triethoxysilane (BIB-APTES)[84] on TiO_2 (Figure 9.6a, step 1). Direct photocatalytic micropatterning of the initiator was achieved through UV-irradiation with 365 nm UV light from a halogen lamp using a TEM grid on the substrate as a photomask (Figure 9.6a, step 2a, and Figure 9.6b).

Photocatalytic degradation could be easily followed on dedicated substrates by water contact angle measurements (Figure 9.6c). The water contact angle for surfaces functionalized with BIB-APTES, stored in the dark, was 75°. After 1 h of irradiation, the θ_w decreased to less than 15° and the disappearance of nitrogen and bromine signals from the XPS spectra gave definitive evidence of complete deactivation of the initiator molecules (discussed below, and Table 9.1). On the other hand, BIB-APTES grafted on surfaces with no photoactivity, like silicon wafer or glass, was unaffected even after more than 5 h of UV irradiation as confirmed by the unchanged water contact angle and ability to start the growth of polymer brushes. That confirmed the critical role of TiO_2 for the photo-patterning of initiator; 365 nm-lamp (lamp Jelosil HG500, see Appendix C) does not allow photolysis of the adsorbates.

Surface-initiated atom transfer radical polymerization (SI-ATRP), a controlled free radical polymerization process, was used to amplify the obtained initiator pattern into a poly(methyl methacrylate) (PMMA) brush[85, 86]. As a proof of concept, methyl methacrylate (MMA) monomer was chosen but, in principle, any ATRP-friendly monomer can be used. Activators regenerated by electron transfer (ARGET) ATRP was selected because, in contrast to classical ATRP, offers improved oxygen tolerance and permits the adoption of milder conditions[87]. PMMA brush growth was carried out at 30° in a 4:1 v/v methanol-water mixture using a $CuBr_2$/tris(2-pyridylmethyl)amine (TPMA) catalyst activated by an excess of ascorbic acid. Polymerization on BIB-APTES-functionalized substrates proceeded smoothly, leading to PMMA brushes with thicknesses up to 200 nm depending upon the amount of time allowed for polymerization (Figure 9.6d*). Successful grafting of polymer brushes was confirmed by water contact angle measurement (68°, which is consistent with previous wetting experiments with water on PMMA

*A deviation from linearity is observed for longer reaction times, that could be explained by increased steric interference to chain growth as polymer brushes grow longer and by the occurrence of irreversible chain termination. It is not clear why such deviation appears to be more pronounced for silicon substrates

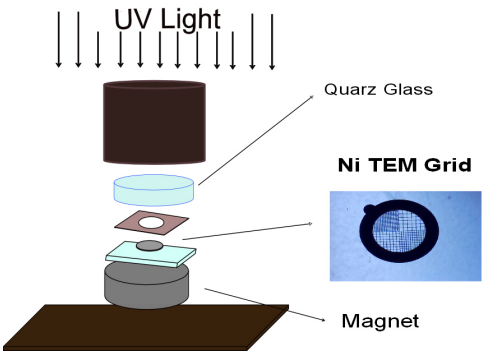

(a) UV lithography on TiO_2 thin film. Schematic.

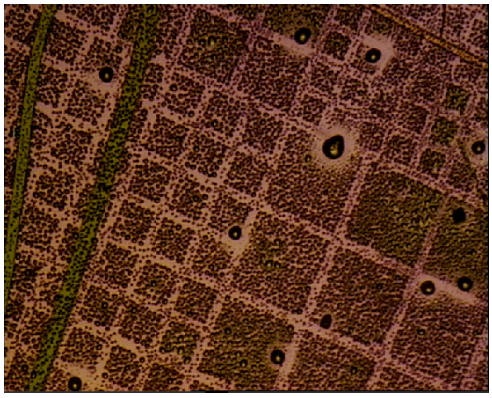

(b) UV lithography on TiO_2 thin film. Optical microscopy.

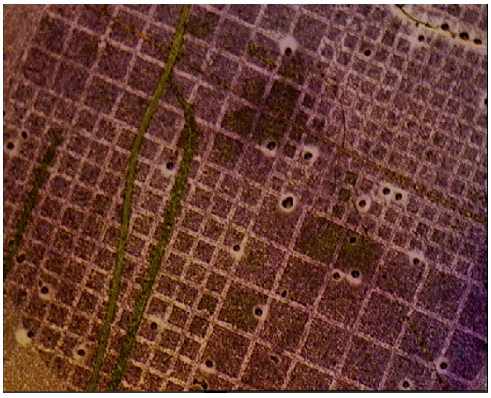

(c) UV lithography on TiO_2 thin film. Optical microscopy.

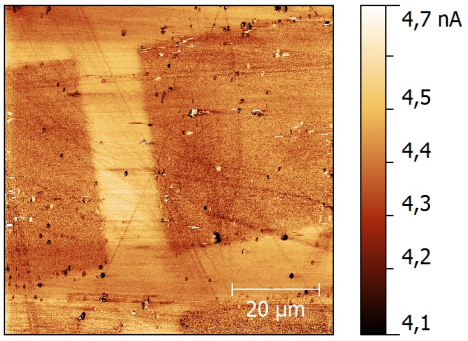

(d) UV lithography on TiO_2 thin film. AFM lateral force, contact mode.

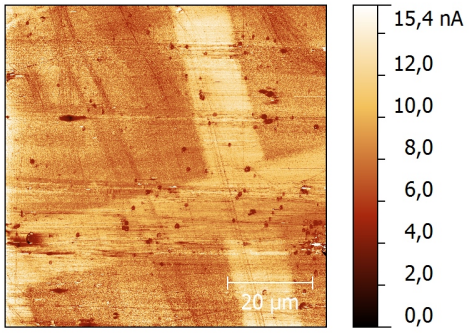

(e) UV lithography on TiO_2 thin film. AFM lateral force, contact mode.

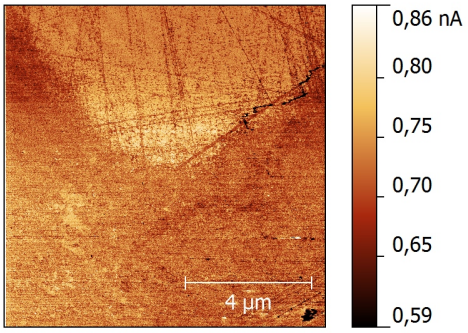

(f) UV lithography on TiO_2 thin film. AFM lateral force, contact mode.

Figure 9.4: *UV lithography on TiO_2 thin film.*

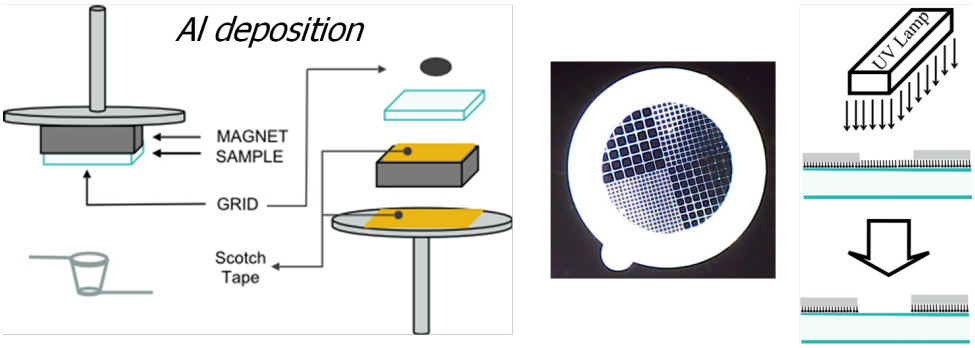

(a) UV lithography on TiO_2 thin film, invesce pattern. Schematic.

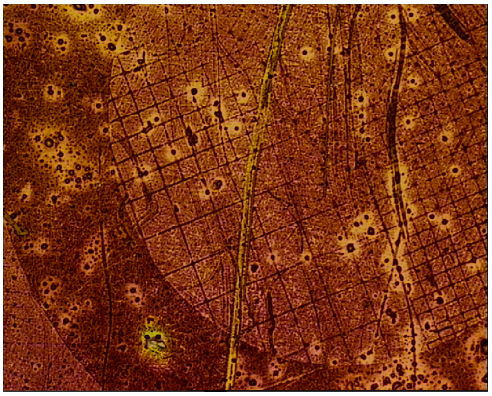

(b) UV lithography on TiO_2 thin film, inverse pattern. Optical microscopy.

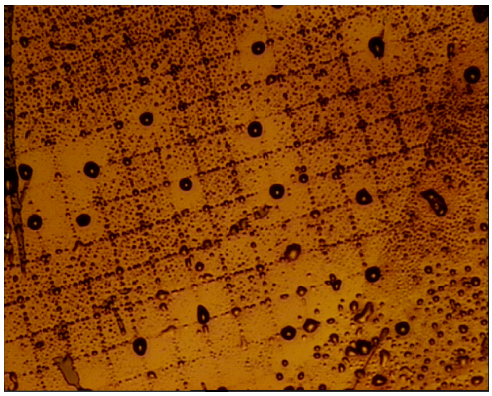

(c) UV lithography on TiO_2 thin film, inverse pattern. Optical microscopy.

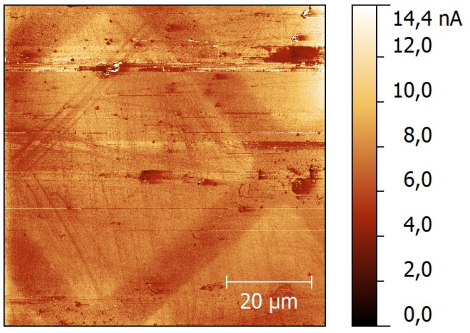

(d) UV lithography on TiO_2 thin film, inverse pattern. AFM lateral force, contact mode.

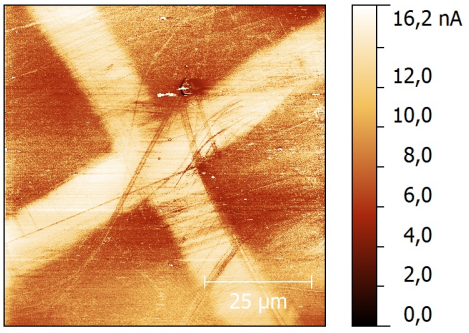

(e) UV lithography on TiO_2 thin film, inverse pattern. AFM lateral force, contact mode.

Figure 9.5: *UV lithography on TiO_2 thin film, inversed pattern.*

brushes[88]) and FTIR analysis (Figure 9.7b). The brush thickness is linearly correlated with polymerization time (over at least 8 h) suggesting a good control of the polymerization (Figure 9.6d). Figure 9.8 shows that the grid patterns have been successfully replicated onto the TiO_2 surface and 10 μm-wide PMMA lines were obtained with very good resolution. Remarkably, the brushes were able to restart the polymerization of MMA with excellent ($\geq$ 90%) re-initiation efficiency (Figure 9.7a) and allowed also formation of block-copolymers: for example PMMA-b-PS brushes, with a PS block up to 80 nm thick, could be obtained by subsequent polymerization of styrene on a PMMA brush as shown by the increase in contact angle (from 68° to 90°, in accordance with literature findings[89]) and FTIR analysis (Figure 9.7†).

Remote approach As discussed in the introduction, the quality of the titania layer (deposited by electrochemical assisted deposition, Chapter 8, on common glass) in terms of transparency, homogeneity and smoothness was critical to obtain a good resolution patterning, avoiding lateral oxidation, partial degradation and scattering effects. Remote photocatalytic patterning was performed by irradiating with 365 nm UV light BIB-APTES-functionalized silicon substrates through our titania-coated glass, pre-cleaned by UV irradiation for 1 h, using a 100 μm-thick Teflon spacer (Figure 9.6a, step 2b). Micropatterning was achieved using a TEM grid and patterns were amplified with PMMA brushes, as already discussed for direct photolithography. Water contact angle decreased from 70° to 33° after 2 h irradiation of the initiator-functionalized substrate. In addition, as for the direct approach, XPS showed complete disappearance of the bromine signal (Table 9.1). Nevertheless, the best pattern resolution was achieved with an irradiation time of 5 h. Complete optical and electron microscopy characterization was reported in Figure 9.9.

XPS analysis Results obtained with XPS are summarized in Table 9.1 and Table 9.2, page 156. Table 9.1 reports the quantification of XPS survey peaks for BIB-APTES modified substrates. It can be seen from the relative atomic percentages that there is a C:N ratio of ca. 8:1 and of ca. 9:1 for BIB-APTES grafted on TiO_2 and on silicon respectively. These values are in good accordance with the 7:1 C:N ratio expected for BIB-APTES perfectly adsorbed in a *tripod structure* with each of the three Si-O groups forming a siloxane bond with -OH-terminated TiO_2 or silicon surface, suggesting that although some molecules may still retain ethoxy functional groups on their Si-O tails, a ordered monolayer has formed. The Br 3d signal is apparently underestimated, thus preventing its quantification; however, complete disappearance of both nitrogen and bromine signals after direct and remote photocatalytic lithography confirms successful degradation of the initiator molecules. Table 9.2 reports the energetic positions of principal peaks. For carbon, signals relating to C-C (285.0 eV) and C=O (288.5 eV) are observed, in accordance with the molecular structure of BIB-APTES. For BIB-APTES on TiO_2 after 1 h

†**Figure 9.7b:** Comparison of FTIR spectra for a poly(methyl methacrylate) (PMMA) brush, thickness 106 $\pm$ 1 nm, and for a block copolymer brush obtained by restarting polymerization from PMMA brush with styrene (PS thickness 86 $\pm$ 2 nm). Substrate: silicon wafer. Both brushes show characteristic IR absorption spectra[90, 91] with the most pronounced differences occurring in the C-H stretching regions. A strong peak due to C=O stretching at 1730 cm^{-1} is visible in both spectra. In the PMMA spectrum the main features are at 2951 cm^{-1} (CH_2 asimmetric stretching and CH_3 asimmetric stretching) and at 2996 cm^{-1} (CH_2 of OCH_3 asimmetric stretching). In the PMMA-PS block copolymer spectrum, the diagnostic peaks are at 699 cm^{-1} and 755 cm^{-1} (wagging of the 5 H of the aromatic ring), 2847 cm^{-1} (CH_2 simmetric stretching), 2927 cm^{-1} (CH_2 asimmetric stretching); the peaks at 2998 cm^{-1}, 3026 cm^{-1} , 3060 cm^{-1}, 3083 $cm^{-}1$ are all due to the aromatic C-H stretching). **Figure 9.7c:** Comparison of FTIR spectra for a poly(methyl methacrylate) (PMMA) brush, thickness 83 $\pm$ 1 nm and for a block copolymer brush obtained by restarting polymerization from PMMA brush with styrene (PS thickness 83 $\pm$ 2 nm). Substrate: TiO_2 . Both brushes show characteristic IR absorption spectra[90, 91] with the most pronounced differences occurring in the C-H stretching regions. In the PMMA spectrum the peaks at 2946 cm^{-1} (CH_2 asimmetric stretching and CH_3 asimmetric stretching) and at 2999 cm^{-1} (CH_3 of OCH_3 asimmetric stretching) are visible. In the PS spectrum the peaks at 2849 cm^{-1} (CH_2 simmetric stretching) and at 2918 cm^{-1} (CH_2 asimmetric stretching) can be recognized.

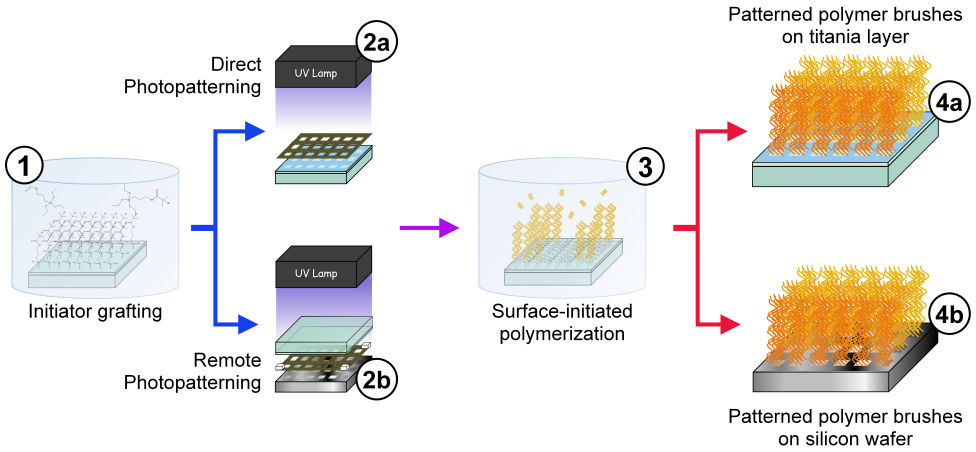

(a) Scheme of patterned brushes preparation. Grafting of the ATRP initiator (1), pattern formation using both direct (2a) and remote (2b) photocatalytic lithography, SI-ATRP (3) and the obtained polymer patterns (4a, 4b).

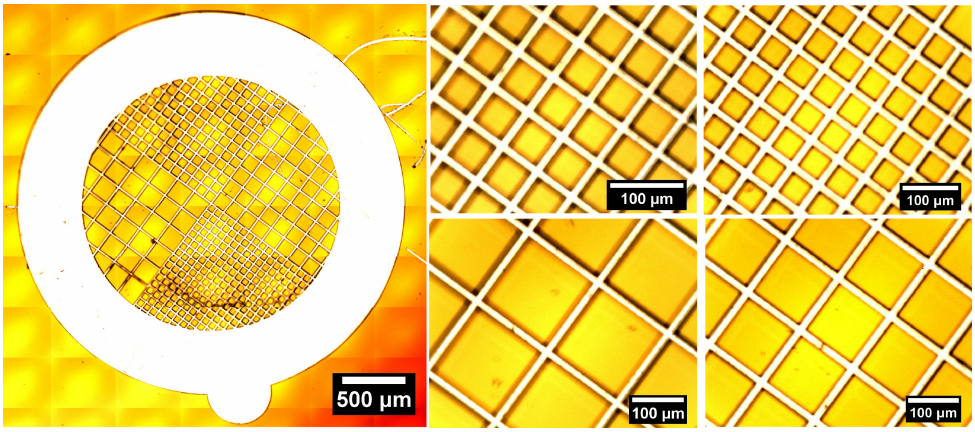

(b) Optical microscopy images of the TEM grid used for photopatterning.

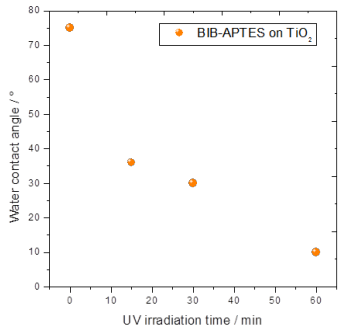

(c) Water contact angle kinetics for the photodegradation of BIB-APTES grafted on TiO_2 .

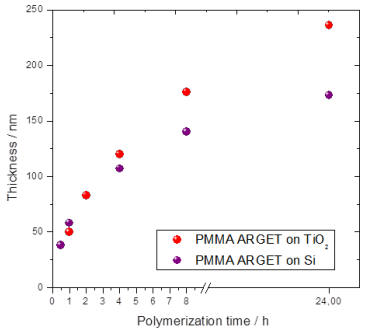

(d) Evolution of PMMA brushes thickness as a function of the polymerization time.

Figure 9.6: *Schematic of the polymer brush lithography, mask and kinetics. Ref.[92]. Published by The Royal Society of Chemistry.*

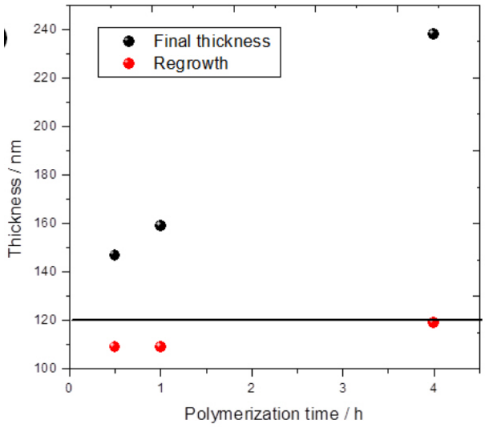

(a) PMMA brushes restarting polymerization efficiency was demonstrated. The straight line represents the mean thickness h_{4h} for a 4 h-grown PMMA brush. Results indicate very good macroinitiator efficiency (I $\geq$ 90%), *i.e.* the fraction of the original growing chains capable to restart polymerization. That is defined as $I = (\Delta h/h_{4h}) \cdot 100$, where Δh is the thickness increase after restarting polymerization with MMA.

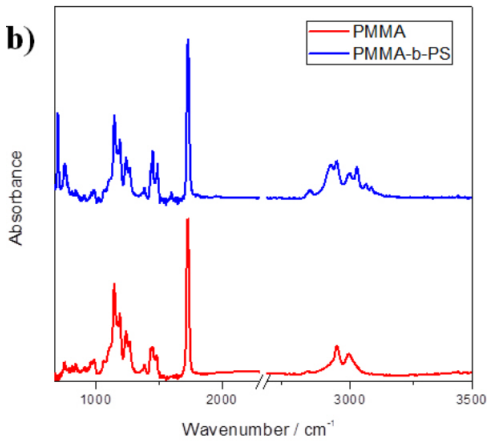

(b) Comparison of FTIR spectra for a poly(methyl methacrylate) (PMMA) brush, thickness 106 $\pm$ 1 nm, and for a block copolymer brush obtained by restarting polymerization from PMMA brush with styrene (PS thickness 86 $\pm$ 2 nm). Substrate: silicon wafer.

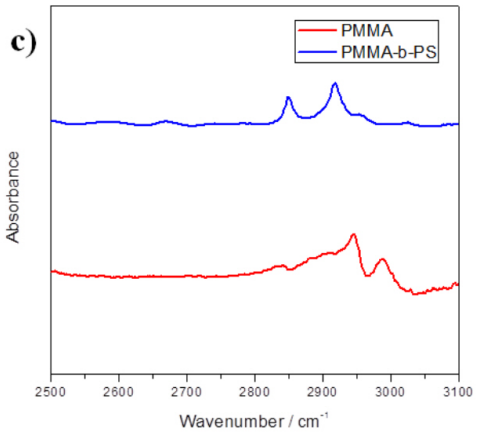

(c) Comparison of FTIR spectra for a poly(methyl methacrylate) (PMMA) brush, thickness 83 $\pm$ 1 nm and for a block copolymer brush obtained by restarting polymerization from PMMA brush with styrene (PS thickness 83 $\pm$ 2 nm). Substrate: TiO_2 .

Figure 9.7: *PMMA brushes restarting polymerization efficiency. Ref.[92]. Published by The Royal Society of Chemistry.*

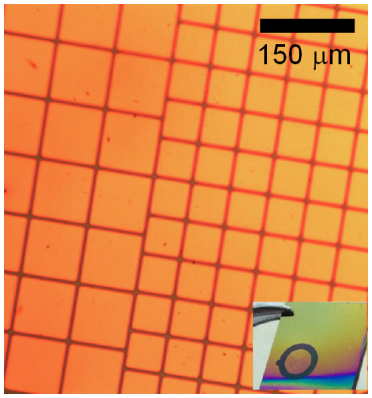

(a) Optical microscopy; inset: picture of the typical sample.

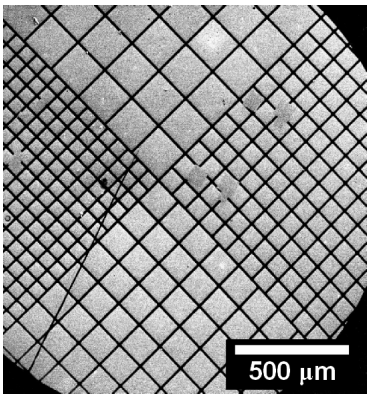

(b) Scanning electron microscopy image.

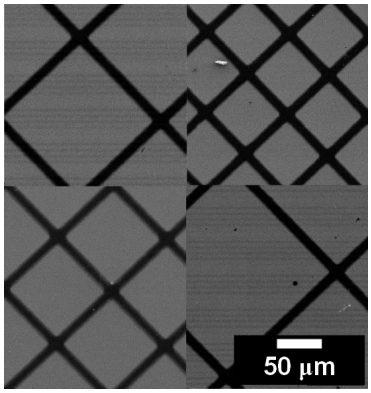

(c) Assemblage of scanning electron microscopy images.

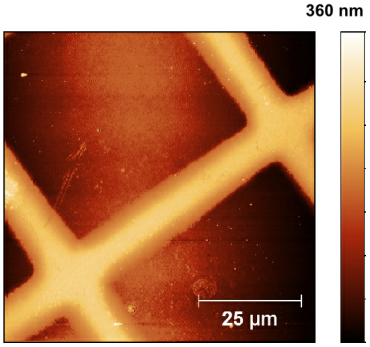

(d) AFM image: tophography, tapping mode.

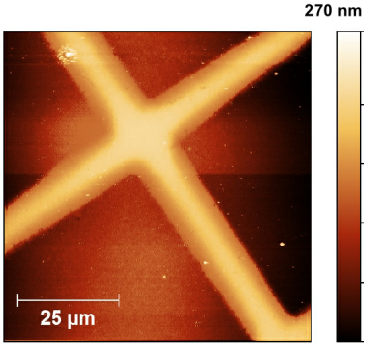

(e) AFM image: tophography, tapping mode.

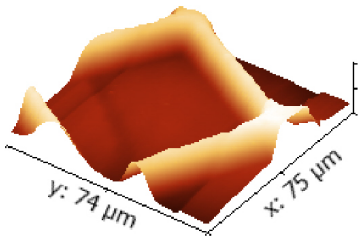

(f) AFM 3D topography picture, tapping mode.

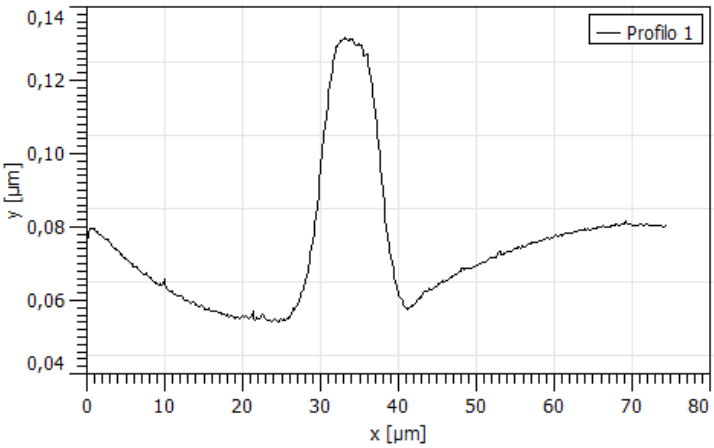

(g) AFM line profile.

Figure 9.8: *Direct photocatalytic lithography of initiator and subsequent SI-ATRP. Ref.[92]. Published by The Royal Society of Chemistry.*

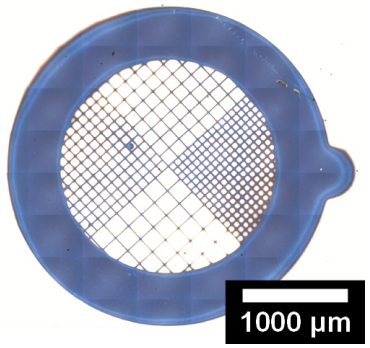

(a) Optical microscopy picture; time of irradiation 5 h.

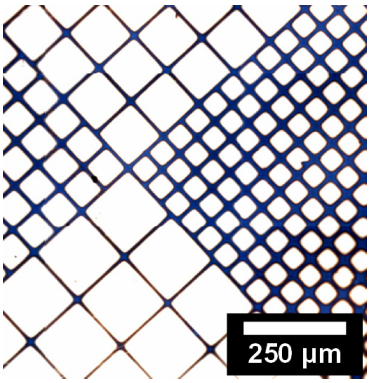

(b) Scanning electron microscopy image; time of irradiation 5 h.

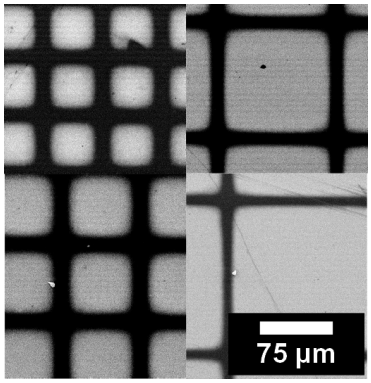

(c) Assemblage of scanning electron microscopy images; time of irradiation 5 h.

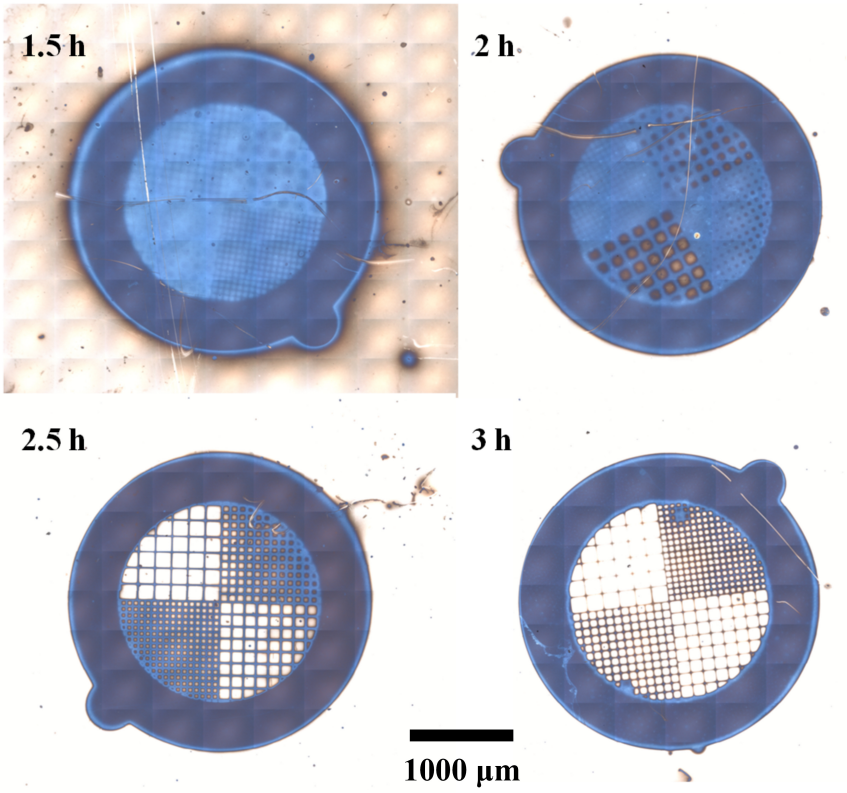

(d) Optical microscopy images of the pattern evolution of remote photocatalytic lithography on silicon. For a UV irradiation time of 1.5 h the photomask is clearly replicated with 120 nm-thick PMMA brushes but the internal microstructuration is barely visible; also the surrounding surface is heavily stained with polymer (thickness ca. 39 nm). After 2 h, the exposed surface is completely free from polymer and after 2.5 h the pattern replica is completely developed. The resolution of the latter is improved after 3 h of irradiation. The blue color of brushes is due to optical effects.

Figure 9.9: *Remote photocatalytic lithography of initiator and subsequent SI-ATRP. Ref.[92]. Published by The Royal Society of Chemistry.*

of UV irradiation a shoulder appears at 286.5 eV which is attributable to -C-OH groups. The position of N 1s peak at 400 eV was assigned to the amide species. The oxygen peak position depends on the surface nature: 530.5 eV for TiO_2 , 533.0 eV for SiO_2. The position of the silicon peak depends on the number of bonded oxygen atoms: 99.5 eV, no bound oxygen atoms; 102.5 eV, three bound oxygen atoms; 103.5 eV, four bound oxygen atoms.

Patterning of pH-responsive polymer brushes Peculiar properties arise from polymer brushes with specific structure, making them powerful tools in surface engineering. Examples include control of phase-segregation in response to external stimuli, wetting control, lubrication, adsorption of molecules and particles (including proteins and cells)[28]. Especially, brushes made of polyelectrolytes are able to respond to a wide range of external stimuli such as pH, temperature and ionic strength, which induce structural (e.g. swelling) and chemical (e.g. functional group modification) changes in the individual polymer chain leading to a collective, amplified response of the brushes[27, 30, 40]. Poly(2-(dimethylamino)ethyl methacrylate) (PDMAEMA), for its pH-responsivity, is a very good candidate for the development of smart surfaces, sensors and actuators[35, 42].

After patterning of BIB-APTES initiator, polymerization of DMAEMA was performed using ATRP in presence of 5 mol% $CuBr_2$ to achieve better control of the polymerization process[93]. The film thickness could be tuned by increasing the polymerization time up to 4 h. A linear increase of thickness as a function of the polymerization time (Figure 9.10a) suggested a controlled process. Successful formation of PDMAEMA brushes was confirmed also by FTIR spectroscopy (Figure 9.10b): BIB-APTES-functionalized substrates show only peaks from the $-CH_2-$ groups while extra peaks at 2760 cm^{-1} and 2810 cm^{-1} (symmetric stretching) and a peak at 2930 cm^{-1}, associated with C-H vibration modes of $-CH_3$ of the tertiary amine groups $-N(CH_3)_2$, are visible after DMAEMA polymerization[94–96].

Optical microscopy and scanning electron microscopy were used to examine the pattern quality of the obtained brushes and the resolution attained (Figures 9.10c, 9.10d and 9.10e): the images revealed well defined patterns (~ 10 μm-width), demonstrating the effectiveness of photocatalytic lithography also in this case.

PDMAEMA is a weak polybase with pKa ~ 7, thus its tertiary amine group is protonated at pH < 7 and deprotonated at pH > 7[97]. Protonation introduces electrostatic charges which cause the chains to repel each other and swell by absorption of water, so pH changes are accompanied by changes in the brushes hydrophilicity which can be easily followed by water contact angle measurements. This behavior is completely reversible, the brushes (water contact angle $\sim 55°$) can be made more hydrophilic ($\sim 14°$) or less hydrophilic ($\sim 60°$) by simple immersion in acid or base solutions, respectively (Figure 9.10f).

9.2 Conclusion

In this chapter, a brief overview of some of the most promising patterning techniques using TiO_2 was reported. Their relevance in the 3D micro-fabrication of complex structures with high applicative interest was demonstrated for the first time by polymer brushes ATRP.

Stamp lithography, the evolution of selective electro-oxidation on organic SAM, was here first obtained on titanium dioxide. The requirement of a conductive or partially conductive substrate forced me to the synthesis of TiO_2 thin films (procedure in Chapter 8) on conductive glass (ITO). Notwithstanding the difficulties in finding the needed conditions, good results were obtained in term of resolution.

The use of a photo-active TiO_2 film (see Chapter 8) inevitably leads to its application fot photocatalytic lithography. Here, two different approaches were tested, in such a way to obtain the positive

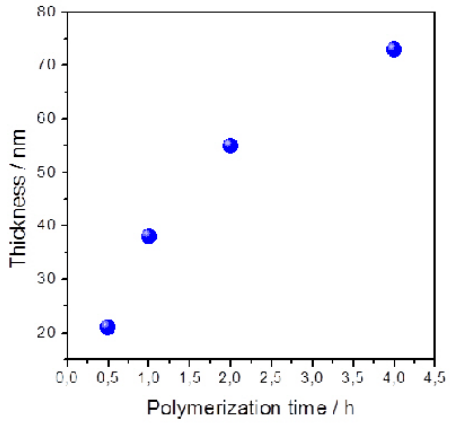

(a) Polymerization kinetic.

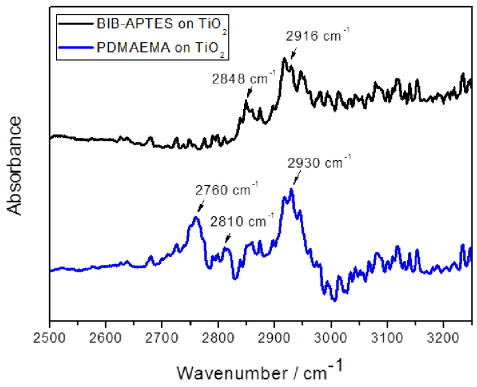

(b) FTIR analysis.

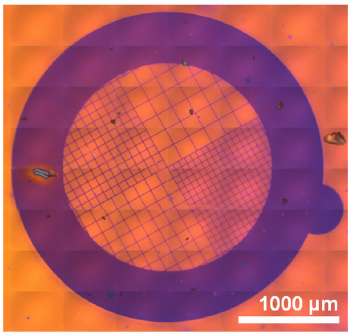

(c) Optical microschopy.

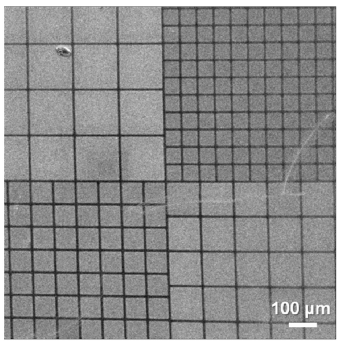

(d) Scanning electron microscopy.

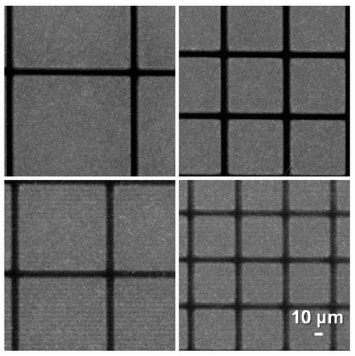

(e) Scanning electron microscopy.

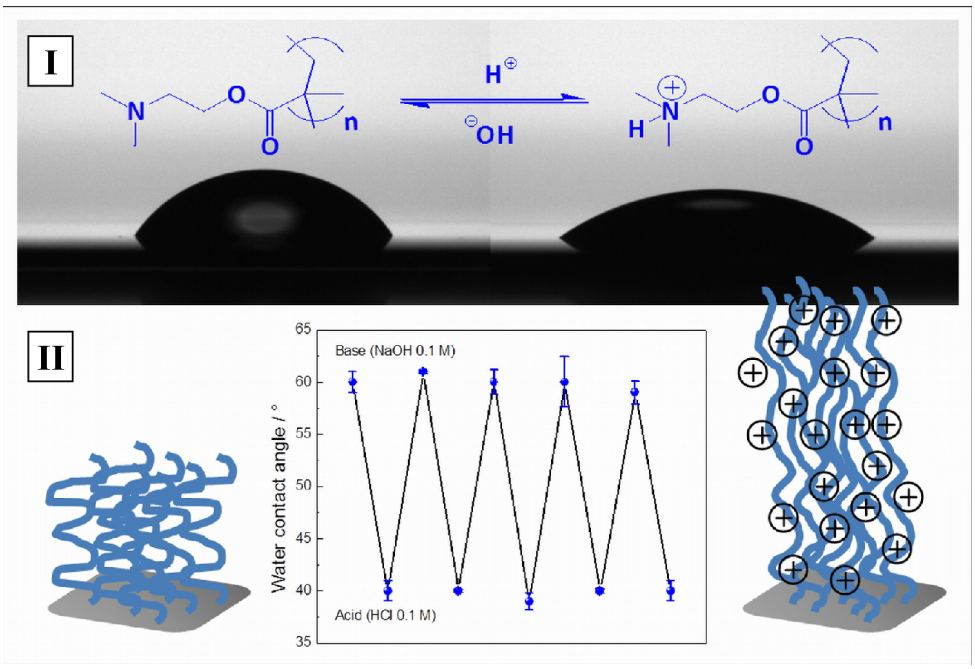

(f) (I) pH-responsive behavior and (II) contact angle switching of PDMAEMA brushes.

Figure 9.10: *Patterned PDMAEMA brushes obtained on TiO_2 thin film.*

and negative of the same picture (mask). An adequate layout and the tuning of the irradiation condition lead to a pattern with high resolution (less then 5 μm). Such technique does not require expensive or hazardous instrumentation and the sample can be processed in less than thirty minutes.

The growing excitement in the field of polymer brushes and the proved request for efficient patterning means urge the introduction of more facile and low-cost method to develop such architectures. Here for the first time, the use of photocatalytic lithography for making patterned polymer brushes was discussed, showing how innovative this approach could be. TiO_2 thin film with high photoactivity was employed to selectively degrade initiators of polymerization (previously grafted at the surface) under near-UV irradiation through a photomask, and the obtained patterns were replicated by SI-ATRP. While direct photocatalytic lithography could be obtained only on the surface of a thin titania layer, the remote approach allowed us to achieve photocatalytic patterning on, virtually, any kind of substrate thanks to the migration of oxidizing species from a TiO_2 interface. Both approaches lead to sharp edges and high line resolution. The remote approach is especially relevant being a general, non-invasive and high-throughput lithographic technique. We deliberately chose cheap materials (*e.g.* glass instead of quartz slides) to make it affordable to a wider spectrum of researchers. Long time irradiation was correlated with a low-energetic lithographic lamp (safe and simple to handle); in such a way, high resolution is simple to reach. In addition, our process can be scaled up to the wafer scale, with the future final goal to design controlled areas with different functionalities, useful for applications, *e.g.* in microfluidics and for the development of cell-responsive surfaces.

9.3 Specific procedures

Monomers were filtered through an inhibitor-remover column and stored at $-18\ ^{\circ}C$ until use. Bicyclohexyl (BCH) was distilled over Na before use.

In this chapter, two types of silica were used: double side polished p-type silicon wafers (100), obtained from University Wafer (resistivity: 10 - 20 (Ω cm)) was utilized in Subsection 9.1.1; silicon (100) wafers, single-polished, n-type, phosphorus doped, 3 - 6 (Ω cm), with a native oxide layer ca. 1.5 nm thick, purchased from Ultrasil Corporation were used in Subsection 9.1.2.

9.3.1 Micrometric lithography

OTS SAM synthesis The TiO_2 or SW were pre-treated in plasma cleaner for 5 minutes. OTS monolayers were prepared by immersing the substrate in a solution of OTS (5 μL) in BCH (1 mL) for 1 minute, followed by sonication in toluene. Finally, the slides were dried in a stream of Ar. To be suitable for lithography, the final water contact angle was 107°. The obtained monolayers were analyzed by atomic force microscopy in tapping mode and by Fourier transform infrared spectroscopy in the grazing angle reflectance/transmittance mode (FT-IR, Bruker Hyperion spectrometer) to check the complete coverage and the state of order of the layer.

Stamp lithoraphy Rigid metal stamps consisting of TEM copper grids (SPI Supplies, West Chester, PA) mounted in a special Teflon holder were cleaned by 5 minutes Ar plasma, followed by exposure to HNO_3 vapor (twice 1 min on each side), sonication for several minutes in ultrapure water, and finally drying in a stream of Ar. A freshly cleaned grid attached to a piece of Scotch tape was placed for 15 s above a beaker filled with hot water and then pressed manually against a self-assembled OTS monolayer specimen while applying (for $\sim$ 10 s for $\sim$ 5 s) a voltage bias of 30 V for SW and 10 V for TiO_2 between

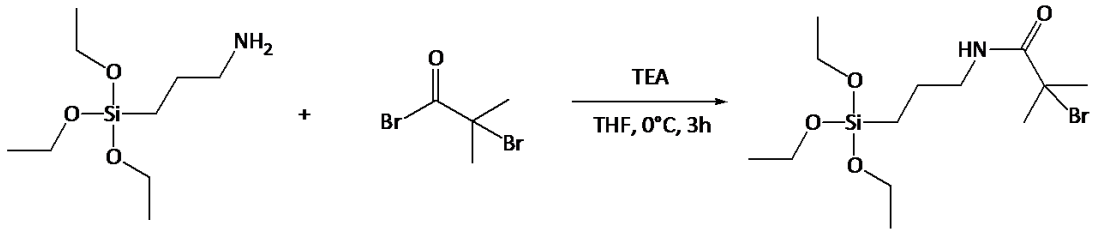

Figure 9.11: *Synthesis of BIB-APTES (scheme).*

the grid (negative) and the silicon wafer substrate (positive). Electrical contact with the grid was realized through an Al foil immobilized together with the grid on the same piece of Scotch tape.

UV lithography A nickel grid (Gilder Grids, nickel, d 3.05 mm, square mesh) was used as a mask. A magnet was placed under the TiO_2 sample; thanks to the ferromagnetic properties of Ni, the grid strongly adhere at the surface. Furthermore, a quartz glass covered the sample, to avoid the grid motion. A black open box protected the sample from lateral irradiation. As a lithographic lamp, a UVACUBE 100 (Hole UV technology) equipped with a Hg lamp was used.

The inverse pattern was obtained by attaching the Ni grid to the TiO_2 by the magnet and putting it in a metal evaporator. The TiO_2 /OTS sample was covered by an Al thin layer, in except for the area covered by the grid. After grid removal, the sample was irradiated under UV Lamp. The Al was removed by soft scrubbing with acetone (Figure 9.5a).

9.3.2 Patterning of polymer brushes

Cleaning and activation of TiO_2 films were accomplished using a Spectroline crosslinker equipped with 254 nm UV lamps. Photocatalytic patterning was achieved using a Jelosil HG500 halogen lamp (described in Appendix C).

TEM grids (Gilder Grids, nickel, d 3.05 mm, square mesh) were used as photomasks (Figure 9.6b).

Optical microscopy images and high resolution FTIR spectra were acquired using a Nicolet^{TM} iN^{TM}10 Infrared Microscope in transmittance (for silicon samples) or reflectance (for titania samples) mode, with a liquid nitrogen-cooled MCT detector (spectral range 4000 - 675 cm^{-1}, resolution 4 cm^{-1}, aperture 150 x 150 μm). Background (500 scans) was collected before each sample (1000 scans) from cleaned silicon or titanium dioxide. Baseline correction was performed automatically by the acquisition software.

Synthesis of ATSP initiator (BIB-APTES) 7 mL (30 mmol) 3-aminopropyltriethoxysilane (APTES) and 5 mL (36 mmol) triethylamine were dissolved in 50 mL anhydrous THF in a three-necked 100 mL round bottom flask, equipped with a dropping funnel, a nitrogen inlet and a mechanical stirrer, immersed in an ice bath. 4.45 mL (36 mmol) 2-bromoisobutyrylbromide (BIBB) were added dropwise under stirring and the reaction was allowed to continue at room temperature for 3 h. The white solid (triethylammonium bromide) was filtered off and the volatiles removed at 50 $^{\circ}C$ using rotavapor. The product was redissolved in anhydrous THF, filtered through silica gel to separate a brown impurity. After evaporation of the solvent, a quantitative yield of a viscous, colorless liquid was obtained (Scheme 1) and stored at +4 $^{\circ}C$. Density: 1.17 (g mL^{-1}). ^{1}H NMR ($CDCl_2$, 400 MHz, ppm): 0.64 (t, 2H, $SiCH_2$), 1.22 (br, 9H, CH_3), 1.65 (q, 2H, CH_2), 2.02 (s, 6H, CH_3), 3.26 (t, 2H, CH_2NH), 3.83 (q, 6H, CH_3CH_2OSi), 6.85 (s br, 1H, NH).

Graftig of the initiator To improve grafting of initiator molecules, the TiO_2 surface was activated by irradiation with 254 nm UV (0.25 (J cm^2)). This treatment is useful to remove organic contamination and increase the surface hydroxyl groups. For functionalization with BIB-APTES, the substrates were immersed in a 10 mM BIB-APTES solution in anhydrous toluene for 4 h at 55 $°C$, left overnight at 30 $°C$, washed and gently sonicated with toluene, acetone and ethanol and dried with a nitrogen stream. The functionalized substrates were stored at room temperature in the dark until use. BIB-APTES was grafted with a similar procedure on silicon wafer previously cleaned using piranha solution.

SI-ARGET ATRP of methyl methacrylate (MMA) and SI-ATRP of styrene (S) In a nitrogen-purged Schlenk flask 0.021 g ($\sim$ 0.07 mmol) of tris(2-pyridylmethyl)amine (TPMA), 0.002 g ($\sim$ 0.01 mmol) of copper(II) bromide and 0.023 g (0.13 mmol) of ascorbic acid are dissolved in 10 mL of a 4:1 v/v methanol-water mixture previously degassed by nitrogen bubbling. 10 mL (94 mmol) of degassed MMA are added and the mixture is stirred under nitrogen. A 5 mL-aliquot of this mixture is poured over the initiator-functionalized substrates placed separately in nitrogen-purged Schlenk flasks which are immersed in an oil bath at 30 $°C$ to allow polymerization. The polymerization time was varied from 0.5 to 8.0 h to control thickness. Samples are then rinsed extensively with THF, gently sonicated in the same solvent and dried under a nitrogen stream.

For the ATRP of styrene, the following procedure was adopted: in a nitrogen-purged Schlenck flask 0.1 g (0.7 mmol) of copper(I) bromide are dissolved in a degassed solution of 270 μL (1.3 mmol) of pentamethyldiethylenetriamine (PMDETA) in 10 mL DMSO. Then 30 mL ($\sim$ 260 mmol) of degassed styrene are added and the mixture is stirred under nitrogen. A 5 mL-aliquot of this mixture is poured over each initiator-functionalized substrate placed in a nitrogen purged Schlenck flask immersed in an oil bath at 90 $°C$ to allow polymerization. After reaction, the sample is rinsed extensively with THF, gently sonicated in the same solvent and dried under a nitrogen stream. A $\sim$ 80 nm-thick block of polystyrene (PS) was successfully obtained from PMMA brushes after 4 h of polymerization as was confirmed by contact angle measurements (from 68° to 90°, typical for PS) and FTIR (Figures 9.7b and 9.7c).

Further details about synthetic procedures and characterizations can be found in Appendix C.

Sample	Treatment	O 1s (at.% ± 10%)	Ti 2p (at.% ± 10%)	C 1s (at.% ± 10%)	Si 2p (at.% ± 10%)	N 1s (at.% ± 10%)	Br 3d (at.% ± 10%)
BIB-APTES on TiO_2	None	54.9	22.2	17.9	2.1	2.2	0.78
	1 h UV	62.9	26.2	8.9	2.0	-	-
BIB-APTES on SW	None	38.0	-	24.6	34.5	2.6	0.33
	5 h remote	49.6	-	4.9	45.5	-	-

Table 9.1: *Atomic composition of BIB-APTES-functionalized surfaces before and after direct and remote photocatalytic lithography determined by XPS.*

Sample	Treatment	O 1s (eV ± 0.5 eV)	Ti 2p (eV ± 0.5 eV)	C 1s (eV ± 0.5 eV)	Si 2p (eV ± 0.5 eV)	N 1s (eV ± 0.5 eV)	Br 3d (eV ± 0.5 eV)
BIB-APTES on TiO_2	None	530.5	459.0	285.0 288.5	102.5	400.0	71.0
	1 h UV	530.5	459.0	285.0 286.5 289.0	102.5	-	-
BIB-APTES on SW	None	533.0	-	285.5 288.5	99.5 103.5	400.5	71.0
	5 h remote	533.0	-	285.0	99.5 103.5	-	-

Table 9.2: *Binding energy for the principal elements detected by XPS.*

References

[1] K. Nakata, A. Fujishima, *J. Photochem. Photobio. C* **2012**, *13*, 169 –189.

[2] J. W. Menezes, J. Ferreira, M. J. L. Santos, L. Cescato, A. G. Brolo, *Adv. Funct. Mater.* **2010**, *20*, 3918–3924.

[3] G. Si, Y. Zhao, J. Lv, M. Lu, F. Wang, H. Liu, N. Xiang, T. J., A. J. Danner, J. Teng, Y. J. Liu, *Nanoscale* **2013**, *5*, 6243–6248.

[4] D. Meroni, S. Ardizzone, U. Schubert, S. Hoeppener, *Adv. Funct. Mater.* **2012**, *22*, 4376–4382.

[5] A. Zeira, D. Chowdhury, R. Maoz, J. Sagiv, *ACS Nano* **2008**, *2*, 2554–2568.

[6] C. Haensch, S. Hoeppener, U. S. Schubert, *Chem. Soc. Rev.* **2010**, *39*, 2323–2334.

[7] J. Berson, D. Burshtain, A. Zeira, A. Yoffe, R. Maoz, J. Sagiv, *Nature materials* **2015**, *14*, 613–621.

[8] M. Petrunin, A. Nazarov, Y. N. Mikhailovski, *J. Electrochem. Soc.* **1996**, *143*, 251–257.

[9] G. Soliveri, D. Meroni, G. Cappelletti, R. Annunziata, V. Aina, G. Cerrato, S. Ardizzone, *J. Mater. Sci.* **2014**, *49*, 2734–2744.

[10] G. Soliveri, R. Annunziata, S. Ardizzone, G. Cappelletti, D. Meroni, *J. Phys. Chem. C* **2012**, *116*, 26405–26413.

[11] M. Moxey, A. Johnson, O. El-Zubir, M. Cartron, S. S. Dinachali, C. N. Hunter, M. S. M. Saifullah, K. S. L. Chong, G. J. Leggett, *ACS Nano* **2015**, *9*, 6262–6270.

[12] G. Hu, Y. Liu, J. Zhao, S. Cui, Z. Yang, Y. Zhang, *Bioelectrochem.* **2006**, *69*, 254 –257.

[13] S. Onclin, B. J. Ravoo, D. N. Reinhoudt, *Angew. Chem. Int. Edit.* **2005**, *44*, 6282–6304.

[14] H. Sugimura, K. Ushiyama, A. Hozumi, O. Takai, *Langmuir* **2000**, *16*, 885–888.

[15] H. Sugimura, T. Hanji, O. Takai, T. Masuda, H. Misawa, *Electrochim. Acta* **2001**, *47*, 103 –107.

[16] E.-S. Kwak, J. Henzie, S.-H. Chang, S. K. Gray, G. C. Schatz, T. W. Odom, *Nano Lett.* **2005**, *5*, 1963–1967.

[17] N. Saito, H. Haneda, T. Sekiguchi, N. Ohashi, I. Sakaguchi, K. Koumoto, *Adv. Mater.* **2002**, *14*, 418–421.

[18] Y. Masuda, W. S. Seo, K. Koumoto, *Langmuir* **2001**, *17*, 4876–4880.

[19] S. Hoeppener, R. Maoz, J. Sagiv, *Nano Lett.* **2003**, *3*, 761–767.

[20] S. Hoeppener, R. Maoz, J. Sagiv, *Adv. Mater.* **2006**, *18*, 1286–1290.

[21] M. Yang, D. Wouters, M. Giesbers, U. S. Schubert, H. Zuilhof, *ACS Nano* **2009**, *3*, 2887–2900.

[22] A. Fujishima, X. Zhang, D. A. Tryk, *Surf. Sci. Rep.* **2008**, *63*, 515 –582.

[23] W. Kubo, T. Tatsuma, A. Fujishima, H. Kobayashi, *J. Phys. Chem. B* **2004**, *108*, 3005–3009.

[24] H. Haick, Y. Paz, *J. Phys. Chem. B* **2001**, *105*, 3045–3051.

[25] H. Haick, Y. Paz, *J. Phys. Chem. B* **2003**, *107*, 2319–2326.

[26] T. S. Druzhinina, S. Hoeppener, U. S. Schubert, *Small* **2012**, *8*, 852–857.

[27] R. Barbey, L. Lavanant, D. Paripovic, N. Schwer, C. Sugnaux, S. Tugulu, H.-A. Klok, *Chem. Rev.* **2009**, *109*, 5437–5527.

[28] S. G. Boyes, A. M. Granville, M. Baum, B. Akgun, B. K. Mirous, W. J. Brittain, *Surf. Sci.* **2004**, *570*, 1 –12.

[29] O. Azzaroni, *J. Polym. Sci. Part A: Polym. Chem.* **2012**, *50*, 3225–3258.

[30] T. Chen, I. Amin, R. Jordan, *Chem. Soc. Rev.* **2012**, *41*, 3280–3296.

[31] M. E. Welch, C. K. Ober, *J. Polym. Sci. Part B: Polym. Phys.* **2013**, *51*, 1457–1472.

[32] G. J. Dunderdale, J. R. Howse, J. P. A. Fairclough, *Langmuir* **2011**, *27*, 11801–11805.

[33] C. R. Daniels, L. J. Tauzin, E. Foster, R. C. Advincula, C. F. Landes, *J. Phys. Chem. B* **2013**, *117*, 4284–4290.

[34] M. Singh, O. Odusanya, G. M. Wilmes, H. B. Eitouni, E. D. Gomez, A. J. Patel, V. L. Chen, M. J. Park, P. Fragouli, H. Iatrou, N. Hadjichristidis, D. Cookson, N. P. Balsara, *Macromol.* **2007**, *40*, 4578–4585.

[35] G. J. Dunderdale, J. P. A. Fairclough, *Langmuir* **2013**, *29*, 3628–3635.

[36] J. Cui, O. Azzaroni, A. del Campo, *Macromol. Rapid Commun.* **2011**, *32*, 1699–1703.

[37] C. Xu, X. Fu, M. Fryd, S. Xu, B. B. Wayland, K. I. Winey, R. J. Composto, *Nano Lett.* **2006**, *6*, 282–287.

[38] H. C. McCaig, E. Myers, N. S. Lewis, M. L. Roukes, *Nano Lett.* **2014**, *14*, 3728–3732.

[39] H. Ma, J. He, X. Liu, J. Gan, G. Jin, J. Zhou, *ACS Appl. Mater. Interfaces* **2010**, *2*, 3223–3230.

[40] T. Chen, R. Ferris, J. Zhang, R. Ducker, S. Zauscher, *Prog. Polym. Sci.* **2010**, *35*, 94 –112.

[41] I. Tokareva, I. Tokarev, S. Minko, E. Hutter, J. H. Fendler, *Chem. Commun.* **2006**, 3343–3345.

[42] S. Kumar, Y. L. Dory, M. Lepage, Y. Zhao, *Macromol.* **2011**, *44*, 7385–7393.

[43] H. J. Snaith, G. L. Whiting, B. Sun, N. C. Greenham, W. T. S. Huck, R. H. Friend, *Nano Lett.* **2005**, *5*, 1653–1657.

[44] G. Gunkel, M. Weinhart, T. Becherer, R. Haag, W. T. S. Huck, *Biomacromol.* **2011**, *12*, 4169–4172.

[45] D. Falconnet, G. Csucs, H. M. Grandin, M. Textor, *Biomaterials* **2006**, *27*, 3044 –3063.

[46] S. Peng, B. Bhushan, *RSC Adv.* **2012**, *2*, 8557–8578.

[47] F. Zhou, W. T. S. Huck, *Phys. Chem. Chem. Phys.* **2006**, *8*, 3815–3823.

[48] S. Dai, P. Ravi, K. C. Tam, *Soft Matter* **2008**, *4*, 435–449.

[49] A. Olivier, F. Meyer, J.-M. Raquez, P. Damman, P. Dubois, *Prog. Poly. Sci.* **2012**, *37*, 157 –181.

[50] D. M. Jones, W. T. S. Huck, *Adv. Mater.* **2001**, *13*, 1256–1259.

[51] S. Santer, A. Kopyshev, H.-K. Yang, J. Rhe, *Macromol.* **2006**, *39*, 3056–3064.

[52] O. A. Guskova, C. Seidel, *Macromol.* **2011**, *44*, 671–682.

[53] S. Santer, A. Kopyshev, J. Donges, J. Rhe, X. Jiang, B. Zhao, M. Mueller, *Langmuir* **2007**, *23*, 279–285.

[54] Y.-K. Lai, Z. Chen, C.-J. Lin, *J. Nanoengin. Nanomanufact.* **2011**, *1*, 18–34.

[55] M. Geissler, Y. Xia, *Adv. Mater.* **2004**, *16*, 1249–1269.

[56] Q. Liu, C. Wu, H. Cai, N. Hu, J. Zhou, P. Wang, *Chem. Rev.* **2014**, *114*, 6423–6461.

[57] E. Menard, M. A. Meitl, Y. Sun, J.-U. Park, D. J.-L. Shir, Y.-S. Nam, S. Jeon, J. A. Rogers, *Chem. Rev.* **2007**, *107*, 1117–1160.

[58] Y. Li, J. Zhang, L. Fang, L. Jiang, W. Liu, T. Wang, L. Cui, H. Sun, B. Yang, *J. Mater. Chem.* **2012**, *22*, 25116–25122.

[59] T. Chen, D. P. Chang, R. Jordan, S. Zauscher, *Beilstein J. Nanotech.* **2012**, *3*, 397–403.

[60] T. Chen, R. Jordan, S. Zauscher, *Polymer* **2011**, *52*, 2461 –2467.

[61] Y. Tsujii, M. Ejaz, S. Yamamoto, T. Fukuda, K. Shigeto, K. Mibu, T. Shinjo, *Polymer* **2002**, *43*, 3837 –3841.

[62] S. J. Ahn, M. Kaholek, W.-K. Lee, B. LaMattina, T. H. LaBean, S. Zauscher, *Adv. Mater.* **2004**, *16*, 2141–2145.

[63] M. Kaholek, W.-K. Lee, B. LaMattina, K. C. Caster, S. Zauscher, *Nano Lett.* **2004**, *4*, 373–376.

[64] E. ul Haq, Z. Liu, Y. Zhang, S. A. A. Ahmad, L.-S. Wong, S. P. Armes, J. K. Hobbs, G. J. Leggett, J. Micklefield, C. J. Roberts, J. M. R. Weaver, *Nano Lett.* **2010**, *10*, 4375–4380.

[65] X. Fan, L. Lin, J. L. Dalsin, P. B. Messersmith, *Polymer Preprints* **2005**, *46*, 442.

[66] J.-K. Chen, Z.-Y. Chen, H.-C. Lin, P.-D. Hong, F.-C. Chang, *ACS Appl. Mater. Interf.* **2009**, *1*, 1525–1532.

[67] N. Herzer, S. Hoeppener, U. S. Schubert, *Chem. Commun.* **2010**, *46*, 5634–5652.

[68] S. A. Ahmad, G. J. Leggett, A. Hucknall, A. Chilkoti, *Biointerphases* **2011**, *6*, 8–15.

[69] R. Iwata, P. Suk-In, V. P. Hoven, A. Takahara, K. Akiyoshi, Y. Iwasaki, *Biomacromol.* **2004**, *5*, 2308–2314.

[70] S. Tugulu, M. Harms, M. Fricke, D. Volkmer, H.-A. Klok, *Angew. Chem. Int. Edit.* **2006**, *45*, 7458–7461.

[71] O. P. Khatri, H. Sano, K. Murase, H. Sugimura, *Langmuir* **2008**, *24*, 12077–12084.

[72] M. Yamaguchi, K. Ikeda, M. Suzuki, A. Kiyohara, S. N. Kudoh, K. Shimizu, T. Taira, D. Ito, T. Uchida, K. Gohara, *Langmuir* **2011**, *27*, 12521–12532.

[73] S. Sun, G. J. Leggett, *Nano Lett.* **2007**, *7*, 3753–3758.

[74] S. Nishimoto, A. Kubo, K. Nohara, X. Zhang, N. Taneichi, T. Okui, Z. Liu, K. Nakata, H. Sakai, T. Murakami, M. Abe, T. Komine, A. Fujishima, *Appl. Surf. Sci.* **2009**, *255*, 6221 –6225.

[75] Z. Xie, C. Chen, X. Zhou, T. Gao, D. Liu, Q. Miao, Z. Zheng, *ACS Appl. Mater. Interf.* **2014**, *6*, 11955–11964.

[76] K. Liu, M. Cao, A. Fujishima, L. Jiang, *Chem. Rev.* **2014**, *114*, 10044–10094.

[77] T. Tatsuma, S. ichiro Tachibana, . Tetsuya Miwa, D. A. Tryk, A. Fujishima, *J. Phys. Chem. B* **1999**, *103*, 8033–8035.

[78] W. Kubo, T. Tatsuma, *J. Am. Chem. Soc.* **2006**, *128*, 16034–16035.

[79] T. Tatsuma, W. Kubo, A. Fujishima, *Langmuir* **2002**, *18*, 9632–9634.

[80] D. M. Spori, N. V. Venkataraman, S. G. P. Tosatti, F. Durmaz, N. D. Spencer, S. Zrcher, *Langmuir* **2007**, *23*, 8053–8060.

[81] T. Tatsuma, S. ichiro Tachibana, A. Fujishima, *J. Phys. Chem. B* **2001**, *105*, 6987–6992.

[82] H. Sugimura, A. Hozumi, T. Kameyama, O. Takai, *Surf. Interface Anal.* **2002**, *34*, 550–554.

[83] V. Naik, A. Fiore, L. Horowitz, H. Singh, C. Wiedinmyer, A. Guenther, J. De Gouw, D. Millet, P. Goldan, W. Kuster, A. Goldstein, *Atmos. Chem. Phys.* **2010**, *10*, 5361–5370.

[84] X. He, W. Yang, X. Pei, *Macromol.* **2008**, *41*, 4615–4621.

[85] K. Matyjaszewski, P. J. Miller, N. Shukla, B. Immaraporn, A. Gelman, B. B. Luokala, T. M. Siclovan, G. Kickelbick, T. Vallant, H. Hoffmannand, T. Pakula, *Macromol.* **1999**, *32*, 8716–8724.

[86] S. Edmondson, V. L. Osborne, W. T. S. Huck, *Chem. Soc. Rev.* **2004**, *33*, 14–22.

[87] K. Matyjaszewski, H. Dong, W. Jakubowski, J. Pietrasik, A. Kusumo, *Langmuir* **2007**, *23*, 4528–4531.

[88] Y. Ma, X. Cao, X. Feng, Y. Ma, H. Zou, *Polymer* **2007**, *48*, 7455 –7460.

[89] A. Samadi, S. M. Husson, Y. Liu, I. Luzinov, S. Michael Kilbey, *Macromol. Rapid Commun.* **2005**, *26*, 1829–1834.

[90] S. G. Boyes, . William J. Brittain, X. Weng, S. Z. D. Cheng, *Macromol.* **2002**, *35*, 4960–4967.

[91] J.-B. Kim, M. L. Bruening, G. L. Baker, *J. Am. Chem. Soc.* **2000**, *122*, 7616–7617.

[92] G. Panzarasa, G. Soliveri, K. Sparnacci, S. Ardizzone, *Chem. Commun.* **2015**, *51*, 7313–7316.

[93] H. Zhang, B. Klumperman, W. Ming, H. Fischer, R. van der Linde, *Macromol.* **2001**, *34*, 6169–6173.

[94] C. Xu, T. Wu, C. M. Drain, J. D. Batteas, M. J. Fasolka, K. L. Beers, *Macromol.* **2006**, *39*, 3359–3364.

[95] H.-J. Koo, K. V. Waynant, C. Zhang, R. T. Haasch, P. V. Braun, *Chem. Mater.* **2014**, *26*, 2678–2683.

[96] S. Sanjuan, P. Perrin, N. Pantoustier, Y. Tran*, *Langmuir* **2007**, *23*, 5769–5778.

[97] P. van de Wetering, N. J. Zuidam, M. J. van Steenbergen, O. A. G. J. van der Houwen, W. J. M. Underberg, W. E. Hennink, *Macromol.* **1998**, *31*, 8063–8068.

Chapter 10

Double side self-cleaning polymeric materials

Plastic materials have had a crucial role in the last century. Nevertheless the growing technologies connected to polymeric materials and their applications in fields ranging from civil architecture to energy production (e.g. solar cells) still need to provide solutions regarding materials durability and self-cleaning[1].

Starting from academic laboratories up to high-tech companies, materials with self-cleaning properties have become a central issue in architecture. Many inorganic materials and coatings equipped with self-cleaning functionalities are now on the market; windows, glasses, outdoor and indoor wall coatings, roofs and pavements are realities in modern cities and houses[2]. The growing request for light and shatterproof materials, strictly connected with the development of high-tech polymers, can be implemented thanks to the proper choice of the kind of polymer to be synthesized and to the study of polymerization conditions.

As described in the previous chapters, the self-cleaning behavior of a surface can be ascribed to two different mechanisms. The first can be connected to the wettability of the surface, the second to its photocatalytic features[3]. Highly hydrophobic surfaces work preventing polar molecules to adsorb at the material interface[4]; water droplets roll away bringing dirt with them. On the other hand, photoactive surfaces capture the incident light (indoor or outdoor), creating oxidative radicals able to mineralize organic molecules adsorbed onto the surface itself. Here, not only the feasibility and the efficiency of the above mentioned proprieties on specific polymeric materials are proved, but also the combination of the two different self-cleaning properties in the same material, in such a way to localize the two functionalities at the two sides of the polymeric film.

Self-cleaning TiO_2 films on polymeric substrates require low temperature and mild synthetic procedures connected to the intrinsic nature of macromolecules[5, 6]. As well explained by Langlet *et al.*[7], these conditions may be very limiting in obtaining efficient photo-induced electron-hole pair generation due to the poor crystallinity of TiO_2 . Langlet and co-authors, in several works[5, 7, 8], proposed the dissolution of tetraisopropyl orthotitanate in ethanol favouring a first crystallinity growth step in acidic or basic conditions; after a spin-coating deposition, the sample was autoclaved to complete the growth. More recently, Horiuchi *et al.*[6] suggested a novel preparation method in which tetraethyl orthotitanate, as Ti source, was stabilized by structure-directing agents that were successively removed under UV radiation. Fateh *et al.*[1, 9] produced a double (SiO_2 + SiO_2/TiO_2) layer onto a polycarbonate support, in which the first layer acts as UV protection to avoid the polymer oxidation and the second, the photoactive one, was obtained by a mixture of commercial photoactive TiO_2 nanopowders and tetraethyl orthosilicate in

acidic ethanol.

Polycarbonate (PC), polyethersulfone (PES) and sulfonated polyethersulfone (SPES) are polymeric materials widely used as a substitutes for heavy and fragile glass, due to their thermal, optical and mechanical properties[10]. PC is very well known and adopted material; PES and SPES are used thanks to their excellent thermal and UV tolerance (*e.g.* very high glass transition temperature and low thermal expansion coefficient), optical features (refractive index: n = 1.63 at λ = 589.3 nm), chemical stability, oxidation resistance, as well as their good mechanical properties and the possibility to easily obtain films or layers[11]. Despite the hydrophilic properties of SPES, due to the presence of sulfonated comonomer, its wetting properties can be modulated thanks to an innovative synthesis with Ionic Liquids (I.Ls.), through an ionic exchange reaction between the potassium cation of sulfonated hydroquinone comonomer of SPES and the cation of I.Ls., that can be substituted with different apolar groups. After the addition of I.Ls., the hydrophobic properties increase as the quantity of sulfonated groups increase due to the higher number of potassium ions available for substitution with I.L. cations.

The hydrophobic properties of I.Ls. are widely known in literature and their features are crucial for resulting hydrophobic self-cleaning materials. As widely described in literature, starting from the fundamental studies of Wenzel[12], in principle, the roughness increases of hydrophobic materials can increase the water contact angle (hydrophobicity) of the material (see Appendix B). The control of a micrometer rough morphology during the synthesis may therefore promote the formation of highly hydrophobic surfaces.

SPES film are flexible and do not offer enough stiffness for long-lasting materials. On the other side, they have high thermal and UV resistivity. In this chapter, a SPES/PC_TiO_2 is therefore designed in order to yield a stable and stiff material with high tolerance to environmental exposure and a double functionality for self-cleaning. On one side, highly hydrophobic surfaces are obtained combining rough morphological features and synthetic skills. SPESs with different sulfonation degrees are successfully synthesized using a sulfonated monomer, 2,5-dihydroxybenzene-3-sulfonate potassium salt (also referred to as sulfonated hydroquinone); ionic liquids (I.Ls.) are used in order to obtain polymeric materials with enhanced hydrophobic features through a cation exchange reaction with SPESs. On the other hand, the polymer was supported by a transparent film of commercial PC (Lexan® 9030) activated by a titania layer. A novel procedure was employed to grow a mechanically stable and photoactive titanium dioxide film onto the polycarbonate support in the absence of any severe thermal treatment. Anti-sticking self-cleaning experiments were performed to show the effectiveness against surface staining. The photoactivity was tested by the degradation of siloxane previously chemisorbed on the surface, as a suitable test in the finger print / oily stain photoactive removal.

10.1 Results and discussion

Here, the synthesis of a double-layer polymeric material aimed at showing one highly hydrophobic anti-sticking side and a second photoactive side was proposed. The double functional material was obtained by promoting adhesion between SPES and PC/TiO_2 films during the final step of SPES drying: dimethyle acetamide(DMAc) acts as an etching agent for both polymers giving rise to a stable composite. The image reported below is representative of the final material (Figures 10.1a and 10.1b).

The hydrophobic side is composed by SPES. After trying several different polymeric materials, we decided to use SPESs due to its relevant mechanical and thermal properties and also due to the good adhesion towards polycarbonate surfaces. This material shows also excellent durability with respect to atmospheric exposure[13, 14].

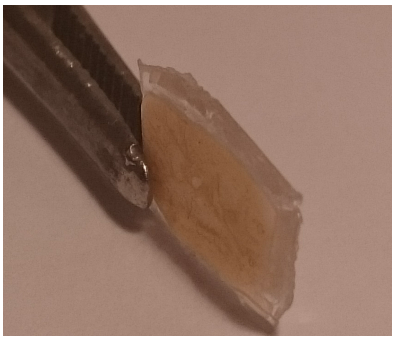

(a) Picture of the final material.

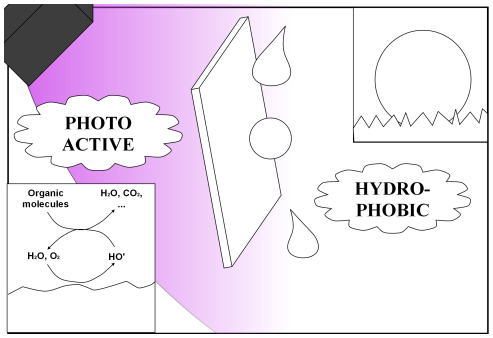

(b) Schematic of the final material.

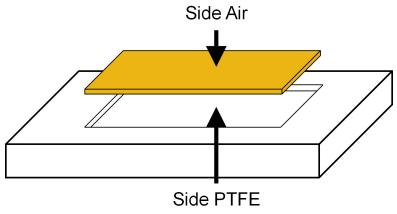

(c) Schematic of the two polymer sides.

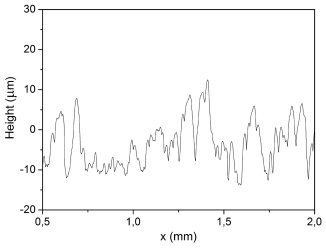

(d) Profilometry of the SPES side with controlled roughness.

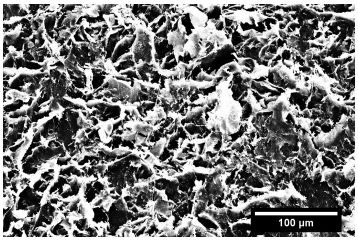

(e) SAM picture of the SPES side with controlled roughness.

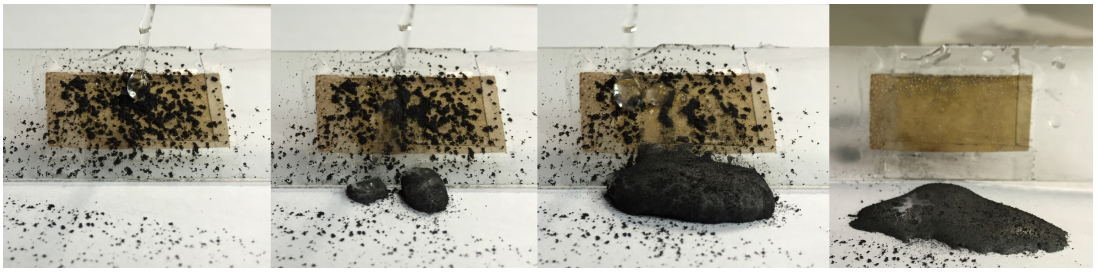

(f) Freeze-frames of a video, which shows water drops rolling on the soiled film as a proof of self-cleaning efficiency.

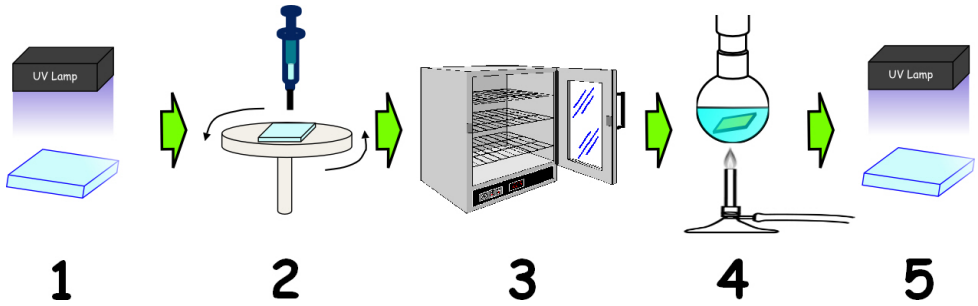

(g) Schematic of the titania film deposition: 1) UV pre-treatment; 2) deposition by spin-coating; 3) thermal treatment in the oven; 4) wet treatment in water and acidic water; 5) UV post-treatment.

Figure 10.1: *Synthesis and structure of the material. Reprinted from Coll. Surf. A, Vol. 483, G. Soliveri et al., Double side self-cleaning polymeric materials: The hydrophobic and photoactive approach, pp. 285-91, Copyright 2015, with permission from Elsevier*

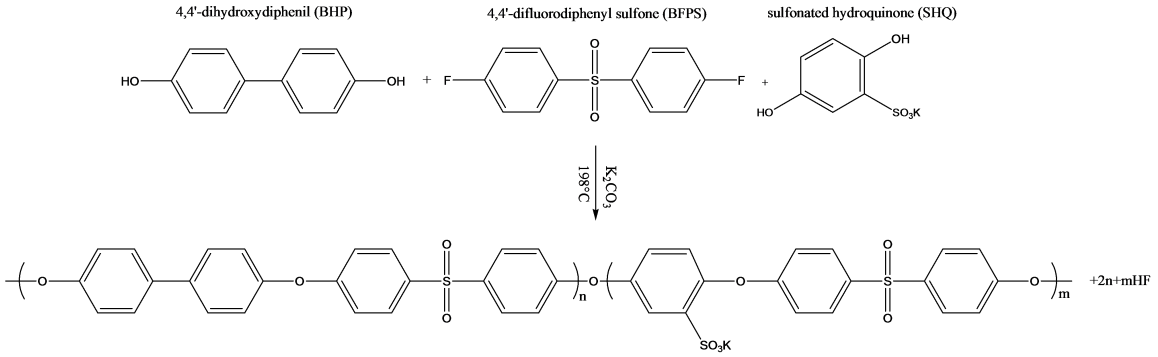

(a) Synthetic route for sulfonated PES.

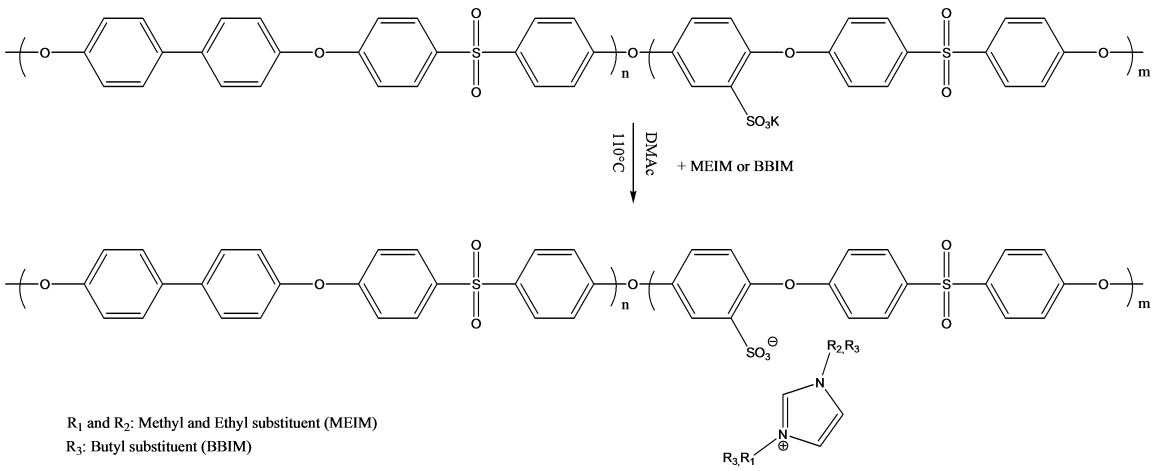

(b) Synthetic route for the synthesis of SPESs with I.Ls.

Figure 10.2: *Synthetic rout of the polymer.*

10.1.1 Highly hydrophobic polymer film

SPES were obtained by a copolymerization among 4,4-difluoro diphenyl sulfone(BFPS), 4,4-dihydroxy diphenyl (BHP) and a sulfonated monomer hydroquinone (Figure 10.2a). Further, together with the more traditional reaction, a novel SPES synthesis was also achieved by adopting the use of ionic liquid cations to promote hydrophobicity in the polymer chain (Figure 10.2b). SPESs with I.Ls. were obtained by ionic exchange reaction between the potassium cation of SPES and the imidazolinium cation of ionic liquids. As a matter of fact, the imidazolinium cations in the ionic liquid, that we synthesized, have apolar alkyl chains with different length that confer hydrophobic properties to the polymer. Table 10.1 reports the SPESs synthesized by classical procedure and by I.Ls. and their substitution degree obtained by ^{1}H NMR results reveal successful ionic exchange reaction for all the SPESs_I.Ls. prepared.

The thermal stability range of all the SPESs synthesized in the present work were evaluated by differential scanning calorimetry (DSC) and Thermogravimetric analysis (TGA) and the glass transition temperatures (Tg) obtained are reported in Table 10.2. All the Tg were found to be higher than 240 $°C$; by TGA curves, it is possible to observe that no weight loss occurs for all samples during the isothermal analyses at 200 $°C$ for 15 hours in air, confirming the high thermal stability of all the samples (data not reported).

Water contact angle analysis is generally used as a test for the wettability of a surface. Here, the relative hydrophilicity or hydrophobicity of a polymer surface were characterized; static water contact angles for films of SPESs and SPESs with I.Ls., obtained from solution casting, were evaluated. The

Samples	SPES	I.L.	% Substitution
SPES_0.5	0.5	-	96
SPES_0.75	0.75	-	93
SPES_1	1	-	98
SPES_I.L_1	0.5	MEIM	81
SPES_I.L_2	0.75	MEIM	68
SPES_I.L_3	1	MEIM	78
SPES_I.L_4	0.5	BBIM	96
SPES_I.L_5	0.75	BBIM	87
SPES_I.L_6	1	BBIM	94

Table 10.1: *SPESs synthesized by classical procedure and by I.Ls., and their substitution degree obtained by* ^{1}*H NMR.*

SPES Samples	Tg ($^\circ C$)	SPES_I.L. Samples	Tg ($^\circ C$)
SPES_0.5	248.7	SPES_I.L_1	247.9
		SPES_I.L_4	246.1
SPES_0.75	302.7	SPES_I.L_2	299.5
		SPES_I.L_5	292.3
SPES_1	270.3	SPES_I.L_3	263.2
		SPES_I.L_6	272.4

Table 10.2: *The table reports the glass transition temperature (Tg) of SPES and SPES with I.Ls. samples.*

samples were solution casted onto a PTFE mold, obtaining a film having a thickness of 120 μm; the wetting properties of the films were measured both at the air-side surface and at the PTFE-side surface (Figure 10.1c). Table 10.3 shows the results obtained. Contact angles of SPESs obtained by ionic liquids are in any case higher than those obtained on the other SPESs. In this latter case, contact angles decrease as the quantity of -SO_3K^+ groups increases due to the high polarity of the -SO_3- groups. The increase of θ_w observed on the PTFE-side with respect to the air-side was probably due to the organization of the polymeric chains occurring during the evaporation of the solvent and to the interaction with the high hydrophobic PTFE surface.

As described in the introduction, the control of the surface morphology can further increase the hydrophobicity of the material and, consequently, enhance its self-cleaning performances. Consequently, a purposely roughened mold was adopted to promote roughness on the PTFE-side of SPES_I.L. polymers. Table 10.4 reports the water contact angle measured at both sides of the material. As expected, the θ_w at the air-side surface were mostly unchanged, while a definite increase of contact angle at the PTFE-side

Samples	θ_w (air side)	θ_w (PTFE side)
SPES_0.5	69 ± 2	83 ± 1
SPES_0.75	60 ± 2	74 ± 1
SPES_1	53 ± 3	59 ± 2
SPES_I.L.1	86 ± 1	108 ± 1
SPES_I.L.2	85 ± 2	116 ± 2
SPES_I.L.3	89 ± 1	121 ± 2
SPES_I.L.4	88 ± 1	123 ± 1
SPES_I.L.5	84 ± 1	124 ± 1
SPES_I.L.6	91 ± 2	128 ± 2

Table 10.3: *Water contact angle of the synthetized SPES films on smooth mold on the two sides.*

Samples	θ_w (air side)	θ_w (PTFE side)
SPES_I.L.1	84 ± 1	134 ± 1
SPES_I.L.2	83 ± 1	137 ± 1
SPES_I.L.3	85 ± 2	141 ± 1
SPES_I.L.4	89 ± 1	136 ± 1
SPES_I.L.5	81 ± 1	141 ± 1
SPES_I.L.6	89 ± 1	143 ± 1

Table 10.4: *Water contact angle of the synthetized SPES films on controlled rough mold on the two sides.*

was observed. Angles reached values up to 143° in the case of SPES_I.L.6. As described by Wenzel[12] (Wenzels equation), a roughness increase on hydrophobic surface (see Appendix B). The roughness recorded in a representative SPES_I.L. sample shows an average roughness of 14 μm (root mean square roughness); a profilometry profile of the surface is reported in Figure 10.1d. The SEM image (Figure 10.1e) shows the roughened surface in which random horizontal scales promote the floating of water drops over the surface.

Self-cleaning surfaces are one of the main areas of application for highly hydrophobic materials. The self-cleaning efficacy of the present films was thus tested. Carbonaceous stains were simulated by homogeneously spreading a graphite fine powder on a representative sample. Figure 10.1f reports the freeze-frames of a video, which shows water drops rolling on the soiled film. The drops roll or jump on the surface, carrying the black dust with them. After a few drops dripping from the top, the surface appears to be clean. The lack of adhesion between the drop and the solid is at the heart of the phenomenon; the pseudo-spherical drop can thus roll away even at low tilting angles of the surface, carrying the carbonaceous residues with it, without leaving any stain on the layer. A fully comparable behavior was shown by all the samples with controlled roughness.

10.1.2 Photocatalytic self-cleaning films

The literature is rich in synthetic examples of photoactive TiO_2 films on glass or on metals[2, 15, 16]. Generally, such films have been synthesized either by complex and invasive physical procedures or by sol-gel, through thin film deposition and subsequent thermal treatment above 350 $°C$. Those procedures cannot be adopted on a polymeric material. Generally, temperatures higher than 150-200 $°C$ or high energetic treatments damage the polymer. As discussed above, few authors handled the problem of depositing crystalline TiO_2 onto polymeric material. Here, the photoactivity and the stability of the film was obtained by low temperature treatments through the combination of different simple steps. A homogeneous non-aqueous titania sol, previously developed by us for different applications[15, 17, 18], was presently promoted with highly crystalline anatase nanopowders as seeds for crystallization. This procedure, as described below, increased the photoactivity enhancing the surface area (roughness) and the total crystallinity of the film[5, 6]. Silica nanopowders were also added to the sol to promote mechanical and UV resistance. Homogeneous films were deposited onto cleaned and UV activated polycarbonate laminas by a spin coating deposition procedure (step 1-2, Figure 10.1g). A first drying step under nitrogen flow and a second in a forced ventilation oven (step 3, Figure 10.1g) were crucial in order to increase the adhesion between the film and the polymer; a soft xerogel with good adhesion was obtained[8]. Furthermore, the aging process in oven for 20 hours promoted the growth of crystallites inside the layer.

The hydrolysis was completed by a wet treatment, first in milliQ water (at spontaneous pH), and subsequently in acidic conditions (10^{-4} M, HNO_3) at 70 $°C$ (step 4, Figure 10.1g). Different strong acids

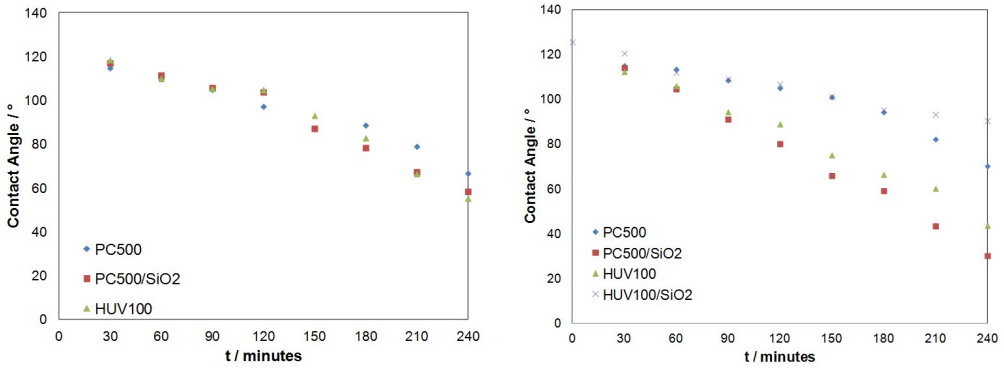

(a) 2-layer. **(b)** 10-layer.

Figure 10.3: *Degradation kinetics of the siloxane chains on titania films filled by different nanopowders and after the deposition of a different number of spin-coated layers. Reprinted from Coll. Surf. A, Vol. 483, G. Soliveri et al., Double side self-cleaning polymeric materials: The hydrophobic and photoactive approach, pp. 285-91, Copyright 2015, with permission from Elsevier.*

was tested at different concentrations. The present conditions were chosen as a trade-off between kinetics of hydrolysis and mechanical film and substrate stability. The nitric acid, furthermore, contributes to the oxidation of the organic surfactant (detrimental for the photoactivity) inside the film[2, 6]. A final step of UV irradiation (step 5, Figure 10.1g) was required for further mineralizing organics in the film, thanks to photolysis and photo-production of radicals. After the irradiation the contact angle changed from 40-50° to almost 0°. The sample stored for 20 hours in the dark showed that the contact angle rised back to 40-60°; again under UV illumination, it fell to less than 10°. That behavior was cyclical and reproducible. This phenomenon is well known as photo induced hydrophylicity and this was the first proof of photoactivity of the film[2].

A further confirmation of photoactivity was achieved by degradation of chemisorbed hydrophobic organic chains (SILRES 1701) monitoring the water contact angle decrease by a procedure previously reported in literature for the simulation of finger print / oily stain self-cleaning[16, 17, 19]. The presence of silane molecules chemisorbed at the film, shifted the θ_w value from hydrophilic (40 - 0°) to $\sim$ 120°. Under UV light, electron-hole pairs were created at the film interface making the surface reactive. Peroxide and superoxide radicals were generated[2, 20, 21], oxidizing the organic moieties of the chemisorbed siloxanes, bringing back the θ_w to the hydrophilic value. Figure 10.3 shows the degradation kinetics of the siloxane chains on titania films filled with different nanopowders and after the deposition of a different number of spin-coated layers. All the 2-layers samples (Figure 10.3a) seem to degradate the siloxane film with the same kinetics. The 10-layer ones resulted much faster than the two layer ones, mainly in the case of the sample composed by 1:1 weight ratio of silica/titania (PC500), as fillers, in the sol. The sample turned from hydrophobic to hydrophilic (less than 30°) after 4 hours. After many hours of irradiation, the PC substrates, by the naked eye, appear not to be modified by the treatment. It is interesting to observe that the deposition of the titania layer improves the surface hardness of the PC film: the hardness measured by the Wolff-Wilbourne procedure passes from 2B for the pristine PC to H for the TiO_2 covered PC. H-label actually represents an increasing hardness with respect to B or F labels (See Appendix C).

10.2 Conclusion

The general request of polymeric materials with tailored technological features is a driving force for scientific and industrial research in this area. Here, one of the crucial aspects connected with the large scale

Samples	Nominal DS	BFPS		BHP		SHQ		K_2CO_3	
	meq SO_3 g_{pol}^{-1}	g	mmol	g	mmol	g	mmol	g	mmol
SPES_0.5	0.5	3.17	12.45	1.85	9.92	0.58	2.55	3.72	26.89
SPES_0,75	0.75	3.15	12.36	1.69	9.05	0.76	3.34	3.70	26.77
SPES_1	1	3.10	12.18	1.32	7.10	1.16	5.10	3.64	26.31

Table 10.5: *Reagents composition for SPESs with different substitution degree.*

utilization of polymeric materials was approached, *i.e.* the need of keeping the surfaces clean, free from dust and dirt. Starting from a structured, multilayer, organic/inorganic composite, we developed a highly versatile material in which one side degradates adsorbate stains and pollutants under irradiation, thanks to a thin photoactive titania layer supported on polycarbonate. The other side prevents the adhesion of stains and pollutants, thanks to a highly hydrophobic SPES_I.Ls. film with controlled morphology in the micrometer scale. While polycarbonate confers stiffness to the final material, both titania and SPES films, in addition to the self-cleaning properties, provide UV and thermal resistivity, making the material suitable for both indoor and outdoor applications. Further, depending on the final application, the composite can also be easily colored. In fact the polar character introduced in SPES by the sulfonation allows inorganic pigments to be fully compatible with the polymer chains and consequently to impart different colors and shades to the final material.

10.3 Specific procedures

Synthesis of sulfonated polyethersulfones (SPESs) Three SPESs with increasing degree of sulfonation (DS, expressed as meq SO_3 g^{-1} of polymer), -SPES_0.5, SPES_0.75, SPES_1- have been synthesized. The amount of the monomers used for the syntheses are reported in Table 10.5. 4,4-difluoro diphenyl sulfone (BFPS), 4,4-dihydroxy diphenyl (BHP), 2,5-dihydroxy benzene- 3-sulfonate potassium salt (SHQ) and K_2CO_3 were introduced into a 100 cm^3 one neck round-bottom flask equipped with magnetic stirring. Toluene (Tol, 30 mL) and N-methyl-2-pyrrolidone (NMP, 25 mL) were loaded in order to have a 10 % mass/volume concentration of the reactants in the solution. The flask, equipped with a modified Dean-Stark device and under nitrogen atmosphere, was immersed in an oil bath and the polymerization reaction was carried out under reflux for 7 hours. Then temperature was gradually increased from room temperature to 198 $°C$; water formed during the reaction was removed as an azeotrope with toluene through the modified Dean-Stark device. After complete water removal, the reaction mixture was kept at 198 $°C$ for 18 hours and, then, let to cool till room temperature. A viscous dark-purple solution was precipitated into a large excess of water under stirring and a brown solid precipitate was obtained. The solid was recovered by filtration and then residual monomers and K_2CO_3 were removed carefully washing the solid with milliQ water; the purification procedure was repeated for several times. The resultant polymer was dried in a vacuum oven (about 4 mbar) at 50 $°C$ for 24 hours. Real DS was evaluated by ^{1}H NMR.

Synthesis of ionic liquids (I.Ls.) Two ionic liquids were prepared: 1-Ethy-l,3-Methyl-Imidazolinium-ethyl sulfate (MEIM) and 1,3-dibutyl-imidazolinium-dibutyl phosphate (BBIM). To synthesise MEIM, diethyl sulfate (2.87 g; 1.86 10^{-2} mol) and 1-methylimidazole (1.25 g; 1.52 10^{-2} mol) were introduced in a one-neck round bottom flask equipped with magnetic stirring; the flask, under nitrogen atmosphere, was put into an oil bath and the synthesis was kept at 110 $°C$ for 1 hour and then cooled to room temperature.

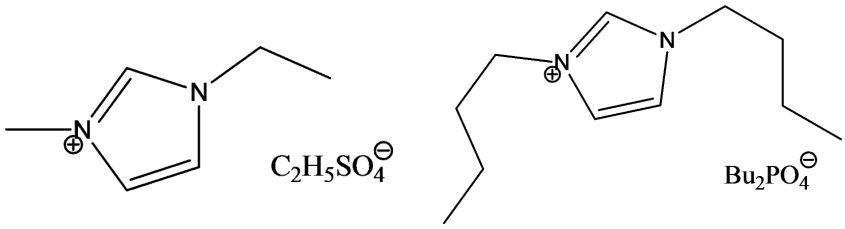

(a) 1-Ethy-l,3-Methyl- Imidazolinium- ethyl sulfate (MEIM).

(b) 1,3-dibutyl- imidazolinium- dibutyl phosphate (BBIM).

Figure 10.4: *Cation and anion structures employed.*

The product was purified with respect to unreacted monomers by several washings with dichloromethane. Purity was evaluated by ^{1}H NMR. The synthesis of BBIM, from 1-bromobutane (2.55 g; 1.86 10^{-2} mol) and 1-butylimidazole (1.89 g; 1.52 10^{-2} mol), was performed according to the procedure reported for MEIM and then the bromide anion was replaced by mixing the reaction mixture with potassium dibutyl phosphate (2.53 g; 1.86 10^{-2} mol) in water. The product successfully passed nitrate tests for bromide impurities. Figure 10.4 shows the structures and abbreviations of all the ions used.

Synthesis of SPESs with I.Ls. An ionic exchange reaction between the potassium cation of SPESs and the cations of the two I.Ls. synthesized, BBIM and MEIM, was conducted. The cation exchange reaction was performed as follows: SPES and I.L. were introduced in a one-neck round bottom flask containing dimethylacetamide (DMAc, 10 mL) equipped with magnetic stirring; the synthesis was kept under nitrogen atmosphere for 24 hours at 150 $°C$ in an oil bath and then cooled to room temperature. The reaction mixture was precipitated by a large amount of water and recovered via filtration; the product was purified in order to eliminate the residual monomers by several washings with water. The resultant polymer was finally collected by filtration and fully dried in a vacuum oven (about 4 mbar) at 50 $°C$ for 24 hours. The degree of substitution of the cation was measured via ^{1}H NMR.

Characterization of polymers ^{1}H NMR (nuclear magnetic resonance) data were obtained with a BRUKER spectrometer (400 MHz). Samples for the analyses were prepared by dissolving 10-15 mg of polymer (SPESs and SPESs with I.L.s) in 1 ml of dimethyl sulfoxide-d6 (DMSO-d6) and 8-10 mg of I.L.s in 1 ml of D_2O. DSC analyses were conducted using a Mettler Toledo differential scanning calorimetry (DSC), on samples weighting from 5 to 10 mg each. Glass transition temperature (Tg) of SPESs and SPES_I.Ls. were measured using the following temperature program: heating from 25 $°C$ to 330 $°C$ at 10 $°C$ min^{-1} followed by 5 min at 330 $°C$ to eliminate residual internal stresses after the synthesis; cooling from 330 $°C$ to 25 $°C$ at 10 $°C$ min^{-1}; 5 min at 25 $°C$ and heating from 25 $°C$ to 330 $°C$ at 10 $°C$ min^{-1}. Tg was obtained from the second cycle time and read as the midpoint of the curve. Thermogravimetric analysis (TGA) were performed at 200 $°C$ for 15 hours in air using a TGA4000 Perkin Elmer instrument; tests were conducted on samples weighting from 5 to 10 mg each.

Preparation of SPESs-I.Ls. films SPESs films with I.Ls. were obtained by solution casting; polymers were dissolved in DMAc using 21 % mass/volume concentration. The solution was cast onto a PTFE (polytetrafluoroethylene) mould either smooth (S) or with controlled roughness (R) and the solvent was evaporated for 18 hours in a vacuum oven (about 4 mbar) at 40 $°C$.

Characterization of the polymeric film Film thickness was evaluated by Nikon eclipse ME600 optical microscope with Nikon digital camera light DS-Fi1, software Nis-Elementi BR, magnification 50X. The roughness of the films was characterized by profilometry, using a Bruker DektakXT contact profilometer.

Synthesis of the PC TiO_2 side High optical grade PC laminas (PC Lexan 9030, thickness 1 mm) were carefully cleaned by quick immersion in concentrated H_2SO_4 and then rinsed in milliQ water. The dried surface was then irradiated under UV-light in order to increase its hydrophilicity. A previously employed TiO_2 sol (Appendix C, page 231) was promoted by nanometric silica (Sigma Aldrich, 5-15 nm) and by commercial anatase powders: Millenium PC500 or Hombikat UV 100. 1 mg of nano-powder (titania or the mixture of titania and silica) was dispersed in 1 mL of ethanol; then, 1 mL of titania sol was added and a homogeneous mixture was obtained by sonication. After the deposition by spin-coating onto the polycarbonate support, the film was dried under N_2 flow for few minutes, and quickly treated in an oven (forced ventilation) at 90 $^\circ C$ for 20 hours. The dried sol-gel film (xerogel) obtained was aged in milliQ water at 70 $^\circ C$ for 20 minutes and subsequently in a HNO_3 solution (10^{-4} M) for 10 minutes at the same temperature. The acidity was removed by milliQ water flow, followed by drying under N_2. Then, the sample was irradiated under UV lamp for 4 hours. A double functional material was obtained by promoting adhesion between SPES and PC/TiO_2 films during the final step of SPES drying: DMAc acts as an etching agent for both polymers giving rise to a stable composite.

Photoactivity test the photocatalytic activity of the device was tested by following in time the degradation of a layer composed by the hydrophobic SILRES 1701 previously deposited onto the titania layer. The molecules were chemisorbed at the tested surface by the chemical vapor deposition protocol previously reported in Appendix C, page 232.

Further details about synthetic procedures and characterizations can be found in Appendix C.

References

[1] R. Fateh, R. Dillert, D. Bahnemann, *Langmuir* **2013**, *29*, 3730–3739.

[2] A. Fujishima, X. Zhang, D. A. Tryk, *Surf. Sci. Rep.* **2008**, *63*, 515 –582.

[3] I. P. Parkin, R. G. Palgrave, *J. Mater. Chem.* **2005**, *15*, 1689–1695.

[4] M. Callies, D. Quere, *Soft Matter* **2005**, *1*, 55–61.

[5] M Langlet, A Kim, M Audier, C Guillard, J. Herrmann, *Thin Solid Films* **2003**, *429*, 13 –21.

[6] Y. Horiuchi, H. Ura, T. Kamegawa, K. Mori, H. Yamashita, *J. Mater. Chem.* **2011**, *21*, 236–241.

[7] M. Langlet, A. Kim, M. Audier, C. Guillard, J. Herrmann, *J. Mater. Sci.* **2003**, *38*, 3945–3953.

[8] M. Langlet, A. Kim, M. Audier, J. Herrmann, *J. Sol-Gel Sci. Tech.* **2002**, *25*, 223–234.

[9] R. Fateh, A. A. Ismail, R. Dillert, D. W. Bahnemann, *J. Phys. Chem. C* **2011**, *115*, 10405–10411.

[10] M. Al-Ibrahim, H. K. Roth, S. Sensfuss, *Appl. Phys. Lett.* **2004**, *85*, 1481–1483.

[11] Y. Li, C. Cao, T.-S. Chung, K. P. Pramoda, *J. Membrane Sci.* **2004**, *245*, 53 –60.

[12] R. N. Wenzel, *Ind. Engin. Chem.* **1936**, *28*, 988–994.

[13] H. WenYu, W. BeiBei, G. Li, W. Feng, D. NanSheng, et al., *Fresenius Environ. Bull.* **2009**, *18*, 2259–2267.

[14] J.-D. Kim, A. Donnadio, M.-S. Jun, M. L. D. Vona, *Int. J. Hydrogen En.* **2013**, *38*, 1517 –1523.

[15] G. Maino, D. Meroni, V. Pifferi, L. Falciola, G. Soliveri, G. Cappelletti, S. Ardizzone, *J. Nanopart. Res.* **2013**, *15*, 2087.

[16] A. Antonello, G. Soliveri, D. Meroni, G. Cappelletti, S. Ardizzone, *Catal. Today* **2014**, *230*, 35 –40.

[17] G. Soliveri, V. Pifferi, G. Panzarasa, S. Ardizzone, G. Cappelletti, D. Meroni, K. Sparnacci, L. Falciola, *Analyst* **2015**, *140*, 1486–1494.

[18] A. Antonello, G. Brusatin, M. Guglielmi, V. Bello, G. Mattei, G. Zacco, A. Martucci, *J. Nanopart. Res.* **2011**, *13*, 1697–1708.

[19] Y. Paz, *Beilstein J. Nanotech.* **2011**, *2*, 845–861.

[20] T. Tatsuma, W. Kubo, A. Fujishima, *Langmuir* **2002**, *18*, 9632–9634.

[21] W. Kubo, T. Tatsuma, *Appl. Surf. Sci.* **2005**, *243*, 125 –128.

Chapter 11

Self-cleaning properties in engineered sensors for dopamine electronalytical detection

New types of sensing devices have been recently attracting tremendous attention because of environmental concerns and biomedical demands[1–7]. The fast development of nanotechnology has paved the way for the design of tailored systems exhibiting superior properties[8–12].

Composite oxide/metal systems employing silver nanoparticles (Ag NPs) have gained increasing attention[10, 11, 13] especially in the case of electroanalysis for trace detection, due to Ag NPs unique properties. Silver possesses the highest electrical conductivity and a good stability at different potentials and pH, and, more relevantly, it shows large electrocatalytic properties compared to other metals. For these reasons, it is a widely used electrode material and the advent of nanotechnology has further improved its possibilities. As a matter of fact, compared to the traditional bare noble metal electrodes, nanostructured surface morphologies can enhance the response of the sensing systems. The high surface to volume ratio, proper of nano-dimensions, enormously increases the availability of interaction sites for the analyte, improving sensitivity and lowering detection limits, fundamental characteristics for trace analysis. Moreover, the small dimensions may allow to control locally the sensing process, in terms of analyte diffusion mechanism and site-analyte recognition. The effects described above are particularly maximized in the case of well ordered structures. A problem often encountered during the use of these nanosized, complex devices, is represented by passivation and fouling phenomena leading to a poor reusability[1, 10].

Passivation and fouling are mainly due to electrochemically produced byproducts or interfering compounds present in the analyzed complex real matrix, chemisorbed at the electrode surface. The conventional cleaning procedures applied to bulk metal electrodes (mechanical or electrochemical etching) are inapplicable in the case of metal nanoparticles, since these systems can be irreversibly modified or the nanoparticles even removed from the electrode surface. This is a critical limitation for a commercial sensor which, apart from high sensitivity, low detection limits and high selectivity, should be also characterized by portability, online and onsite usability and especially re-usability[1, 4]. In this context, self-cleaning electrodes could represent a step beyond the current state of the art, and TiO_2 can play a central role in the development of such technology. A very recent work by Kamat et al.[14] has reported a *detect and destroy* approach for SERS analyses, in which the combination of SERS experiments supported by Ag

NPs, with the photocatalytical degradation of the molecule by TiO_2 is described.

On the other hand, the study of self-cleaning layers potentially applicable on whatever electrode surface to prevent passivation, caused either by silver oxidation or by interferents presence, has not been explored before. Literature reports only few examples of self-cleaning electrodes for hydrogen detection[15], and for methanol electro-oxidation or glucose determination[16, 17]. These systems are based on anodized titania nanotubes supports decorated with noble metals (Pt and Pd), where the titania photoeffect is exploited to restore the activity of the device. In the literature, neither a proper electrode design for re-usability, nor a deep study of fouling/cleaning effects on the electroanalytical parameters are investigated.

In this very promising context, an innovative self-cleaning engineered device is proposed in this chapter to be used as an electroanalytical sensor. The device is composed by a transparent metal-oxide composite multilayer in which Ag NPs are deposited to give a controlled and organized structure between a bottom silica and a top titania layer. Each component of the device was chosen for its relevant properties: the silica layer was essential to govern the distribution of silver nanoparticles, which were the actual sensing tool, imparting electrocatalytic properties and conductivity between the two semiconducting oxides; the top titania film was used to confer the self-cleaning properties, but also to protect Ag NPs from irreversible oxidation and deterioration.

First, in order to check the applicability of the designed device in a real, challenging and complex system, the electroanalytical detection of dopamine was studied[18, 19]. Dopamine is a neuro-transmitter with great biomedical and analytical interest, since the molecule anomalous levels are diagnostic for the Parkinsons disease and for many neurological pathologies. In the literature, its determination has been faced by different electrodes and strategies[20–22], but, in almost all cases, fouling and passivation of the electrode surface affected the measurements. In particular, the chemisorption of dopamine or of its byproducts at metal and oxide interfaces makes the reusability of the electrode generally impossible[18]. The present self-cleaning sensor is *ad hoc* designed for the detection of such critical molecules, affording a total sensitivity recovery after fouling and cleaning by a simple UV irradiation step. Moreover, aging, over-usage and environmental conditions did not introduce appreciable modifications of the initial characteristics of the electrode.

To favor the applicability in non specialized laboratories, different cleaning lamps and layout were tested, with the final aim to make the procedure simpler and safer. Moreover, such self-cleaning device appears particularly interesting for *in-situ* application. The cleaning of the electrode immersed in the analyte solution was also proved.

11.1 Results and discussion

11.1.1 Device assembly and structure

The device, described here, was engineered with the aim of tuning its photocatalytic and electrochemical properties in order to obtain an electroanalytical sensor for the detection of molecules with biomedical interest. The synthesis was controlled in order to promote the self-cleaning properties and tune the electocatalytic features by modulating the sandwich composition and Ag NPs organization, preserving the film transparency. Figure 11.1a shows the material architecture.

Each layer/component was finely designed in order to control the final performance: support, silica layer, bifunctional siloxane ((3-Aminopropyl)triethoxysilane, APTES), Ag NPs, titania. As the support, a conductive glass, withstanding calcination, FTO, was selected. The subsequent presence of a silica

layer was chosen in order to promote the dispersion of the Ag NPs. The layer of silica was obtained by dip coating the FTO surface in a non-aqueous sol, synthesized by the procedure reported by Wang et al.[23] (Appendix C). The subsequent calcination conditions were chosen in order to decompose the organic components of the sol while maintaining the film transparency and increasing its mechanical stability and adhesion onto the support. The role played by time, temperature and atmosphere were preliminarily studied to tune the reactivity of the surface. A calcination step of one hour at 400 $°C$ in N_2 flow was finally adopted. The calcined silica layer was further grafted by a bifunctional siloxane in order to promote stable attachment of Ag NPs. APTES was chosen as a coulombic binder between the SiO_2 surface and the Ag NPs. APTES ethoxy groups generally react with OH groups at the oxide surface, exposing NH_3^+ groups at the interface[24]. The negative charged Ag NPs (Z-potential measurement, Figure 11.1e) strongly interact with NH_3^+ groups, so that the number and the arrangement of APTES molecules highly influence the concentration and disposition of Ag NPs at the surface.

The Ag NPs, synthesized by the procedure of Panzarasa[25], were stabilized by PVP10 to avoid the presence of agglomerates and multilayers at the functionalized surface. The HR TEM picture (Figure 11.1e, inset) shows particles of around 10 nm with high crystallinity (the lattice spacing of $\sim$ 230 pm corresponds to (111) planes of silver *fcc* cell) and quite sharp distribution. The aqueous particle suspension presented the typical plasmonic resonance associated with Ag NPs of dimensions lower than 30 nm (Figure 11.1f, inset)[26]. After dipping 15 minutes in such a suspension, the material showed the orange colour correlated with the spectrum reported in Figure 11.1f. The red-shift of the band derived from a change of environment, as reported by Evanoff et al.[27] Finally, the engineered sensor is covered by a TiO_2 layer with the aim to impart photoactivity and self-cleaning properties (see Chapter 8 and Appendix C). The oxide external layer was demonstrated to confer further crucial properties to the material, such as protection for the Ag NPs from unavoidable oxidation/deactivation ensuing from the contact with the environment. The TiO_2 film was obtained by dip-coating the multilayer device in a non-aqueous sol, synthesized following a procedure previously developed by our group[28]. Temperature and, particularly, the atmosphere of calcination were chosen in order to prevent Ag oxidation. In the absence of the protective TiO_2 layer, Ag degradation is generally observed after few days of environmental condition exposure, dramatically changing both the chemical nature and the morphology of such particles. We tested different times and conditions for the TiO_2 crystallization and growth. A fast calcination of 1 hour at 400 $°C$ under N_2 flow allowed the organic compounds mineralization and the growth of the oxide crystallinity, without altering the film transparency (Figure 11.1b).

The XRD lines (Figure 11.1d) of the sandwich show the predominance of the anatase polymorph, with traces of brookite. The peaks of cassiterite (SnO_2), proper of the FTO support are also appreciable. The size of anatase crystallites was evaluated to be 17 nm. The cross-section SEM picture, reported in Figure 11.1c, reveals two distinct and homogenous layers, 550 nm and 150 nm in thickness, for SiO_2 and TiO_2 , respectively. Thickness data were confirmed by Filmetrics, showing reproducible values in different areas of the film. The SEM top picture shows good homogeneity of the surface.

The role of silver in electrocatalysis both as massive electrodes and as nanoparticles has been amply discussed in the literature[30–32] also for sensing applications[10, 11, 33], where Ag can change favourably the potential of redox reactions, also allowing interferences management.

The actual presence of Ag in the device was shown by cyclic voltammetry performed in the absence of an electroactive probe. In fact, when no probe reactions are present (absence of redox current), the surface of the electrode, in terms of its intrinsic nature, can be studied. Electrodes without Ag behaved similarly to bare FTO, showing completely capacitive voltammograms without peak formation (Figure 11.2a, curve 1), typical of oxide materials. In the presence of Ag (Figure 11.2a, curve 2 and 3), oxidation and reduction

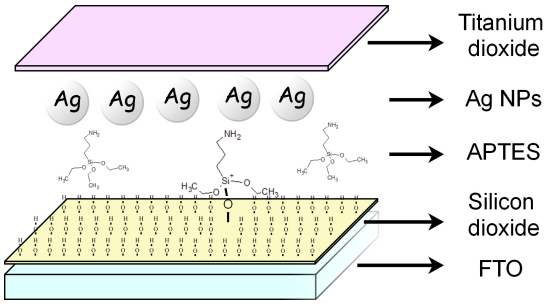

(a) Schematic description of the architecture.

(b) Photograph of the final device on printed white paper, in order to show transparency.

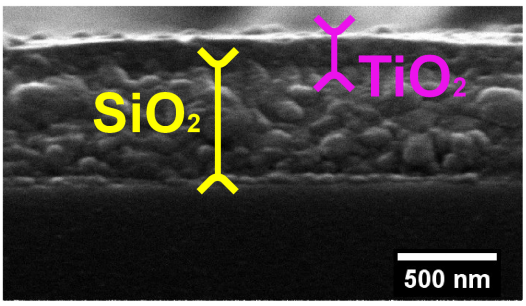

(c) X-ray diffraction pattern of the titania top layer.

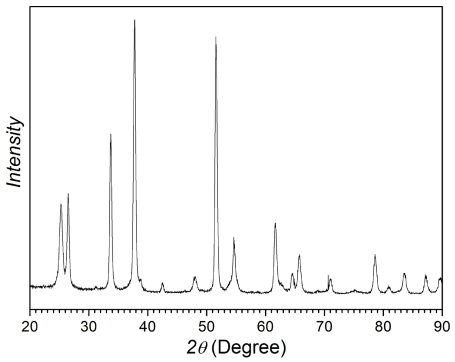

(d) SEM cross section of the films.

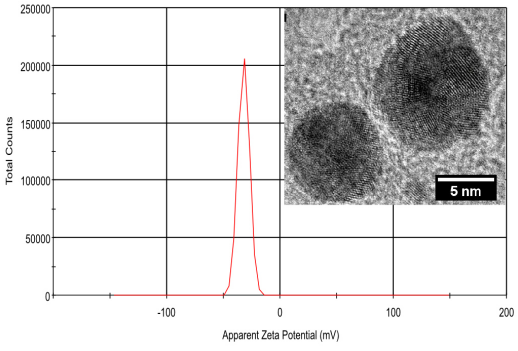

(e) Z-potential spectrum of Ag NP suspension; inset: Ag NP TEM picture.

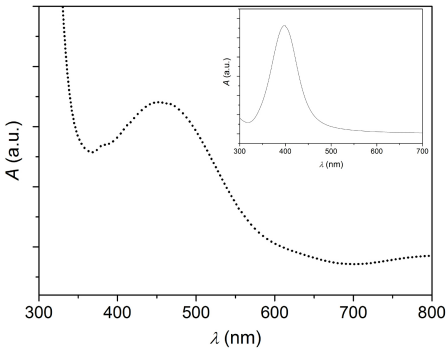

(f) UV-vis spectrum of the Ag NPs grafted on the silica surface; inset: UV-vis spectrum of the Ag NP suspension.

Figure 11.1: *Structural characterization of the sensor. Ref.[29]. Published by The Royal Society of Chemistry.*

peaks around + 0.25 V (SCE) and + 0.1 V (SCE) appeared, as generally reported[34, 35], since silver, as other metals, can be reduced or oxidized by varying the potential.

Moreover, silver, due to its reactive nature, can be oxidized by oxygen present in the air, with passivation effects. To avoid this phenomenon, protective oxides are often used on metal surfaces[36]. In our case, the titania layer provided a protective action for Ag NPs. This effect can be proved by comparing the final electrode (Figure 11.2a, curve 3) with a device prepared in the same manner, but without the final TiO_2 layer (Figure 11.2a, curve 2). In the case of titania covered silver nanoparticles, higher Ag peak currents were observed, reflecting the presence of more active and non-oxidized silver nanoparticles. A key point to take into consideration in the use of modified electrodes supporting silver for sensor applications is the density, distribution and organization of nanoparticles on the electrode surface[10]. In electroanalysis, the analyte reacts on the surface of the electrode, generating an increase of the measured current. The resulting signal is the sum of the capacitive background current and of the reaction current, which is the sole related to the analyte concentration . The voltammograms shape is related to the NPs size and density[37, 38]: a steady-state sigmoidal step can be registered for convergent independent diffusion at NPs low coverage (Figure 11.2c, Scheme 1), while a peak is obtained in the case of planar diffusion regime at high NPs coverage (Figure 11.2c, Scheme 2). In order to obtain high sensitivity and low detection limits, high faradaic and low capacitive currents have to be preferred. An optimal disposition for this purpose is an ordered array of well isolated nanoparticles, where the convergent mass transport must be predominant[38, 39]. In this case, the current response is greater with respect to that of a macroelectrode. In fact, while the current at a macroelectrode follows the Randles-Sevčik equation (Equation 11.1)[40]:

$$I_{peak} = 2.69 \cdot 10^5 \, n^{3/2} \, D^{1/2} \, C_{bulk} \, \nu^{1/2} \, A \tag{11.1}$$

(where I_{peak} is the current in amperes, n is the number of electrons involved in the reaction, D is the diffusion coefficient in ($cm^2\ s^{-1}$), C_{bulk} is the bulk concentration of active species in (mol cm^{-3}), ν is the potential scan rate in (V s^{-1}) and A is the surface area in cm^2), in the case of a nanoparticle array of the same macrodimensions of the previous macroelectrode in which the nanoparticles are at a distance of 10 r (where r is the radius of the nanoparticle), the limiting current at each nanoparticle and the total array current[10–12, 39] are given by:

$$I_{lim} = 8.71 \, n \, F \, D \, C_{bulk} \, r \tag{11.2}$$

$$I_{tot} = I_{lim} \, \frac{A}{(10\, r)^2} = \frac{(8.71 \, n \, F \, D \, C_{bulk} \, A)}{100 r} \tag{11.3}$$

In Equation 11.3, it is evident the current dependence from the particle radius (the smaller, the better) and the independence from the potential scan rate, since a convergent mechanism is attained. Using typical values for the parameters and a value of $r = 10\ nm$, a current increase of seven hundred times can be obtained[10] with respect to the macroelectrode. It is worthwhile noticing that the above considerations are valid assuming that the nanoparticles are sufficiently far apart as to be diffusionally independent. Too closely packed electrodes result in the overlapping of the diffusion layers, characterized by the loss of convergent diffusion. The nearest-neighbours NPs minimum distance of 10 r required for diffusional independency, although debated[38, 41], is assumed to be a good indicative value[10]. Moreover, the NPs array is characterized by a larger surface area-to-volume ratio of the electrocatalytic material. This fact lowers the costs of the electrodes and, increasing the active sites, enhances the signal-

to-noise ratio, particularly abating the capacitive background currents, which are dependent to the real active surface area[10].

Devices based on ordered arrays are normally produced lithographically by long, difficult and costly procedures and only few papers rely on simple and effective techniques[39], since simpler methodologies usually produce random or uncontrollable distributions. The preparation method presented in this work allows the obtainment of organized and regularly distributed arrays of Ag NPs by a simple and low cost procedure. The key factor is represented by the interaction sites for silver, produced by NH_3^+ APTES groups, in terms of quantity and distribution. The conditions of APTES deposition and silica calcination were carefully tuned in order to produce well-organized and separated sites. With the method reported by Moon et al.[42], the concentration of amino groups at the surface was almost double for bare FTO (10 (NH_2 nm^{-2})) compared to FTO covered by silica (5 (NH_2 nm^{-2})). In the latter case, a lower quantity of silver nanoparticles was expected on the silica layer. Figure 11.2b shows voltammograms registered for the two Ag NPs electrodes, differing only for the presence or absence of the silica layer. When Ag nanoparticles are deposited on silica (Figure 11.2b, curve 1), a lower quantity of metal is present, as demonstrated by the above considerations, and a lower peak current is registered in comparison with Ag NPs directly deposited on bare FTO (Figure 11.2b, curve 2). It is important to say that the current registered in the presence of the non-conductive silica layer is, anyway, really high and of the same order of magnitude of the electrode without silica. The contribution brought by the distribution (array) of isolated NPs (convergent diffusion) is evident and will be of paramount importance in the detection of analyte at trace levels, as already explained. The distribution of silver nanoparticles on silica was studied by registering cyclic voltammograms, this time in the presence of a redox probe ($K_4[Fe(CN)_6]$), before TiO_2 deposition (Figure 11.2c). Only in the presence of a redox reaction the diffusion mechanism and, as a consequence, the distribution of nanoparticles can be studied. Figure 11.2c curve 1 shows a step-shaped voltammogram typical of a convergent diffusion mechanism on isolated ordered nanoparticles (scheme 1) in the case of Ag NPs anchored on silica. On the other hand, a peak-shaped voltammogram (Figure 11.2c, curve 2), reflecting semi-infinite diffusion on non isolated particles (scheme 2), was observed in the case of silver directly deposited on FTO.

Figure 11.2d shows electrochemical impedance spectroscopy (EIS) measurements in the presence of the redox probe $K_4[Fe(CN)_6]$. The analyses were performed on different electrodes at different steps of preparation and at different compositions of the sandwich. Impedance analysis measures the current response of the device to an external potential variation and allows modelling the systems by an electrical circuit. In the complex plane plots (Figure 11.2d, Bode plots shown in Figure 11.2e), the semicircle shape common to all the combinations can be represented by the same equivalent circuit (Figure 11.2f), composed by the solution resistance (R_Ω) in series with a parallel formed by the charge transfer resistance (R_{CT}) and the double layer capacitance (CPE_{DL}). This trend of experimental data and circuits derived from modelling are typical for a redox reaction of a model probe at the electrode. From the diameter of the semicircle, we obtained the values of the charge transfer resistance (Table 11.1), critical to describe the electron transfer between the model probe and the electrode. As expected, these values increase enhancing the number of layers, while the introduction of Ag NPs produces a drastic decrease of resistance in otherwise identical conditions. We demonstrated the crucial presence of Ag nanoparticles in order to enhance the electrode conductivity in the architecture of our final device, since electrons of the probe reaction can more easily pass throughout the two semiconductor layers.

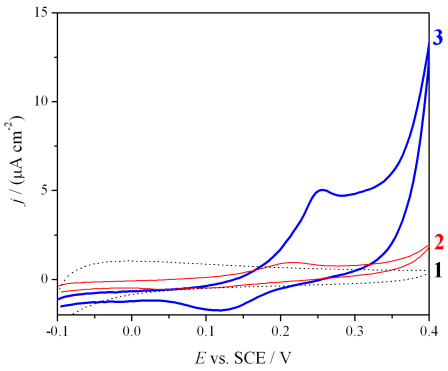

(a) Study of the effect of titania layer by CV in absence of probe molecules (curve 1: FTO+SiO_2+TiO_2 ; curve 2: FTO+SiO_2+Ag; curve 3: FTO+SiO_2+Ag+TiO_2).

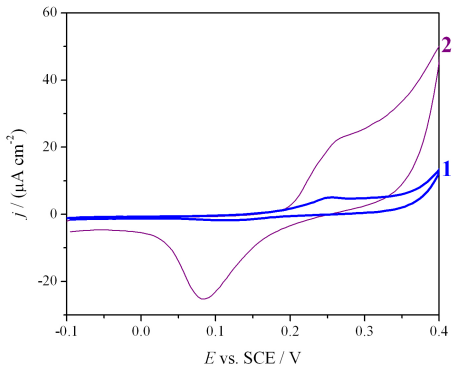

(b) Study of the effect of silica layer by CV in absence of probe molecules (curve 1: FTO+SiO_2+Ag+TiO_2 ; curve 2: FTO+Ag+TiO_2).

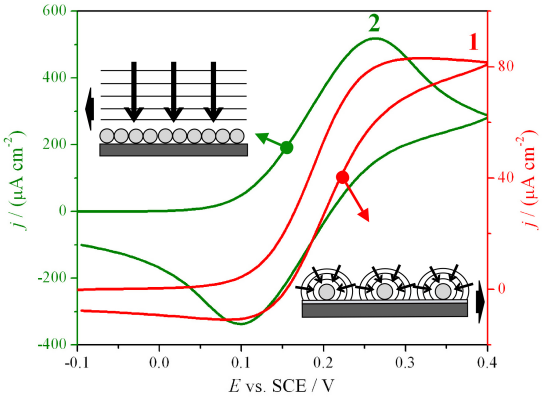

(c) Study of the distribution of Ag NPs by CV in presence of $K_4[Fe(CN)_6]$ as probe molecule (curve 1: FTO+SiO_2+Ag; curve 2: FTO+Ag).

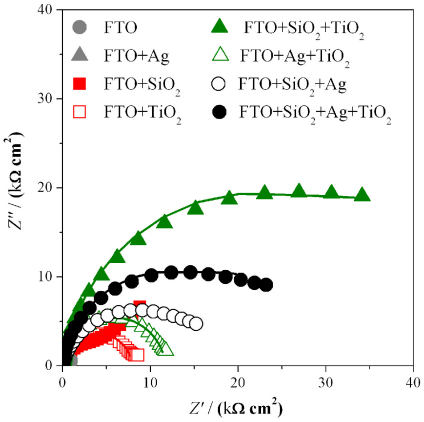

(d) Complex plane plot spectra for all the electrode architectures, registered at + 0.1 V (SCE)in the presence of probe molecule $K_4[Fe(CN)_6]$.

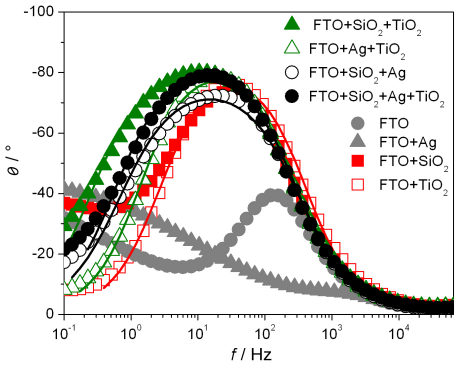

(e) Bode plot for all the electrode architectures, registered at + 0.1 V (SCE) in the presence of probe molecule $K_4[Fe(CN)_6]$.

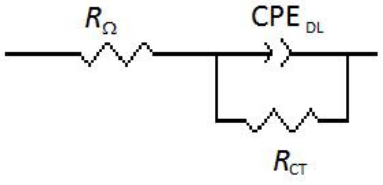

(f) Equivalent circuit used to fit data in EIS analysis.

Figure 11.2: *Electrochemical characterization of the sensor. Ref.[29]. Published by The Royal Society of Chemistry.*

Samples	$\mathbf{R}_{CT}$ /(kΩ cm^2)
FTO	0.29
FTO + Ag	0.02
FTO + SiO_2	4.48
FTO + TiO_2	7.87
FTO + SiO_2 + TiO_2	44.12
FTO + Ag + TiO_2	11.62
FTO + SiO_2 + Ag	15.74
FTO + SiO_2 + Ag + TiO_2	23.78

Table 11.1: *Charge transfer resistance (R_{CT}) values calculated from the fitting of the complex plane plot (Figure 11.2d).*

11.1.2 Top layer photoactivity

The role played by TiO_2 as an external layer in protecting Ag NPs from oxidation has already been discussed. The self-cleaning properties of the final device can be achieved by the presence of TiO_2 on the top of the sandwich. The accurate engineering of the final layer aimed at imparting photoactivity at the interface without altering transparency, mechanical properties and the state of Ag NPs. As a matter of fact, crystallinity growth (and the degradation of the organic components) promoted by the calcination step is crucial in order to impart photoactivity[43]. Here, the careful modulation of the sol composition associated with a rapid calcination at 400 $°C$ under an inert atmosphere not only assured high photoactivity under UV-A irradiation, but also preserved the transparency of the film. Photoactivity was proved by the degradation of chemisorbed hydrophobic organic chains (SILRES 1701) monitoring the water contact angle decrease by a procedure previously reported in literature for the simulation of finger print/oily stain self-cleaning[44, 45]. The presence of silane molecules chemisorbed at the electrode surface, shifted the θ_w value from hydrophilic $(0 - 30°)$ to $\sim 110°$. Under irradiation in the UV region, electronhole pairs were created at the TiO_2 interface. This makes the surface reactive. Peroxide and superoxide radicals were generated[43], reacting and oxidizing the organic chains of the chemisorbed siloxane, bringing back θ_w to the hydrophilic value.

Figure 11.3a shows the degradation kinetic of the siloxane chains on the device, monitored by θ_w decrease, compared to bare silica. Whilst the water contact angle of bare silica was almost constant upon irradiation, the device, covered by a titania layer, showed fast kinetics of contact angle decrease. This proves that the organic chain mineralization was carried out by the radicals produced by the active titania and not by a simple photolytic degradation of the molecule. Eventually, we proved the high activity of the interface as a self-cleaning electrode.

11.1.3 Determination of dopamine

Dopamine, an important molecule of biomedical interest[18, 19], was chosen for testing the electroanalytical performances of the optimized multilayer electrodes. After an extensive literature research and experimental investigation, differential pulse voltammetry (DPV) was chosen as the best technique for the detection of dopamine. Figure 11.3b shows the calibration plot, obtained in the case of the final device (FTO + SiO_2+Ag NP + TiO_2 , empty circles) in the 535 ppm dopamine concentration range, and, as an inset, the corresponding differential pulse voltammograms.

Dopamine can be detected with a good sensitivity also on a device without a silica layer (FTO + Ag + TiO_2 , Figure 11.3b, full circles), although the calibration plot obtained is not linear and a strong saturation effect is observed. This problem was overcome when the silica layer was present, obtaining a

linear range. Moreover, it is worthwhile saying that, in the case of the presence of silica, a convergent diffusion on silver NPs can be reached (see Figure 11.2c), with important advantages at the trace level of analyte concentration, particularly in terms of lower limits of detection. Preliminary results in this sense are validating these conclusions.

In dopamine detection, silver has the double function of both facilitating the electron transfer through the semiconductor layers, in order to provide the required conductivity (see previously reported impedance discussion, Figure 11.2d), and of allowing the metal electrocatalytic effect on the analyte. The latter is demonstrated in Figure 11.3c, showing a decrease in dopamine peak potential from + 0.26 V (curve 1) to + 0.15 V (SCE) (curve 2) in the case of the presence of Ag in the sandwich. As discussed in the *introduction* of the present chapter, chemisorption and the consequent fouling of the electrode surface is a general concern in electroanalysis, particularly in the detection of organic analytes at trace levels[1, 18]. This affects the analytical sensitivity and requires strong surface polishing treatments or even the complete replacement of the electrode. In the present case, the fouling phenomenon was significant, causing an analytical sensitivity decrease (evaluated by the decrease in the calibration plot slope in Figure 11.3d, triangles, compared to the fresh one, circles) for consecutive analyses performed using the same electrode.

In order to clean the surface, removing all the byproducts and the residues of dopamine detection, after recording a complete calibration curve, the electrode was simply irradiated with UV-A light for one hour, exploiting the photoactivity of the external titania layer. The sensitivity was completely recovered as revealed in Figure 11.3d (squares), where the recovered electrode calibration plot completely overlaps the pristine electrode ones (circles).

For a better understanding of the phenomenon, in a fresh solution of electrolyte (in the absence of dopamine), cyclic voltammograms of the same electrode in different moments of the fouling-cleaning process were recorded (Figure 11.3e). Line 1 corresponds to the clean electrode before sensing and shows the presence of Ag NP peaks around + 0.2 V, as expected; line 2 represents the voltammogram registered at the electrode, washed with water, after one dopamine calibration experiment (ten additions of 10^{-2} M dopamine). Line 3 was obtained on the washed electrode after two dopamine calibration analyses. Voltammograms 2 and 3 are significantly different compared to curve 1, showing a clear evidence of progressive fouling at the sandwich surface. Both voltammograms show peak shoulders (around + 0.35 V), and a narrowing of the accessible potential window, probably due to the presence of adsorbed dopamine or other fouling byproducts derived from the reaction. Line 4 shows the voltammogram after one hour of UV-A irradiation and 24 h of storage in the dark. In this case, the electrode completely recovers the initial shape (line 1), demonstrating the high efficiency of the cleaning process; the removal of the adsorbed species was achieved and the possibility of electrode reuse was proved.

Finally, the robustness of the optimized device in aging and wear out was considered. The sensor maintained the same sensitivity and behaviour after many months, detections and irradiations without adopting any specific care in storage.

11.1.4 Safer instrumentation

The device was developed with the final aim to be used by scientists with different backgrounds, not only in academic research, but also in clinical and industrial laboratories. That requires the implementation of a methodology which uses safer and more commonly available lamps. In the previous sections, we obtained the self-cleaning effect by irradiating the device with a UV lamp, *ad hoc* developed for photocatalytic studies. However, such a lamp is not commonly available in analytical labs and produces significant UV

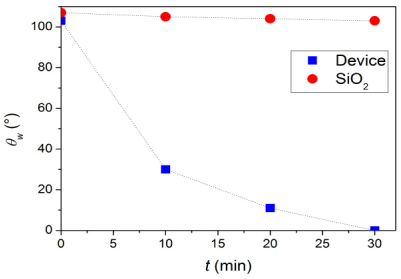

(a) Kinetic of θ_w decrease of the device covered by a chemisorbed siloxane layer under UV irradiation.

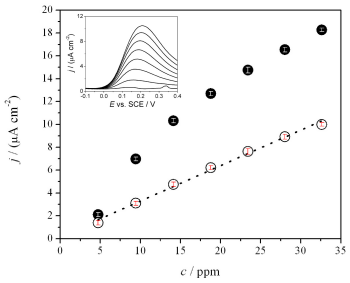

(b) DPV calibration plots obtained for dopamine detection on two different electrode architectures (FTO+Ag+TiO_2 (•); FTO+SiO_2+Ag +TiO_2 (○)); inset: differential pulse voltammograms referred to (○) data.

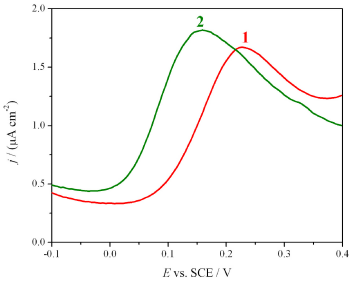

(c) Differential pulse voltammograms, showing electrocatalytic peak displacement caused by Ag NPs (curve 1: FTO+SiO_2+TiO_2 ; curve 2: FTO+SiO_2+Ag+TiO_2).

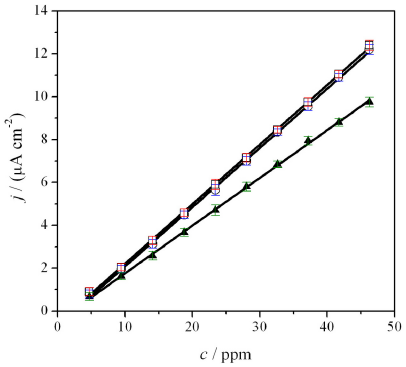

(d) Dopamine calibration plots obtained at different analytical steps (squares (□): first calibratio plot; triangles (▲): calibration plot after fouling; circles (○): calibration plot after UV cleaning).

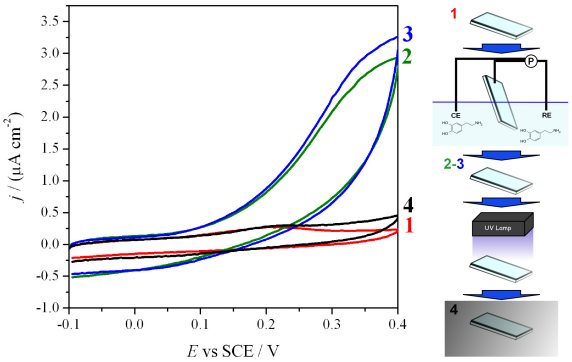

(e) Cyclic voltammograms registered at 0.1 (V s^{-1}) at different analytical steps during the fouling/cleaning procedure and the relevant schematic.

Figure 11.3: *Self-cleaning properties of the sensor. Ref.[29]. Published by The Royal Society of Chemistry.*

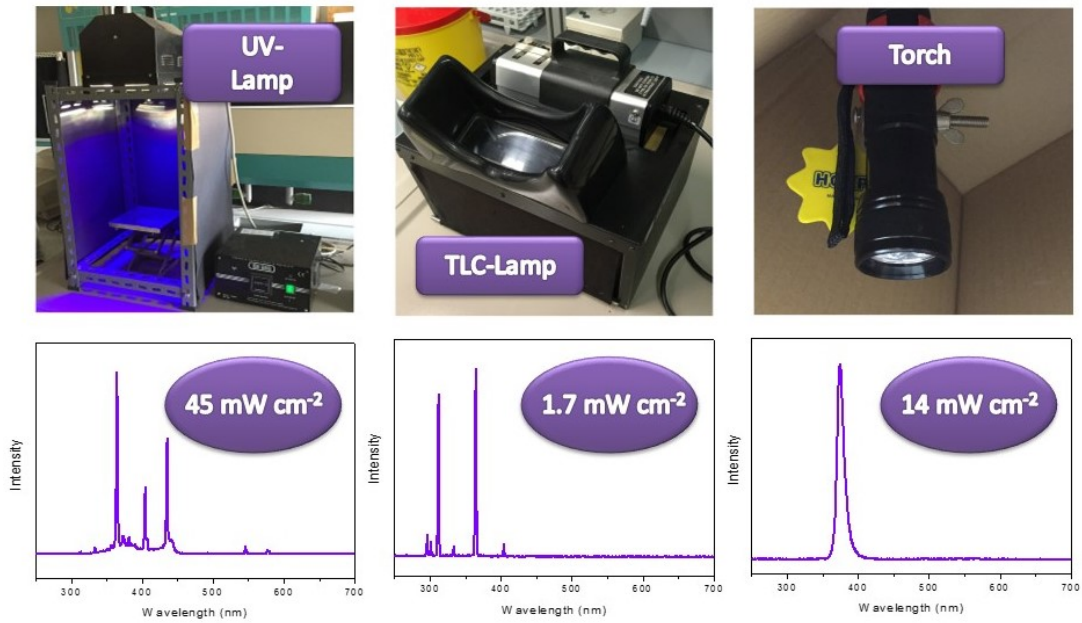

Figure 11.4: *Photographs, emission spectra and effective power density of the three lamps employed for self-cleaning experiments. ref.[46]. Published by The Royal Society of Chemistry..*

exposure hazard. For this reason, we moved to less powerful UV sources, *e.g.* a UV LED-torch (online commercially available at an average price of 30 $) and a conventional lamp for the visualization of TLC plates, with the final scope to make such technology portable, simple and user-friendly (Figure 11.4).

As shown by the UV-vis transmittance spectrum (Figure 11.5a) of the device, we expect the titania surface to be active in the near-UV region. The effectiveness of two low-cost, commercially available lamps, compared to a photochemistry layout, was tested. Figure 11.4 shows the emission spectra and effective power density of the three adopted setups: 1) UV-LAMP: the powerful (45 mW cm^{-2}) iron-halogenide lamp developed for photocatalysis (used in previous chapters), with one major emission peak in the UV region at 360 nm and two further peaks in the visible region (400 and 440 nm); 2) TLC-LAMP: a typical mercury lamp for thin layer chromatography (TLC) analysis, commonly found in chemistry and biology laboratories, emitting mostly at 310 and 360 nm (1.7 mW cm^{-2}); 3) TORCH: a commercially available LED torch with a quite sharp emission at 380 nm (14 mW cm^{-2}), without any specific safety requirements. The self-cleaning efficiency of the sensor with respect to irradiation conditions (time and lamp power) was investigated by an *ad hoc* fouling/cleaning procedure comprising three steps: 1) background acquisition, 2) fouling and 3) cleaning. Dopamine (1 mM, in 0.1 M phosphate buffer solution at pH = 7.4) was utilized as fouling agent and probe, and Differential Pulse Voltammetry (DPV, range 0.1 V / + 0.4 V (SCE), modulation time 0.05 s, interval time 0.5 s, step potential 0.005 V, modulation amplitude 0.05 V) as electroanalytical technique.

For the background acquisition (Figure 11.5b, curve 1), the electrode was dipped in the phosphate buffer solution (in the absence of dopamine). Only the oxidation peak of silver nanoparticles at + 0.165 V (SCE) could be detected, representing an indication of the clean and active surface. This peak is that affected by dopamine fouling. The fouling effect is really strong and it is present also at dopamine very low concentration (below 0.3 μM, which is the LOD of our device). However, in order to promote fast deactivation and test the potentialities of our self-cleaning device, a concentrated 1 mM solution of dopamine was specifically adopted. After the addition of dopamine, the voltammetric cycling caused the

electrode fouling by the adsorption of dopamine itself and of its by-products onto titania[47, 48].

The voltammogram acquired in fresh phosphate buffer (in the absence of dopamine, Figure 11.5b, curve 2), after dopamine detection and chemisorptions, clearly shows the disappearance of the Ag NPs oxidation peak and the persistence of the dopamine shoulder at + 0.3 V[9]. The electrode was removed from the solution, irradiated for a chosen time and tested again in pure phosphate buffer solution (Figure 11.5b, curve 3-4). As a function of irradiation time, the dopamine shoulder decreased while the Ag nanoparticles peak increased, as a clear evidence of the successful cleaning process. The time of irradiation was varied from 0 to 30 minutes for all the three lamps tested and also a blank test was acquired, where the electrode was not exposed to UV light source (dark). In order to describe the fouling and cleaning process of the electrode surface, a % Reactivation parameter was defined:

$$\%Reactivation = \frac{\phi - I(t)}{\phi - B} \cdot 100 \tag{11.4}$$

where ϕ is the value of the current measured at + 0.3 V (dopamine peak) after the fouling step, I(t) is the current measured at + 0.3 V after irradiation for a time (t) and B is the current measured at + 0.3 V for the background scan. According to this definition, reactivation values of 0 % and 100 % correspond to the completely fouled and the perfectly clean electrode, respectively.

Figure 11.5c shows the *%Reactivation* parameter with respect to the irradiation time obtained for the three different tested lamps and for an electrode stored in the dark for the same time (identified as blank). The value measured for the blank was 0 % for all the tested times, demonstrating the crucial effect of UV light for electrode regeneration. In fact, complete reactivation (100%) was obtained after at least 20 minutes of irradiation, with different rates, depending on the lamp features. The most efficient lamp was the UV-LAMP, in which the combination of high power and low wavelengths (high energy, Figure 11.5) led to faster degradation of the fouling products. With such a lamp, after only 5 minutes of irradiation, the electrode recovered more than 90 % of its initial condition and recovered totally after 10 minutes. Irradiation wavelengths also seem to be a crucial variable to consider for evaluating the lamp performance. TLC-LAMP displays an emission component of 310 nm (higher energetic radiation, Figure 11.5). Notwithstanding its low irradiation power, TLC-LAMP presents an efficient absorption of radiation by the titania layer and consequently an abundance of photo-catalytic events, leading to a high cleaning efficiency. The results obtained with the simple UV LED TORCH are, in our opinion, the most intriguing and valuable. TORCH emits a low energy radiation, near to the visible edge (Figure 11.5), which refers to a safer behavior with respect to the other two lamps. However, it shows a similar cleaning kinetics compared to UV-LAMP and TLC-LAMP, allowing complete regeneration of the electrode after 20 minutes.

11.1.5 On-field application: a proof of concept.

The intrinsic portability makes it perfect for on-field and on-line applications. For this purpose, the development of a procedure that allows direct, on site, cleaning of the device without the need to remove it from the working environment would be highly desirable. As a proof of concept, the device was fouled according to the previously reported procedure and immersed in the electrolyte solution. TORCH was chosen as the UV source and the irradiation of the electrode was performed from outside the reactor (Figure 11.5d). Figure 11.5e shows the decrease of fouling at the electrode for different irradiation times. The percentages of fouling (*%Fouling*) are calculated as the ratio between the current of the tested device and of the completely fouled electrode, measured at + 0.3 V (SCE). Despite the use of the less performing lamp, the intrinsic filter effect of water and of the glass container (borosilicate glass), the fouling species

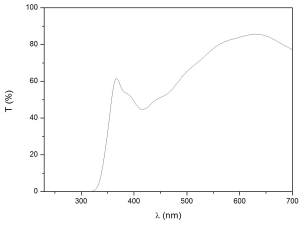

(a) UV-Vis transmittance spectrum of the device.

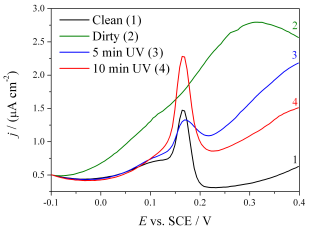

(b) Differential pulse voltammograms: in the absence of dopamine (curve 1); after fouling (curve 2), after UV cleaning at different time (curve 3-4).

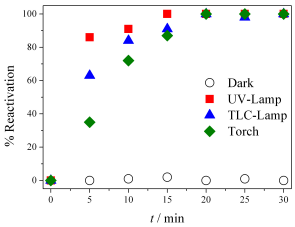

(c) %Reactivation values obtained for irradiation with the three lamps and in the dark.

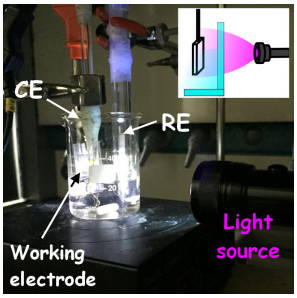

(d) Scheme of the on-site experiment.

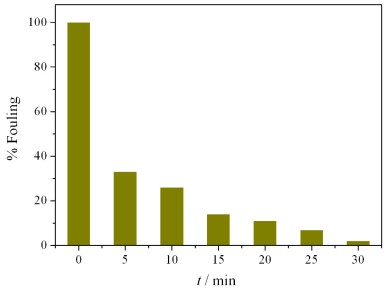

(e) Study of fouling/recovery directly in the electrolyte solution after performing the cleaning procedure in situ with the TORCH.

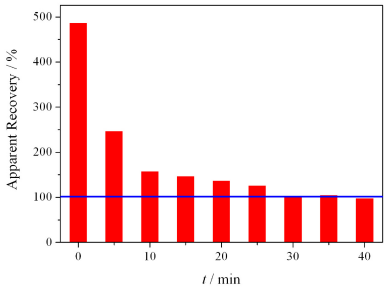

(f) Study of *Apparent Recovery* for 1 μM of dopamine after performing the cleaning procedure in situ with the TORCH.

Figure 11.5: *Different lamps and on-site trials. Ref.[46]. Published by The Royal Society of Chemistry.*

totally disappeared after 30 minutes.

In order to further demonstrate the robustness of the method in on-site analytical applications, an on-purpose fouled electrode (soiled after dipping and CV cycling in 1 mM dopamine solution) was immersed in a freshly prepared solution, spiked with dopamine, yielding a final concentration of 1 μM. The sample analysis was performed as previously described, registering the *Apparent Recoveries* at fixed time (every 5 minutes) during the cleaning procedure. As expected, see Figure 11.5f, *Apparent Recoveries* higher than 100 % are calculated, indicating heavy fouling and thus overestimation of the analyte. But, after 30 minutes of on-site irradiation, the device was completely cleaned and reactivated, with *Apparent Recovery* (IUPAC[27]) values around 100 %. Further, cleaning does not affect the recovery values, demonstrating that only fouling compounds are degraded and no soluble by-products are electrochemically detected, while dopamine in solution is not affected by the cleaning procedure. It is worthwhile noticing that this is not an obvious result: the photocatalytic degradation, only confined to the electrode surface, allows the degradation of adsorbates without altering the very low concentration of the analyte, since photolysis does not occur.

Finally, it is important to underline that the fouling conditions adopted in these tests were selected to be extremely hard. Dopamine was chosen, not only because it is an important neurotransmitter analyte, but also since it is a strong passivating molecule recognized to irreversibly chemisorb and polymerize at the oxide surface[49, 50]. In this context, to demonstrate the potentialities of the self-cleaning layer, a concentrations much higher than those found in body fluids (40 nM) was employed [19]. Apart from the previously proved robustness, trueness and precision of the device, here, the possibility to use short-time cleaning steps with low energy and low power UV-LED sources was demonstrated. Moreover, the cleaning procedure can be performed directly on site, in the solution of interest. For all the above reasons, it is

possible to forecast an on-line/on-field application: a small UV emitting LED incorporated in the final device, for example, could switch on and off for few minutes between two subsequent analyses. This could permit the continuous regeneration of the electrode surface, eliminating the need of any other maintenance work and allowing the use of this sensor in remote integrated monitoring systems and flow analysis, where shorter detection time are crucial.

11.2 Conclusion

Fouling and fragility of complex engineered electrochemical devices for the detection of biomolecules are solved by the development of sandwich structured electrodes endowed with a photoactive top layer. The lack of investigation in this field has caused scarce applicability of many specific sensors for the detection of highly relevant molecules in biomedical and environmental protection fields. Here, a simple system was engineered with the purpose to detect an organic biomolecule with absolute relevance in the medical context, dopamine. First, the problem of chemisorption and fouling of such molecules was solved by covering the sandwich with a photoactive external top layer. The total recovery of sensitivity was proved after irradiating the device by using a UV-A lamp for a short time. No change in the electrode signal was observed after numerous usages and irradiation. Silver nanoparticles, deposited in a controlled manner inside the sandwich, were not only critical for the detection of dopamine, but were demonstrated to recover their metallic nature after each irradiation. Hence, as the proof of concept, sensors which are highly applicative and commercially appealing, reusable and potentially not affected by aging, were demonstrated. The described know-how, derived from the ability to create such transparent, photoactive, multilayer structures, can be potentially employed on other electrode supports and tailored on different target molecules, solving, once and for all, the problem of the cleaning process.

11.3 Materials and methods

Device synthesis The fluorine doped tin oxide coated glass slides (FTO, Sigma-Aldrich, $\sim$ 7 Ω *sq*, 2 x 3 cm) adopted as conductive supports were previously sonicated in a cleaning solution (H_2O : acetone: propanol = 1:1:1) and irradiated for 1 hour under UV light.

The silica sol was prepared by the procedure reported by Wang *et al.*[23] Briefly, 10 g of TEOS was added into a solution containing 25 g of ethanol and 4.5 g of hydrochloric acid solution (0.1 M). The mixture was stirred at lab temperature for 2 hours and then refluxed at 60 $°C$ for 60 min. Eventually, 25 g of an ethanol solution of the CTAB cationic surfactant (2 g in 25 mL) was dissolved in the as-obtained solution by slowly stirring at lab temperature for 1 hour. The FTO was dipped in such a sol and quickly calcined at 500 $°C$ for 1 hour under N_2 flow. The functionalization by (3-aminopropyl)triethoxysilane (APTES) was performed by irradiating the absorbent for 1 hour (either the silica layer or the bare FTO layer), and then dipping in anhydrous toluene under N_2 at 70 $°C$. After 1 hour, a solution of APTES in anhydrous toluene was added to obtain a final concentration of 5 μM. After 3 hours at 70 $°C$ the sample was cleaned by sonication for a few minutes in toluene, ethanol and water in order to eliminate the un-grafted silane and eventually dried under a nitrogen stream.

The sample was then immersed in a solution of Ag NPs for 15 minutes and dried under N_2 flux. The final titania layer was obtained by dipping the sample in a titania sol and calcinating it under N_2 flow for 1 hour at 400 $°C$. The titania sol preparation is described in Appendix C, page 231.

Silver nanoparticles (Ag NPs) were synthesized by adapting the procedure reported by Panzarasa[25]. Briefly, 0.15 g of silver nitrate were dissolved in 25 mL of water and this solution was added under stirring

to a solution of 0.5 g of trisodium citrate and 0.25 g of poly(vinylpyrrolidone) (PVP10, $M_w \sim 10\ 000$ (g mol^{-1})) in 125 mL of water. The resulting solution was poured in a three-necked, round-bottomed 250 mL flask equipped with a mechanical stirrer and a dropping funnel. The solution was cooled in an ice bath and an ice-cooled solution of sodium borohydride, obtained by dissolving 12 mg of solid in 30 mL of water, was added dropwise under stirring. The resulting dark brown suspension was left under stirring for 5 minutes after the addition, aged at + 40 $°C$ for 24 hours before use and stored at this temperature.

The Z-potential was determined by a Malvern Zetasizer Nano-ZS equipped with a universal dip cell (Malvern) and standard polystyrene cuvettes. Film thicknesses were evaluated using a Filmetrics F20 reflectometer (Filmetrics).

CV and EIS experiments were carried out with an Autolab PGStat30 (Ecochemie, The Netherlands) potentiostat/galvanostat equipped with an FRA module and controlled by GPES and FRA softwares. Impedance data were processed with Z-View 3.1 software. Cyclic voltammetric characterization was performed in a 0.1 M $NaClO_4$ aqueous solution at room temperature, in a three-electrode conventional cell, with a saturated calomel and a platinum wire as the reference and counter electrodes, respectively. No N_2 degassing of the solution was necessary, since the dissolved O_2 did not affect the measurements. The potential was varied between − 0.1 V and + 0.4 V (SCE) at 0.1 (V s^{-1}) scan rate. The potential window was chosen considering the Pourbaix diagrams[43] for TiO_2 and metallic Ag. Electrochemical impedance spectra were registered at − 0.1, + 0.1 and + 0.25 V (SCE), with a range of frequencies between 65 (thin space (1/6-em))000 and 0.1 Hz and an amplitude of 10 mV under the same experimental conditions of cyclic voltammetry. The behaviour of the electrodes was studied both in the presence and in the absence of a redox reaction, using $K_4[Fe(CN)_6]$ as a model probe molecule.

Photoactivity test the photocatalytic activity of the device was tested by following in time the degradation of a hydrophobizing organic molecule deposited on the titania layer. The adopted hydrophobizing/staining molecule (SILRES BS 1701) is produced and commercialized by Wacker Chemie AG. It is a mixture of isomeric octyltriethoxysilanes with iso-octyltriethoxysilane as the main component. The molecules were chemisorbed on the tested surface by the chemical vapor deposition protocol (Appendix C, page 232)[51]. The device was placed in a glass container together with a Teflon cup filled with siloxane. The container was placed in an oven at 100 $°C$ for 3 hours to vaporize siloxane. Eventually, the substrate was sonicated in toluene and dried. The degradation of the organic moieties was monitored by measuring the water contact angle as a function of the time of UV irradiation.

Dopamine detection dopamine hydrochloride was of analytical purity and purchased from Sigma-Aldrich. It was detected using Differential Pulse Voltammetry, scanning the potential between − 0.1 V and + 0.4 V (SCE), with the following parameters: modulation time 0.05 s, interval time 0.5 s, step potential 0.005 V, modulation amplitude 0.05 V, in a three electrode cell. Three voltammograms at each dopamine concentration were recorded. The calibration curve was repeated three times, with comparable results. Saturated calomel, Pt wire and modified FTO were used as the reference, counter and working electrodes, respectively. Phosphate buffer (pH 7.4, 0.1 M) was used as the supporting electrolyte.

UV Lamps Three different lamps were adopted for the cleaning step (Figure11.5):

- UV-LAMP: UV iron halogenide lamp Jelosil HG500: effective power density 45 (mW cm^{-2}) at 40 cm (sample location), emitting mostly between 350 and 450 nm (see Appendix C, page 236);
- TLC-LAMP: Spectroline Model ENF-240C/FE: effective power density 1.7 (mW cm^{-2}), emitting between 280 and 400 nm;

- UV LED TORCH: HQRP effective power density 14 (mW cm^{-2}), maximum emission at 380 nm.

Further details about synthetic procedures and characterizations can be found in Appendix C.

References

[1] C. Brett, *Pure Appl. Chem.* **2001**, *73*, 1969–1977.

[2] L. Rassaei, F. Marken, M. Sillanp, M. Amiri, C. M. Cirtiu, M. Sillanp, *Trends Anal. Chem.* **2011**, *30*, 1704 –1715.

[3] M. Pumera, S. Snchez, I. Ichinose, J. Tang, *Sensors Actuat. B: Chem.* **2007**, *123*, 1195 –1205.

[4] G. Hanrahan, D. G. Patil, J. Wang, *J. Environ. Monit.* **2004**, *6*, 657–664.

[5] S.-J. Bao, C. M. Li, J.-F. Zang, X.-Q. Cui, Y. Qiao, J. Guo, *Adv. Funct. Mater.* **2008**, *18*, 591–599.

[6] X. Ma, W. Hu, C. Guo, L. Yu, L. Gao, J. Xie, C. M. Li, *Adv. Funct. Mater.* **2014**, *24*, 5897–5903.

[7] M. Zhang, C. Liao, Y. Yao, Z. Liu, F. Gong, F. Yan, *Adv. Funct. Mater.* **2014**, *24*, 978–985.

[8] Q. Wang, Y. Yun, *Microchim. Acta* **2013**, *180*, 261–268.

[9] X. Luo, A. Morrin, A. Killard, M. Smyth, *Electroanalysis* **2006**, *18*, 319–326.

[10] C. Welch, R. Compton, *Anal. Bioanal. Chem.* **2006**, *384*, 601–619.

[11] F. Campbell, R. Compton, *Analytical and Bioanalytical Chemistry* **2010**, *396*, 241–259.

[12] I. Streeter, R. Baron, R. G. Compton, *J. Phys. Chem. C* **2007**, *111*, 17008–17014.

[13] D. Meroni, S. Ardizzone, U. Schubert, S. Hoeppener, *Adv. Funct. Mater.* **2012**, *22*, 4376–4382.

[14] R. Alam, I. V. Lightcap, C. J. Karwacki, P. V. Kamat, *ACS Nano* **2014**, *8*, 7272–7278.

[15] G. K. Mor, M. A. Carvalho, O. K. Varghese, M. V. Pishko, C. A. Grimes, *J. Mater. Res.* **2004**, *19*, 628–634.

[16] Y.-Y. Song, Z. Gao, K. Lee, P. Schmuki, *Electrochem. Commun.* **2011**, *13*, 1217 –1220.

[17] Y.-Y. Song, Z.-D. Gao, P. Schmuki, *Electrochem. Commun.* **2011**, *13*, 290 –293.

[18] K. Jackowska, P. Krysinski, *Anal. Bioanal. Chem.* **2013**, *405*, 3753–3771.

[19] M. Perry, Q. Li, R. T. Kennedy, *Anal. Chim. Acta* **2009**, *653*, 1 –22.

[20] N. G. Shang, P. Papakonstantinou, M. McMullan, M. Chu, A. Stamboulis, A. Potenza, S. S. Dhesi, H. Marchetto, *Adv. Funct. Mater.* **2008**, *18*, 3506–3514.

[21] X. Wang, X. Liu, L. Lai, S. Li, J. Weng, Z. Zhou, Q. Cui, X. Chen, M. Cao, Q. Zhang, *Adv. Funct. Mater.* **2008**, *18*, 1809–1823.

[22] M. Wei, L.-G. Sun, Z.-Y. Xie, J.-F. Zhii, A. Fujishima, Y. Einaga, D.-G. Fu, X.-M. Wang, Z.-Z. Gu, *Adv. Funct. Mater.* **2008**, *18*, 1414–1421.

[23] X. Wang, R. Xiong, G. Wei, *Surf. Coat. Tech.* **2010**, *204*, 2187 –2192.

[24] R. G. Acres, A. V. Ellis, J. Alvino, C. E. Lenahan, D. A. Khodakov, G. F. Metha, G. G. Andersson, *J. Phys. Chem. C* **2012**, *116*, 6289–6297.

[25] G. Panzarasa, *J. Chem. Edu.* **2014**, *91*, 696–700.

[26] D. D. Evanoff, G. Chumanov, *ChemPhysChem* **2005**, *6*, 1221–1231.

[27] D. D. Evanoff, R. L. White, G. Chumanov, *J. Phys. Chem. B* **2004**, *108*, 1522–1524.

[28] G. Maino, D. Meroni, V. Pifferi, L. Falciola, G. Soliveri, G. Cappelletti, S. Ardizzone, *J. Nanopart. Res.* **2013**, *15*, 2087.

[29] G. Soliveri, V. Pifferi, G. Panzarasa, S. Ardizzone, G. Cappelletti, D. Meroni, K. Sparnacci, L. Falciola, *Analyst* **2015**, *140*, 1486–1494.

[30] V. Pifferi, G. Facchinetti, A. Villa, L. Prati, L. Falciola, *Catal. Today* **2015**, *249*, 265 –269.

[31] L. Falciola, A. Gennaro, A. A. Isse, P. R. Mussini, M. Rossi, *J. Electroanal. Chem.* **2006**, *593*, 47 –56.

[32] C. Bellomunno, D. Bonanomi, L. Falciola, M. Longhi, P. Mussini, L. Doubova, G. D. Silvestro, *Electrochim. Acta* **2005**, *50*, 2331 –2341.

[33] V. Pifferi, V. Marona, M. Longhi, L. Falciola, *Electrochim. Acta* **2013**, *109*, 447 –453.

[34] M. Giovanni, M. Pumera, *Electroanal.* **2012**, *24*, 615–617.

[35] I. Boskovic, S. Mentus, M. Pjescic, *Electrochim. Acta* **2006**, *51*, 2793 –2799.

[36] S. D. Standridge, G. C. Schatz, J. T. Hupp, *Langmuir* **2009**, *25*, 2596–2600.

[37] Y.-G. Zhou, F. W. Campbell, S. R. Belding, R. G. Compton, *Chem. Phys. Lett.* **2010**, *497*, 200 –204.

[38] G. Herzog, V. Beni, *Anal. Chim. Acta* **2013**, *769*, 10 –21.

[39] A. O. Simm, S. Ward-Jones, C. E. Banks, R. G. Compton, *Anal. Sci.* **2005**, *21*, 667–671.

[40] A. J. Bard, L. R. Faulkner, *Electrochemical methods: fundamentals and applications*, *Vol. 2*, Wiley New York, **2001**.

[41] T. J. Davies, R. G. Compton, *J. Electroanal. Chem.* **2005**, *585*, 63 –82.

[42] J. H. Moon, J. W. Shin, . Sang Youl Kim, J. W. Park, *Langmuir* **1996**, *12*, 4621–4624.

[43] A. Fujishima, X. Zhang, D. A. Tryk, *Surf. Sci. Rep.* **2008**, *63*, 515 –582.

[44] A. Antonello, G. Soliveri, D. Meroni, G. Cappelletti, S. Ardizzone, *Catal. Today* **2014**, *230*, 35 –40.

[45] Y. Paz, *Beilstein J. Nanotech.* **2011**, *2*, 845–861.

[46] V. Pifferi, G. Soliveri, G. Panzarasa, S. Ardizzone, G. Cappelletti, D. Meroni, L. Falciola, *RSC Adv.* **2015**, *5*, 71210–71214.

[47] J. Liebscher, R. Mrowczynski, H. A. Scheidt, C. Filip, N. D. Hadade, R. Turcu, A. Bende, S. Beck, *Langmuir* **2013**, *29*, 10539–10548.

[48] W. Harreither, R. Trouillon, P. Poulin, W. Neri, A. G. Ewing, G. Safina, *Anal. Chem.* **2013**, *85*, 7447–7453.

[49] R. A. Zangmeister, T. A. Morris, M. J. Tarlov, *Langmuir* **2013**, *29*, 8619–8628.

[50] M. C. Henstridge, E. J. Dickinson, M. Aslanoglu, C. Batchelor-McAuley, R. G. Compton, *Sensors Actuat. B* **2010**, *145*, 417 –427.

[51] G. Soliveri, D. Meroni, G. Cappelletti, R. Annunziata, V. Aina, G. Cerrato, S. Ardizzone, *J. Mater. Sci.* **2014**, *49*, 2734–2744.

Chapter 12

Microwave-assisted silver nanoparticle film synthesis.

The actual relevance of silver (Ag) nanoparticles (NPs) is testified by the abundance of publications in the last few years reporting results on the topic. Such interest results from several distinctive properties, such as a good conductivity, optical peculiarity, chemical stability, catalytic and antibacterial activity. Silver is widely known as an important industrial catalyst, as, *e.g.*, in the case of the oxidation of methanol to ethylene oxide and formaldehyde [1]. Recently, Fuku et al.[2] described the synthesis of size controlled Ag NPs supported on mesoporous silica and, for the first time, the enhancement of the catalytic activity assisted by localized surface plasmon resonance (LSPR) was reported. The plasmonic resonance is associated with the collective oscillation of conduction electrons of typically noble metal NPs; Ag exhibits, among all, the highest efficiency of excitation[3]. Anti-microbial, anti-bacterial and anti-cancerous cell activity is one of the further reasons for the high commercial fortune of this material[4]. Sharma et al.[5] recently reported an explanation of the nature of the interactions between the bacteria cell membrane and Ag nano-particles. Next to these, other applications of Ag NPs in electronics, photonics, optoelectronic and sensing have to be mentioned[6, 7].

Several approaches have been reported for the synthesis of Ag NPs. The most extensively adopted are traditional solution phase reductions, mostly performed in the presence of capping agents, stabilizers and organic solvents, which might imply risks for environmental or biological systems[7, 8]. More recently the use of microwave irradiation (MW) for the synthesis of Ag NPs has been proposed as a more environmentally friendly approach allowing a rapid and uniform heating and a lower energy consumption[9, 10]. Over the past 25 years, microwave chemistry has moved from a laboratory curiosity to a well-established synthetic technique used in many academic and industrial laboratories, and it is nowadays very close to be scaled-up. MW heating is a dipolar phenomenon that, thanks to the speed and homogeneity of the locally produced heating, allows a rapid synthesis of the nanostructures with high control of shape and dimensions. This is quite well experimentally demonstrated by Horikoshi el al.[11]; the authors performed the same reduction, with the same experimental conditions, both by MW and traditional heating. Different reaction procedures supported by MW irradiation have been recently reported to obtain Ag NPs in suspension. Liu et al.[12] report a facile method to synthesize stable Ag nanoparticles (Ag NPs) with a narrow size distribution in water by using quaternized carboxymethyl chitosan both as stabilizing and reducing agent. Raveendran et al.[13] introduced the use of glucose and starch, respectively, as reducing and protecting agent. Hu[6] combined amino acids and soluble starch, while Nadagouda[9] reviewed the

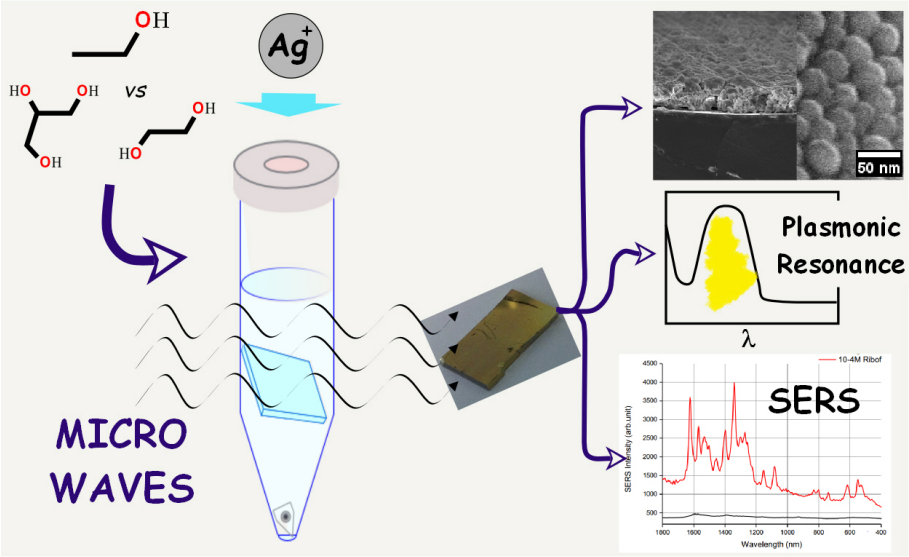

Figure 12.1: *The synthetic procedure, the film and the characterizations.*

frequent use of polyvinyl pirrolidone in the polyol synthesis.

Papers reporting the direct reduction and deposition of Ag NPs in films, by either traditional heating or MW irradiation, are so far not been found in the literature, although the exclusive properties of Ag NPs have recently shown their relevance also in the field of surface modification and film reactivity. In particular, films of Ag NPs have been notably studied as surface enhancement Raman spectroscopy (SERS) substrates[14, 15]. Literature data concerning the preparation of Ag NPs films, by chemical procedures, are mostly related to different procedures of deposition of preformed particles. In the case of SERS applications Zhang et al.[16] analyzed the effect of different shapes and dimensions of Ag NPs prepared in solution and, subsequently, when deposited onto silicon wafers and Lu et al.[17] suggested a Langmuir-Blodgett method to deposit Ag NPs onto polymer membranes. In the case of applications for electric circuits, Magdassie et al.[18], studied the sintering of preformed Ag NPs by a spontaneous 3D coalescence process supported by charge neutralization and stabilizer desorption. Long et al.[19] described a complex process for the deposition of particles, with a sub-layer of dopamine, and a subsequent immersion in a plating solution. The MW irradiation was adopted by Schubert et al.[20, 21] to promote sintering of commercial Ag NPs, previously deposited by ink-jet printing, for applications in microelectronics. Hu et al.[6], instead deposited Ag NPs obtained in solution by MW irradiation by drop casting; the homogeneity of the film, in this case, was ensured only in small and localized areas.

One of the problems associated with the use of Ag NPs is related to the separation between the Ag NPs themselves and the reducing/stabilizing agents being part of the traditional synthetic route, as underlined by Liu et al.[12] That may critically limit applications in many fields, particularly those connected with biomaterials and medical devices[22].

In this chapter, for the first time, a facile, fast and environmentally friendly method is reported for the production of thin and robust films, composed of self-assembled silver nanoparticles, without the use of any stabilizing or strong reducing agent. The film is obtained starting from silver acetate, ethanol and water; the formation and the self-assembly steps proceed simultaneously supported by microwave radiation. Reducing agents different from ethanol were also tested. Morphological, structural and optical characterizations of the films are performed and the critical process parameters were investigated; substrates with different degree of hydrophilicity are tested. The formation of stable films homogeneously

covering objects with different shape and size is documented, even the inner part of tubes and fibers could be efficiently coated by silver nanoparticle films. This opportunity is intrinsically connected with the adopted synthetic strategy. The direct application of the procedure for the formation, for example, of conductive layers or biocompatible objects is straightforward, also due to the extremely simple reaction and due to the limited instrumental requirements. As a representative practical application, the SERS activity of the obtained Ag NPs covered substrate was tested.

12.1 Results and discussion

12.1.1 Optimization of the experimental conditions.

The aim of the present work was to develop a simple and facile method to synthesize and homogeneously self-assemble Ag NPs at the surface of a glass support, utilizing non-hazardous chemicals and heating by MW irradiation. We directed our efforts towards achieving an adequately robust film, composed of small and well packed particles and the utilization of the superficial sintering to preserve the properties of the NPs.

Three different solvents acting as reducing agents were studied: ethanol, ethylene glycol and glycerol. The first part of the article exclusively deals with results obtained in ethanol. Alcohols generally show high dielectric loss for MW irradiation and posses a strong reduction ability. Therefore, they are regarded ideal solvents for MW rapid reduction reactions.[23] Silver acetate was used as silver source and glass substrates were utilized as routine supports.

Capped MW vials with the glass substrate immersed in the reaction solution were exposed to the microwave irradiation under stirring, and the temperature was gradually raised up to 170 $^{\circ}C$. The temperature was maintained for 2 minutes and was then quenched by an air flow. Mild conditions were required as to avoid overheating and excessive sintering of the NPs; this was achieved by a slow rise of the microwave power in the heating phase of the irradiation process. A typical power/temperature/pressure plot of such a synthesis process is reported in Figure 12.8.

At the end of the reaction, the internal wall of the vial and the glass substrate were totally covered with a yellowish metallic or an even shiny layer. The optical appearance of the film looked highly homogeneous and compact.

The remaining reaction solution in the vial was transparent and no evidence of significant changes were detected by UV-vis spectrometry compared to the starting pre-reaction mixture. TEM picture obtained by blotting the final solution directly onto a TEM grid showed only very few small particles, normally grouped in dimers or trimers with a size of about 20 nm.

The choice of the specific conditions to be adopted in order to obtain a homogeneous and compact layer was first investigated. The role of temperature, Ag salt concentration and reducing agent amount are not discussed herein. On the grounds of these results, the optimal reaction conditions could be determined resulting in densely packed, homogeneous films. A reaction mixture of 1 mL of ethanol, 2 mL of water, 1 mg of silver acetate are reacted at temperature of 170 $^{\circ}C$.

With this parameters, the particle formation kinetic in the time of irradiation was investigated in detail. Two steps formed the total time of irradiation: first, a temperature raising step of about 2.6 minutes, then, the power of irradiation was controlled to make the temperature constant inside the vial. The MW irradiation was stopped after 1, 2, 3 and 4 minutes from the start of the irradiation, and the samples were quickly cooled down to room temperature. The top view SEM pictures (Figure 12.2.a-d) were compared with the sample kept for 2 minutes at 170 $^{\circ}C$ (that correspond at about 4.6 minutes

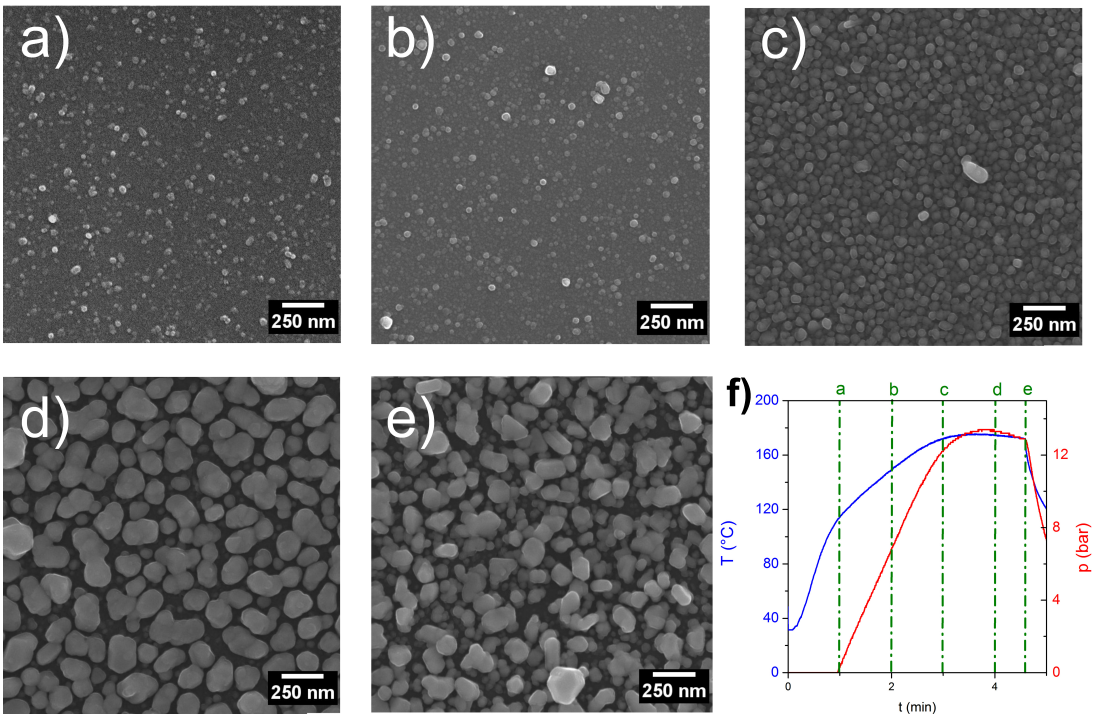

Figure 12.2: *(a-d) SEM top-view pictures of films obtained after 1, 2, 3 or 4 minutes from the beginning of the MW irradiation; (e) SEM top-view pictures of the film at the end of the programmed reaction (2 minutes at 170 °C). (f) Temperature/pressure plot vs time of irradiation.*

of total irradiation, Figure 12.2.e), that can be considered to be the optimum condition. Figure 12.2.f shows the variation of temperature and pressure during the course of the reaction; Figure 12.1 reports the pictures of the obtained films. In the first minute, the film was still totally transparent; only few particles were present on the surface. The dimension of these particles was approximately 30 nm (Figure 12.2.a). After two minutes, the surface was well covered with nanoparticles and the substrate was changing in color to yellowish. The particles diameter was in the range of 30 to 40 nm (Figure 12.2.b). After three minutes, the temperature reached the optimal value of 170 $°C$. At this stage the film was not transparent anymore; the dimension of the individual particles on the surface was still small, however, the films appeared to be more homogeneous and the particles are more densely packed (Figure 12.2.c). In the fourth minute, the particles size strongly increased; the particles lost the rounded shape and showed a more aggregated appearance (Figure 12.2.d). Figure 12.2.e shows a better homogeneity of the film and a narrow size distribution of surface particles compared to the previous ones. No changes were recorded at the surface by further increasing the reaction time. Two minutes at 170 $°C$ was estimated the shortest time that resulted in good particle coverage at the surface and only negligible Ag salt amount in the remaining reaction mixture.

12.1.2 Film Characterization

Figure 12.3 shows the UV-vis spectrum of the covered substrate (obtained at 170 $°C$ for two minutes, the same sample reported in Figure 12.2.e). The peak around 390 nm is identified as an optical resonance, associated with the collective oscillation of conduction electrons, typical for noble-metal nanoparticles (NPs), termed surface plasmon polarization resonance (SPPR)[3]. This phenomenon is commonly reported for Ag NPs well dispersed in solution. Such plasmonic resonances identify the presence of Ag NPs

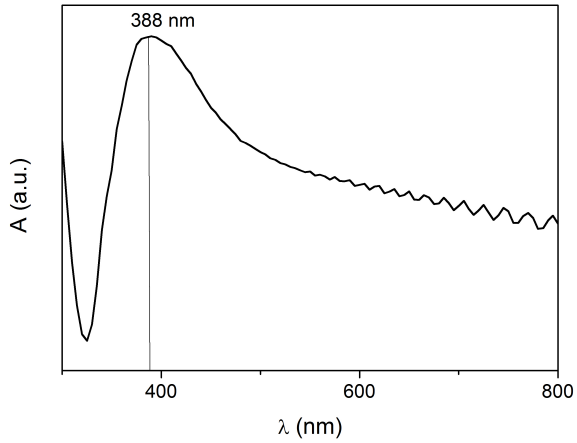

Figure 12.3: *UV-vis spectroscopy of the sample obtained after 2 minutes at* 170 $^{\circ}C$ *using ethanol as reducing agent.*

with dimensions much smaller than the wavelength of the irradiation light. As reported by Evanoff *et al.*,[3, 24] the surrounding medium critically affects the shape and position of the peak. Nevertheless, the peak could be associated to particles with a quite small dimension, around 30 to 40 nm. The high noise present in the high wavelength portion could be associated with scattering and optical phenomena due to the interface between the substrate and the film.

The corresponding AFM picture exhibits comparable results with the SEM analysis previously reported (Figure 12.2.e). Both pictures show a well covered and homogeneous surface. AFM topographic analysis identified uniform roughness along all the areas. SEM pictures disclosed the presence of particles aggregates of dimensions in the range 100-150 nm. The substrate was totally covered and the presence of underlying-layers of particles is slightly visible at higher magnification.

SEM cross-section analyses are reported in Figure 12.4. Figure 12.4a shows an Ag layer thickness between 5 and 6 μm; the layer depth appeared to be constant all along the cross section and was reproducible for different samples. Figure 12.4b shows the existence of large aggregates between 1 and 2 μm. Higher magnifications showed the presence of much smaller round shaped particles, which form the aggregates and appear to be well packed. Those particles, with a quite reproducible diameter between 30 and 35 nm (Figure 12.4c) were found to be homogeneous along all the section. Those latter particles are supposed to be the ones dominating the obtained optical results presented above.

A further proof of the shape and dimensions of the Ag NPs in the inner part of the layer was obtained by high resolution transmission electron microscopy (HR TEM). The film was scratched as to investigate the particles inside the layer. Figures 12.4d and 12.4e reports the TEM pictures of few Ag NPs highly packed together. Here, the shape and the dimension were confirmed, thanks to a higher resolution on the single particles. The clear and uniform lattice fringes revealed the highly crystallinity of the particles. The lattice spacing of $\sim$0.23 nm corresponds to (111) planes of silver.

The X-ray diffraction pattern of the NPs film (Figure 12.5) confirmed the face-centered cubic (fcc) silver crystal structure (JCPDS card No.04-0783). The lattice constant calculated from this pattern was 4.080 Å, which is a value very close to the reported one (a = 4.086 Å, JCPDS card No.04-0783). Calculated over the (111) reflection, using the widely used Scherrer equation,[25] the average crystallite diameters was founded to be $\sim$28 nm. This result shows that the pristine Ag NPs observed by the SEM and TEM analysis are actually single crystals. This latter occurrence justifies the shape and the narrow

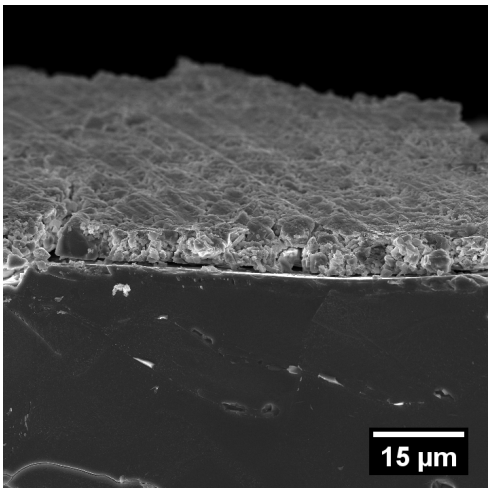

(a) SEM cross section picture.

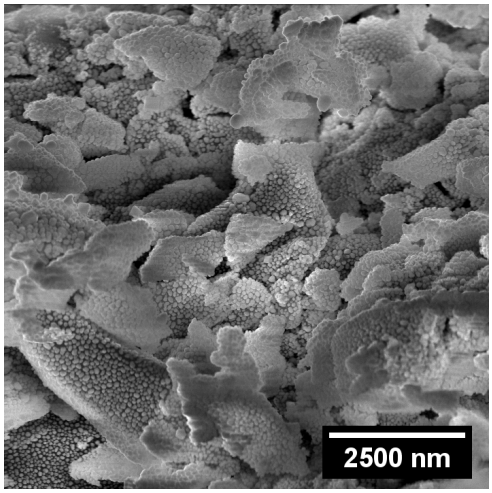

(b) SEM cross section picture.

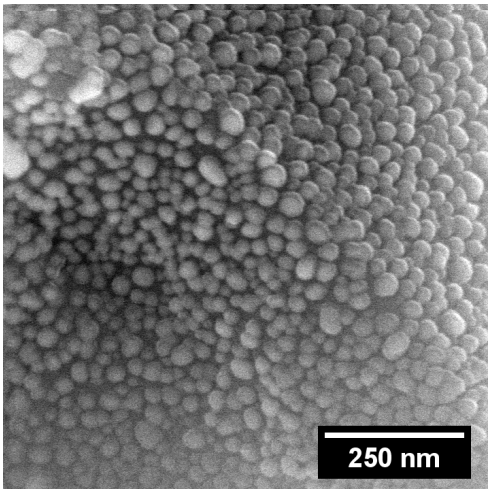

(c) SEM cross section picture.

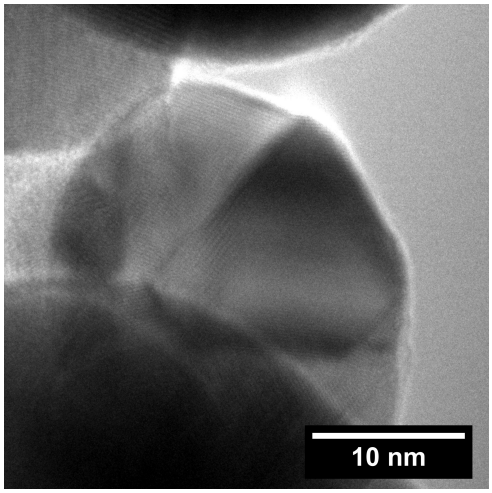

(d) HR TEM picture of the sample scratched.

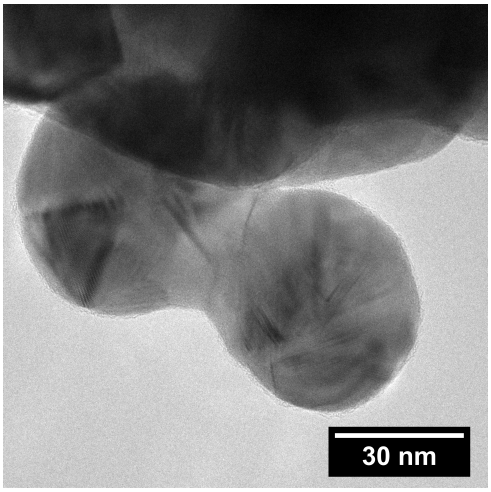

(e) HR TEM picture of the sample scratched.

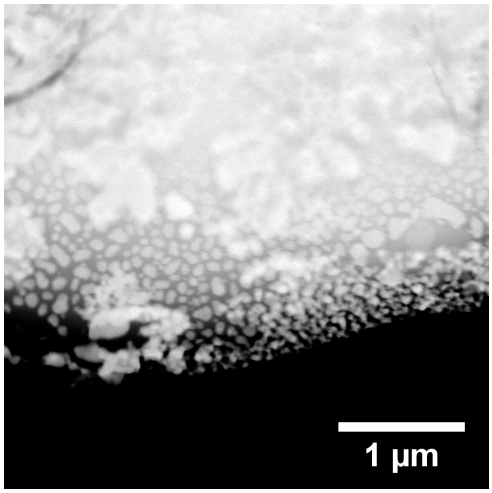

(f) STEM picture of the sample scratched.

Figure 12.4: *Electron microscopy analysis of the sample obtained after 2 minutes at* 170 $^{\circ}C$*, using ethanol as the reducing agent at different magnifications.*

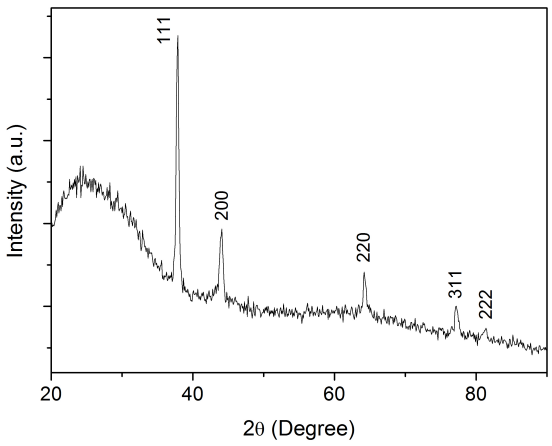

Figure 12.5: *X-ray diffraction pattern of the sample obtained after 2 minutes at* 170 $^{\circ}C$*, using ethanol as reducing agent.*

controlled dimensions of such particles. The calculated crystallite size was a little bit smaller compared to those estimated by electron spectroscopy. Chen et al.[25] reported that the Scherrer equation generally tends to underestimate the real size of the NPs, probably due to the contribution of other components to the broadening of line width (structural stress of Ag NPs, instrumental effects, etc.).

Additionally, an aging test of the surface was performed. The coverage with a carbon coating and the SEM analysis was performed both two hours after the synthesis and after one week. No appreciable differences were found by inspection of the surface by electron microscopy.

Mechanical tests of the film were also performed. The scotch tape test was performed with good results. After the tape removal, no changes were observed by naked eye at the surface. Only a small amount of particles was visible on the tape. Sonication in water for ten minutes did not provoke the detachment of a significant amount of particles to the solution, thus, suggesting very good adhesion properties of the silver nanoparticles on the glass substrates.

12.1.3 Different reducing agents

Based on these promising results for the coating of glass substrates with uniform Ag NPs different alternative reducing agents were tested. On the grounds of chemical similarity and literature data, the same procedure was applied using ethylene glycol and glycerol as reducing agents. Ethylene glycol is a well known reducing agent for the synthesis of Ag NPs for MW controlled reactions. This solvent is used, for example, for the polyol synthesis, in which the nucleation and growth of silver atoms are performed in solution to produce a huge variety of shapes.[26, 27] The temperature-dependent reducing power, its high boiling point, its high relative permittivity[23] and its ability to solvate many metal precursors make ethylene glycol ideal in the synthesis of many metal nanoparticles. However, in the present case, the reaction did not yield a satisfying, robust film as in the case of ethanol. The substrate became only lightly yellowish, while the reaction occurred mainly in suspension, without any control of shape and size of the particles. Possibly this outcome is the result of the quite good suspending power of ethylene glycol[28] which promotes the nucleation and the grow of the particles preferentially in the suspension and not their deposition onto the substrate.

Results related to the synthesis of metal NPs in glycerol have been far less reported in literature,

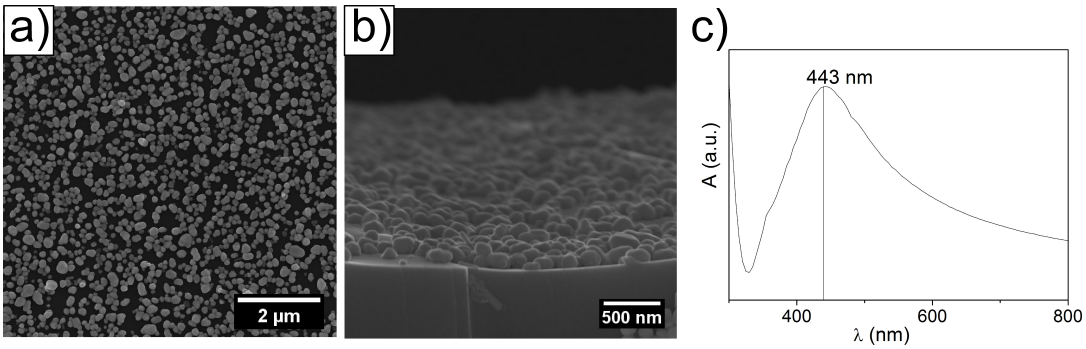

Figure 12.6: *(a) top-view and (b) cross section SEM pictures of the sample obtained using glycerol as the reducing agent. (c) UV-Vis spectrum of the same sample.*

compared to ethanol and ethylene glycol. The solvent is generally reported both as a reducing agent as well as the reaction medium, occasionally combined with a protective agent, like PVP.[29] Ullah et al.[30] reported, that the stability of the Ag NPs synthesized in glycerol without a stabilizing surfactant is generally much higher compared to the one, for example, in ethylene glycol. This higher stability in glycerol is explained by the higher viscosity of ethylene glycol leading to slower diffusion. In the present work, the film was obtained at the same conditions than the previous ones. Only the amount of silver acetate needed to be lowered to 0.5 mg to obtain a more homogeneous film. The final results were critically different compared the two previous systems.

The solution was not transparent anymore; a yellowish-white suspension was obtained. The first observation on the substrate was a clear change in color: greenish-metallic with a strong yellowish reflection. The apparent change in color was supported by the UV-vis spectroscopy of the film. Figure 12.6.c shows a broader peak with a maximum at 443 nm. This is linked to bigger NPs, about 90-100 nm in diameter due to a higher scattering component.[3]

The top-view of the layer obtained by SEM (Figure 12.6.a) reveals the presence of a quite broad size distribution, between 80 and 150 nm, with an average spherical shape. The layer seems not to cover completely the substrate and no under-layer particles were evident. The cross section of the sample (figure 12.6.b) revealed the same observations. The particles were self-assembled at the surface, not forming a 3D robust and packed layer, but only a sub-monolayer. This behavior, out of our initial aim, could be extremely interesting in applications and investigations that need only a very small amount of Ag NPs at the surface.

12.1.4 Covering surfaces with different chemical nature

In order to investigate the role of the support surface on the interaction and subsequent deposition of the NPs, different conditions of wettablity of the glass plate were tested. The glass substrate was covered by a self-assembled monolayer of OTS, as *e.g.* reported by Meroni et al.[31], to convert the hydrophilic glass to an hydrophobic surface (contact angle about 108°), without change of the surface morphology. After the Ag NPs synthesis, the final layer was investigated both by UV-vis spectroscopy and SEM analysis. Both showed the formation of an Ag NPs film totally comparable with the one, previously made on to the hydrophilic glass. Instead the TEFLON stirring bar placed in the reaction vial, was only lightly and partially covered by Ag NPs.

This evidence may suggest that the self assembling behavior of Ag NPs is not correlated with the hydrophilicity but to the polar momentum of the surface. Literature reports suggest that the momenta of

siloxanes are far from zero,[32, 33] while polytetrafluoroethylene has a very low dielectric constant. That observation is in total agreement with the prediction of a reaction route that goes through the formation of hot spots on the surface under MW radiation, as reported by Tsuji et al.[23].

The feasibility to cover further insulating or semiconductor materials was briefly investigated. Good results were obtained both on a silicon wafer and on a thin titanium dioxide layer supported, in its turn, on a glass slide.[34]

12.1.5 Discussion about the Ag NPs formation.

On the grounds of results reported above, the major steps involved in the Ag NPs film formation can be discussed. As suggested by Tsuji et al.,[23] in the case of MW synthesis, the high dielectric (and dielectric loss) constant of the groups at the surface of the support may give rise to hot spots that highly promote the preferential nucleation of silver clusters. The formation of those hot spots at the surface, as described by Zhang et al.,[35] could locally increase the temperature up to $100 - 200\ ^{\circ}C$ above the bulk temperature, hence, dramatically changing the thermodynamics of reactions; they are highly correlated with the momenta of atoms and molecules at the surface (native or adsorbed), but not with the wettability of the material. The local high temperature, is reached very quickly and promotes the formation of single crystal, round shaped small particles. The electrostatic charge of the substrate may support the formation of a compact and robust layer. Further, the first deposited layers of metal particles itself develops local hot spots at the surface, favoring the nucleation of new particles. That proceeds up to the total consumption of the Ag salt in solution. At that point, possibly, the temperature at the water/Ag NPs interface locally increases, promoting the sintering process in the first layers. That critically influences all the proprieties described above, imparting chemical and mechanical stability without affecting the optical and technological advantages connected to the small NPs kept inside the layer.

The huge differences in the layer formation observing in passing from ethanol to ethylene glycol and glycerol could be ascribed to the noticeable differences in physical constants of the solvents (Table 12.1). The heating process of a liquid under MW radiation is highly correlated with its dielectric loss constant[23]. As shown in the data reported in the table, ethanol is characterized by the lowest. That, associated with the lowest viscosity and surface tension, suggests that Ag nano-clusters may nucleate directly at the surface and at the same time self-assemble without any obstacle. In the case of glycerol, the high dielectric loss constant causes a prevalence of NP formation in solution. The high viscosity of the medium and the protecting power of glycerol molecules adsorbed around the small Ag clusters[36] may prevent coalescence leading to aggregates at the surface. Concurrently, the absence of an overheated area (on the surface), due to the lack of accumulation of metallic NPs (like in the case of ethanol), may slow down the kinetics of nucleation and create stable and long life clusters in solution, next to bigger particles. Ethylene glycol presents all intermediate properties. Reasonably, in this case, the nucleation and growth happens both on the surface and in the liquid phase with particles showing different shapes and dimensions (different nucleation spots and local temperature). The suspending power is not enough and agglomerates tend to form and immediately be attracted by the surface.

12.1.6 Emerging possibilities and applications

The film formation is independent on the particular shape of the substrate (unlike other coating techniques, *i.e.* evaporation[19, 37, 38]) and potentially allows also the covering of concave and hollow objects. This might provide new aspects and enables the straight forward and reliable coating of complex object. Silver nanoparticle films are frequently employed to enhance the sensitivity of Raman measurements.

	Ethanol	**Ethylene glycol**	Glycerol
Viscosity / cP	12	161	1412
Boiling point / $°C$	78	197	290
Density / kg L^{-1}	0.789	1.113	1.261
Dielectric constant	24	37	42
Surface tension / ^{nM} m^{-1}	22	48	63

Table 12.1: *Solvent physico chemical properties.*

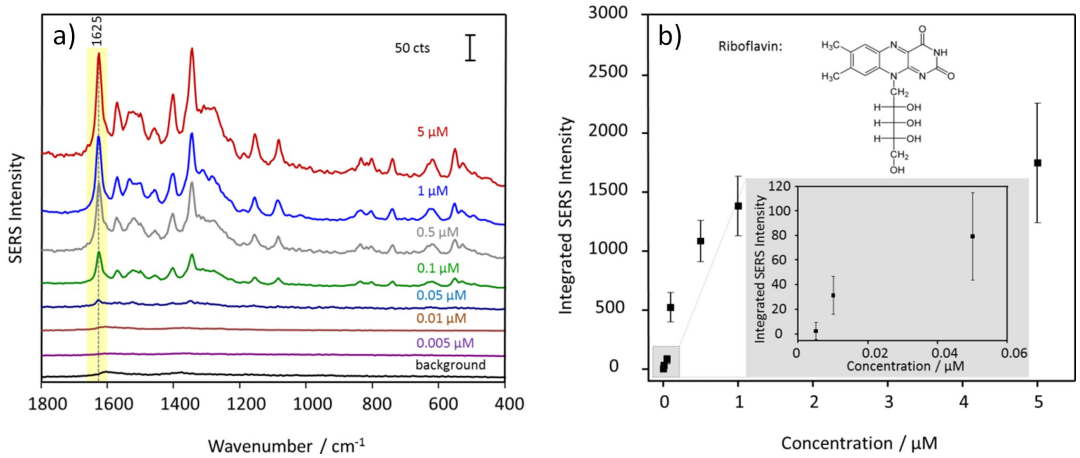

Figure 12.7: *Average SERS spectra of riboflavin with different concentrations (a) and integrated SERS intensity at 1625 cm^{-1} of riboflavin (b) The inset highlights the low concentration regime and indicates the limit of detection.*

For this purpose, uniform nanoparticles and dense films are frequently used. As such the fabricated substrates were tested for their SERS sensitivity. This was done by application of a 10^{-4} M solution of rivoflavin onto the surfaces and analysis of the Raman signal. Figure 12.7.a shows the average SERS spectra of riboflavin with different concentrations. The most dominant C-C stretching vibrational mode at 1625 cm^{-1} of riboflavin is integrated and plotted versus various different concentrations (see Figure 12.7.b). It is cearly visible, that the signal intensity increases as function of the concentration until a plateau is reached for concentrations higher than 1 μM. This is attributed to the saturation of all free binding sites on the metallic surface by riboflavin. Concentrations down to 0.01 μM are detectable. Thus, microwave assisted silver nanoparticles are promising SERS substrates for analytical detection schemes of concentrations down to the sub-μM and nM range.

12.2 Conclusion

A simple and fast method for the controlled synthesis of Ag NP films has been developed using an in-situ approach to obtain the direct fabrication of the films.

The employment of MW irradiation allowed to avoid the use of additional chemicals and stabilizing agents, which might be difficult to remove in post-reaction treatments. Ethanol, ethylene glycol and glycerol were alternatively used as reducing agents.

On the grounds of results obtained in this work we propose that the presented reaction is ruled by a balance between surface and solution effects. MW irradiation promotes the formation of hot spots on the surface of the support. The local high temperature allows a fast kinetic of nucleation close to the surface and a subsequent self-assembly on it. By changing the reducing agents (from ethanol to ethylene

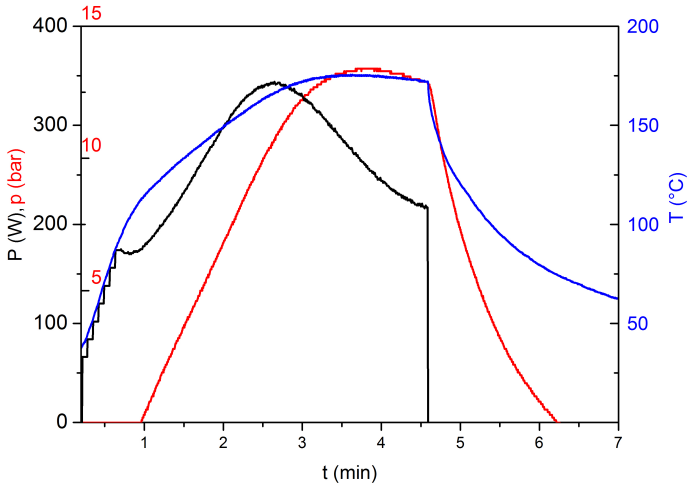

Figure 12.8: *Pressure(p) / power(P) / temperature(T) plot vs time of irradiation of the sample obtained after 2 minutesat* 170 $^{\circ}C$*, using ethanol as the reducing agent.*

glycol and glycerol), we observed the absolute relevance of the physical properties of such solvents. While ethylene glycol did not yield a homogeneous layer, in the case of glycerol, a NPs monolayer was observed by SEM cross section substrate. That was ascribe to particular properties of the solvent, like the reported suspending power of Ag nano clusters and the high dielectric loss constant, that promotes the nucleation in the bulk solution instead on the surface.

Consequently, by changing the reaction conditions, tailored films can be obtained, for different applications. The mechanically robust films obtained in water/ethanol mixtures, in the absence of any adsorbed organic species, are excellent candidates for bio and medical applications; high SERS activity could open up their application in the field of trace sensoring. The thin monolayer instead obtained in glycerol, can be exploited in all applications needing a thin conductive layer.

12.3 Specific procedures

Film Synthesis Microscopy glass slides, cut into rectangular pieces of 0.8 x 1.25 cm size, were used as routine substrates for the synthesis. Before the reaction, an argon plasma treatment (300 W, Plasma system Nano, Diener Electronic) was applied to the substrates to remove organic residues and to obtain a hydrophilic surfaces. Different reaction conditions were tested, *i.e.*, temperature (150 - 190 $^{\circ}C$), reagent ratio and reducing agents (ethanol, ethylene glycol and glycerol). The MW vial was filled with a total of 3 mL of solvent, composed of distilled water, the reducing agent (ethanol, ethylene glycol or glycerol, respectively) and dissolved silver acetate. The treated glass support was immersed in the solution. The vial was then capped and exposed to a microwave radiation (Biotage Initiator) with 2.45 GHz frequency under magnetic stirring. The power rising of the irradiation protocol was planned to allow a mild heating of the solution (Figure 12.8) and the irradiation was stopped after 2 minutes at 170 $^{\circ}C$ and was quenched by an air flow until room temperature was reached. The sample was cleaned with distilled water and dried under nitrogen flow. To test the effect of the hydrophilicity of the substrate, the wettability of the glass slide was switched from hydrophilic to hydrophobic by the formation of a n-octadecyltrichlorosilane (OTS) monolayer, adopting the procedure reported by Meroni et al.[31].

Characterization Scanning electron microscopy images were acquired with a LEO 1530 Gemini (Zeiss) scanning electron microscope with InLense detector. The samples were carbon coated before the analysis. For transmission electron microscopy, a CM 120 (Philips) with 120 kV acceleration voltage, was used. High resolution transmission electron microscopy analysis was performed by Room-temperature X-ray diffraction (XRD) patterns were collected between 20° and 90° with a Siemens D500 diffractometer, using Cu K radiation. The average diameter of the crystallites was estimated from the most intense reflection (111) using the Scherrer equation. Atomic force microscopy pictures were obtained by Ntegra Aura AFM (NT-MDT) device, in tapping mode, with NSC35/AIBS tips (μmasch). UV-vis analysis of the films was obtained from a microplate reader (Genios Pro, Tecan GmbH), while of the suspensions were analyzed by a Specord 250 spectrophotometer (Analytic Jena). Water contact angle analysis was performed on a Dataphysics CA10 system. The mechanical stability was tested both by tape adhesion test and by immersion of the coated substrates in water and applying ultrasonic action. In the former test the sample was half covered with a tape (MAGIC). When the tape was removed, both the difference between the two parts and the amount of layer left on the tape was evaluated by eyes. The difference between tested and un-tested parts of the film was evaluated additionally by SEM analysis.

The SERS activity of the nanoparticle layers was tested on Ag NPs films synthesized on glass substrates, in ethanol at 170 $°C$. The test was performed with Riboflavin. Riboflavin was purchased from Sigma Aldrich (Steinheim, Germany). 10 mM stock solution of riboflavin in distilled water was prepared and aliquots of the solution were diluted to obtain the appropriate concentrations. SERS spectra were measured by using a confocal Raman microscope (WITec GmbH, Ulm, Germany) equipped with 488 nm laser excitation. The Raman signal was collected by the same objective which is used for irradiation. The spectrometer has a 600 lines/mm grating with a 1024127 pixel CCD camera at a working temperature of 200 K. SERS spectra of riboflavin were recorded with a 100x Olympus objective (NA: 0.9) and the incident laser power onto the surface was 30 μW. Each substrate was incubated 30 minutes with the target molecule; then, the substrates were washed with distilled water and dried with pressured air. SERS spectra were recorded within a 60x60 μm area and 400 spectra with 0.2 seconds of integration time were collected.

References

[1] A. Nagy, G. Mestl, *Appl. Catal. A Gen.* **1999**, *188*, 337–353.

[2] K. Fuku, R. Hayashi, S. Takakura, T. Kamegawa, K. Mori, H. Yamashita, *Angew. Chem. Int. Ed. Engl.* **July 2013**, *52*, 7446–50.

[3] D. D. Evanoff, G. Chumanov, *Chemphyschem* **2005**, *6*, 1221–31.

[4] C.-H. Xue, J. Chen, W. Yin, S.-T. Jia, J.-Z. Ma, *Appl. Surf. Sci.* **2012**, *258*, 2468–2472.

[5] V. K. Sharma, R. a. Yngard, Y. Lin, *Adv. Colloid Interface Sci.* **2009**, *145*, 83–96.

[6] B. Hu, S.-B. Wang, K. Wang, M. Zhang, S.-H. Yu, *J. Phys. Chem. C* **2008**, *112*, 11169–11174.

[7] Z. V. Saponjic, R. Csencsits, T. Rajh, N. M. Dimitrijevic, *Chem. Mater.* **2003**, *15*, 4521–4526.

[8] N. R. Jana, X. Peng, *J. Am. Chem. Soc.* **Nov. 2003**, *125*, 14280–1.

[9] M. N. Nadagouda, T. F. Speth, R. S. Varma, *Acc. Chem. Res.* **2011**, *44*, 469–78.

[10] I. Bilecka, M. Niederberger, *Nanoscale* **2010**, *2*, 1358.

[11] S. Horikoshi, H. Abe, K. Torigoe, M. Abe, N. Serpone, *Nanoscale* **2010**, *2*, 1441–7.

[12] B. Liu, X. Li, C. Zheng, X. Wang, R. Sun, *Nanotechnology* **2013**, *24*, 235601.

[13] P. Raveendran, J. Fu, S. L. Wallen, *Green Chem.* **2006**, *8*, 34.

[14] C. J. Orendorff, A. Gole, T. K. Sau, C. J. Murphy, *Anal. Chem.* **2005**, *77*, 3261–6.

[15] L. Xia, H. Wang, J. Wang, K. Gong, Y. Jia, H. Zhang, M. Sun, *J. Chem. Phys.* **2008**, *129*, 134703.

[16] J. Zhang, X. Li, X. Sun, Y. Li, *J. Phys. Chem. B* **2005**, *109*, 12544–8.

[17] Y. Lu, G. L. Liu, L. P. Lee, *Nano Lett.* **2005**, *5*, 5–9.

[18] S. Magdassi, M. Grouchko, O. Berezin, A. Kamyshny, *ACS Nano* **2010**, *4*, 1943–8.

[19] Y. Long, J. Wu, H. Wang, X. Zhang, N. Zhao, J. Xu, *J. Mater. Chem.* **2011**, *21*, 4875.

[20] J. Perelaer, B.-J. de Gans, U. S. Schubert, *Adv. Mater.* **2006**, *18*, 2101–2104.

[21] J. Perelaer, M. Klokkenburg, C. E. Hendriks, U. S. Schubert, *Adv. Mater.* **2009**, *21*, 4830–4.

[22] P. Raveendran, J. Fu, S. L. Wallen, *J. Am. Chem. Soc.* **2003**, *125*, 13940–1.

[23] M. Tsuji, M. Hashimoto, Y. Nishizawa, M. Kubokawa, T. Tsuji, *Chemistry* **2005**, *11*, 440–52.

[24] D. D. Evanoff, R. L. White, G. Chumanov, *J. Phys. Chem. B* **2004**, *108*, 1522–1524.

[25] M. Chen, Y.-G. Feng, X. Wang, T.-C. Li, J.-Y. Zhang, D.-J. Qian, *Langmuir* **2007**, *23*, 5296–304.

[26] B. Wiley, Y. Sun, Y. Xia, *Acc. Chem. Res.* **2007**, *40*, 1067–76.

[27] Y. Sun, Y. Xia, *Science* **2002**, *298*, 2176–9.

[28] H. Jiang, K.-s. Moon, Z. Zhang, S. Pothukuchi, C. P. Wong, *J. Nanoparticle Res.* **2006**, *8*, 117–124.

[29] a. Nirmala Grace, K. Pandian, *Mater. Chem. Phys.* **2007**, *104*, 191–198.

[30] M. H. Ullah, K. Il, C.-S. Ha, *Mater. Lett.* **2006**, *60*, 1496–1501.

[31] D. Meroni, S. Ardizzone, U. Schubert, S. Hoeppener, *Adv. Funct. Mater.* **2012**, *22*, 4376–4382.

[32] G. Cappelletti, S. Ardizzone, D. Meroni, G. Soliveri, M. Ceotto, C. Biaggi, M. Benaglia, L. Raimondi, *J. Coll. Inter. Sci.* **2013**, *389*, 284 –291.

[33] G. Soliveri, R. Annunziata, S. Ardizzone, G. Cappelletti, D. Meroni, *J. Phys. Chem. C* **2012**, *116*, 26405–26413.

[34] G. Maino, D. Meroni, V. Pifferi, L. Falciola, G. Soliveri, G. Cappelletti, S. Ardizzone, *J. Nanopart. Res.* **2013**, *15*, 2087.

[35] X. Zhang, D. O. Hayward, D. M. P. Mingos, *Chem. Commun.* **1999**, 975–976.

[36] M. Rele, S. Kapoor, G. Sharma, T. Mukherjee, *Phys. Chem. Chem. Phys.* **2004**, *6*, 590–595.

[37] D. W. Sheel, L. A. Brook, H. M. Yates, *Chem. Vap. Depos.* **2008**, *14*, 14–24.

[38] X. Y. Ling, R. Yan, S. Lo, D. T. Hoang, C. Liu, M. A. Fardy, S. B. Khan, A. M. Asiri, S. M. Bawaked, P. Yang, *Nano Res.* **2013**, *7*, 132–143.

Chapter 13

Conclusions and prospectives

Nothing ventured, nothing gained.

G. Chaucer
The Canterbury Tales

Chapter 9 and Chapter 11 can be considered the apex of my three years work. At the beginning of my doctoral studies, I approached different projects, apparently unrelated and very fundamental. But, the information and the knowledge that I and my collaborators acquired, were, I would say, fundamental for the development of the next steps. Day after day, the topics started to mix up and to shape one big project focused on the exploration of TiO_2 as the best candidate for the next generation of sensors.

What reported in those two chapters, and in the whole thesis, is the development of proof-of-concept procedures for applicative devices manufacture. That is just the beginning of stimulating and appealing research projects that will be dealt with, in the next years, by my present group and my collaborators. Some of these projects are beginning at the moment I am writing this thesis.

We discovered that polymer brushes, grown on silicon wafer, make silicon electrochemically active. The presence of micrometric structures, like those obtained (in Chapter 9) by remote photocatalysis, seems to enhance the electrochemical response, making feasible, in the next future, the manufacture of integrated electrochemical microsensors. After this new preliminary results, a lot of work must be done for the search of the best micro-structure and the best polymer for each specific analyte.

The self cleaning sensor described in Chapter 11 is, for sure, the most appealing result in this thesis*. In this days, I and my colleagues are working, successfully, to test the detection limit for different neurotransmitters of critical importance in human body. Dopamine, serotonin and norepinephrine are being detected with very good sensitivity and selectivity, also in presence of interferences and in simulated body fluids. The next steps will be, on one hand, the creation of a collaborative network with hospitals and biochemical laboratories, to test it in real biological fluids, the engineerization of the device to make it scalable and, on the other hand, the deep understanding of phenomena that occur during the detection and the self cleaning steps. As a matter of fact, the sensor described was just a proof-of-concept; the TiO_2 assisted self-cleaning feature may constitute a critical component in the next generation of electrochemical sensors.

*The topic was matter for two published papers and one submitted. G. Soliveri *et al.*, *Analyst*, **2015**, *140*, 1486-94 was classified as Analyst *'hot article'*, selected for a note inside *'Chemistry World'*, the magazine of the Royal Society of Chemistry, and featured inside **Scientific American** web page.

Appendix A

Titanium dioxide

Since its commercial production in the early twentieth century, titanium dioxide (TiO_2) has been widely used as a pigment in paints and in personal care products.

In 1972, Fujishima and Honda discovered the phenomenon of photocatalytic splitting of water on a TiO_2 electrode under ultraviolet (UV) irradiation[1]. This event marked the beginning of a new era in heterogeneous photocatalysis. Since then, researchers have devoted great efforts in understanding the fundamental processes and in enhancing the photocatalytic efficiency of TiO_2 [2].Therefore several promising applications have emerged in areas ranging from photovoltaics and photocatalysis to photo-/electrochromics and sensors. Many of these applications depend not only on the properties of the TiO_2 material itself but also on the modifications of the TiO_2 material host and on the interactions of TiO_2 materials with the environment [3]. A great deal of work has been performed over the years, and has led to an understanding that is unprecedented for metal oxide surfaces. One way we have to track this great activity on TiO_2 as photocatalyst is to monitor the Fujishima 1972 paper citations and citations in TiO_2 photocatalysis in general, as shown in Figure A.1.

A.1 TiO_2: Structure and properties

Titanium is the world fourth most abundant metal (exceeded only by aluminium, iron, and magnesium) and the ninth most abundant element (constituting about 0.63% of the earth's crust); it was discovered in England in 1791 by Reverend William Gregor, who recognized the presence of a new element in *ilmenite*. The element was rediscovered several years later by the German chemist Heinrich Klaporth in rutile ore who named it Titanium, after the Titans of the Greek mythology[4].

Titanium dioxide crystallizes in three major different structures: Rutile, Anatase and Brookite. Two additional high-pressure forms have been synthesized from rutile: TiO_2 (II), which has the α-PbO_2 structure, and TiO_2 (H) with the hollandite structure.

Rutile is the most common and stable TiO_2 polymorph. It is present as an accessory mineral in high-pressure and high-temperature metamorphic and igneous rocks. Rutile is the preferred polymorph in such environment because it has the lowest molecular volume among the three polymorphs (the highest density). The first major ore of rutile was discovered in 1803 by Werner in Spain. The name derives from the Latin word *rutilus* (red), in reference to the deep red color observed in some specimens when viewed by transmitted light. It is commonly reddish brown but also yellowish, bluish or violet. Rutile may contain up to 10 % iron, and other impurities such as tantalum, niobium, chromium, vanadium and tin. It is associated with minerals such as quartz, tourmaline, barite, hematite and silicates. Rutile is a

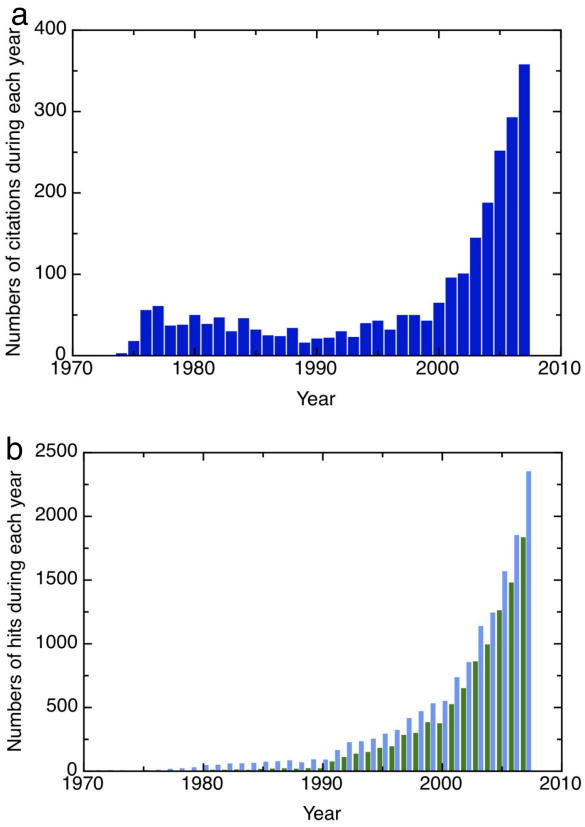

Figure A.1: ***a*** *Citations per year of the 1972 Nature paper: Electrochemical photolysis of water at a semiconductor electrode;* ***b*** *Numbers of research articles appearing on photocatalysis per year: search results in the period of 1972–2007 with the Web of Science (a) by the keyword "photocataly⋆" (blue bars) and (b) the keywords "TiO2 AND photocataly⋆" (green bars). Reprinted from Surf. Sci. Rep., Vol. 63, A. Fujishima et al., TiO_2 photocatalysis and related surface phenomena, pp. 515-582 [1] Copyright 2015 with permission from Elsevier.*

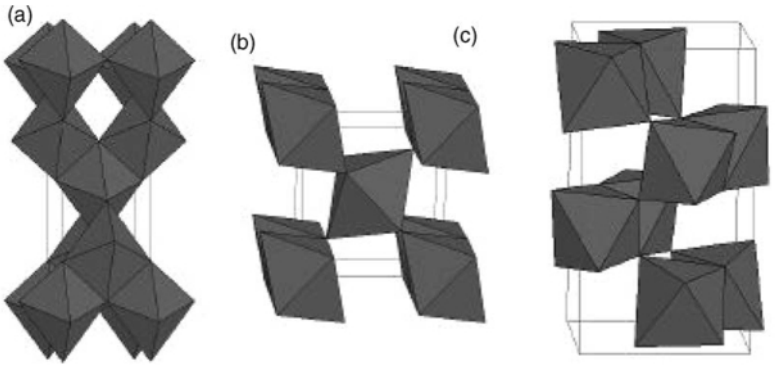

Figure A.2: *Crystal structures of anatase (a), rutile (b), and brookite (c). Reprinted from Progr. Solid State Chem., Vol. 32, O. Carp, C.L. Huisman, A. Reller, Photoinduced reactivity of titanium dioxide, pp. 33-177, Copyright 2015, with permission from Elsevier[4].*

mineral with very high refractive index (2.95), for this reason, it is hugely used as a white pigment.

Brookite was named in honour of the English mineralogist H.J. Brooke; it was discovered by A. Levy in 1825 on the Mount Snowdon (Wales, England). Its crystals are dark brown to greenish black opaque. Crystal forms small tabular to platy crystals, with a pseudohexagonal outline. Associate minerals are anatase, rutile, quartz, feldspar, chalcopyrite, hematite, and sphene. Brookite is the TiO_2 with the grater structural complexity.

Anatase, earlier called Octahedrite, was named by R. J. Hauy in 1801 from the Greek word *anatasis* (extension), due to its longer vertical axis compared to rutile one. It is usually found in nature in small crystals with a variable coloration (from blue to yellow), depending on the type of impurities. It is associated with rock crystal, feldspar, axinite in crevices of granite, mica schist in Dauphine (France) or to the walls of crevices in the gneisses of the Swiss Alps.

The structures of rutile, anatase and brookite can be discussed in terms of (TiO_6^{2-}) octahedrals. The three crystal structures differ by the distortion of each octahedral and by the assembly patterns of the octahedral chains. Anatase can be regarded to be built up from octahedrals that are connected by their vertices, rutile, by the edges, and brookite, by both vertices and edges.

Thermodynamic calculations based on calorimetric data predict that rutile is the most stable phase at all temperatures and pressures up to 60 kbar. For higher pressures, TiO_2 (II) becomes the thermodynamic favourite phase. Anatase and Brokite are metastable, but the small differences in the Gibbs free energy (420 kJ mol^{-1}) between the three phases suggest that they are almost as stable as rutile at normal pressures and temperature.

Since the differences in Gibbs free energy are so small, the relative phase stability can be reversed as a function of particle size. Decreasing the particle size, the surface/volume ratio increases, leading the surface free energy and the surface stresses to grow. Thus, the relative phase stability may be reversed when particle size decreases to a sufficiently low value. The stability size dependence of various TiO_2 phases has recently been described. Rutile is the most stable phase for particles above 35 nm in size, Anatase below 11 nm and Brookite for nanoparticles in the 11 - 35 nm range [1]. These restrictions are not so strong; something different is sometimes reported experimentally.

A.1.1 Basic principle of TiO_2 photocatalysis

The initial process in photocatalysis is the generation of an electron-hole pair in the semiconductor, caused by the light-induced electron promotion from the valence band (VB) to the conductive band (CB). Unlike metals, semiconductors do not possess a continuum of interband energetic levels that can assist the e^- - h^+ recombination. Thus, the e^--h^+ pair has a sufficient lifetime to allow the transfer of the photoexcited electron or hole to a reagent adsorbed at the photocatalyst surface. The process is called heterogeneous photocatalysis if the semiconductor remains intact and the charge transfer to the adsorbed species is continuous and exothermic.

The charge transfer happens at the surface of the photocatalyst. Therefore, electron and hole must migrate to the semiconductor surface, where the electron can reduce an acceptor species (generally O_2 in an aerated environment giving rise to $O_2^{-\cdot}$ superoxide radical and consequently to H_2O_2) and the hole can combine with an electron released by the oxidation of a donor species[5, 6].

The interface charge transfer is more effective if reagents are pre-adsorbed at the photocatalyst surface. Photogenerated holes, h^+, often combine with hydroxyl species adsorbed at the TiO_2 surface, giving rise to hydroxyl radicals OH·, which are active intermediates in the oxidation of other substances[7].

More exhaustive information about TiO_2 , its modification and its photoactivity can be found in many

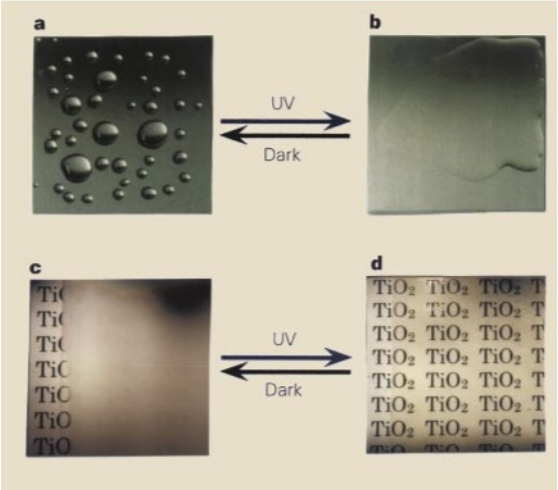

Figure A.3: ***a*** *A hydrophobic surface before ultraviolet irradiation.* ***b*** *A highly hydrophilic surface on ultraviolet irradiation.* ***c*** *Exposure of a hydrophobic TiO_2 -coated glass to water vapour. The formation of fog (small water droplets) hindered the view of the text on paper placed behind the glass.* ***d*** *Creation by ultraviolet irradiation of an antifogging surface. The high hydrophilicity prevents the formation of water droplets, making the text clearly visible. Reprinted by permission from Macmillan Publishers Ltd: Nature (Ref.[11]), copyright 2015.*

review works, *e.g.* Ref. [1, 3, 4, 8–10].

A.1.2 Photo-induced hydrophilic (PIH) effect

Photo-induced phenomenon is fundamental in surfaces and materials development and applications. I am briefly reviewing the characteristics and the mechanism of this effect.

Fujishima's group first discovered that the contact angle of titania films decreased to 0° when the film was irradiated by UV light (Figure A.3)[11]; they termed it *Light-induced amphiphilic surface*. With friction force microscopy, they observed the presence of two different patterns before and after irradiation, as shown in Figure A.4. They hypothesized that the presence of the two types of surfaces at nanometric scale (20-30) were responsible for the hight affinity for both water and organic liquids, hence the term *amphiphilic surface*

More detailed article, published in the following years, showed clearly the reversible growth and decay of a peak (3695 cm^{-1}), assigned to the formation of hydroxyl groups, presumably at the site where there had been dissociative adsorption of water at oxygen vacancies.

Anyway, different mechanisms have been described in literature:

Deposition of organic films. This is the simplest explanation of the phenomenon and the Fujishima group's initial declared thought when first observed photo-induced effect. This mechanism describes PIH effect and photocatalysis in the same way. The less hydrophilic surface is caused by organic pollutant adsorption, that is eliminated under irradiation. When the sample was stored in dark, organic molecules adsorb at the surface, again. Two major works support this opinion.

White et al.[12], through temperature programmed desorption (TPD) studies, came to these conclusions:

- the original TiO_2 surface is hydrophobic without UV illumination, because it is not clean;
- the presence or absence of oxygen vacancies has not discernible effect on the apparent interaction with water;

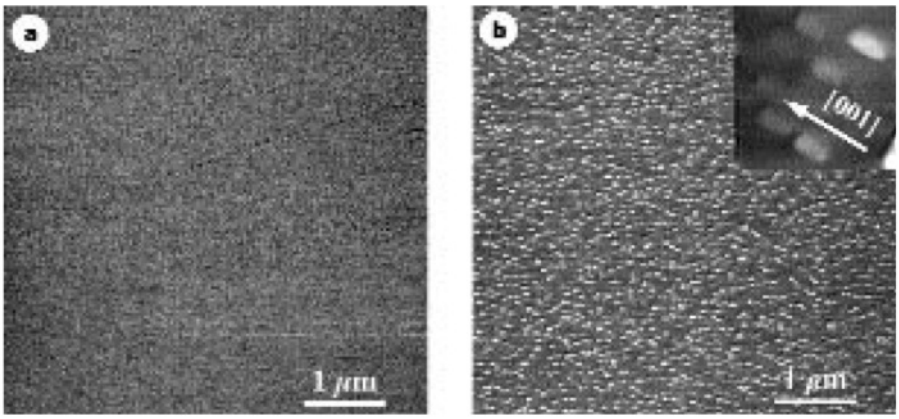

Figure A.4: *FFM images of a rutile TiO_2 (110) single crystal surface.* ***a*** *A $5 \times 5\mu m^2$ image before ultraviolet irradiation.* ***b*** *The same surface after irradiation. Inset, topographic image ($245 \times 245nm$) acquired by rotating the sample stage through 45° to the large-scale image. The tip of the Si_3N_4 cantilever is hydrophilic, so hydrophilic areas are bright and hydrophobic areas are dark.Reprinted from Surf. Sci. Rep., Vol. 63, A. Fujishima et al., TiO_2 photocatalysis and related surface phenomena, pp. 515-582 [1] Copyright 2015 with permission from Elsevier.*

- the photocatalytic removal of an organic monolayers leads to a recovery of hydrophilic properties.

Zubkov et al. [13] show the variance in contact angle adding different amount of exane in gas phase, above the sample. These results are supported by data obtained irradiating in different oxygen amount atmosphere.

Reductive mechanism. UV light produces oxygen vacancies, at which water then dissociates, creating two hydroxyl groups [1]. Menzhenny et al. shows the lack of an effect of reasonable light intensities on the appearance of rutile (100) surfaces with scanning tunnelling microscopy (STM)[14]. Even if there are indeed oxygen vacancies present on the surface, they do not have a measurable effect on the hydrophilic properties, as White showed [12]. It was immediately clear that this mechanism needed to be modified.

Oxidative mechanism. The fact that positive polarization has a strong effect on the hydrophilic phenomenon, demonstrates the importance of photogenerated holes in PIH effect. The mechanism shown in Sakai paper invoked the production of oxygen vacancies, and this could be a weakness, for the reason already discussed. [15]

Combined redox mechanism The photocatalytic mechanism is used to describe the PIH, too. This explanation is particularly useful, because it combines oxidative and reductive mechanism. As Figure A.5 shows, this could explain why oxygen (in Zubkov experiment, [13]) influences the rate[1].

A definitive answer has not already been given. True might be in the middle, as showed by Yan et al. in a recent work [16]; two different stages with two different mechanisms have been observed. The firs step, from higher ranges (*e.g.*, 60°) to the 10° range, might be caused by the destruction of the organic film ($\lambda <$ band gap). The second step, till $\sim 0^\circ$, by a separate effect (not dependent by wavelength).

Most of the experiments that were carried out involved pure anatase TiO_2 films, but it was found that the addiction of 10-30% SiO_2 to a TiO_2 film improved the hydrophilic properties. The presence of SiO_2 helped the films to retain higher surface area and to oppose the thermal conversion of anatase to rutile during film heat treatment[17]. These new kind of material are extremely important for many applications, described later.

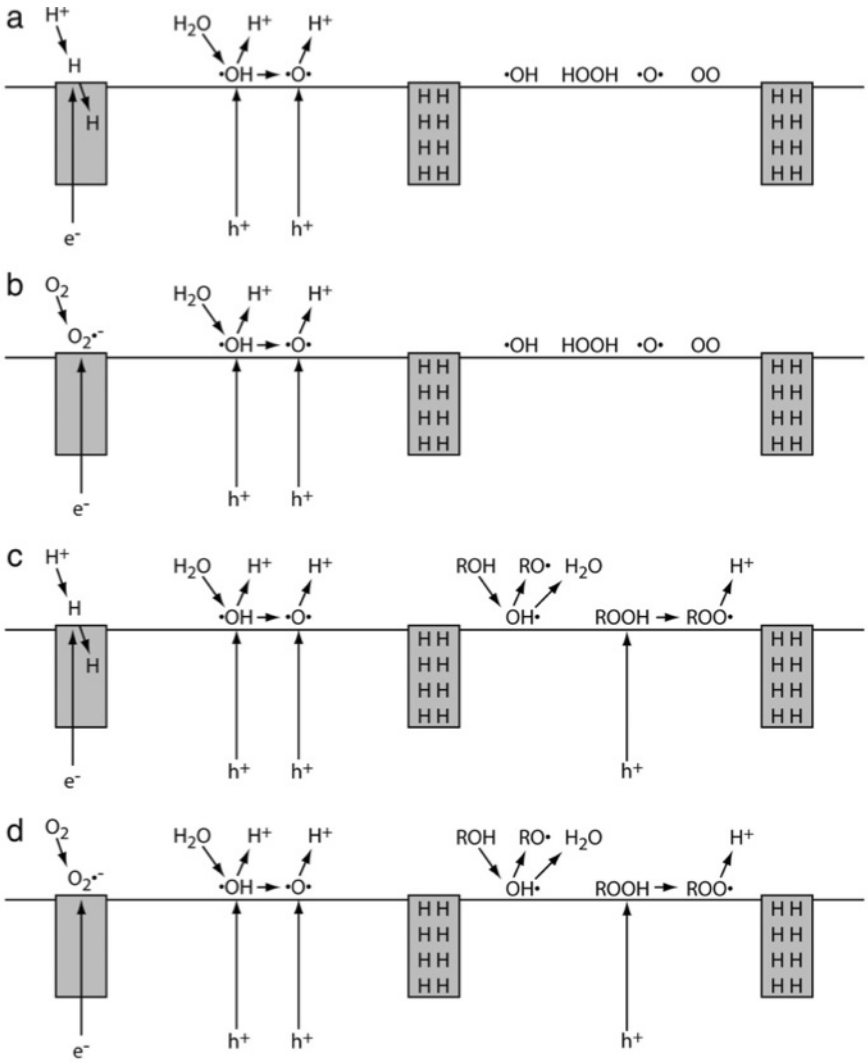

Figure A.5: *Combined reductiveoxidative model for the photo-induced hydrophilic (PIH) effect, in which reducing and oxidizing regions are spontaneously formed:* ***a*** *in the absence of oxygen, protons are reduced to produce interstitial hydrogen atoms (no organic compound present).* ***b*** *in the presence of oxygen, the latter is reduced to superoxide or hydrogen peroxide (no organic compound present);* ***c*** *in the absence of oxygen, protons are again reduced, while an organic compound is oxidized;* ***d*** *in the presence of oxygen, the latter is again reduced, while an organic compound is oxidized. In* ***a*** *and* ***b****, holes react with water to produce a variety of possible hydrophilic moieties.Reprinted from Surf. Sci. Rep., Vol. 63, A. Fujishima et al., TiO_2 photocatalysis and related surface phenomena, pp. 515-582 [1] Copyright 2015 with permission from Elsevier.*

A.2 Applications

Titanium dioxide has received great attention due to its chemical stability, non-toxicity, low cost and other advantageous properties. TiO_2 is used in heterogeneous catalysis, as a photocatalyst, in solar cells for the production of hydrogen and electric energy, as gas sensor, as white pigment (*e.g.* in paints and cosmetic products), as a corrosion-protective coating, as an optical coating, in ceramics, and in electric devices. It plays a role in the biocompatibility of bone implants, is being discussed as a gate insulator for the new generation of MOSFETS (metal-oxide-semiconductor field-effect transistor) and as a spacer material in magnetic spin-valve systems; it finds applications in nanostructured form in Li-based batteries and electrochromic devices.

At the beginning of the 20th century, titanium dioxide replaced toxic lead oxides in the industrial production of white pigment. The volume of pigments produced worldwide is stunning (currently ca. 4 million tons per year). It is used as white pigment in paints (51 %), plastic (19 %), and paper (17 %); the use of TiO_2 has increased in the last few years in a number of minor sectors such as textiles, food, leather, pharmaceutical (from tablet coatings to toothpastes, from sunscreens to cosmetic products) and various titanate pigments.

As a result of its high reflective index, it is used as anti-reflection coating in silicon solar cell and in many thin-film optical devices.

Semiconducting metal oxides may change their conductivity upon gas adsorption, thus, TiO_2 sensors are able to determine oxygen and CO concentrations at high temperatures ($> 600\ ^\circ C$), determining CO/O_2 and CO/CH_4 ratios.

Titanium implants in the humane body have a significant economic and clinical impact in the biomaterial field; there is an increasing interest in the physicochemical nature of the oxide on the surface that provides corrosion resistance, and also contributes to the biological performance of Ti at molecular and tissue level.

TiO_2 is also used in many catalytic reactions as a promoter, as a carrier for metals or metal oxides, as addictive or as catalyst: the selective reduction of NO_x to N_2, hydrogen production by gas shift, Fischer-Tropsch synthesis, CO and H_2S oxidation, reduction of SO_2 by CO, and NO_2 storage are just some of many industrial process in which it is involved.

In the above mentioned areas, the dimension of the titania aggregates is not strictly determinant; in general, milli and micro particles is used. Whereas the most modern and technological applications, in particular those which involve an interaction with an electromagnetic field, need a strict control of the dimension at the nanometric scale.

Really solar cells and photocatalysis represents the most important fields. After the preliminary work of Fujishima and Honda [18], many applications have been developed in these fields. Unfortunately, TiO_2 has low quantum yield for the photochemical conversion of solar energy. However, the use of colloidal suspensions with the addiction of dye molecules improves the efficiency of solar cells so much that has moved TiO_2 -based photoelectrochemical converters into the realm of economic competitiveness. By far, the most actively pursued applied research is its use for photo-assisted degradation of organic compound through the production of radical species. Photogenerated radicals attack any organic molecule adsorbed and this can lead to a complete decomposition into CO_2 and H_2O. Applications range from self-cleaning to self-sterilizing surfaces, from water purification to protective coating in marble (such as the preservation of ancient Greek statues against environmental damage). One of the first commercialized product was the self-cleaning cover glass for highway tunnel lamp in Japan. Nowadays, many buildings are covered by this kind of material in metropolis (in particular in Japan, Figures A.6 and A.7).

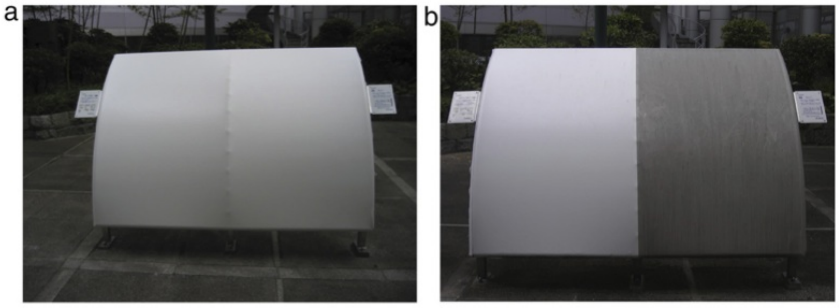

Figure A.6: *Outdoor exposure test for a PVC tent material manufactured by Taiyo Kogyo done in the Photocatalyst Museum, KAST. The left half part of the tent material was coated with TiO_2 .* ***a*** *Picture taken in July 22, 2004.* ***b*** *Picture taken in April 23, 2007. Reprinted from Surf. Sci. Rep., Vol. 63, A. Fujishima et al., TiO_2 photocatalysis and related surface phenomena, pp. 515-582 [1] Copyright 2015 with permission from Elsevier.*

TiO_2 has different application in the water decontamination field. An interesting application is the removal of endocrine disruptor chemicals in the aqueous environment; but this tecnology is also used to water disinfection, remediation of metal contaminates, redox reaction. Normally, no toxic byproducts are generated in the photocatalytic decontamination process; this mark is very attractive for cleaning the water environment, even so cleaning drinking water (for developing country, this is a way to improve public health[19])[1]. The few examples include commercial wastewater treatment installations from Zentox Corporation, Matrix Photocatalytic Inc., Clearwater Industries, Photox Bradford Ltd., Lynntech Inc., and Purifics Environmental Tech- nologies Inc. The principal lack of industrial application is due, principally, to the low photocatalytic efficiency (and the difficulty in the evaluation this efficiency in relation of reactor shape) and to the absence of scale up studies. Many other problems are present:

- the shape of the reactor;
- the material of the transparent walls;
- the post reaction separation of the catalyst;
- the promotion of the reactant adsorption on the catalyst surface and the product desorption.

To solve these problem the use of optical fibers coated with the catalyst was proposed; this is theoretically a good solution, but the efficiency of optical fibre in light transport is still inadequate[20]

The purification of indoor air is another important issue; the available air-cleaning devices based on photocatalytic filters include air cleaners, air conditioners, air-cleaner units for refrigerators, etc. Normally, the range of concentrations of air pollutant that can be efficiently removed is from 0.1 ppm to 10 ppm. The Italian cement company *Italcementi* has created several demonstration projects (in Rome and Paris) to check the actual photocatalytic effect of TiO_2 -coated highway in the conversion of NO_x and SO_x to more environmentally benign forms. In the last few months, Fujishima et al.[21] developed an air purifier with TiO_2-impregnated titanium mesh filter used to remove the cigarette smoke as principal indoor air pollutant. The U-VIX Corporation already developed a commercial prototype (the TITANIUM POWER, Figure A.8).

The PIH effect is already exploited in the anti-fogging area. The fogging of the surfaces of mirrors and glass occurs when moist air cools down on these surfaces, forming many water droplets. Therefore, he visual clarity is impaired drastically. Watanabe and co-workers found that $TiO_2 - SiO_2$ surface could became extremely hydrophilic under UV illumination[22]. The water spreads in a very thin layer with

Figure A.7: *Applications of self-cleaning exterior building materials.* ***a*** *Picture of the MM Towers, in Yokohama, coated with self-cleaning tiles (courtesy of TOTO).* ***b*** *Picture of the Matsushita Denso building covered with self-cleaning glass (courtesy of Nippon Sheet Glass).* ***c*** *Picture of the self-cleaning sound-proof wall (courtesy of Sekisui).* ***d*** *Eco-life-type houses using self-cleaning tiles and glass (courtesy of PanaHome).* ***e*** *Self-cleaning roof of a train station in Motosumiyoshi (courtesy of Taiyo Kogyo). Reprinted from Surf. Sci. Rep., Vol. 63, A. Fujishima et al., TiO_2 photocatalysis and related surface phenomena, pp. 515-582 [1] Copyright 2005 with permission from Elsevier.*

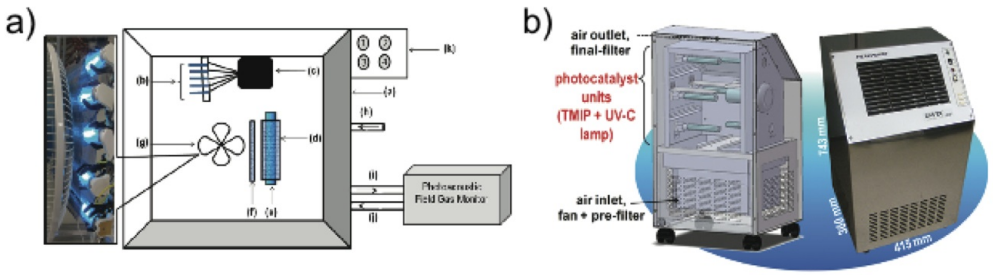

Figure A.8: ***a*** *Schematic diagram of the experimental setup: (a) 1 m^3 reactor; (b) five burned cigarettes; (c) automatic smoker; (d) rolled TMiP catalyst; (e) 10 W UV lamp; (f) flat TMiP catalyst; (g) fan; (h) injection port; (i) gas inlet; (j) gas outlet; and (k) control buttons.* ***b*** *An overview of TITAN POWER. Reprinted with permission from H. Slimen et al., Ind. Eng. Chem. Res., 2012, 51, 587-590[21]. Copyright 2015 American Chemical Society."*

a high visual clarity. The first commercial application of this phenomenon has been for automobile side-view mirrors. The uses of anti-foggy technology are not limited to mirror and glass. One example in our day life is air-conditioner, where an excessive amount of water on the heat exchanger (made by condensation) can reduce the efficiency. Coating the heat exchanger surface with superhydrophilic TiO_2 can hider the fogging and remove the condensed water more effectively.

Moreover rutile is investigated as a dielectric gate material for MOSFET devices as a result of its high dielectric constant ($\varepsilon > 100$), instead of SiO_2 that shows problem in miniaturization. Doped anatase films might be used as a ferromagnetic material in spintronics. Eventually, in batteries, the anatase form is used as an anode material in which lithium ions can intercalate reversibly.

This list of application is far from complete; new ideas and new goals in this fields are only work in progress[1, 4, 9].

A.2.1 Industrial Production

The two principal processes for the production of TiO_2 as pigment start from sulfate and chlorine. In the sulfate process, ilmenite is transformed into iron sulfate and titanium sulfate by reaction with sulphuric acid. Titanium hydroxide is precipitated by hydrolysis and calcinated at 900 $°C$. In this condition, only anatase is produced. To obtain rutile, seed crystals are added during the hydrolysis step. This process has two big disadvantages: the production of iron sulfate waste and the low TiO_2 quality. For these reasons, the chlorine process has become the dominant method. This method produces rutile and starts from ilmenite by Becher process. The iron is reduced in metal iron and reoxidized separating out titanium dioxide (91-93 % purity). The process involves a high temperature furnace to heat the ilmenite with coal and sulfur. The slurry of reduced ilmenite (which consists of a mixture of iron and titanium dioxide in water) is oxidized with air and can be separated in settling ponds. The iron oxide is returned to the mine site as waste and for land filling process. The rutile is reacted with chlorine to produce titanium tetrachloride, which is purified and reoxidized, yielding very pure TiO_2 . The chlorine gas is recycled[4]

Although the wide range and amount of applications, nanometer scale titanium dioxide is suspected to induce DNA damage and genetic instability (as verified in mice by Trouiller et al.[23]). It should be noted that epidemiologic studies of workers exposed to pigment-grade TiO_2 conducted thus far have not been able to detect an association between occupational exposure to TiO_2 and an increased risk for lung cancer. But the presence of more or less nanoscale particles in a so huge commercial products, could be a problem for future human health.

References

[1] A. Fujishima, X. Zhang, D. A. Tryk, *Surf. Sci. Rep.* **2008**, *63*, 515 –582.

[2] A. Linsebigler, G. Lu, J. Yates Jr, *Chem. Rev.* **1995**, *95*, 735–758.

[3] X. Chen, S. S. Mao, *Chem. Rev.* **2007**, *107*, 2891–2959.

[4] O. Carp, C. Huisman, A. Reller, *Prog. Sol. State Chem.* **2004**, *32*, 33 –177.

[5] W. Kubo, T. Tatsuma, *J. Am. Chem. Soc.* **2006**, *128*, 16034–16035.

[6] W. Kubo, T. Tatsuma, *Appl. Surf. Sci.* **2005**, *243*, 125 –128.

[7] L. Rimoldi, MA thesis, University of Milan, **2015**.

[8] K. Nakata, A. Fujishima, *J. Photochem. Photobio. C* **2012**, *13*, 169 –189.

[9] U. Diebold, *Sur. Sci. Rep.* **2003**, *48*, 53–229.

[10] K. Liu, M. Cao, A. Fujishima, L. Jiang, *Chem. Rev.* **2014**, *114*, 10044–10094.

[11] R. Wang, K. Hashimoto, A. Fujishima, M. Chikuni, E. Kojima, A. Kitamura, M. Shimohigoshi, T. Watanabe, *Nature* **1997**, *388*, 431–432.

[12] J. White, J. Szanyi, M. Henderson, *J.Phys.Chem.C* **2003**, *107*, 9029–9033.

[13] T. Zubkov, D. Stahl, T. Thompson, D. Panayotov, O. Diwald, J. Yates Jr, *J. Phys. Chem. B* **2005**, *109*, 15454–15462.

[14] S. Mezhenny, P. Maksymovych, T. Thompson, O. Diwald, D. Stahl, S. Walck, J. Yates, *Chemical physics letters* **2003**, *369*, 152–158.

[15] N. Sakai, A. Fujishima, T. Watanabe, K. Hashimoto, *J. Phys. chem. B* **2001**, *105*, 3023–3026.

[16] X. Yan, R. Abe, T. Ohno, M. Toyofuku, B. Ohtani, *Thin Solid Films* **2008**, *516*, 5872–5876.

[17] M. Machida, K. Norimoto, T. Watanabe, K. Hashimoto, A. Fujishima, *J. Mater. Sci.* **1999**, *34*, 2569–2574.

[18] A. Fujishima, K Honda, *Nature* **1972**, *238*, 37–38.

[19] A. Rincón, C. Pulgarin, *Solar Energy* **2004**, *77*, 635–648.

[20] T. Van Gerven, G. Mul, J. Moulijn, A. Stankiewicz, *Chem. Engin. Process.* **2007**, *46*, 781–789.

[21] H. Slimen, T. Ochiai, K. Nakata, T. Murakami, A. Houas, Y. Morito, A. Fujishima, *Ind. Eng. Chem. Res.* **2012**, *51*, 587–590.

[22] T. Watanabe, A. Nakajima, R. Wang, M. Minabe, S. Koizumi, A. Fujishima, K. Hashimoto, *Thin Solid Films* **1999**, *351*, 260–263.

[23] B. Trouiller, R. Reliene, A. Westbrook, P. Solaimani, R. Schiestl, *Cancer Res.* **2009**, *69*, 8784.

Appendix B

Wettability

Let us start with a kitchen experiment: take a piece of glass, and pass it through the yellow part of the flame of a match. The glass quickly darkens, owing to the deposition of soot. Wait till the temperature gets uniform, and deposit a water drop on this substrate. Through water partially spread on glass (wetting may even be complete if the glass is perfectly clean), the globule adopts on soot the shape of a pearl which rolls off very easily (and in the process becomes coated by the soot particles). If the drop impacts the soot layer, it bounces back; further evidence of water repellency[1].

When a drop of liquid is placed on a solid surface, the triple interface formed between solid, liquid, and gas will move in response to the force arising from the three interfacial tensions until an equilibrium position is established. Figure B.1 shows a droplet of liquid (L) on a solid surface (S) with air (G) as the third phase. The angle θ between the solid and the tangent of the liquid-gas iterface (at the triple interface) is know as contact angle (CA); it is measured by convention in the liquid phase.[2]

The position of the triple interface will change in response to the horizontal component of the interfacial tension acting on it. At the equilibrium, these tensions are in balance:

$$\gamma_s = \gamma_{ls} + \gamma_l cos\theta \qquad \text{(B.1)}$$

This is the Young equation, reported for the first time by Thomas Young in 1805[3]. From this equation, just a value of θ is expected. Although, in real system, even in static condition, at least two angles can be measured, the advancing (θ_a) and receding (θ_r) contact angles. The difference between them is called contact angle hysteresis ($\Delta\theta$)[4]. The hysteresis is due to deviation of a surface from the ideal condition. The existence of many thermodynamic metastable states for system having three-phases boundaries results in hysteresis. A different intrinsic θ is associated with each metastable state. Erbil et al. [5] described five types of causes for hysteresis: surface roughness, microscopic chemical heterogeneity of the surface, drop size effect, molecular reorientation and deformation at the surface, and the size of liquid molecules.

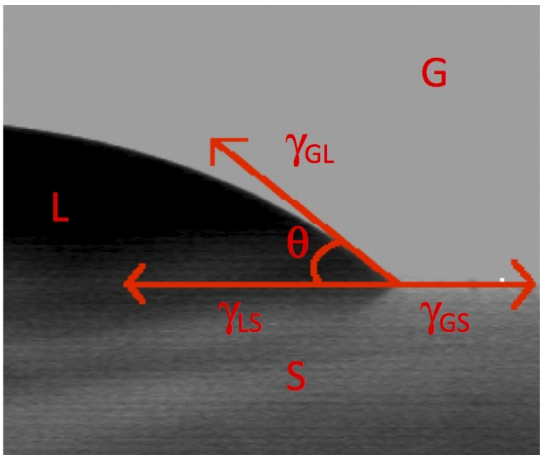

Figure B.1: *The forces acting at the triple interface for a drop of water on a titania surface*

B.1 Determination of the SFE: Owens-Wendt model

Adhesion is one of the basic physical phenomena appearing in various fields of technology and it is significant for many industrial processes. It plays an important role in gluing, printing and coating of polymeric materials. In order to obtain high strength of adhesive joints, the substrate surface has to be fully wetted by the glue, ink, or coating. The physical values of the contact angle (CA) and the surface free energy (SFE) are utilized to characterize and predict adhesive properties of the polymeric materials. Measurements of SFE are a powerful analytical tool widely used in many industrial sectors and for many practical applications, especially for coating, gluing and printing.

The Young's equation (B.1), well known for 200 years, represents a pillar for the determination of SFE of solids. However, in the second half of the 20th century, rapid progress in the interface and wettability field occurred. As a result, new calculation methods for the determination of the SFE were developed, on the ground of contact angle measurements and drop-shape analysis.

Contact angle measurements for SFE determination presents many technical restrictions and scientific dilemmas, *e.g.* the issues of thermodynamic equilibrium, metastable states, shapes, physical interpretation of advancing and receding contact angles[6].

The main methods for the determination of the SFE are those of Zisman [7, 8], Owens-Wendt (OW, known also as the Kaelble method)[9], Wu[10], Neumann's equation of state[11], and the method of van Oss-Chaudhury-Good (vOCG)[12].

In this thesis, the OW method was mostly applied to determine the SFE of smooth surfaces. This model was first described by Owens and Wendt in 1969 [9].

For a better comprehension of the method, the origin of the surface tension in a liquid surface needs to be considered. The tension was generally thought to lie in the superficial first monolayer; even so, in some systems, the contribution of the second or of the third ones were demonstrated. This space is generally called *surface region*, or *interfacial region*. Molecules in the surface region of the liquid phase are under the effect of attractive forces from adjacent molecules, which come from in a net attraction into a bulk phase in the direction normal to the surface. The attraction tends to reduce the number of molecules in the surface region, and that results in an increase of the intramolecular distance. The extension (as in the case of a spring) requires work, and the return of work to the system upon release[13].

As suggested by Fowkes, it is possible to distinguish two main interaction forces in a liquid. One is the function of the specific chemical nature, such as metallic bond or hydrogen bond. The other are correlated to the London dispersion forces, that occur in every kind of existing matter and always make an attractive force between adjacent atoms or molecule similar in chemical nature.

$$\gamma = \gamma^p + \gamma^d \tag{B.2}$$

where (γ^p), (γ^d) are the polar and disperse components, respectively.

First, Fowkes considers the interaction between mercury and a suitable reference liquid, a saturated hydrocarbon; that is particularly useful because of the intramolecular interactions due to London disperse forces (figure B.2). The interface is composed by the two adjacent interfacial regions, and the interfacial tension must therefore be the sum of the tensions in each of this region. In the interfacial region of the hydrocarbon, the molecules are attracted toward the bulk hydrocarbon by intermolecular forces which tend to produce a tension equal to the surface tension of the hydrocarbon (γ_1). However, at the interface, there is also an attraction by the London dispersion forces of the mercury for those hydrocarbon molecules in the interfacial region. These molecules are in a different force field compared to those at the surface of the hydrocarbon because of such interaction, and so the tension in this layer is a function of the

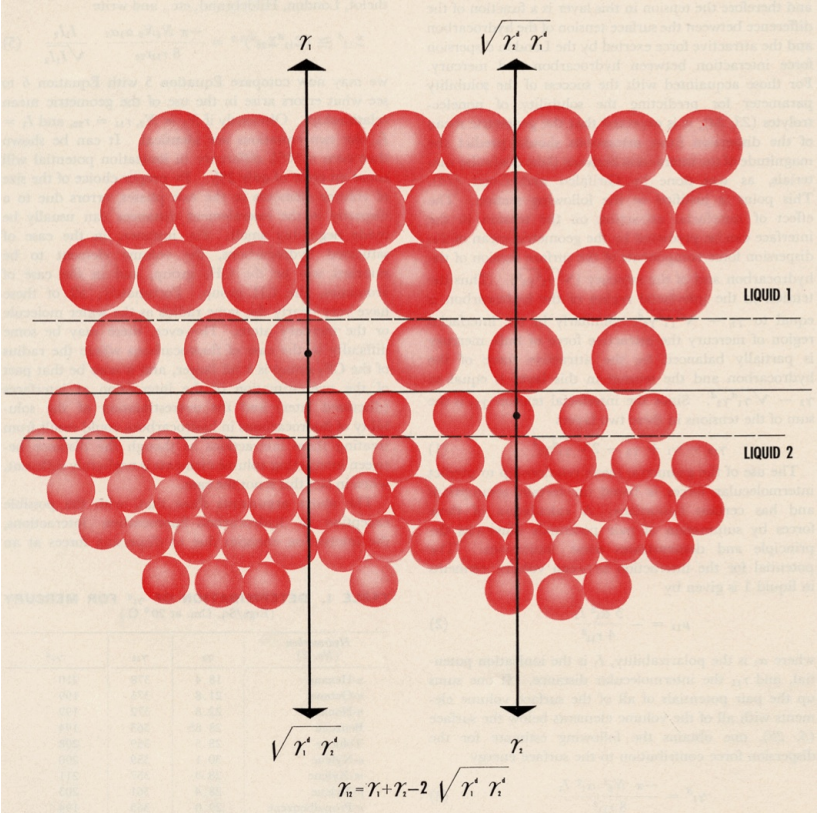

Figure B.2: *Although a very simple model of the interface is used, it gives accurate predictions of wetting, adsorption, and spreading behaviour for many fluids. At the interface between mercury and a saturated hydrocarbon the molecules in the two interfacial regions are subject to the resultant force field mode up of components arising from bulk attractive forces in each phase and the London dispersion forces operating across the interface itself. Reprinted with permission from F. M. Fowkes, Indust. Engin. Chemistry, 1964, 56, 40-52[13]. Copyright 2015 American Chemical Society.*

difference between the surface tension of the hydrocarbon and the attractive force exerted by the London dispersion force interactions between hydrocarbon and mercury. Citing previous study about solubility of nonelectrolytes[14, 15], Fowkes[13] claimed that the geometric mean of the dispersion force attractions should predict the magnitude of the interaction between these dissimilar materials. Thus, the tension in the interfacial region of the hydrocarbon is equal to $\gamma_1 - \sqrt{\gamma_1^d \gamma_2^d}$. The same can be done for the mercury region; the sum of the tensions in these two layers is:

$$\gamma_{12} = \gamma_1 + \gamma_2 - 2\sqrt{\gamma_1^d \gamma_2^d} \tag{B.3}$$

Assuming that $\pi_e = 0$ (equilibrium pressure of adsorbed vapor of the liquid on the solid), this equation could be used in the case of solid-liquid interfaces:

$$\gamma_{sl} = \gamma_s + \gamma_l - 2\sqrt{\gamma_s^d \gamma_l^d} \tag{B.4}$$

Coming back to the Young equation (equation B.1), Fowkes derived:

$$1 + \cos\theta = 2\sqrt{\gamma_s^d}\left(\frac{\sqrt{\gamma_l^d}}{\gamma_{lv}}\right) \tag{B.5}$$

As reported by Owens and Wendt [9], for occurrences in which both cases operate, the eq. B.4 was assumed to have the more general form:

$$\gamma_{sl} = \gamma_s + \gamma_l - 2\sqrt{\gamma_s^d \gamma_l^d} - 2\sqrt{\gamma_s^p \gamma_l^p} \tag{B.6}$$

which can be expressed as:

$$\gamma_{sl} = \left(\sqrt{\gamma_s^d} - \sqrt{\gamma_l^d}\right)^2 + \left(\sqrt{\gamma_s^p} - \sqrt{\gamma_l^p}\right)^2 \tag{B.7}$$

So, in the more general form of eq. B.7, the equation eq. B.5 can be written:

$$1 + \cos\theta = 2\sqrt{\gamma_s^d}\left(\frac{\sqrt{\gamma_l^d}}{\gamma_l}\right) + 2\sqrt{\gamma_s^p}\left(\frac{\sqrt{\gamma_l^p}}{\gamma_l}\right) \tag{B.8}$$

or in a more useful way:

$$\frac{\gamma_l(1 + \cos\theta)}{2\sqrt{\gamma_l^d}} = \sqrt{\gamma_s^p}\sqrt{\frac{\gamma_l^p}{\gamma_l^d}} + \sqrt{\gamma_s^d} \tag{B.9}$$

Testing smooth surfaces with different solvents, of which the disperse and the polar components of the γ_l are known (reported in tab. B.1), it is possible to linearise the equation B.9 in order to obtain the polar and disperse components of the SFE (as reported in figure B.3).

B.2 On water repellency

Water-repellency is a property of some materials which makes water hardly sticking to them: drops roll very easily off and bounce back upon impacting them. This phenomenon was discovered very early, but only in the late nineties it was described deeply by two works: a systematic study of water reppellency in plants (emphasizing the role of micro-texture of the surface)[23] and the description of the manufacture of fractal hydrophobic surface by Kao Engineers (reporting an angle as hight as 174°)[24].

Solvent	γ	γ_d	γ_p	Ref.
Water	72.8	21.8	51.0	[16] [17] [18]
Ethylene Glycol	48.2	18.9	29.3	[19] [18]
EG20-W80	64.3	20.9	43.4	[19]
EG50-W50	57.9	20.0	37.9	[19]
EG70-W30	53.4	19.6	33.8	[19]
EG90-W10	50.5	19.1	31.3	[19]
Diiodomethane	50.8	48.5	2.3	[17]
Diethylene Glycol	44.8	31.6	13.2	[20]
Formamide	58.0	39.0	19.0	[17] [18]
Toluene	28.4	26.1	2.3	[21]
Glycerol	64.0	37.0	27.0	[17]
Glycerol	62.7	21.2	41.5	[22]

Table B.1: *Polar and disperse component of surface tension of different pure solvents used for contact angle analysis.*

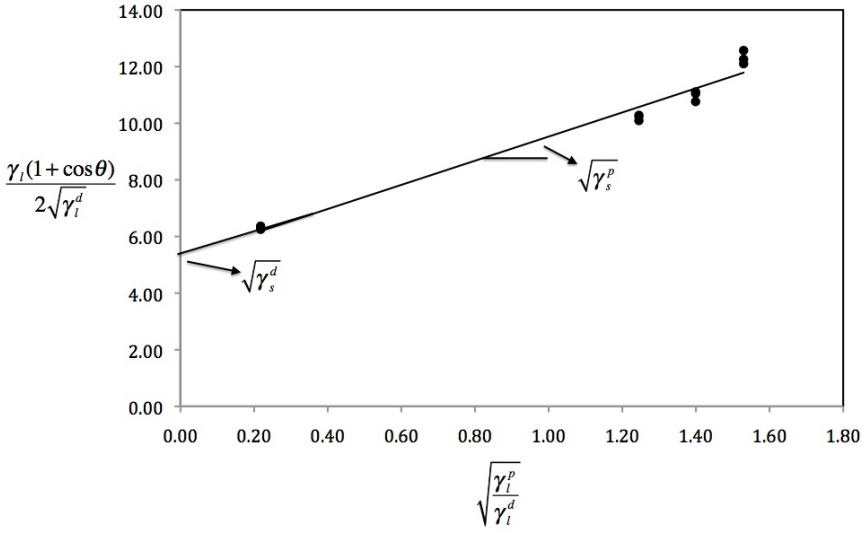

Figure B.3: *Owens Wendt model: linearisation of the eq. B.9. The slope of the line is correlated with the polar component of the SFE, the intercept with the disperse one.*

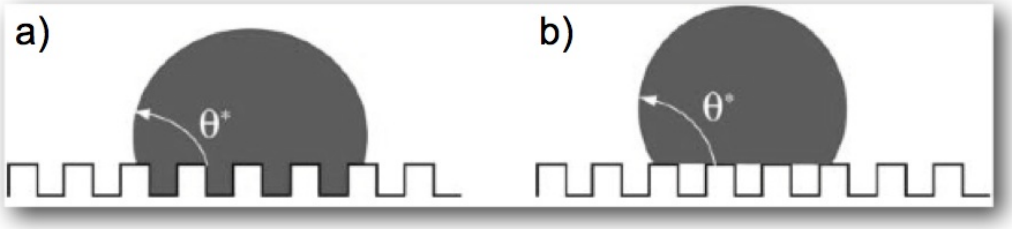

Figure B.4: *The two superidrophobic states:* ***a*** *Wenzel state;* ***b*** *Cassie-Baxter state. Reproduced from Ref. [1] with permission of The Royal Society of Chemistry*

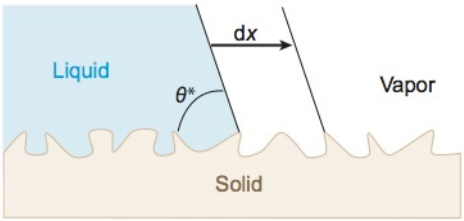

Figure B.5: *The Wenzel picture. One can obtain the apparent contact angle θ^* by considering a small apparent displacement of the contact line and looking at the corresponding variation in surface energy, assuming that the liquid follows the accidents of the solid surface.Reproduced from Ref. [1] with permission of The Royal Society of Chemistry*

Water repellency on solid materials has more than one pysico-chemical origin. These materials are certainly hydrophobic, but they are also microtextured. Two distinct behavior can be described: 1) the liquid fully covers the solid surface (Wenzel scenario); 2) the presence of an air cushion between the liquid and the solid (Cassie-Baxter model). This two models are shown in Figure B.4.

B.2.1 Wenzel model

As described above, the roughness impacts the contact angle hysteresis. That also affects the typical or apparent angle, which is (very) different from that one expected from equation B.1. This was first appreciated by Wenzel[25], using a geometrical argument based on the roughness factor, r, the ratio between the actual surface area and the apparent surface area of a rough surface.

A drop placed on a rough surface (figure B.5) will spread until it finds its equilibrium configuration, characterized by a contact angle θ^* (generally different from the Young angle θ). The key assumption of the model is sketched in figure B.5. As the contact line progresses on the dry solid, it is assumed to follow all the topological variations of the material so that each piece of liquid/air interface gets replaced by a solid/liquid interface of the same surface area. The surface energy variation dE, arising from a displacement dx of the line, can be written (per unit length of the contact line) as:

$$dE = r(\gamma_{sl} - \gamma s)dx + \gamma_l dx \cos\theta^* \tag{B.10}$$

where the second term on the right corresponds to the change of liquid/vapor surface area as the drop spreads. The roughness increases both the solid energies, enhanced geometrically by a factor r. The minimum of E ($dE = 0$) yields equation B.1, if the solid is flat ($r = 1$); if not, we find:

$$\cos\theta^* = r\cos\theta \tag{B.11}$$

where θ is the Young contact angle given by equation B.1. The Wenzel relation (eq. B.11) predicts that roughness enhances wettability. If the factor r is larger than 1, a hydrophilic solid (θ <90°) becomes more hydrophilic when the rough increases ($\theta^* < \theta$). Conversely, a hydrophobic solid ($\theta > 90°$) shows increased hydrophobicity ($\theta^* > \theta$). Although these tendencies are generally (but not always) observed, agreement with equation B.11 is far from to be quantitative. For example, there is no limitation for the effect: the roughness factor can be made arbitrarily large, which seems to imply that complete wetting ($\cos\theta^* > 1$) or complete drying ($\cos\theta^* > -1$) should be induced by large roughness ($r \gg 1$). We show that such behavior is not observed because Wenzel assumptions often are not satisfied. Even when Wenzel relation is likely to be obeyed, it is difficult to check directly whether the relation is being followed. Because the liquid conforms to the roughness, pinning of the contact line is particularly strong in this state, both on the edges of and along the defects. Besides, pushing a Wenzel drop leaves behind cavities filled with liquid such that the drop can also be pinned by the liquid itself. As a consequence, a Wenzel state is generally characterized by very low receding angles and thus giant hysteresis ($\Delta\theta \sim \theta_a$). In such conditions, it is very difficult to extract the sole angle θ^* or to check equation B.11[1].

B.2.2 Cassie-Buxter surfaces

For rough hydrophobic materials with specific morphology, the energy stored for the full interaction between the solid and the liquid is much larger than the energy associated with the air pockets shown in figure B.4-b. In this state (first suggested by Cassie and Baxter[26]), the liquid is in contact with the solid only through the top of the asperities, on a fraction that is described by ϕ_s. If no contact is shown between the solid and the liquid (as for a water drop on a very hot plate, Leidenfrost effect[27]), the *contact angle* would be 180°. Small ϕ_s are close to this extreme situation, and thus associated to high hydrophobicity. More precisely, the contact angle θ^* of such a *fakir* drop (fig. B.4-b) is an average between the angles on the solid ($\cos\theta$), and on the air ($\cos\theta - 1$), respectively weighed by the fractions ϕ_s and $(1 - \phi_s)$, which yields:

$$\cos\theta^* = -1 + \phi_s(\cos\theta + 1) \tag{B.12}$$

For $\theta = 110°$ and $\phi_s = 10\%$,we find that θ^* is about 160°. In this case, 90% of the drop base contacts air. Such circumstance is related to very low hysteresis (typically around 5° to 10°), as first reported by Johnson and Dettre[28]; the liquid has very little interactions with its substrate. θ^* monotonously increases as ϕ_s decreases, suggesting that ϕ_s should be made as small as possible. But reducing ϕ_s also decreases the roughness, so that we reach the critical roughness r_c below which the Wenzel state is favored. The quantity r_c is easily deduced from the intersection of eq. B.11 and eq. B.12, and is found to be:

$$\frac{\phi_s - 1}{\cos\theta} + \phi_s \tag{B.13}$$

which is generally close to $-1/\cos\theta$ (since we will often have: $\phi_s \ll 1$). For θ =120° (a highest value for the Young angle, obtained on fluorinated substrates), the fakir state will thus be favored for roughness factors larger than 2. Conversely, Öner and McCarthy experimentally observed that below a critical density of defects (*i.e.* below a critical roughness), there is indeed a serious deterioration of the water-repellent properties[29].

B.2.3 Water repellent materials and application

More than 200 plants, and many insects are (at least partially) water-repellent (to protect themselves against water). The morphology of the plant surfaces was studied comprehensively by Barthlott and

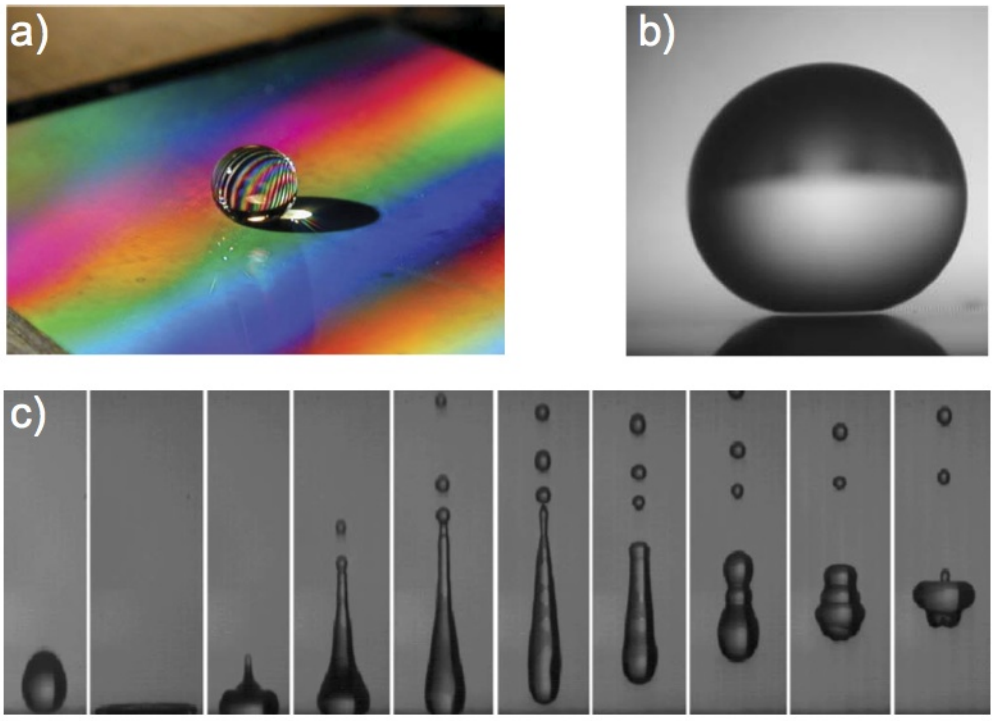

Figure B.6: ***a*** *Millimetric water drop on a hydrophobic surface textured with regularly-spaced micropillars;* ***b*** *millimetric water droplet deposited on a superhydrophobic substrate;* ***c*** *millimetric water droplet bouncing off a superhydrophobic material[29].*

Neinhuis, and many different designs were reported[23]. However, it seems that the most efficient ones (in term of contact angle) consist of two hierarchical structures: typically bumps of about 10 nm, and submicronic microfibers. Such structures decorate, for example, the surface of the lotus leaf, the archetype of a natural water-repellent surface.

These surfaces are thus very rough, which favours robust fakir states. Extending the idea of hierarchical structures naturally leads to fractal surfaces, which were achieved by the Kao group[24], and were indeed found to be superhydrophobic. Contact angles as high as 174° were measured on these surfaces, with a corresponding hysteresis smaller than 5°-yielding amazing non-stick properties for water drops.

On the other hand, microfabrication techniques recently promoted much more regular structures such as pillars (as sketched in figure B.6-a), and such textures was also shown to induce super-hydrophobicity. The picture shows a millimetric water drop sitting on such a substrate, whose colours originate from the regularity of the structures. This was also observed for spherical regularly spaced microbeads; that suggests more generally the possibility of taking advantage from the microtextures to induce further appealing features.

Potentially, the list of applications is impressive: waterproofing of clothes, concrete or paints, anti-rain windshields and window panes, materials of very low friction in water (boat or swimsuits coatings, plastics for microfluidics), etc. The list is even longer considering the improperly so-called *self-cleaning* materials (these surfaces certainly do not self-clean, but they are observed to be cleaner than usual ones). Their *self-cleaning* properties are due to a low surface energy (they are hydrophobic), so that less particles settle on them; rain will wash them, taking with it the dust present at the surface, just because drops do not stick. This is often called the *lotus* effect[29]. Currently, such materials have a limited market penetration due to low hardness and durability, and high costs of manufacture.

B.3 Modification of the surface

There are different ways to modify the surface properties of an oxide material. In the last few year, the most attractive and popular one has been the use of self-assembled monolayer. The term *self-assembled monolayer (SAM)* was coined in 1983 in *New Scientist* in an anonymous report describing the work of Lucy Netzer and Jacob Sagiv[30] on the chemically controlled layer-by-layer self-assembled of multilayer films. From here, SAMs have attracted significant attention; a large variety of self-assembled systems has been studied, including thiols on gold[31], and alkylsilanes on silicon[32], which represents the most popular combinations of self-assembling molecules and substrates[33].

Especially, the use of alkylsilanes on oxide materials has great advantages; silane monolayers show a higher physical and chemical stability in contrast to thiol one. Therefore, it is possible to apply a broader range of chemical reactions to the monolayer. However, the formation of silane SAMs is more complex than the assembly of thiol molecules onto gold substrates. The self-assembled of silane molecules represents additionally an interesting research area as they form covalently attached monolayers on technologically relevant surfaces, in particular, silicon and glass. The functionalization of surfaces provides the possibility to tailor the properties of surfaces, e.g. the wettability, friction, adhesion, and conductivity in a controlled fashion as the modification of the terminal end groups offers the effective tuning of these properties. These surfaces find many applications in a wide range of research areas, such as microelectronics, opto-electronics, thin-film technology, protective coatings, chemical sensors, biosensors, nanotechnology, bioactive surfaces, cell adhesion, protein adsorption and others[34].

Alkylsiloxane monolayers are usually prepared by a covalent adsorption process of self-assembling molecules, such as trichloro-, trimethoxy- or triethoxysilanes, onto the solid substrate (Figure B.7). Not a conclusive answer was done in literature about the reaction mechanism. Whereas Sagiv proposed, for example, the hydrolysis of the chlorosilane molecules and subsequent reaction of te -OH groups with the surface or with other OTS molecules to obtain a polymerized network, other groups proposed a mechanism which go through the reaction of the grafting molecules with an adsorbed layer of water at the substrate. This resulted in the formation of a two-dimensional, cross-linked network of Si-O-Si bonds with only a few bonds to the surface. Additionally, controversy exists in literature concerning the formation of an island-type and/or homogeneous growths. However, the self-assembly process depends on several parameters, such as the water content, the adopted solvent, the age of the solution, the deposition time and the applied temperature, which play an important role in the formation of the monolayer and might have a significant influence also on the monolayer formation process itself, which makes the results rather difficult to compare[34].

The self-assembled molecules consist generally of three parts: the head group, the alkyl chain and the terminal end group. The head group, *i.e.*, trichloro-, trimethoxy- or triethoxysilane, is responsible for the anchoring of the molecules onto the substrate. The alkyl chain provides the stability of the monolayer, due to Van der Waals interactions, and has a significant influence on the ordering of the SAM; the terminal end group introduces chemical functionality into the monolayer system and it is important for the overall properties of surfaces.

All this previous described studies were performed on silicium plates or on glass slides. Scarce investigation on the TiO_2 surfaces is present in the literature, expecially in the case of smooth surfaces (excluding some investigation on monocrystalline TiO_2).

Generally speaking, a comprehensive comparison between SAMs on silica and SAMs on titanium dioxide is somehow problematic as the latter were by far less-extensively studied than the former. It is commonly claimed that silanes capable of cross linking (*i.e.*, having at least three leaving groups) grow by

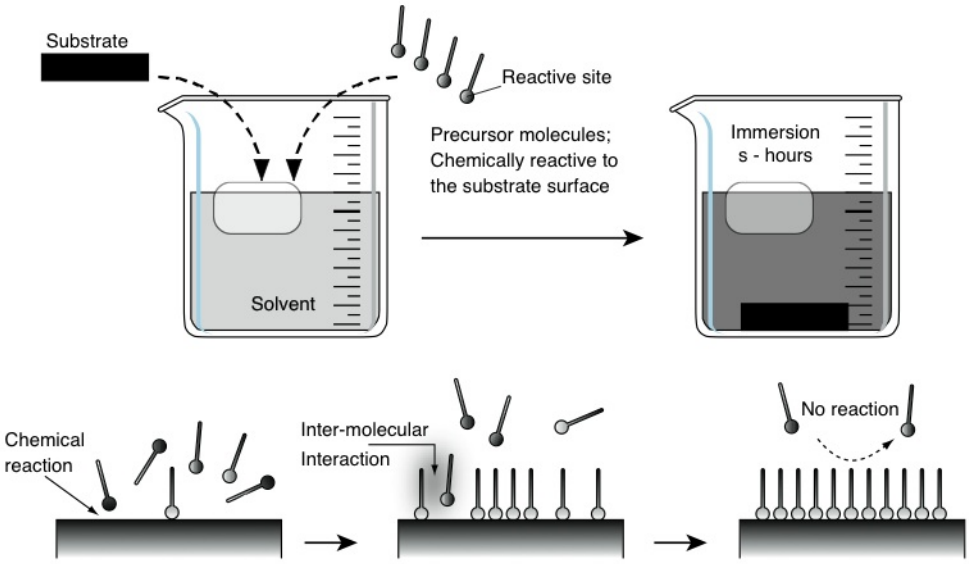

Figure B.7: *Preparation procedure for self-assembled monolayer (SAM)[35].*

an island-like mechanism, whereas SAMs that are not capable of cross linking grow by a uniform growth mechanism. While this is well-established for SAMs on Si, results for organosilanes SAMs on titanium dioxide are much more ambiguous. The lower electronegativity of titanium suggests that the condensation reaction is faster than on SiO_2, and as a consequence the grafting of octadecyl trichlorosilane (OTS) on TiO_2 is faster. Since island formation of OTS molecules requires lateral mobility, which may be impeded if the chemisorption is too strong, the OTS islands on TiO_2 may be expected to be smaller than on SiO_2. There are several indications (most of them based on the FTIR signal of the C-H stretch envelope) that the amount of chemisorbed trichlorosilane molecules is higher in TiO_2 than in SiO_2, possibly due to the presence of surplus water or, in the case of TiO_2 films consisting of sintered nanocrystalline TiO_2, due to a difference between the geometrical area and the true area. Conversely, the density of a protein, immobilized on a substrate through an alkylsilane with a terminal amine group, was observed to be lower on a TiO_2 substrate than on a SiO_2 substrate. Paz et al.[36] claimed that the more ionic character of the Ti-O bond can require higher energies to form Ti-OH groups, leading to lower density of surface hydroxyl groups.

References

[1] M. Callies, D. Quere, *Soft Matter* **2005**, *1*, 55–61.

[2] G. Barnes, I. Gentle, *Interfacial science*, Oxford University Press Oxford, **2005**.

[3] T. Young, *Phil. Trans.* **1805**, *95*, 65–87.

[4] E. Chibowski, *Adv. Coll. Inter. Sci.* **2003**, *103*, 149–172.

[5] H. Erbil, G. McHale, S. Rowan, M. Newton, *Langmuir* **1999**, *15*, 7378–7385.

[6] M. Żenkiewicz, *Polymer Testing* **2007**, *26*, 14–19.

[7] H. Fox, W. Zisman, *J. Coll. Science* **1952**, *7*, 428 –442.

[8] H. Fox, W. Zisman, *Journal of Colloid Science* **1952**, *7*, 109 –121.

[9] D. K. Owens, R. C. Wendt, *J. Appl. Polym. Sci.* **1969**, *13*, 1741–1747.

[10] S. Wu, *J. Adhes.* **1973**, *5*, 39–55.

[11] D Li, A. Neumann, *J. Coll. Interf. Sci.* **1992**, *148*, 190 –200.

[12] C. Van Oss, R. Good, M. Chaudhury, *J. Coll. Inter. Sci.* **1986**, *111*, 378–390.

[13] F. M. Fowkes, *Indust. Engin. Chemistry* **1964**, *56*, 40–52.

[14] J. H. Hildebrand, R. L. Scott, *Solubility of Non-Electrolytes*, Reinhold, N.Y., 3rd ed., **1950**.

[15] J. H. Hildebrand, R. L. Scott, *Regular Solutions*, Prentice-Hall, Edgiwood Cliffs, N.J., **1962**.

[16] E. Chibowski, K. Terpilowski, *J. Colloid Interf. Sci.* **2008**, *319*, 505 –513.

[17] M. Żenkiewicz, *Int. J. Adhes. Adhes.* **2005**, *25*, 61–66.

[18] H. Angellier, S. Molina-Boisseau, M. Belgacem, A. Dufresne, *Langmuir* **2005**, *21*, 2425–2433.

[19] B. Janczuk, T. Bialopiotrowicz, W. Wójcik, *J. Colloid Interf. Sci.* **1989**, *127*, 59–66.

[20] J. Panzer, *J.Colloid Interf. Sci.* **1973**, *44*, 142–161.

[21] J. Schultz, K. Tsutsumi, J. Donnet, *J. Colloid Interf. Sci.* **1977**, *59*, 277–282.

[22] H. Busscher, A. Van Pelt, P. De Boer, H. De Jong, J. Arends, *Coll. Surf.* **1984**, *9*, 319–331.

[23] C. Neinhuis, W. Barthlott, *Ann. Botany* **1997**, *79*, 667–677.

[24] T. Onda, S. Shibuichi, N. Satoh, K. Tsujii, *Langmuir* **1996**, *12*, 2125–2127.

[25] R. N. Wenzel, *Ind. Engin. Chem.* **1936**, *28*, 988–994.

[26] A. B. D. Cassie, S. Baxter, *Trans. Faraday Soc.* **1944**, *40*, 546–551.

[27] J. Leidenfrost, *Int. J. Heat Mass Transf.* **1966**, *9*, 1153–1166.

[28] R. Johnson, R. Dettre, *Adv. Chem. Ser.* **1964**, *43*, 112–135.

[29] D. Qur, *Annu. Rev. Mater. Res.* **2008**, *38*, 71–99.

[30] L. Netzer, J. Sagiv, *J. Am. Chem. Soc.* **1983**, *105*, 674–676.

[31] A. Ulman, *Chemical Reviews* **1996**, *96*, 1533–1554.

[32] S. Wasserman, Y. Tao, G. Whitesides, *Langmuir* **1989**, *5*, 1074–1087.

[33] S. Onclin, B. J. Ravoo, D. N. Reinhoudt, *Angew. Chem. Int. Edit.* **2005**, *44*, 6282–6304.

[34] C. Haensch, S. Hoeppener, U. S. Schubert, *Chem. Soc. Rev.* **2010**, *39*, 2323–2334.

[35] H. Sugimura, Self-Assembled Monolayer on Silicon, Department of Materials Science and Engineering, Kyoto Universuty, **2006**.

[36] Y. Paz, *Beilstein J. Nanotech.* **2011**, *2*, 845–861.

Appendix C

Materials and methods

This Appendix describes all the synthetic and characterization procedures frequently utilized during my thesis work.

C.1 Synthetic procedures

All of the chemicals used in this Thesis were of reagent grade purity and were used without further purification; doubly distilled water passed through a Milli-Q apparatus was utilized.

C.1.1 Synthesis of TiO_2 nanoparticles (NPs)

TiO_2 NPs for superhydrophobic coatings Nanometric TiO_2 powders were prepared by a sol-gel synthesis starting from Ti propoxide (0.13 mol) in 2-propanol (48 mL) by adding water fast under stirring at 65 $°C$ at spontaneous pH (225 mL). The resulting suspension was dried at room pressure at 90 $°C$ and subsequently calcined at 300 $°C$ for 5 h under O_2 stream.

C.1.2 Titania thin films by electrochemically assisted deposition

TiO_2 films were deposited under potentiostatic conditions onto inert substrates from a Ti(IV) stable sol. The sol was synthesized at room temperature by adding HCl 37% (11 mmol) to 160 mL of a 0.6 M solution of $Ti(OC_3H_7)_4$ in ethanol. A non-ionic surfactant (Lutensol ON70, BASF) was then added as a stabilizer (0.47 g dissolved in 130 mL ethanol). Prior to film deposition, the substrates were carefully cleaned by sonication in several solvents (acetone, isopropanol, water). The working and counter electrodes were titanium plates (35 x 150 mm^2), placed at 25 and 20 mm from the substrate, respectively. The two counter electrodes were tilted at 45° with respect to the substrate. The film deposition was performed at 25 $°C$ by applying a 3.6 V deposition voltage between the electrodes for 60 s. The coated substrate was subsequently calcined at 400 $°C$ for 1 h under O_2 flux. Single and multilayers were obtained by repeating the deposition procedure up to 5 times.

C.1.3 Silica films

The silica sol was prepared by the procedure reported by Wang et al.[1] Briefly, 10 g of TEOS was added into a solution containing 25 g of ethanol and 4.5 g of hydrochloric acid solution (0.1 M). The mixture was stirred at lab temperature for 2 hours and then refluxed at 60 $°C$ for 60 min. Eventually, 25 g of an

ethanol solution of the CTAB cationic surfactant (2 g in 25 mL) was dissolved in the as-obtained solution by slowly stirring at lab temperature for 1 hour. The FTO was dipped in such a sol and quickly calcined at 500 $°C$ for 1 hour under N_2 flow.

C.1.4 Oxide functionalization by siloxanes

Substrate pretreatment The Si wafer and the glass slide were cleaned with water and acetone sonication, then treated in Piranha solution (3:1 v/v of H_2SO_4 98% and H_2O_2 30%; *caution!!!* it reacts violently with organic matter) for one hour at 80 $°C$ until a complete water spreading was observed. The substrate was rinsed with water, then dried under N_2 flux. In the powders, the pretreatment in hot piranha solution was replaced by a prolonged UV light irradiation.

Chemical vapor deposition (CVD) In this thesis, the functionalization by CVD was obtained by using a procedure adapted from Sujimura et al.[2]. The substrate was placed in a glass container filled with N_2 gas together with a teflon cup containing 80 mg of the chosen alkylsilane. The container was then placed in an oven at a fixed temperature for 3 h. Different functionalization temperatures were tested in Chapter 5. Finally, the substrate was sonicated in toluene to remove the excess/unreacted alkylsilane. The powders were functionalized using a comparable experimental procedure, in which the amount of alkylsilane was increased to compensate for the larger oxide surface area. The powders were spin-coated (from an alcoholic medium) on a glass slide before insertion in the chamber.

Wet impregnation in alcoholic media In the wet procedure, oxides were functionalised with siloxane molecules as follows: 0.2 g of the oxide powder was dispersed in 10 mL of 2-propanol by sonication. The chosen amount of siloxane (generally 33% w/w) was subsequently added to the titania slurry under vigorous stirring. The solvent was evaporated under reduced pressure (400 mbar, 40 $°C$) using a vacuum oven. The siloxane-TiO_2 composite powders (0.1 g) were suspended in 2-propanol (2 mL), and the resulting dispersion was spin coated (2000 rpm, 20 s) onto previously cleaned glass slides to obtain thin films.

C.2 Characterization procedures

C.2.1 Surface area and porosity

The specific surface area of the oxide samples was determined by means of the Brunauer-Emmett-Teller (BET) procedure using a Coulter SA 3100 apparatus. Desorption isotherms were used to determine the pore size distribution using the Barrett, Joyner, and Halenda (BJH) method.

C.2.2 X-ray diffraction

Room-temperature X-ray diffraction (XRD) patterns were collected on films between 5° and 90° with a powder diffractometer Philips X'Pert $\theta/2\theta$ in grazing angle geometry, $\omega = 1.0°$, utilizing X Cu $K\alpha$ radiation ($\lambda = 1.5416$ Åand power 1.6 kW). The results were obtained on the basis of the Hanawalt method on the data set of PDF-2 (Powder Diffraction File, ICDD).

X-ray powder diffraction (XRPD) experiments were performed using a Philips PW 3710 Bragg-Brentano goniometer equipped with a scintillation counter and 1° divergence slit, 0.2 mm receiving slit, and 0.04° Soller slit systems. Graphite-monochromated Cu K radiation was employed at 40 kV x 40 mA

nominal X-ray power. $\theta : 2\theta$ scans were performed between 20° and 90°. A step size 0.1° wide, for a total counting time of 70 min, was selected on the basis of our past experience on similar samples to maximize the trade-off between the desired accuracy and the available beamtime. A microcrystalline Si powder standard was employed[3] to correct for instrumental line broadening effects. Rietveld refinement was performed by the GSAS software to investigate the microstructure and the crystallographic structure of the TiO_2 powders. A pseudo-Voigt function[4] was employed to model the experimental profile, together with a power series in $Q^{2n}/n!$ and $n!/Q^{2n}$ for describing the background. Surface roughness[5], surface shift and 2θ zero terms were explicitly accounted for in the model. Preferred orientation of crystallites was also modeled by refining suitable spherical harmonic terms[6]. During the last cycles of the refinement, scale coefficient(s), cell parameters, positional coordinates of anatase, and thermal factors were all allowed to vary as well as background and profile coefficients. The integral breadths of individual h0l reflections up to $\sin(\theta/\lambda) = 0.30$ Å^{-1} were computed from the refined profile coefficients[7] and then employed to estimate the average volume-weighted crystallite dimensions, $< D_v >$, by means of the Williamson-Hall method.

C.2.3 UV-Vis spectroscopy

UV-Vis spectra of films and transparency tests were obtained by Beckman DU640 and Shimadzu UV-2600 UV-Vis spectrophotometer.

C.2.4 Dinamic light scattering

The particle size distribution of the oxide powders suspended in water was determined by dynamic light scattering (DLS) using a Nanosizer N4 (Beckman Coulter) and a Zetasizer Nano S ZEN1600 (Malvern Instruments), equipped with mobile lens and laser beam with wavelength 623.8 nm.

C.2.5 Filmetrics

Thickness analyses were performed using a Filmetrics F20 reflectometer. Each value is the average of at least three measurements performed on different spots of a same sample.

C.2.6 Electron microscopies

Scanning electron microscopy(SEM) SAM images of the different oxide particles (Chapter 6) and films (Chapters 11,10) were acquired by a Zeiss LEO 1430 (30 keV), equipped with a backscattered electron detector as well as an energy dispersive X-ray analysis system. The size of the aggregates was evaluated by means of SEM image analysis using the ImageJ software (U.S. National Institute of Health, Bethesda, Maryland, USA, 1997-2012).

SEM picture in Chapters 9 and 11 was performed using a Jeol JSM 7600f Schottky Field Emission Scanning Electron Microscope.

High resolution transmission electron microscopy(HRTEM) HRTEM images were acquired using a JAM 2010 equipped with a LAB6 electron gun (beam energy 200 keV) and a Gatan CCD camera allowing high resolution imaging.

Solvent	γ	γ_d	γ_p	Ref.
Water	72.8	21.8	51.0	[8] [9] [10]
Ethylene Glycol	48.2	18.9	29.3	[11] [10]
EG20-W80	64.3	20.9	43.4	[11]
EG50-W50	57.9	20.0	37.9	[11]
EG70-W30	53.4	19.6	33.8	[11]
EG90-W10	50.5	19.1	31.3	[11]
Diiodomethane	50.8	48.5	2.3	[11]
Diethylene Glycol	44.8	31.6	13.2	[12]
Formamide	58.0	39.0	19.0	[9] [10]
Toluene	28.4	26.1	2.3	[13]
Glycerol	64.0	37.0	27.0	[9]
Glycerol	62.7	21.2	41.5	[14]

Table C.1: *Polar and disperse component of surface tension of different pure solvents used for contact angle analysis.*

C.2.7 Atomic force microscopy

Morphological and further physical properties of surfaces were investigated by atomic force microscopy. Different devices and settings were used, according to the specific need. In Chapter 4 a NTMDT Solver PRO-M working in tapping mode was used; the roughness factor (root mean square) was obtained on areas of 50 x 50 μm^2. In Chapter 9, AFM pictures were acquired on a Ntegra Aura AFM (NT-MDT) device in contact mode, with CSC37 tips (μmasch), and tapping mode, with NSC35/AIBS tips (μmasch).

C.2.8 Wettability

The determination of the wettability properties of distinct surfaces investigated in this thesis was obtained by contact angle (CA) analysis and subsequent calculation of the surface free energy (SFE), by one of the methods described in Appendix B. Static contact angle (θ) measurements of siloxane films were performed on a Krüss Easy Drop using a selected solvents. A drop of 3 μL was produced and gently placed on the surface; the drop profile was extrapolated using an appropriate fitting function. The average of at least five determinations on different parts of the layer, for all the tested film were acquired.

Dynamic CA measurements (advancing (θ_a) and receding (θ_r)) of hybrid siloxane-TiO_2 films were obtained by the following procedure: a drop of 3 μL was placed on the surface (static CA), then the drop size was changed with a speed of 18 μL min^{-1} (dynamic CA). Movies with 100 images were recorded. The reported CAs values are the average of at least five independent determinations taken at different sample locations.

Several high purity solvents were used for the contact angle determinations and subsequent SFE calculation. The purity was in all cases larger than 99.5%. Table C.1 reports the literature surface tensions of the tested liquids with their relative disperse and polar components[8–14]. The choice of the more suitable solvents for each substrate was made on the grounds of both numerical elaborations (total surface tension and polar/disperse ratio) and chemical compatibility.

C.2.9 Thermogravimetric analyses

Thermogravimetric analysis (TGA) of the deposited and uncalcined powders scratched from the film was performed using a Perkin Elmer TGA 7.

C.2.10 X-ray photoelectron spectroscopy (XPS)

XPS analyses were performed by a PHI-5500 Physical Electronics spectrometer, equipped with a monochromatized source with aluminum anode (K = 1486.6 eV) operating at a 200 W of applied power. Samples were placed in UHV (10-9 Torr) and irradiated with 200 kV X-rays, survey scans were recorded at a 23.50 eV pass energy, 0.2 s time per step and 0.5 eV energy-step. XPS spectra were collected at takeoff angles of 45°. The analysis area was 0.8 mm^2 and the depth was within 10 nm. The spectrometer was calibrated assuming the Ag(3d 5/2) binding energy (BE) at 368.3 eV with respect to the Fermi-level and the measured full width half maximum (FWHM) was 0.46 eV. The quantitative analysis data were reported as atomic percentage of elements and the normalization was performed without including hydrogen.

C.2.11 Solid state nuclear magnetic resonance (NMR)

In this thesis, solid state NMR was found to be a powerful tool to describe the organization and the order state of the silane chemisorbed at the oxide surface from a molecular point of view. Here, solid state NMR analyses were carried out using a Bruker Avance 500 spectrometer equipped with a 4-mm MAS broadband probe. ^{13}C and ^{29}Si MAS NMR spectra were recorded at 125.62 and at 99.36 MHz, respectively, packing approximately 0.15 g of solid sample into a 4-mm MAS rotor spinning at 10 kHz and at 300 K. No resolution improvement was found at higher spinning rate and/or temperature. ^{13}C and ^{29}Si nuclei were observed using direct polarization (DP) or cross polarization (CP) methods adopting a procedure that has been previously reported. All chemical shifts were externally referenced to tetramethylsilane.

Concerning ^{29}Si NMR, two different scenarios can be observed depending to the substrate analyzed:

- All the ^{29}Si NMR spectra acquired on SiO_2 display two sets of signals, the first between -85 and -110 ppm (Q^n signals) and the second one between -50 and -70 ppm (T^{n*} signals). The former can be related to the unsubstituted silica surface, while the latter can be assigned to the Si atoms covalently bound to the alkylsilane molecules. Figure 5.6c shows as a representative example that the Q^n and T^{n*} signals of H_150 are composite peaks, showing three resolved resonances. This suggests the co-presence of several Si species with different chemical structures. The same species are present in all other spectra. The peak resolution is not high because the shift between the peaks is small and the width is large. However, we were able to determine the different components by a deconvolution program. On the basis of literature studies[15–17], the three high-field resonances can be assigned (at -93/94, -101 and -108/110 ppm) to geminal silanols Q^2 [$(\equiv SiO)_2$ $Si(OH)_2$], single silanols Q^3 [$(\equiv SiO)_3SiOH$)] and alkoxysilane groups Q^4 [$(\equiv SiO)_4Si$)], respectively. Instead, the low-field resonances (at -51, -59 and -69 ppm) can be related to silicon atoms in position [$(\equiv SiO)SiR(OH/Et)_2$] (denominated as T^{1*}), [$(\equiv SiO)_2Si(OH/Et)R$] (T^{2*}) and [$(\equiv SiO)_3SiR$] (T^{3*}), respectively. A fitting analysis was performed using Lorentzian and Gaussian curves to deconvolute the components and determine the relative ratio of the coexisting structures (Figure 5.6c).

- Concerning TiO_2 samples,typical single signal in the range -50/-60 ppm was observed, corresponding to silicon atoms involved in Si-O-Si and Si-O-Ti bonds between the siloxane molecules and the TiO_2 surface. This signal shows three resolved resonances, suggesting the co-presence of silicon species with different chemical structures. The relative percentages of the coexisting structures of silicon sites were obtained by deconvolution of DP MAS spectra. The fitting analysis, performed with Gaussian curves, and the structures related to the different components are reported in Figure 6.2c. From literature data previously reported for silicon atom coordination[18–20], the three different

resonances at -51.0, -59.0, and -68 ppm, can be attributed to different structures depending on the attachment modes of the siloxane molecule to the TiO_2 surface, respectively, named T^1, T^2 and T^3. In the T^1 structure, the siloxane moieties are bound to the oxide surface only by one Si-O-Ti bond. While in the T^2, the Si atom has two Si-O-Si/Si-O-Ti bonds and one residual OH/OR group. In this case, there are two possible different structures, not discriminated by ^{29}Si NMR: they result from either siloxanes making two Ti-O-Si bonds with the TiO_2 surface (T^2_{Ti}) or siloxanes making one TiOSi bond with the TiO_2 and one Si-O-Si bond with a neighboring siloxane group (T^2_{Ti}). In the T^2 structure, the siloxanes form one Si-O-Ti bond with the titania surface and two Si-O-Si bonds with adjacent siloxane moieties.

C.2.12 Electron paramagnetic resonance (EPR)

EPR spectra were measured at room temperature and at 77 K using an X-band EPR spectrometer (Bruker Elexsys) at the working frequency of 9.4 GHz. The Bruker SimFonia program was used to perform the spectral simulations.

C.2.13 Fourier transform IR (FTIR) analyses

FTIR measurements were carried out with a on a Bruker IFS 113v spectrometer (Chapter 6), equipped with MCT detector, and Bruker IFS 28 spectrometer (Chapter 5) equipped with both MCT and DTGS detectors. Spectra were collected in the 4000-400 cm^{-1} spectral range (4 cm^{-1} resolution and 128 scans). Before the FTIR analyses, all samples were pressed into self-supporting pellets ($\approx$ 10 (mg cm^{-1})), placed in a quartz cell equipped with KBr windows and activated in-vacuo at room temperature by connecting the quartz cell to a conventional high-vacuum glass line (residual pressure $\sim$ 10-4 Torr) in order to remove the species physisorbed at the surface.

C.2.14 Hardness tests

Wolff Wilborn TQC model VF2378 according to the ISO 15184

Adhesion test TQC model CC3000 according to the ISO 2409

C.3 Instrumentation

C.3.1 Lamps for photocatalytic tests

UV lamp. UV iron halogenide lamp Jelosil HG500, effective power density 45 mW cm^{-2} at 40 cm (sample location), emitting mostly between 350 and 450 nm. Emission spectrum in Figure 11.5 (Chapter 11, page 185).

Solar simulator lamp. Halogen lamp by Lot Oriel, effective power density 1 mW cm^{-2} in the range 280-400 nm and 14 mW cm^{-2} in the range 400-800 nm (Figure C.1).

Lamps emissions and power. The emission spectra and the effective power densities were measured by a SM442 Spectrometer (Spectral Products) and a PM100A Optical Power Meter (Thorlabs), respectively.

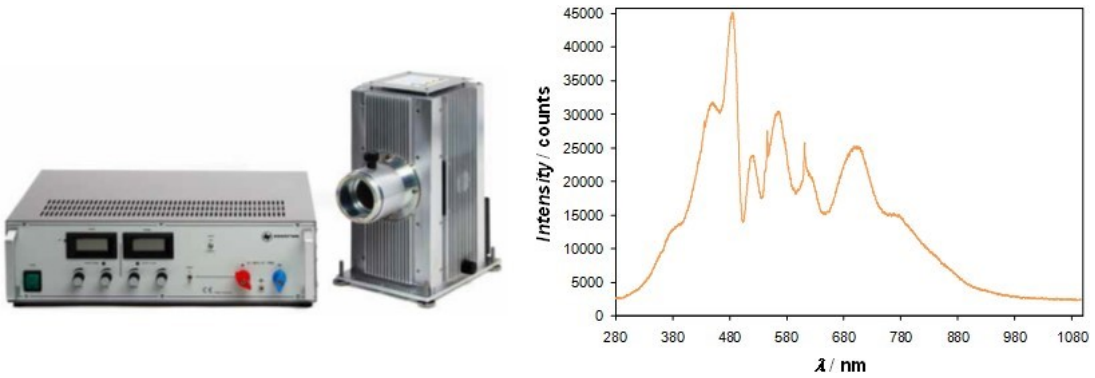

Figure C.1: *The solar simulator lamp and its emission spectrum.*

References

[1] X. Wang, R. Xiong, G. Wei, *Surf. Coat. Tech.* **2010**, *204*, 2187 –2192.

[2] A. Hozumi, K. Ushiyama, H. Sugimura, O. Takai, *Langmuir* **1999**, *15*, 7600–7604.

[3] B. H. Toby, *J. Appl. Cryst.* **2001**, *34*, 210–213.

[4] P. Thompson, D. E. Cox, J. B. Hastings, *J. Appl. Cryst.* **1987**, *20*, 79–83.

[5] W. Pitschke, H. Hermann, N. Mattern, *Pow. Diff* **June 1993**, *8*, 74–83.

[6] H.-J. Bunge, *Texture analysis in materials science: mathematical methods*, Elsevier, **2013**.

[7] D. Balzar, N. Audebrand, M. R. Daymond, A. Fitch, A. Hewat, J. I. Langford, A. Le Bail, D. Louër, O. Masson, C. N. McCowan, N. C. Popa, P. W. Stephens, B. H. Toby, *J. Appl. Cryst.* **2004**, *37*, 911–924.

[8] E. Chibowski, K. Terpilowski, *J. Colloid Interf. Sci.* **2008**, *319*, 505 –513.

[9] M. Żenkiewicz, *Int. J. Adhes. Adhes.* **2005**, *25*, 61–66.

[10] H. Angellier, S. Molina-Boisseau, M. Belgacem, A. Dufresne, *Langmuir* **2005**, *21*, 2425–2433.

[11] B. Janczuk, T. Bialopiotrowicz, W. Wójcik, *J. Colloid Interf. Sci.* **1989**, *127*, 59–66.

[12] J. Panzer, *J.Colloid Interf. Sci.* **1973**, *44*, 142–161.

[13] J. Schultz, K. Tsutsumi, J. Donnet, *J. Colloid Interf. Sci.* **1977**, *59*, 277–282.

[14] H. Busscher, A. Van Pelt, P. De Boer, H. De Jong, J. Arends, *Coll. Surf.* **1984**, *9*, 319–331.

[15] G. Soliveri, D. Meroni, G. Cappelletti, R. Annunziata, V. Aina, G. Cerrato, S. Ardizzone, *J. Mater. Sci.* **2014**, *49*, 2734–2744.

[16] S. Huh, H.-T. Chen, J. W. Wiench, M. Pruski, V. S.-Y. Lin, *Angew. Chem. Int. Edit.* **2005**, *44*, 1826–1830.

[17] D. Kovacek, Z. Maksic, S. Elbel, J. Kudnig, *J. Mol. Struct.* **1994**, *304*, 247 –254.

[18] D. Meroni, S. Ardizzone, G. Cappelletti, M. Ceotto, M. Ratti, R. Annunziata, M. Benaglia, L. Raimondi, *J. Phys. Chem. C* **2011**, *115*, 18649–18658.

[19] F. Milanesi, G. Cappelletti, R. Annunziata, C. Bianchi, D. Meroni, S. Ardizzone, *J. Phys. Chem. C* **2010**, *114*, 8287–8293.

[20] J. Kujawa, W. Kujawski, S. Koter, A. Rozicka, S. Cerneaux, M. Persin, A. Larbot, *Coll. Surf. A* **2013**, *420*, 64 –73.

Appendix D

List of publications

- G. Panzarasa*, S. Aghion, G. Soliveri, G. Consolati, R. Ferragut, Positron Annihilation Spectroscopy: A New Frontier for Understanding Nanoparticle-Loaded Polymer Brushes, *Nanotech.*, **2015**, *accepted*.

- L. Rimoldi, C. Ambrosi, G. Di Liberto, L. Lo Presti*, M. Ceotto, C. Oliva, D. Meroni, S. Cappelli, G. Cappelletti, G. Soliveri, S. Ardizzone, Impregnation versus Bulk Synthesis: How the Synthetic Route Affects the Photocatalytic Efficiency of Nb/Ta: N Codoped TiO_2 Nanomaterials *J. Phys. Chem. C*, **2015**, *in press*.

- V. Pifferi, G. Soliveri, G. Panzarasa, S. Ardizzone, G. Cappelletti, D. Meroni, L. Falciola*, Electrochemical sensors cleaned by light: a proof of concept for on site applications towards integrated monitoring systems, *RSC Advances*, **2015**,*5*, 71210-71214.

- G. Soliveri*, V. Sabatini, H. Farina, M.A. Ortenzi, D. Meroni, A. Colombo, Double side self-cleaning polymeric materials: the hydrophobic and photoactive approach, *Colloids Surf., A*, **2015**, *483*, 285-291.

- G. Soliveri, V. Pifferi, R. Annunziata, L. Rimoldi, V. Aina, G. Cerrato, L. Falciola, G. Cappelletti, D. Meroni*, Alkylsilane-SiO_2 hybrids. A concerted picture of temperature effects in vapor phase functionalization, *J. Phys. Chem. C*, **2015**, *119*, 15390-15400.

- G. Panzarasa*, G. Soliveri, S. Ardizzone,K. Sparnacci, Photocatalytic lithography: an innovative approach to obtain patterned pH-responsive polymer brushes, *Mater. Today: Proceedings*, **2015**, *2*, 4183-4189.

- G. Soliveri,V. Pifferi, G. Panzarasa, S. Ardizzone, G. Cappelletti, D. Meroni, K. Sparnacci, L. Falciola*, Self-cleaning properties in engineered sensors for dopamine electroanalytical detection, *Analyst*, **2015**,*140*, 1486-1494.

  - Paper featured in Chemistry World (RSC,*23rd January*) and in **Scientific America** (*27th January*);
  - Paper selected as **Hot Article** by *Analyst*;
  - Paper included in the RSC *top open access articles* collection.

- G. Panzarasa*, G. Soliveri*,K. Sparnacci, S. Ardizzone, Patterning of polymer brushes made easy using titanium dioxide: direct and remote photocatalytic lithography, *Chem. Commun.*, **2015**, *51*, 7313-7316.

- C. Marchiori, G. Di Liberto, G. Soliveri, L. Loconte, L. Lo Presti*, D. Meroni*, M. Ceotto, C. Oliva, S. Cappelli, G. Cappelletti, C. Aieta, S. Ardizzone, Unraveling the Cooperative Mechanism of Visible-light Absorption in Bulk N,Nb Codoped TiO_2 Powders of Nanomaterials, *J. Phys. Chem. C*, **2014**, *118*, 24152-64.

- A. Antonello, G. Soliveri, D. Meroni, G. Cappelletti, S. Ardizzone*, Photocatalytic Remediation of Indoor Pollution by Transparent TiO_2 films, *Catalysis Today*, **2014**, *230*, 35-40.

- G. Soliveri, D. Meroni*, G. Cappelletti, R. Annunziata, V. Aina, G. Cerrato, S. Ardizzone, Engineered organic/inorganic hybrids for superhydrophobic coatings by wet and vapour procedures, *J. Mater. Sci.*, **2014**, *49*, 2734-2744.

- G. Maino, D.Meroni*, V. Pifferi, L. Falciola, G. Soliveri, G. Cappelletti, S. Ardizzone, Electrochemically Assisted Deposition of Transparent, Mechanically Robust TiO_2 Film for Advanced Applications, *J. Nanopart. Res.*, **2013**, *15*, 2087-2096.

- G. Soliveri, R. Annunziata, S. Ardizzone, G. Cappelletti, D. Meroni*, Multiscale Rough Titania Films with Patterned Hydrophobic/Oleophobic Features, *J. Phys. Chem. C*, **2012**, *116*, 26405-26413.

- G. Cappelletti*, S. Ardizzone, D. Meroni, G. Soliveri, M. Ceotto, C. Biaggi, M. Benaglia, L. Raimondi, Wettability of bare and fluorinated silanes: A combined approach based on surface free energy evaluations and dipole moment calculations, *J. Colloid Interface Sci.* **2013**, *289*, 284-291.